Planar Waveguide CO_2 Laser Amplifiers

By

Qiusheng Cao

Thesis submitted for the degree of Doctor of Philosophy

Heriot-Watt University

Opto-electronics and Laser Engineering

Department of Physics

March 2000

谨以此

纪念我的父亲

和

感谢母亲的哺育之恩

For my parents…

TABLE OF CONTENTS

LIST OF FIGURES

LIST OF TABLES

PUBLICATIONS

1. **Q. Cao**, H. J. Baker, D. R. Hall, "High repetition rate microsecond pulse generation for material processing using a planar waveguide CO_2 MOPA system, " CLEO®/Europe-IQEC 2000, September 2000, Nice, France

2. **Q. Cao**, H. J. Baker, D. R. Hall, "High modulation rate, microsecond pulses for micromachining using a planar waveguide CO_2 laser amplifier, " GCL-HPL 2000, September 2000, Florence, Italy

3. H. J. Baker, **Q. Cao**, A. Chesworth, D. R. Hall, "Waveguide Resonators, " (Invited paper) CLEO®-Europe-IQEC 1998, Glasgow, UK

4. F. Villarrel, P. R. Murray, **Q. Cao**, G. A. Markillie, H. J. Baker, D. R. Hall, "Enhancement of the micromachining capability of CO_2 slab waveguide lasers, " ICALEO®1999, November 1999, San Diego, USA

5. H. J. Baker, G. A. Markillie, P. Field, **Q. Cao**, C. Janke, D. R. Hall, "Precision Laser Processing of Optical Microstructures with Slab Waveguide CO_2 Lasers, " AHPLA'99, November 1999, Osaka, Japan.

6. **Q. Cao**, H. J. Baker, D. R. Hall, "Transverse mode propagation and gain coefficients in a RF-excited, planar waveguide CO_2 laser amplifier, " Submitted to IEEE Journal of Quantum Electronics

PUBLICATIONS

1. **Q. Cao**, H. J. Baker, D. R. Hall, "High repetition rate microsecond pulse generation for material processing using a planar waveguide CO_2 MOPA system, " CLEO®/Europe-IQEC 2000, September 2000, Nice, France

2. **Q. Cao**, H. J. Baker, D. R. Hall, "High modulation rate, microsecond pulses for micromachining using a planar waveguide CO_2 laser amplifier, " GCL-HPL 2000, September 2000, Florence, Italy

3. H. J. Baker, **Q. Cao**, A. Chesworth, D. R. Hall, "Waveguide Resonators, " (Invited paper) CLEO®-Europe-IQEC 1998, Glasgow, UK

4. F. Villarrel, P. R. Murray, **Q. Cao**, G. A. Markillie, H. J. Baker, D. R. Hall, "Enhancement of the micromachining capability of CO_2 slab waveguide lasers, " ICALEO®1999, November 1999, San Diego, USA

5. H. J. Baker, G. A. Markillie, P. Field, **Q. Cao**, C. Janke, D. R. Hall, "Precision Laser Processing of Optical Microstructures with Slab Waveguide CO_2 Lasers, " AHPLA'99, November 1999, Osaka, Japan.

6. **Q. Cao**, H. J. Baker, D. R. Hall, "Transverse mode propagation and gain coefficients in a RF-excited, planar waveguide CO_2 laser amplifier, " Submitted to IEEE Journal of Quantum Electronics

ACKNOWLEDGEMENTS

First of all, it is my great pleasure to thank Prof. Denis R Hall, my supervisor, for providing me with the opportunity to work with the Opto-Electronics and Laser Engineering Group within the Physics Department, and for all the help and invaluable advice I have received.

My sincere gratitude also goes to Prof. Howard J Baker for his encouragement and for communicating to me his knowledge and experience, which have been sources of inspiration through the course of my research work.

I gratefully acknowledge the financial support for this research project from Engineering Physics Science Research Council, United Kingdom, and from Rofin-Sinar GmbH.

I would also like to thank all my academic colleagues for their friendship, and for sharing with me both the satisfaction and anxiety arising from research. I must particularly thank Dr. Francisco J Villarreal, Dr. Gavin A J Markillie, Dr. Jozef Wendland, Dr. Adrian Holdsworth, Dr. David Jones, Dr. Richard Abram, Mr. Paul Murry, Mr. Paul Field, Dr. Graham J Friel, Dr. Bartosz Wasilewski, Mr. Krzysztof Nowak, Mr. Jason R Lee, Mr. Roberto J Ramirez, and my office-mate, Dr. Christian Morhain.

I am also very grateful to the technical and secretarial staff of the university, in particular, Mrs. Linda Bruce and Mrs. Kathleen Defty for all their assistance, and Mr. Steve Haughey for his help with computer facilities.

Finally, I would like to take this opportunity to thank all my friends and family members for all they have contributed to bring this research to fruition. I must specially thank my wife, Wei Chen, who has given me tremendous support, understanding, tolerance and encouragement through out the years.

ABSTRACT

The scaling of diffusion-cooled planar waveguide carbon dioxide laser oscillators to very high average power levels (> 5 kilowatts) is limited by mechanical constraints, associated with the physical size of the laser electrodes. Moreover, the operation of such lasers in pulsed mode is limited to pulse duration larger than ~ 50μs. However, there are important laser applications, for example in material processing, where the requirement is for high peak power level and short pulses combined with high *average* power.

The principal objective of this project is to investigate a laser architecture based on the master oscillator power amplifier concept, but involving *planar waveguide* gain medium structures. Such an amplifier system may be used either for simple power amplification (long pulse/cw) or for amplifying short pulses using a 'pulse forming' modulator at the input for the amplifier. The laser excitation method involves transverse radio frequency discharges designed to match the large area slab-like structures. This excitation technique would permit multiple "stacked" slab operation with a single power generator, and in the future, may facilitate an "integrated" MOPA construction.

The gain and power amplification characteristics of RF discharge excited planar waveguide amplifiers have been investigated over a range of operating parameters (gas pressure, RF power density, input beam intensity etc.) for both pulsed and cw input beams and also for single and multiple (folded) passes of the planar amplifier. Short pulses at the input to the amplifier ($\tau_p \geq 1\mu$sec) were generated using a long pulse oscillator and an acousto-optic modulator as a pulse slicer. In all cases, beam transformation optics were designed and utilised to ensure the excitation of the fundamental waveguide mode with minimal mode coupling. Studies of discharge-induced mode matching effects (phase shifts, amplitude variations) have also been conducted, and techniques for the elimination of parasitic oscillation have been developed. The future potential for the MOPA concept utilising this technology is evaluated for high power laser applications.

CHAPTER ONE

INTRODUCTION

1.1 OUTLINE OF THE RESEARCH

The combination of the transverse radio frequency discharge excitation and optical propagation in hollow dielectric waveguides has boosted considerably the performance of gas lasers since the 1980's. This has been owing to the increased molecular density of the gain medium and much enhanced diffusive cooling ability associated with the small inter-electrode separation (~ 1-3mm), which allow very high power deposition for the stable form, α-type RF discharge [1.1]. Furthermore, the nature of the RF discharge has facilitated the use of the planar (slab) waveguide geometry, which provides large volume active gain medium, allowing substantial power extraction from RF-excited, diffusion-cooled laser devices [1.2] combined with the hybrid waveguide unstable resonators.

To date, sealed-off, low cost RF-excited planar waveguide CO_2 lasers have been available in the market at power levels from a few watts to well above 3kW [1.3], and have been successfully employed in material processing and related applications [1.4]. Because of their compact structures, high power extraction efficiency and good beam quality, they are favoured over gas flow CO_2 lasers which are powerful but big in size, high in running cost, and have inferior beam quality. In addition, these lasers may be operated in pulsed mode, producing discharge-modulated laser pulses with duration longer than 50μs, and repetition rates up to 10kHz, at average powers equal to the cw power.

The area-scalability [1.5] has provided an effective approach for the RF-excited, planar waveguide CO_2 lasers to increase power output capability through the use of larger area electrodes. However, difficulties exist in the manufacturing of very large area electrodes, which limit the scaling of such lasers with a single discharge section to an average power level of ~ 5 kilowatts.

The objectives of the research presented in this thesis are:

(1) To investigate the gain and power amplification characteristics of the planar waveguide CO_2 laser amplifying media excited by transverse RF-discharge.

(2) To develop the concept of the planar waveguide CO_2 laser oscillator/amplifier, as a route *to extend the power output capability* of the planar waveguide CO_2 lasers over the limit set by mechanical constraints, and *to produce high peak power, short laser pulses* (τ_p = 1-50μs).

A MOPA (master oscillator and power amplification) system is designed and constructed, using a 100W slab waveguide laser device as the master oscillator and a 1kW planar waveguide device [1.2] configured as the multipass amplifier. This system has been operated with a cw RF discharge to investigate the characteristics of cw power amplification. It has also been employed for pulsed amplification of pulsed input signal, where an acousto-optic modulator is incorporated as a pulse slicer to produce input pulses over a wide range of pulse width ($\tau_p \geq 1\mu s$).

The main issues investigated can be summarised as follows:

a) Design and implementation of beam transformation optical systems using existing real laser beams and beam transformation theory, to provide required beam coupling between the laser oscillator and the laser amplifier.

b) Investigation of beam launching from free space into planar waveguides, aimed at achieving optimum mode matching, i.e., maximising the input power coupled to the fundamental waveguide mode, and minimising the degree of power coupling to other waveguide modes.

c) Studies of discharge-induced effects (amplitude variations, phase shifts etc.) on the transverse modes travelling in an "active" planar waveguide, i.e. one which incorporates a discharge gain medium.

d) Design and implementation of multipass laser beam folding configuration, aimed at maximising the number of fold passes and therefore the fill factor of the planar waveguide amplifier.

e) Measurement of gain and power amplification characteristics in the cw mode as a function of operating conditions (gas pressure, RF power deposition etc.).

f) Measurement of characteristics of pulsed laser amplification for a wide range of input pulses (widths, shapes, intensities etc.) and operating parameters (gas pressure, RF discharge condition etc.).

g) Demonstration of beam quality preservation, which, in the transverse direction, is closely associated with the waveguide mode matching issue and discharge effects to the waveguide modes travelling through the gain medium.

h) Characteristics of parasitic oscillation and practical solutions.

1.2 LAYOUT OF THE THESIS

This thesis consists of nine chapters. Leading on from this introduction are two review chapters. Chapter 2 gives an overview of the fundamentals of laser amplification in the literature in two main sections. The continuous wave laser amplification section concerns basic concepts of small signal gain, gain saturation and power amplification. The section on pulsed laser amplification introduces first a two-level model, which explains the non-linear effects that an optical pulse experiences when passing through a homogeneous gain medium. This is then followed by a discussion on the effects of relaxation pumping processes, particularly in CO_2 laser systems where the pulsed laser amplification process is considerably complicated by the vibrational-rotational energy level structures. Chapter 3 reviews the development of CO_2 waveguide lasers and outlines the CO_2 gas kinetics related to the excitation and de-excitation mechanisms of the rotational-vibrational levels associated with the 10.6μm laser action. A summary is also given of the waveguide laser resonator configurations, the physics of the RF-discharge excitation and the basic techniques to achieve discharge spatial uniformity.

In chapter 4, Gaussian beam theory, including characterisation, propagation and transformation of the fundamental and higher order Gaussian beam is summarised. This leads to a brief review of the M^2 theory, which characterises the beam quality of any real laser beams and their propagation

through free space and optical systems using the well-known M^2 factor and the beam width based on the second moment definition. A discussion is presented of practical optical systems for real laser beam transformation. One-mirror and two-mirror off-axis transformation optical systems are described as examples of beam coupling optics required between the planar waveguides of the master oscillator and the power amplifier.

Chapter 5 presents the results for transverse mode matching and mode coupling for both passive and active planar waveguides. First, a brief review is given of the characteristics of planar waveguide modes, followed by a discussion of a waveguide mode diagnostic technique for quantifying mode coupling effects using computer simulation. Experiments are then presented that were undertaken to quantify the transverse mode content of the light launched into the planar waveguide amplifier and to observe the discharge-induced perturbations in the planar waveguide gain medium.

Chapter 6 investigates the gain and power amplification characteristics of a MOPA format, planar waveguide CO_2 laser oscillator/amplifier system. The laser oscillator is operated at a high pulse repetition rate producing quasi-cw laser output, while the amplifier is driven by cw RF-discharge. Measurements of the small signal gain coefficient and the saturation intensity are presented as a function of gas pressure and RF power deposition. Amplified power output in the 5 and 7-pass configurations are reported for a range of operational conditions.

Chapter 7 examines pulsed laser amplification characteristics of the MOPA system. An acousto-optic modulator is used as a pulse slicer to allow laser pulse amplification over a wide range of pulse width ($\tau_p \geq 1\mu s$) with pulse shape and amplitude modification. Experimental results are presented of the pulse shape distortion, time-varying gain, pulse energy gain and pulse energy/peak power amplification for a range of gas pressure and discharge conditions in the single pass and the 7-pass configuration. The investigation is extended to a numerical analysis using experimental data, to give a broad view of the laser pulse amplification in the planar waveguide structure.

Chapter 8 deals with the parasitic oscillation issue, which is an inherent and potentially serious problem associated with high-gain amplifiers. Firstly, some theoretical background is presented, followed by presentations of measurements of parasitic oscillation induced power output and its effects on the performance of the laser amplification for two different system configurations. This then moves on to the description of techniques for the suppression and elimination of the parasitic oscillation.

Finally, in chapter 9, conclusions are drawn from the investigations of the cw and pulsed laser amplifications based on the multipass planar waveguide MOPA system, and proposals are made for future work.

REFERENCES

1.1 D. R. Hall and C. A. Hill, "*Radiofrequency-Discharge-Excited CO_2 Lasers*," in Handbook of Molecular Lasers, P.K.Cheo, Ed., New York, Marcel Dekker, 1987

1.2 A. D. Colley, H. J. Baker, and D. R. Hall, "*Planar waveguide, 1kW cw, carbon dioxide laser excited by a single transverse rf discharge*," *Appl. Phys. Lett.*, **61**(2), pp.136-138, July, 1992

1.3 See "*Product Catalogue*," Rofin-Sinar Laser GmbH, 1998

1.4 H. J. Baker, G. A. Markillie, P. Field, Q. Cao, C. Janke, D. R. Hall, "*Precision Laser Processing of Optical Microstructures with Slab Waveguide CO_2 Lasers*, " *AHPLA '99*, November 1999, Osaka, Japan.

1.5 K. M. Abramski, A. D. Colley, H. J. Baker and D. R. Hall, "*Power scaling of large-area transverse radio frequency discharge CO_2 lasers*," *Appl. Phys. Lett.*, **54**, pp.1833-1835, 1989

CHAPTER TWO

LASER AMPLIFICATION: A REVIEW

2.1 INTRODUCTION

This chapter presents an overview of the fundamentals of laser amplification, to provide a theoretical background for the main body of this thesis investigating laser amplification in the MOPA format, using *planar waveguide* gain medium structures. Both continuous wave and pulsed laser amplification are outlined, introducing basic concepts, definitions and expressions which may apply to the subsequent chapters.

High power laser devices often face problems such as optical damage, instability, poor beam quality and so on. These problems are usually associated with large electrical or optical power deposition, bulky mechanical size and cooling/heat-dissipation difficulties. It is also hard, if not impossible, at high power levels to carry out any modulation (frequency, pulse or amplitude modulation etc.) to the laser characteristics. Thus, laser amplification has been a common way to achieve high power laser output, simultaneously with good beam quality and excellent modulation capability. The process is first to generate a stable input laser signal from a low power but well-controlled laser oscillator, and then to amplify this signal through one or more stages of laser amplifiers. This is commonly known as a master-oscillator-power-amplifier or **MOPA** system. Fundamental theory on laser amplification has been well described in a number of textbooks (for example, references [2.1-2.2]).

Apart from the use for power enhancement [2.3-2.5], laser amplifiers have also been used to investigate the gain characteristics of laser media [2.6-2.7], and to aid the analysis of the dynamics of molecular energy levels [2.8-2.9] related to laser processes. Besides, preamplifiers for weak signals have been of interest for laser radar systems to enhance the signal level at increased signal to noise ratio [2.10-2.11]. In recent years, a large number of works have been reported in the literature, using the amplification approach for power enhancement and/or high fidelity, high speed modulation of laser diode pumped solid state lasers [2.5, 2.12]. In addition,

theoretical and experimental research has been reported on power amplification of dye lasers [2.3, 2.13-2.15], which were developed mainly for isotope separation owing to their wavelength tunability and narrow linewidth.

In the CO_2 laser area, most relevant to this thesis, a large number of publications are in the literature (see, for example, references [2.16-2.17]). A recent development was reported in 1996 [2.4], which was a slow flow, DC-excited, multipass commercial amplifier system, capable of 1kW average power output with 100% modulation depth and pulse rate in excess of 200kHz assisted with acousto-optic modulation. However, few publications have been noted concerning CO_2 laser amplification using planar waveguide structures, except for several papers [2.18-2.19] related to the work presented in this thesis.

This chapter is organised as follows. Following this introduction, section 2 is concerned with the gain characteristics and power amplification in continuous wave mode. Section 3 covers some of the characteristics of pulsed laser amplification, in which a two-level model is introduced, followed by discussions about the effects of relaxation pumping, particularly as applied to CO_2 laser systems. The amplified spontaneous emission and the parasitic oscillation problem will not be emphasised in this chapter, but will be discussed in detail in Chapter 8.

2.2 CONTINUOUS WAVE LASER AMPLIFICATION

2.2.1 Gain Characteristics

a) Derivation of gain coefficient

Consider an optical signal of total power P entering a thin slice of atomic gain medium of thickness Δz and transverse area A, which contains atom densities N_1 and N_2 in the lower and upper energy levels of some atomic transition. The total number of atoms in this slice is then $N_1 A \Delta z$ for the lower level, and $N_2 A \Delta z$ for the upper level. The net power absorbed by the atoms in the slice from the incident signal carrying a total power P distributed over the area A is:

$$\Delta P_{abs} = (N_1\sigma_{12} - N2\sigma_{21})P\Delta z \tag{2.1}$$

where σ_{12} is the *stimulated absorption cross section* from the lower level to the upper level, and similarly σ_{21} is the *stimulated emission cross section* (p.180 of [2.2]) from the upper level to the lower level, with both being a function of the frequency ν. Thus, the net power growth or decay with distance due to an atomic transition for the optical signal through an atomic medium can be expressed as:

$$\frac{dP}{dz} = -\lim_{\Delta z \to 0}(\frac{\Delta P_{abs}}{\Delta z}) = (N_2\sigma_{21} - N_1\sigma_{12})P \tag{2.2}$$

This relationship may also be written in terms of the power intensity I by simply replacing P with I. For a degenerate transition, following relationship between the two stimulated transition cross sections exists (p.182 of [2.2]):

$$g_1\sigma_{12} = g_2\sigma_{21} \tag{2.3}$$

where g_1 and g_2 are the degeneracies of the lower and upper levels respectively. If we define *the growth rate of the optical signal passing through an amplifying atomic medium* as the gain coefficient γ, which is also a function of the frequency ν, we have:

$$\gamma = \frac{1}{I}\frac{dI}{dz} = [N_2 - (g_2/g_1)N_1]\sigma_{21} = \Delta N_{21}\sigma_{21} \tag{2.4}$$

where $\Delta N_{21} = N_2 - (g_2/g_1)N_1$, representing the population inversion density between the upper and lower levels. Eq. (2.4) describes the gain coefficient in terms of only the population difference and the stimulated emission cross-section. The latter has been given as (p.186 of [2.2]):

$$\sigma_{21}(\nu) = A_{21}\frac{\lambda^2}{8\pi n^2}g(\nu) \tag{2.5}$$

where A_{21} is the spontaneous emission Einstein coefficient, λ the free-space wavelength, n the refractive index of the gain medium, $g(\nu)$ the line shape function. For most transitions, $g(\nu)$ is either Lorentzian or Gaussian, and is strongly dependent on the gas pressure in gas lasers.

b) Small signal amplification

Eq. (2.4) shows that the gain coefficient for an optical signal passing through a laser amplifier is proportional to the population difference on the amplifying transition. If the optical signal is very weak, the population difference will be little changed during the amplification process. Such a circumstance is referred to as *small signal amplification*, and accordingly we have *small signal gain* and a *small signal gain coefficient*. The small signal gain coefficient can be expressed according to Eqs. (2.4) and (2.5) as:

$$\gamma_0(\nu) = A_{21}\frac{\lambda^2}{8\pi^2}g(\nu)\Delta N_{21} \tag{2.6}$$

where ΔN_{21} is independent of the signal intensity. Under small signal gain conditions, an optical signal passing through the amplifying medium from z_0 to z (z is the optical axis) will experience the small signal gain, which can be expressed as:

$$G_0(\nu) = \frac{I(z)}{I(z_0)} = \exp[\gamma_0(\nu)(z - z_0)] \tag{2.7}$$

Thus the power intensity at z will be:

$$I(z) = I(z_0)\exp[\gamma_0(\nu)(z - z_0)] \tag{2.8}$$

It shows that the intensity of the optical signal grows exponentially with distance along the length of the amplifier. Small signal amplification conditions only hold when the intensity of the input signal is sufficiently weak, and also the amplifier is sufficiently short such that the signal passing through the amplifier will not grow to such degree that it is comparable to the saturation intensity, which is to be discussed next.

c) Gain saturation

For a strong enough input signal the stimulated transition rate may become large enough to saturate the population difference, and thus reduce the gain coefficient seen by the signal. This process is commonly referred to as *gain saturation*. The saturation behaviour in any laser

amplifier can be expected whenever the signal intensity becomes strong enough for the signal itself to reduce its growth.

In the presence of gain saturation, the gain coefficient is dependent on the intensity of the signal passing through the amplifier, and can be expressed as (p.293 of [2.1]):

$$\gamma(\nu) = \frac{\Delta N_0 \sigma_{21}}{1 + I/I_s} = \frac{\gamma_0(\nu)}{1 + I/I_s} \tag{2.9}$$

where $\gamma_0(\nu)$ is the small signal gain coefficient, which is expressed in Eq. (2.6). I_s is the *saturation intensity* which is defined as the value of signal intensity passing through the gain medium that saturates the gain coefficient to half its small signal or unsaturated value, and is given by (p.293 of [2.1]):

$$I_s = \frac{h\nu}{\sigma_{21}\tau_{eff}} \tag{2.10}$$

where τ_{eff} is an effective lifetime or recovery time for the transition. For CO_2 lasers, with a two-level model, Eq. (2.10) may be re-written as (p.184 of 2.20]):

$$I_s = \frac{8\pi^2 h\nu\Delta\nu}{\lambda^2}\tau_r\kappa_u \qquad \kappa_u << \kappa_l(g_l/g_u) \tag{2.11}$$

where $\Delta\nu$ is the Lorentzian half line width, τ_r the radiative lifetime of the 001→100 transition, κ_u, g_u and κ_l, g_l, the relaxation rates and degeneracies of the upper and the lower laser levels. The line width $\Delta\nu$ for homogeneously broadened gain medium has been given as [2.21]:

$$\Delta\nu_h = 7.85(\Psi_{co_2} + 0.73\Psi_{N_2} + 0.64\Psi_{He})P(300/T)^{1/2} \quad \text{MHz} \tag{2.12}$$

where ψ is the partial pressure of each gas, T the gas temperature (Kelvin) and P (Torr) the total pressure. On the other hand, the upper level relaxation rate κ_u has been found proportional to the pressure due to volume quenching of the upper states [2.22]. Thus, these two aspects indicate, via Eq. (2.11), that *the saturation intensity increases linearly with the square of the pressure*.

d) Transversely varying saturation

It has been shown that for a given saturation intensity I_s and small signal gain coefficient $\gamma_0(\nu)$, the gain will saturate with dependency on the signal intensity I. Practically, real laser beams usually have non-uniform transverse intensity profiles, with a Gaussian transverse intensity profile being a typical example. Due to the intensity dependency of the gain saturation, when such a non-uniform beam passes through a saturable amplifier, the more intense parts of the beam will saturate more rapidly than the weaker portions. Thus, the beam profile will be distorted, with the higher-intensity peaks being flattened out relative to the weaker parts.

2.2.2 Power Amplification

An optical signal passing through an amplifier will grow in intensity more or less exponentially with the distance it travels along, beginning with a relatively large gain coefficient. If the amplifier is long enough, sooner or later the optical signal will approach the saturation intensity of the laser medium, and the gain coefficient will drop, therefore the growth of the signal intensity will slow down as the result of gain saturation.

For a single pass amplifier, the most serious saturation effects will be at the output end of the amplifier. The saturation region will move towards the input end as the input signal increases. If the intensity of the input signal is large enough, the saturation intensity may be approached and eventually reached at an early point along the amplifier. The result of the saturation effects is that the output signal is not a linear function of the input signal. However, this behaviour is dependent on the nature of the gain saturation, i.e. whether it is homogeneous or inhomogeneous. At a pressure of 10torr or above, the CO_2 medium is dominated by collisional broadening (p.192 of [2.20]), thus it is appropriate to treat the gain saturation characteristics of the CO_2 medium in the planar waveguide amplifier under investigation as homogeneous broadening.

a) Homogeneously saturating amplifiers

Power amplification

For a single pass amplifier with homogeneous gain medium, the basic differential equation governing the growth rate for the signal intensity along the amplifier takes the form:

$$\frac{1}{I(z)}\frac{dI(z)}{dz} = \frac{\gamma_0}{1+I(z)/I_s} \tag{2.13}$$

where γ_0 is the small signal gain coefficient, I_s the saturation intensity and z the optical axis along the amplifier. Assume an input intensity I_{in} at the input end $z = 0$ and an output intensity I_{out} at the output end $z = L$, this equation is solved, giving the following expression (p.298 of [2.1]):

$$\ln(\frac{I_{out}}{I_{in}}) + \frac{I_{out} - I_{in}}{I_s} = \gamma_0 L = \ln G_0 \tag{2.14}$$

where $G_0 = \exp(\gamma_0 L)$ is the small signal or unsaturated power gain. This expression provides an implicit relationship between the input and output signals, the saturation intensity and the unsaturated gain. Note in the above treatment, the effect of any optical loss that may exist in a practical amplifier is not included.

By introducing the actual gain of the amplifier defined as $G = I_{out}/I_{in}$, Eq. (2.14) can be manipulated in variety of forms to assist the analysis of the amplification process. It has been indicated (p.299 of [2.1]) that the actual gain G begins to be saturated below its small signal value G_0 even at output intensities well below the saturation intensity. In addition, at high enough input intensities the gain always saturates down towards the limiting value $G = 1$, or 0 dB, therefore the amplifier tends to become transparent.

Power extraction and available power

The power extraction per unit area is the output power intensity minus the input power intensity (assuming constant beam size), and is given by (p.299 of [2.1]):

$$I_{extr} = I_{out} - I_{in} = \ln(\frac{G_0}{G}) \times I_s \tag{2.15}$$

Analysis of this equation indicates that for low input intensity and high gain ($G \approx G_0$), the output power and the extracted power are rather similar. As the amplifier begins to saturate, the extracted power approaches a limiting value. This limit is the *maximum power available* for extraction from the amplifying medium, and is given by

$$I_{avail} = \lim_{G \to 1} \ln(\frac{G_0}{G}) \times I_s = (\ln G_0) I_s \tag{2.16}$$

Power extraction efficiency

The *power extraction efficiency* is defined as the ratio of actually extracted power over the available power, and can be obtained as:

$$\eta_{extr} = \frac{I_{extr}}{I_{avail}} = \frac{\ln G_0 - \ln G}{\ln G_0} = 1 - G_{dB} / G_{0,dB} \tag{2.17}$$

It is clearly shown that to extract half the available power in a cw amplifier, one must give up half the small signal dB gain of the amplifier. Thus a single pass amplifier must be driven very hard to extract most of the energy potentially available in the laser medium, and it is difficult to obtain full energy extraction in MOPA systems. One possible solution for improving power extraction efficiency is to send the same beam through the amplifying medium several times. However, this may complicate further the gain saturation process (see, for example, section 8.2 of [2.1]).

b) Amplifiers with saturable gain and non-saturable loss

With non-saturable optical losses present in the amplifier, the basic differential equation Eq. (2.13) for a single pass amplifier with homogeneous gain medium, will change to:

$$\frac{1}{I(z)} \frac{dI(z)}{dz} = \frac{\gamma_0}{1 + I(z)/I_s} - \alpha \tag{2.18}$$

where α is the loss coefficient which is independent of the signal intensity I, supposing the losses are non-saturable. By integrating Eq. (2.18) over the total gain length L of the amplifier, a relationship between the input signal I_{in} and the output signal I_{out} can be established, which may be expressed as (p.324 of [2.1]):

$$\ln(\frac{I_{out}}{I_{in}}) = (\gamma_0 - \alpha)L + \frac{\gamma_0}{\alpha}\ln[\frac{\gamma_0 - \alpha(1 + I_{out}/I_s)}{\gamma_0 - \alpha(1 + I_{in}/I_s)}] \tag{2.19}$$

This equation can be solved iteratively to find the output power (intensity) as a function of the input signal, given the small signal gain coefficient γ_0, loss efficient α and saturation intensity I_s.

c) Measurement of saturation intensity

If the distributed loss is much less than the small signal gain coefficient, i.e. $\alpha << \gamma_0$, Eq. (2.19) may reduce to the form of Eq. (2.14), and may be re-written as:

$$I_{out} - I_{in} = -I_s \ln(\frac{I_{out}}{I_{in}}) + I_s\gamma_0 L \tag{2.20}$$

This equation may also be expressed in terms of power as:

$$P_{out} - P_{in} = -P_s \ln(\frac{P_{out}}{P_{in}}) + P_s\gamma_0 L \tag{2.21}$$

assuming constant beam size along the gain path. Thus, by making a series of measurements of the output power for a range of input power and plotting P_{out}-P_{in} (I_{out}-I_{in}) as a function of $ln(P_{out}/P_{in})$ ($ln(I_{out}/I_{in})$), one obtains a straight line with a slope $-P_s$ (I_s). Theoretically, this treatment requires only two data points. However, in practice, a large number of data points are preferred to improve the accuracy. In addition, this approach for determination of the saturation power (intensity) applies for any range of input powers, but is most accurate with large range of input and appreciable saturation. Eqs. (2.20) and (2.21) have been used in the experiments to determine the saturation intensity as described in Chapter 6.

d) Inhomogeneously saturating amplifiers

Apart from homogeneously broadened laser media, which applies to the work reported in this thesis, there are also other laser media which are inhomogeneously broadened, such as most low-pressure Doppler-broadened gas lasers. Inhomogeneously broadened transitions have quite different and substantially more complex saturation properties than do the homogeneous transitions. The essential feature of a homogeneously broadened transition is that every atom in

the collection of atoms has both the same centre frequency and the same lineshape or frequency response. Therefore, a signal applied to the transition has essentially the same effects on all the atoms in the collection. In contrast, if a strong signal is incident on a collection of inhomogeneously broadened atoms, only the population difference for those subgroups of atoms, or spectral packets, having frequencies in resonance or nearly in resonance with the applied signal frequency will be saturated. The spectral packets at more distant frequencies will be essentially unchanged. Consequently, with increasing saturating intensity, the so-called *hole burning* phenomena will be induced in the atomic absorption curve.

A strong monochromatic signal passing through an inhomogeneously broadened single pass amplifier will saturate in the form described as (see p.232 of reference [2.2]):

$$\frac{dI}{dz} = \frac{\gamma_0 I}{(1+I/I_s)^{1/2}} \tag{2.22}$$

Note the square root in the denominator. This leads to an expression providing an implicit way of computing I_{out} against I_{in} for given values of G_0, I_s for inhomogeneously broadened single pass amplifiers as follows:

$$\frac{\sqrt{1+I_{out}/I_{in}}-1}{\sqrt{1+I_{out}/I_{in}}+1} = \frac{\sqrt{1+I_{in}/I_{in}}-1}{\sqrt{1+I_{in}/I_{in}}+1} \times \exp\left[\gamma_0 L - 2\sqrt{1+I_{out}/I_s} + 2\sqrt{1+I_{in}/I_s}\right] \tag{2.23}$$

2.3 PULSED LASER AMPLIFICATON

Laser amplifiers are maybe much more commonly used for amplifying optical pulses than for amplifying cw optical signals. For pulses short enough when sizeable dispersion is present, significant linear effects may be induced, including pulse broadening or narrowing, associated with the bandwidth of the gain medium (see chapter 9 of [2.1]). For much longer pulses, non-linear pulse distortion may occur, due to time-varying gain saturation effects when a laser pulse is amplified in a homogeneously saturable laser amplifier. As this thesis is only concerned with pulsed laser amplification at pulse duration longer than 1μs, here we mainly focus on the non-linear effects, and assume the laser medium is homogeneously broadened.

2.3.1 A Two-level Model

In the literature, some of the basic aspects of the non-linear effects are explained with a two level model which was firstly proposed by Frantz and Nodvik [2.23]. This model provides an insight into the process of the amplification of a short pulse propagating in a homogeneously broadened uniform gain medium. In this model, the laser pulse is assumed long enough that the amplification process can be described by non-linear time dependent radiation transfer equations. It is also assumed that the gain is not frequency dependent over the spectrum range of the pulse. To simplify the analysis, any pumping effects during the propagation of the pulse and any transverse intensity variations are neglected. In addition, the spontaneous emission is neglected as well, since the time duration of the pulse is small compared to the radiative lifetime of the excited state.

We consider a one-dimensional beam of radiation field intensity I propagating in the z direction, which is incident on an inverted medium occupying the region $0 \leq z \leq L$. If we denote the number densities of the upper and lower laser levels as n_2 and n_1 respectively, the population inversion density is thus $\delta = n_2 - n_1$ with an initial value of δ_0 before the beam enters. The change of intensity of the radiation field is given by [2.23]:

$$\frac{\partial I}{\partial t} + c\frac{\partial I}{\partial z} = c\sigma\delta I \tag{2.24}$$

here σ is the stimulated emission cross section and is considered as constant, independent of the pulse spectrum in this model. It is physically the same as σ_{21} in the last section on cw laser amplification, with the subscripts dropped for simplicity. c is the velocity of the optical pulse travelling through the medium. The population inversion density δ changes as [2.23]:

$$\frac{\partial \delta}{\partial t} = -(2\sigma / h\nu)\delta I \tag{2.25}$$

assuming that during the short pulse the population inversion is only influenced by the radiation field. Combining Eqs. (2.24) and (2.25), the solutions for I and δ can be mathematically obtained as [2.23]:

$$I(z,t) = \frac{I_{in}(t-\frac{z}{c})}{1-[1-\exp(-\sigma\delta_0 z)]\exp\left[-\frac{2\sigma}{h\nu}\int_{-\infty}^{t-\frac{z}{c}} I_{in}(t')dt'\right]} \tag{2.26}$$

$$\delta(z,t) = \frac{\delta_0 \exp(-\sigma\delta_0 z)}{\exp\left[\frac{2\sigma}{h\nu}\int_{-\infty}^{t-\frac{z}{c}} I_{in}(t')dt'\right] + \exp(-\sigma\delta_0 z) - 1} \tag{2.27}$$

where $I_{in}(t)$ is the intensity of the input pulse at $z = 0$. The pulse entering the inverted medium at time t leaves it at time $t + L/c$. Thus for an input intensity $I_{in}(t)$ the corresponding output intensity is:

$$I_{out}(t) = I[L,(t+L/c)] \tag{2.28}$$

Substituting Eq. (2.28) into (2.26) gives the intensity distribution of the outgoing pulse as a function of the intensity distribution of the input pulse. We define the *accumulated signal energies* per unit area $E_{in}(t)$ and $E_{out}(t)$ (sometimes also referred to as *energy fluences*) for the input and outgoing pulses as:

$$E_{in}(t) = \int_{-\infty}^{t} I_{in}(t')dt' \tag{2.29}$$

and

$$E_{out}(t) = \int_{-\infty}^{t} I_{out}(t')dt' \tag{2.30}$$

Then we have (Chapter 10 of reference [2.1]):

$$G(t) = \frac{I_{out}(t)}{I_{in}(t)} = \frac{G_0}{G_0 - (G_0 - 1)\exp\left[-\frac{E_{in}(t)}{E_s}\right]} \tag{2.31}$$

and

$$E_{out}(t) = E_s \ln\left[\frac{G_0 - 1}{G(t) - 1}\right] \tag{2.32}$$

where $G(t)$ is the time-varying gain, and $G_0 = \exp(\sigma\delta_0 L)$ is the small signal or unsaturated gain. $E_S = h\nu/2\sigma$ is the saturation energy, which is clearly the pulse analogue to the saturation intensity

for cw laser amplification, expressed by Eq. (2.10). It indicates that if a signal of an energy fluence E_s flows by an atom in a time much less than the atom's recovery time τ_{eff}, the atom has essentially a 50% chance of making a stimulated transition from one level to the other during the pulse. For a given input $I_{in}(t)$ and a given small signal gain G_0, the output pulse $I_{out}(t)$ can be easily obtained using Eq. (2.31).

Gain saturation and pulse shape distortion

In Eq. (2.31), if we let $t \to 0$, we have obviously $E_{in}(t) \to 0$ and subsequently $G(t) \to G_0$. This indicates that the gain at the leading edge of the pulse is independent of the intensity of the pulse. However, it is anticipated that at any other position the gain decreases in an intensity-dependent manner as a result of gain saturation. In other words, the gain immediately saturates from the leading edge of the pulse from an unsaturated value G_0. Consequently, the laser pulse will be distorted during amplification.

Fig. 2.1 illustrates the pulse distortion assuming a square input pulse with a perfectly sharp leading edge. At the output of the amplifier, we will no longer see a square pulse but one with a sloping top. For a weak input pulse, only a small amount of "droop" in the output pulse is produced. If the input pulse is rather intense, a rapid intensity drop will result, leaving a large spike on the leading edge of the output pulse. However, this pulse distortion is a gradually developed process, beginning at the entrance of the amplifier and becoming more and more serious with increased gain path, regardless of the intensity of the input pulse. In other words, even for a weak input, the pulse distortion can still be rather significant, if the gain path is long enough.

This kind of non-linear pulse-shape distortion will normally result in pulse sharpening (p.368 of [2.1]). This pulse sharpening mechanism might be potentially useful in obtaining a shortened output pulse from a much longer input pulse which has a rise time substantially shorter than the desired output pulse length.

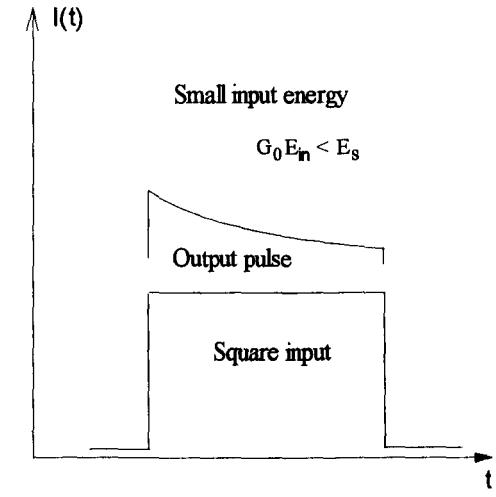

(a) Weak time-varying gain saturation

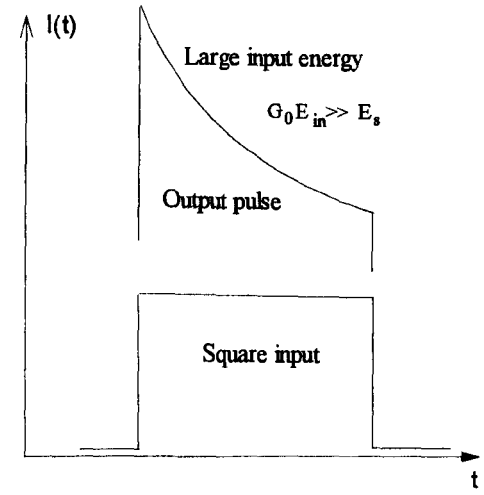

(b) Strong time-varying gain saturation

Figure 2.1 Non-linear distortion of the output pulse with square input

Pulse energy extraction, pulse energy gain and pulse energy efficiency

If we define E_{out} and E_{in} as the total unit area pulse energy contained in the output pulse and the input pulse, E_{out} and E_{in} are then the limits of $E_{out}(t)$ and $E_{in}(t)$ as $t \to \infty$, and the total pulse energy extraction from the gain medium by the complete pulse is thus, according to Eqs. (2.29), (2.31) and (2.32), given as:

$$E_{extr} = E_{out} - E_{in} = E_s \times \ln(G_0/G_f) \tag{2.33}$$

where G_f denotes the final value of $G(t)$ after the pulse has passed, that is, the limit of $G(t)$ as $t \to \infty$. The maximum available energy extraction from the gain medium is obviously obtained when the gain saturates down to $G_f \to 1$. Thus, assuming an input pulse strong enough to completely saturate the initial population inversion, the maximum available energy extraction is given by:

$$E_{avail} = E_s \times \ln G_0 = (h\nu\delta_0 L) / 2 \tag{2.34}$$

which states that the maximum available energy extraction is one half the energy stored in the inverted medium. There are also several other parameters defined to quantify the pulse laser amplification process (see, for example, Chapter 10 of [2.1]). The "*pulse energy gain*" G_{pe} is an overall or averaged effect of the amplification, which is defined as the ratio of the total unit area pulse energy output to the total unit area pulse energy input and is expressed as:

$$G_{pe} = \frac{E_{out}}{E_{in}} \tag{2.35}$$

The *"pulse energy extraction efficiency"* is defined as the ratio of the energy actually extracted from the gain medium to the maximum energy available in the medium and is given by:

$$\eta = \frac{E_{out} - E_{in}}{E_{avail}} = \frac{\ln G_0 - \ln G_f}{\ln G_0} \tag{2.36}$$

A simple expression can be obtained that relates the final gain G_f with the unsaturated gain G_0 and the energy extraction efficiency η:

$$G_f = G_0^{1-\eta} \tag{2.37}$$

This expression shows that if the energy extraction efficiency approaches near 100%, the final saturated gain G_f at the end of the pulse will be much less than the unsaturated gain G_0 at the beginning of the pulse. This requires either a rather strong pulse input, or a very long gain path along which a weak input pulse can grow up considerably. A general relationship between the unsaturated gain G_0, the time-averaged pulse energy gain G_{pe}, and the energy extraction efficiency η, independent of input and output pulse shapes, is given as:

$$G_{pe} = \frac{\ln\left(\frac{G_0 - 1}{G_0^{1-\eta} - 1}\right)}{\ln\left(\frac{G_0 - 1}{G_0^{1-\eta} - 1}\right) - \ln\left(\frac{G_0}{G_0^{1-\eta}}\right)} \tag{2.38}$$

Fig. 2.2 shows how the pulse energy gain rapidly decreases due to saturation as one attempts to achieve increased energy extraction from an amplifier.

2.3.2 Effects of Relaxation Pumping

The two level model has explained some basic aspects for the process of laser pulse amplification. However, the overall laser pulse amplification process is rather complicated in some laser systems, due to the existence of the so-called relaxation pumping [2.24]. In these systems, because of strong coupling among the energy levels, when the upper laser level is depleted by stimulated emission due to the pulse interaction, this level may be refilled by relaxation from other non-lasing levels. These relaxation processes act as pumping sources for the inverted lasing transition and such pumping is referred to as relaxation pumping. A typical example is the CO_2 laser system, which has been extensively studied in the literature to investigate the mechanism of these relaxation processes and their potential influences on the laser pulse amplification [2.25-2.27].

Two physical processes have been recognised in association with laser pulse amplification in CO_2 systems. The first is the interaction of the radiation field with the inverted gain medium, which affects both the pulse shape and the gain distribution under the pulse profile while propagating and is well-described by the two level model. The second process is molecular relaxation. For

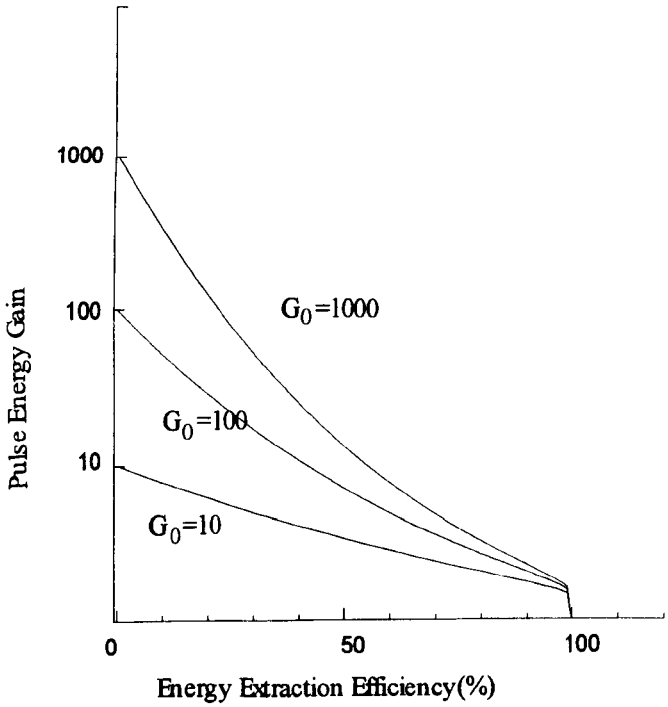

Figure 2.2 Pulse energy gain versus energy extraction efficiency for pulse amplifiers with different unsaturated gain G_0 (reproduced after [2.1])

CO_2 molecules, there are many rotational sublevels that are connected to a vibrational transition and are strongly coupled by molecular collisions. If a rotational upper sublevel is depleted by stimulated emission due to the pulse interaction, this sublevel will be refilled from the non-lasing sublevels in the same vibrational band. Similarly, the population density of the lower sublevel increases as a result of the pulse interaction and a relaxation to other sublevels will follow. In addition, the relaxation process may also take place among vibrational bands during amplification. Moreover, in the presence of N_2 (also CO) in the gas mixture, the resonance energy transfer from excited N_2 (and CO) to $CO_2(00^01)$ may also contribute substantially to the relaxation pumping process, as will be seen in Chapter 7.

The relaxation rates of these processes in CO_2 amplifiers have been found to vary with the gas mixture and pressure of the medium [2.28-2.29]. The effect of the relaxation pumping process must be considered when the product of total gas pressure times the pulse time is comparable to or larger than 5×10^{-10} bar·s [2.24]. Some of these relaxational effects have been numerically analysed by means of a reservoir model [2.25] for pulses of nano-second duration. It appears to be difficult to produce a universal model including all relaxation processes that describes the laser pulse amplification both qualitatively and quantitatively. Thus, in the literature, attention has been mostly devoted to the rotational relaxation effects.

Schappert [2.26] developed a model for short laser pulse amplification taking into account the rotational relaxation effects. In this model, a group of four equations was derived to describe the process of a plane-wave pulse amplifying in a uniform CO_2 medium, considering only the P Branch transition. It is assumed that the equilibrium of the rotational levels in a vibrational state is restored immediately after being disturbed by the radiation field. In addition, two saturation energies are defined as $E_s^0 = h\nu/2\sigma$ and $E_s = E_s^0/P(j)$, where $P(j)$ defines the number of molecules distributed in the rotational level j in a vibrational state. The former has the usual meaning as in the two level model, corresponding to the single rotational level saturation energy and the latter is the all-rotational level or total vibrational level saturation. With this model, the rotational relaxation effects have been investigated in some limiting cases. This model will be

extended in Chapter 7 to include both rotational and vibrational relaxation effects to describe the amplification process for microsecond laser pulses.

2.4 SUMMARY

An overview of the fundamental aspects of laser amplification has been given, providing a theoretical background for the subsequent chapters, particularly Chapter 6 and 7. To characterise a continuous wave laser amplifier, it is essential to have knowledge of the small signal gain coefficient, saturation intensity, as well as the type of the line broadening (homogeneous or inhomogeneous). Chapter 6 will investigate these basic amplification parameters as a function of operational conditions using a planar waveguide gain medium structure in single and multipass configurations.

When an optical pulse propagates through a gain medium, several effects, linear or non-linear, may take place. However, for pulses of micro-second duration, as concerned in this thesis, passing through a homogeneously saturable laser amplifier, it is the non-linear distortion that is dominant, which is the result of *time-varying gain saturation* effects. The two-level model [2.23] has provided a simple but useful approach to explain the mechanism of the evolution of pulse-shapes during the amplification. However, in some practical laser systems such as CO_2, the situations may be more complicated, as energy transfer via relaxation from non-lasing levels to the lasing level exists and acts as a pumping source. It is therefore essential to recognise such relaxation pumping effects for the understanding of the dynamic process of CO_2 laser pulse amplification.

REFERENCES

2.1 A. Siegman, "*Lasers*," University science books, California, 1986

2.2 J. T. Verdeyn, "*Laser Electronics*,", Prentice Hall International Inc., New Jersey, 1995

2.3 R. S. Hargrove and T. Kan, *"High power efficient dye amplifier pumped by copper vapour lasers," IEEE J. Quantum Electron.*, **QE-16**, pp.1108-1113 (1980)

2.4 D. Wheatley, "*A High Power, High Modulation Bandwidth CO_2 Laser*," *SPIE Procee.*, Vol. **3092**, pp.109-113, GCL'96 Edinburgh

2.5 A. C. Wilson, J. C. Sharpe, C. R. Mckenzie, P. J. Manson, and D. M. Warrington, "*Narrow-linewidth master-oscillator power amplifier based on a semiconductor tapered amplifier*," Appl. Physics, **37**, No.21, pp.4871-4875, 20 July 1998

2.6 E. T. Antropov, I. A. Silin-Berkchurin, N. N. Sobolev, and V. V. Sokovikov, "*G-14—Gain Measurement in the CO_2 Laser Discharge*," *J. Quant. Electron.*, **QE-4**, No. 11, November 1968, pp.790-795

2.7 P. K. Cheo and H. G. Cooper, "*Gain Characteristics of CO_2 Laser Amplifier at 10.6 Microns*, " *J. Quant. Electron.*, **QE-3**, No. 2, February 1967, pp.79-84

2.8 I. Burak, Y. Noter, and A. Szoke, "*Vibration-Vibration Energy Transfer in the v_3 Mode of CO_2*," *J. Quant. Electron.*, **QE-9**, No. 5, May 1973, pp.541-544

2.9 R. R. Jacobs, K. J. Pettipiece, and S. J. Thomas, "*Rotational relaxation rate constants for CO_2*," *Appl. Phys. Lett.*, **24**, No. 8, 15 April 1974, pp.375-377

2.10 R. J. Morley, *Ph.D Thesis*, "*RF-Excited CO_2 Amplifiers For Lidar*," *Heriot-Watt University*, 1992

2.11 R. J. Morley, H. J. Baker, D. R. Hall, M. Harris and J. M. Vaughan, "*Enhancement of coherent laser radar performance by predetection amplification*," *Appl. Optics*, **33**, No. 18, pp.3951-3963, 20 June 1994

2.12 T. Graf, U. Roth, M. Schmid, J. E. Balmer, H. P. Weber, "*Diode-pumped Nd:YAG amplifier for intersatellite optical communication*," *Optics Communications*, **152**, No. 4, pp. 302-306(5), 1 July 1998

2.13 M. Maeda and M. Uchiumi, "*Optimum Design of a Multi-Stage Dye-Laser Amplifier Pumped with Cu-Vapor Lasers*," *Rev. Laser Eng.* (The Laser Society of Japan, Osaka) **18**, pp.474-484(1990)

2.14 K. Takehisa, "*New designs and simulations of a 10kW average power longitudinally pumped dye laser amplifier*," *Appl. Opt.*, **33**, pp.6360-6367(1994)

2.15 K. Takehisa, "*Scaling up of a high average power dye laser amplifier and its new pumping designs*," *Appl. Opt.*, **36**, pp.584-592(1997)

2.16 M. B. Klein and R. L. Abrams, "*10.6-μm Waveguide Laser Power Amplifier*," *J. Quant. Electron.*, **QE-11**, No. 8, August 1975, pp.609-615

2.17 S. A. Trushin and V. V. Churakov, "*Theory of high power CO_2 molecular amplifiers*," *Sov. J. Quant. Electron.*, **7**, No. 2, February 1977, pp.212-216

2.18 H. J. Baker, Q. Cao, A. Chesworth, D. R. Hall, "*Waveguide Resonators*, " (Invited paper) *CLEO®-Europe-IQEC 1998*, Glasgow, UK

2.19 F. Villarrel, P. R. Murray, Q. Cao, G. A. Markillie, H. J. Baker, D. R. Hall, "*Enhancement of the micromachining capabilities of CO_2 slab waveguide lasers*, " *ICALEO®1999*, November 1999, San Diego, California, USA

2.20 P. K. Cheo, "*CO_2 Lasers*," *Chapter 2, Lasers*, edited by Levine and Demaria, 1971, Marcel Dekker, Inc., New York

2.21 R. L. Abrams, "*Broadening coefficients for the P(20) CO_2 laser transition*," *Appl.Phys.Lett.*, **25**, 609 (1974)

2.22 L. O. Hocker, M. A. Kovacs, C. K. Rhodes, G. W. Flynn and A. Javan, *Phys. Rev. Lett.*, **17**, No. 5, 233 (1966)

2.23 L. M. Frantz, J. S. Nodvik, "*Theory of pulse propagation in a laser amplifier*," *J. Appl. Phys.*, **34**, pp.2346-2349, 1963

2.24 W. J. Witteman, "*The CO_2 Laser*, " *Chapter 10*, Springer-Verlag, New York, 1987

2.25 F. A. Hopf, C. K. Rhodes, "*Influence of Vibrational, Rotational, and Reorientational Relaxation on Pulse Amplification in Molecular Amplifiers*," *Phys. Rev.* **A8**, pp.912-929, August 1973

2.26 G. T. Schappert, "*Rotational relaxation effects in short-pulse CO_2 amplifiers*," *APPL. Phys. Lett.*, **23**, No.6, 15 September 1973, pp.319-321

2.27 B. J. Feldman, "*MULTILINE SHORT PULSE AMPLIFICATION AND COMPRESSION IN HIGH GAIN CO_2 LASER AMPLIFIERS*," *Opt. Commun.*, **14**(1), May 1975, pp.13-16

2.28 R. R. Jacobs, K. J. Pettipiece, and S. J. Thomas, "*Rotational relaxation rate constants for CO_2*," *Appl. Phys. Lett.*, **24**, No.8, 15 April 1974, pp.375-377

2.29 I. Burak, Y. Noter, and A. Szoke, "*Vibration-Vibration Energy Transfer in the v_3 Mode of CO_2*," *J. Quant. Electronics*, **QE-9**, No.5, May 1973, pp.541-544

CHAPTER THREE

RF-EXCITED CO_2 WAVEGUIDE LASERS

3.1 INTRODUCTION

The work presented in this thesis is aimed to develop a laser architecture for high average or high peak power operations using a planar waveguide CO_2 gain medium. The investigations are conducted with a MOPA system which uses the transverse RF-discharge excitation to match the planar waveguide structure, providing a large active gain volume and thus potential high power extraction. This chapter outlines some of the fundamentals of the RF-discharge excitation technology, CO_2 gas dynamics and waveguide laser theory, to provide a theoretical and practical background for the research work to be presented in later chapters.

The concept of a hollow dielectric waveguide structure for laser action was firstly proposed by Marcatili and Schmeltzer [3.1] in 1964. Smith [3.2] demonstrated the first operation of a waveguide gas laser in 1971 with a He-Ne laser at 6328Å, while the first application of the waveguide laser principle to the CO_2 laser system was reported by Bridges et al [3.3] in 1972. To date, a large body of work has been reported with CO_2 waveguide lasers operating near 10μm. Compared to conventional CO_2 lasers which typically have bore sizes of 5-15mm, waveguide lasers have smaller bore sizes or electrode separations (usually ~ 1-3mm). The increased molecular density due to higher operational pressure, and enhanced cooling ability due to the very close proximity between the water-cooled electrodes and the active gain medium, make higher power deposition possible in the discharge, resulting in substantial increases in gain, power extraction and saturation intensity. Other advantages to be gained from waveguide lasers include increased frequency tunability, excellent beam quality, good power extraction efficiency and so on.

A waveguide laser includes optical waveguiding over at least part of the intracavity path. The propagation of a laser beam inside a hollow waveguide section does not follow the laws of free space propagation. Its field distribution is defined by a combination of eigenmodes supported by

the waveguide, as described by the mode theory for both the circular [3.1, 3.4] and rectangular guides [3.5, 3.6]. In addition, the theory of waveguide laser resonators was developed [3.7-3.9] based on the analysis of the coupling loss of waveguide modes in propagating to a curved mirror and returning back into the waveguide. This theory provides guidelines for the design of practical waveguide resonators with very low loss and a high degree of modal selectivity. The single EH_{11} mode coupling theory identified three low loss waveguide laser resonator configurations [3.9], which have been used as the starting point for almost all practical waveguide laser resonator designs. The waveguide mode theory and waveguide laser resonator theory were reviewed excellently by Degnan [3.10], Hall and Hill [3.11].

The planar (slab) waveguide geometry was developed in the late 1980's, aimed to enlarge the active gain region [3.12]. This area scaling approach, combined with the use of hybrid waveguide unstable resonators, has allowed very high power extraction from RF-discharge excited, diffusion-cooled laser devices [3.13]. Up to date, over $30kW/m^2$ laser power extraction has been demonstrated [3.14] and cw output power well above 3kW has been produced [3.15]. More recently, progress has been made with an array of square waveguide laser [3.16], which employed five slab electrodes in a stacking arrangement, producing total output power of 2kW through 64 channels. Also, interesting results have been found from the pulsed operation of such lasers [3.17], where much higher gain was observed than that in the cw mode operation, and much higher peak RF power deposition (up to $400W/cm^3$) was possible. However, the operation of such lasers in pulsed mode is limited to pulse duration larger than ~ 50μs.

Leading on from this introduction, the second section gives an overview of the CO_2 gas kinetics, which are essential in understanding the laser amplification process, in particular in the pulsed mode as to be discussed in Chapter 7. In section 3, the three basic waveguide laser resonator configurations [3.9] based on the coupling loss analysis in mode-waveguide matching are presented; Case I is used in the planar waveguide amplifier system under investigation to facilitate the configuration of a multiple folded beam path. The fourth section provides a brief review of the physics and technology of RF-discharge, which though is not among the main objectives of this

research, but is employed in the MOPA system to excite the planar waveguides of both the master oscillator and the power amplifier, and plays an important role in the system performance.

3.2 CO_2 GAS KINETICS

CO_2 lasers have probably received more attention than any other lasers in research and development over the last four decades or so, owing to their unique multilevel vibrational-rotational structure, high efficiency and general usefulness in various applications. CO_2 lasers were initially operated with pure CO_2 gas, producing only a few miliwatts laser output power [3.18]. However, the power and efficiency were soon significantly increased by using a gas mixture of He, N_2, CO_2 and Xe as the active medium. This is due to the much enhanced excitation of the CO_2 molecules to the upper laser level and de-excitation from the lower laser level, as well as improved thermal energy transfer, gas cooling capability and the avoidance of excessive molecular dissociation.

3.2.1 CO_2 Molecular Structures

a) Normal modes of vibration

CO_2 is a linear symmetric tri-atom molecule with an axis of symmetry along the nuclei and a plane of symmetry perpendicular to this axis. As illustrated in Fig. 3.1, there are three normal modes of vibration, i.e., ν_1, ν_2 and ν_3, which are associated with the species Σ_g^+, π_u and Σ_u^+, respectively [3.19-3.21]. ν_1 is longitudinal and symmetric (valence or symmetric stretch mode). In the vibration mode ν_1 the C atom remains stationary. ν_2 is a bending mode with two sub-states, ν_{2a} and ν_{2b} of equal frequency, representing the motion of the C atom in a plane perpendicular to the axis of symmetry. The vibration mode ν_3 is also longitudinal but asymmetric (asymmetric valence or stretch mode). For both the vibrations ν_2 and ν_3, during the motion, the distance between the two O atoms remains unchanged. The four vibrations are associated with different wave numbers. In the case where the vibrational motion is only described by the unperturbed harmonic oscillators, the wave numbers are [3.22]:

$$\omega_1 = 1351.2\text{cm}^{-1}, \quad \omega_2 = 672.2\text{cm}^{-1}, \quad \omega_3 = 2396.4\text{cm}^{-1}.$$

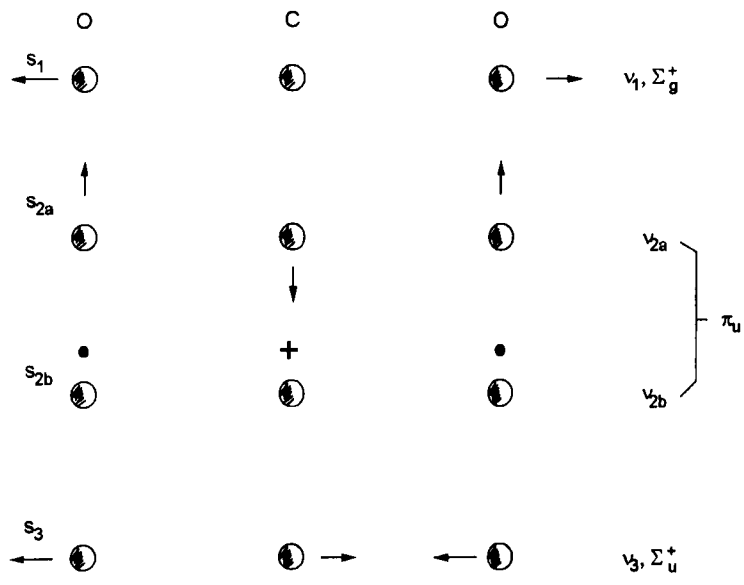

Figure 3.1 Normal vibration of CO_2 molecule: symmetric (ν_1), bent (ν_2) and asymmetric (ν_3) modes (after [3.20])

b) Energy levels

Several textbooks [3.20-3.21] describe the well-known vibrational-rotational structure of the CO_2 molecule and derive the quantum mechanical results. These results are solutions of the Schrödinger equations in the harmonic approximation modified by adding to the vibrational eigenfunction an additional term taking into account the anharmonicity. Fig. 3.2 shows the energy level diagram of a few low-lying vibrational states of the CO_2 molecules. Two extremely strong absorption bands can be seen at 667.33cm^{-1} and 2349.3cm^{-1} belonging to the bending mode ν_2 (species π_u) and the asymmetric mode ν_3 (species Σ_u^+). It is also noted that the lower laser levels 02^00 and 10^00 are almost in resonance, which leads to a perturbation of the energy levels, owing to the anharmonic terms in the potential energy. This phenomenon is normally referred to as Fermi resonance as it was recognised first by Fermi [3.23]. This results in the 10^00 level to shift up and the 02^00 level to shift down, so that the actual separation of the two levels is greater than expected. In addition, at the same time, a mixing of the eigenfunctions of the two levels occur, and stronger mixing corresponds to smaller original energy difference of the two levels.

For each vibrational state, there exists a set of rotational levels, but with slightly different spacing for the different vibrational levels. It has been realised that for degenerate vibrational levels, J must be larger than or equal to l, the angular momentum of the vibrational level. In addition, since CO_2 has a centre of symmetry and the spins of the oxygen nuclei are zero, the negative rotational levels are missing. Thus, for the electronic ground state the molecules with symmetric vibrational levels have only even J numbers (symmetric wave functions) in the rotational spectrum, while only odd J numbers (antisymmetric wave functions) exist for antisymmetric vibrational levels. The rotational energy levels are simply given by the well-known formula as:

$$\frac{E_r}{hc} = F(J) = BJ(J+1) \tag{3.1}$$

where E_r is the rotational energy, $F(J)$ the term value (in cm^{-1}) at the rotational level J, and B the rotational constant. In the thermal equilibrium, the population distribution n_J is governed by the Boltzmann distribution and is described by:

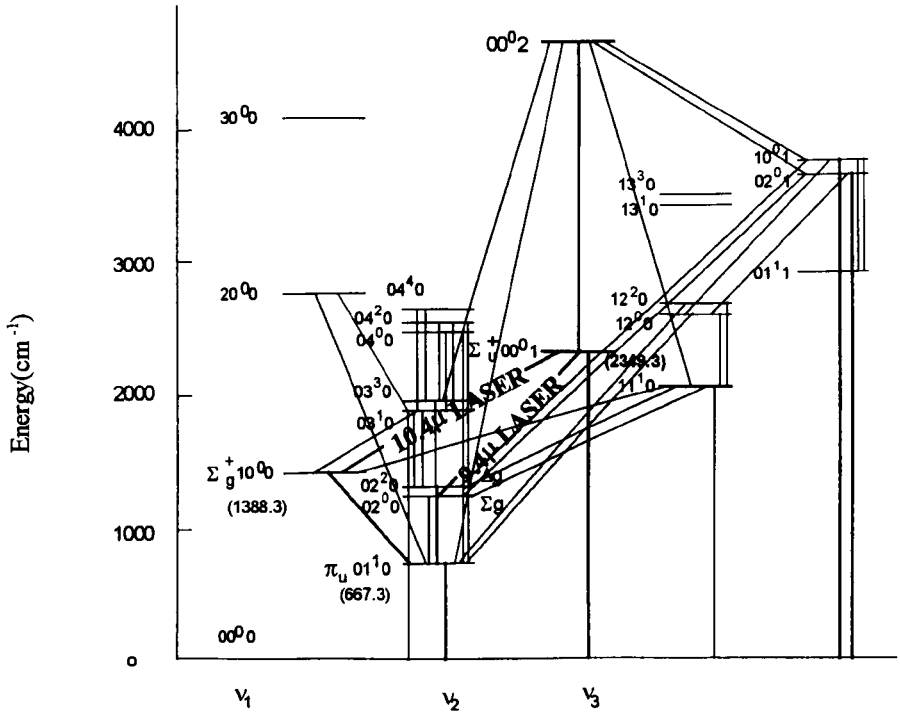

Figure 3.2 Energy level diagram of low-lying vibrational levels of the CO_2 molecule (after [3.20])

$$n_J \cong n_T \left(\frac{hcB}{kT}\right) g(J) \exp\left[-F(J)\frac{hc}{kT}\right] \tag{3.2}$$

where $g(J)$ is the statistical weight representing the degeneracy of the rotational state J, and is equal to $(2J+1)$ for CO_2 molecules in the electronic ground states. The thermal distribution of the rotational levels in the $00^0 1$ upper vibrational state for $B = 0.38714 cm^{-1}$ and $T = 400°K$ is shown in Fig. 3.3. For each vibrational state, there exists a rotational level J_{max} which has the highest population distribution over other rotational levels in the same vibrational state, and is obtained from Eq. (3.2) as:

$$J_{\max} = \left(\frac{kT}{hcB}\right) - \frac{1}{2} \tag{3.3}$$

At $T = 400°K$, $J_{max} = 19$, while at $T = 1000°K$, $J_{max} = 29$. For higher temperature, the distribution of rotational level population spreads over a wider range of J values with correspondingly decreasing amplitude.

c) Laser transitions

The infra-red spectrum of CO_2 molecules resulting from vibration-rotational transitions follows certain selection rules, as summarised in textbooks [3.20, 3.24]. Because the CO_2 molecule has no permanent dipole moment, *transitions between rotational levels in a given vibrational state are not allowed.* The transitions with $\Delta J = -1$ (or $J_{upper} = J_{lower} - 1$) are called the P-branch transitions and those with $\Delta J = +1$ (or $J_{upper} = J_{lower} + 1$) are referred to as R-branch transitions. So-called Q-branch corresponding to $\Delta J = 0$ is not allowed for CO_2 molecules because such transitions would occur between two Σ states for which $l = 0$, thus contravening the selection rules. Two points are worth addressing here, which derive from the analysis of the gain in terms of the populations of the upper and lower rotational levels. First, the gain of the P-branch is always higher than that of the R-branch. Secondly, the P-branch transitions may be obtained even if the total population in the upper vibrational state is lower than that in the lower vibrational state, owing to the so-called partial inversion [3.25].

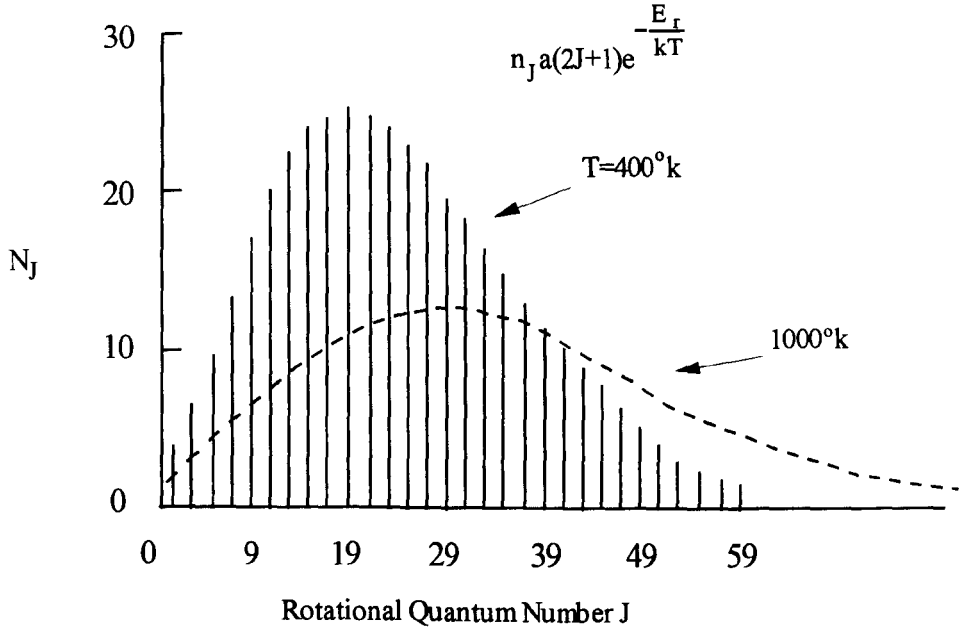

Figure 3.3 Thermal distribution of rotational level population in the $00^0 1$ upper laser state (after [3.20])

Laser oscillation corresponding to over 200 vibrational-rotational transitions has been obtained in CO_2 lasers, with the spectrum in the range of 8-18μm. The two strongest spectral bands are from the vibrational-rotational transitions of the Σ_u^+ and Σ_g^+ vibrational bands ($00^01 \rightarrow 10^00$) and ($00^01 \rightarrow 02^00$), known as the *regular bands*, at laser wavelengths near their band edge 10.4μm and 9.4μm respectively. Laser transitions have been obtained from both the *P*-branch and the *R*-branch of each band. The details are illustrated in Fig. 3.4. Other spectral bands include the $(00^02 \rightarrow 10^01)_{I,II}$ bands, known as the *sequence bands* (10.4μm and 9.4μm) and the $(01^11 \rightarrow 11^10)_I$ band, known as the *hot band* (10.8μm). Most common CO_2 lasers (and amplifiers) work on the *P*-branch of the 10.4μm band of which the line *P*(20) at 10.6μm has given, under normal operational conditions, the highest gain and accordingly the highest contribution to the output power.

3.2.2 Excitation and De-activation Mechanisms

a) Excitation processes

There are two principal mechanisms that have been recognised to contribute to the pumping of the upper energy level 00^01, i.e. the direct electron impact and the resonant energy transfer from vibrationally excited N_2 or CO to CO_2 molecules.

Direct electron impact

Early work on the measurements of the rotational and vibrational excitation cross sections of CO_2 and N_2 by inelastic collisions of electrons at low energies (0-3eV) was reviewed by Phelps [3.26]. Further and more accurate measurements were made by Hake and Phelps [3.27], Boness and Schulz [3.28], and Lowke, Phelps and Irwin [3.29], of the electron excitation cross sections of the low lying vibrational levels. Fig. 3.5 shows the cross sections (after [3.27]) of the vibrational excitation of CO_2 molecules by electron impacts. Resonances at 0.3, 0.6 and 0.9eV are associated with the three levels of the asymmetric mode (ν_3, $2\nu_3$ and $3\nu_3$), while 0.08eV is associated with the lowest bending mode (ν_2).

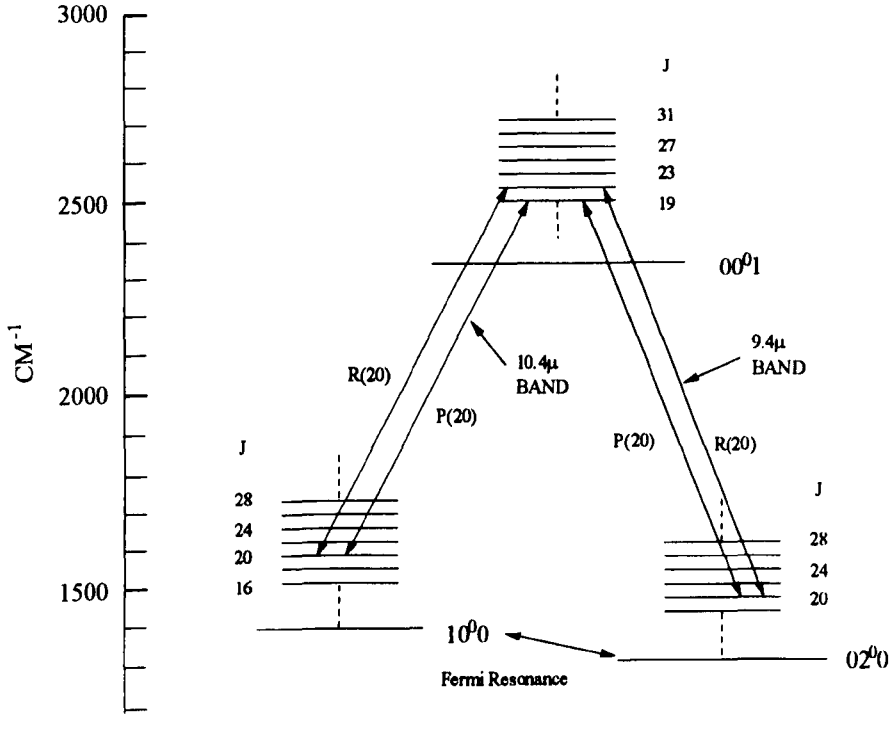

Figure 3.4 A detailed laser transition diagram for the $00^0 1$-$10^0 0$ and $00^0 1$-$02^0 0$ bands, including rotational levels (after [3.20])

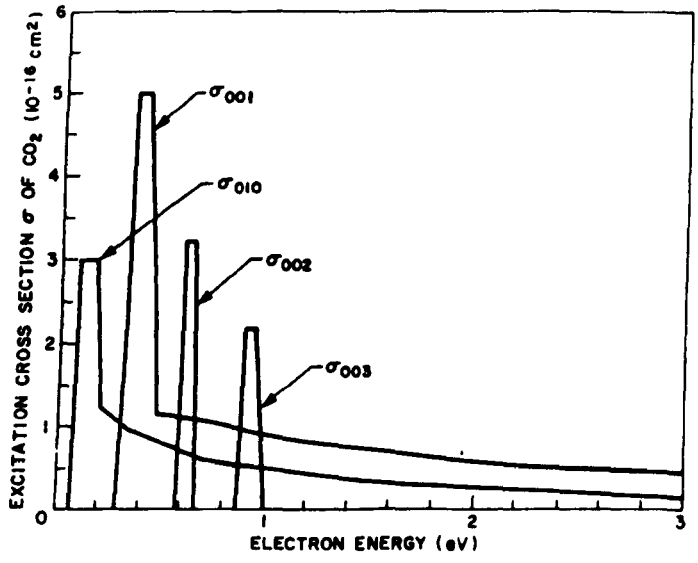

Figure 3.5 Cross section for vibrational excitation of CO_2 by electron impact (after Hake and Phelps [3.27])

It is noted that for CO_2 molecules, the resonance occurs very close to the threshold for onset of the particular energy loss process. On the contrary, for the diatomic molecule N_2, the resonance, as shown in Fig. 3.6 (after [3.28]), occurs at energies well above the ~ 0.3eV threshold for $\upsilon = 1$. This implies that the electron temperature is less critical for the probability of excitation of N_2 ($\upsilon = 1$) by electron impact for $kT_e > 1$eV than for that of CO_2 ($00^0 1$). The results shown in Fig. 3.5 and 3.6, together with the electron temperature measurements [3.30], clearly indicate that excitation of CO_2 ($00^0 1$) by electron impact is in a manner that it is dominated by the direct process but a major portion of the electrons is used in the excitation of N_2 ($\upsilon = 1$), which in turn transfers its energy to excite CO_2 ($00^0 0$) to CO_2 ($00^0 1$).

Further investigation indicates that in a CO_2-N_2-He laser system the average electron energy should be controlled appropriately. On the one hand, the average electron energy must be far above the threshold for excitation of CO_2 ($00^0 1$) in order to avoid direct pumping of the $01^0 0$ level; on the other hand, the average electron energy must be limited to < 3eV to avoid excessive dissociation processes. This indicates the dependence of the laser performance on the operational conditions.

Resonant energy transfer

Resonant energy transfer from excited N_2 molecules is the major channel for the excitation of CO_2 ($00^0 1$) in addition to the direct electron impact. The N_2 molecule has zero permanent dipole moment, therefore it can only decay to the ground state by collisions with other molecules or with the wall of the containing vessel. In the presence of CO_2 molecule the vibrational energy of N_2 ($\upsilon = 1$) can be easily transferred to CO_2 ($00^0 1$), because of the small difference (only $18cm^{-1}$) between these two levels compared to the average kinetic energy kT. This resonance energy transfer occurs at a very rapid rate with $k_e = 1.9 \times 10^4$ $Torr^{-1}$-sec^{-1} [3.28], and produces a mixed state in which the combined population of N_2 ($\upsilon = 1$) and CO_2 ($00^0 1$) are essentially in equilibrium. This process is described by the following reaction:

$$N_2(\upsilon = 1) + CO_2(00^0 0) \xleftrightarrow{k'_e, k_e} N_2(\upsilon = 0) + CO_2(00^0 1) - 18cm^{-1} \qquad (3.4)$$

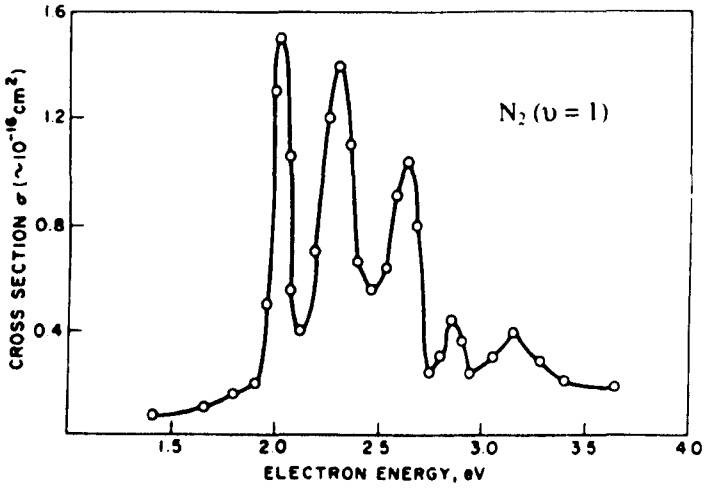

Figure 3.6 Cross section for vibrational excitation of N_2 ($\upsilon = 1$) by electron impact (after [3.28])

It has to be pointed out that the efficient transfer can occur for excited N_2 molecules up to $\upsilon = 4$ because even at this level the anharmonicity of the N_2 molecules still does not lead to quantum values differing from that of the CO_2 ($00^0$1) by more than the average kinetic energy.

A similar energy resonance transfer effect exists between the CO and CO_2 molecules, which is described by the following reaction [3.20]:

$$CO(\upsilon = 1) + CO_2(00^0 0) \xleftrightarrow{k_e(CO)} CO(\upsilon = 0) + CO_2(00^0 1) - 206cm^{-1} \qquad (3.5)$$

where the energy transfer rate k_e(CO) was measured to be 0.79×10^4 $Torr^{-1}$-sec^{-1} [3.31]. In this process, the CO molecules, usually coming from the dissociation of CO_2, can transfer a considerable amount of energy to the ν_3 vibration of the CO_2 because of the large cross section for vibrational excitation of CO, and the small energy difference ($< kT$) between the vibrational level of CO ($\upsilon = 1$) and CO_2 ($00^0$1). However, compared to N_2, CO is less effective in exciting the ν_3 vibration of the CO_2. This is because of the larger excess energy coming from the translation for CO than for N_2, and because of the dipole moment that the CO has which causes spontaneous decay. For this reason, the energy resonance transfer effect related to CO is not emphasised in later chapters upon laser amplification processes.

The role of Xe [3.21]

Practically, in addition to N_2, nearly all efficient CO_2 lasers are added with a small fraction of Xe in the gas mixture. Xenon has an ionisation potential much lower than that of other components in the gas mixture, thus its presence *helps produce new electrons*. As a consequence, the electron energy distribution is changed in a way that the number of electrons with energy smaller than 4eV increases, while the number of those with larger energies decreases, producing a favourable effect on the vibrational excitation of CO_2 and N_2, and a reduction in dissociation.

b) Relaxation processes

The presence of many relaxation processes, which are important in understanding all the aspects of the population inversion mechanism, has made CO_2 laser unique and more complex than most

other existing lasers. A theoretical treatment to the multilevel ($00^0 1$, $10^0 0$, $02^0 0$, $01^1 0$, $00^0 0$) structure is complex, and the mechanism is further complicated by the rotational relaxation and competition effects, in particular for single line operation. To produce high efficiency and high power laser action, the lifetimes of the upper laser level, τ_u, and the lower level, τ_l, must satisfy the following condition:

$$\tau_u{}^r >> \tau_u{}^c >> \tau_l{}^c \tag{3.6}$$

where τ^r and τ^c represent the radiative and collisional (or effective) lifetimes, respectively. In addition, the laser levels should lie near the ground state to achieve high discharge power conversion and to increase greatly the relaxation of the lower laser level by collisions with gas additives. Because the radiative lifetimes of the lower laser levels $10^0 0$, $02^0 0$ and the lowest bending mode $01^1 0$ are very long [3.32], the relaxation via collisions are vital in the establishment of an inversion.

To describe the energy transfer between two vibrational levels or one vibrational and one translational degree of freedom which occurs only through inter- or intramolecular collisions, a parameter Z is defined, which corresponds to the average number of collisions required to deactivate one vibrational quantum to its e^{-1} value and is expressed as (p.150 of [3.20]):

$$Z = \tau / \tau_c \tag{3.7}$$

where τ is the relaxation time or the effective lifetime of the state and τ_c is the time between successive collisions which is inversely proportional to the gas pressure p. $1/Z$ is the probability of deactivation of vibrational energy in one collision. Z depends only on the kinetics of the colliding molecules and thus is a function of gas temperature and independent of p. The relaxation rate k of a collisional process is related to the exponential relaxation time τ by the following expression:

$$k = (p\tau)^{-1} \tag{3.8}$$

In a mixture of CO_2 and a foreign gas M, the relaxation of a vibrationally excited CO_2 molecule can take place through the binary processes by collisions with either a ground state of CO_2 and/or with M at a relaxation rate given by

$$k = xk_{CO_2\text{-}CO_2} + (x-1)k_{CO_2\text{-}M} \tag{3.9}$$

where x is the mole fraction of CO_2, $k_{CO_2\text{-}CO_2}$ and $k_{CO_2\text{-}M}$ are the respective rates for the CO_2-CO_2 and CO_2-M collisions.

Relaxation of 01^10 level

Relaxation of the lowest bending mode 01^10 is one of the dominant factors in controlling the gain and power of CO_2 lasers, because the population inversion densities associated with the 00^01-10^00 and 00^01-02^00 laser transitions are essentially limited by the relaxation rate of this level [3.33, 3.34]. This relaxation process involves a vibrational-translation energy exchange, as described by

$$CO_2(01^10) + M \xrightarrow{k_{v_2}(M)} CO_2(00^00) + M + 667cm^{-1} \tag{3.10}$$

Other gases such as He, H_2, H_2O, CO and N_2 are also found to enhance the relaxation rate of the 01^10 level. Relaxation rates k_{v_2} for CO_2 mixed with these gases can be found in textbooks [3.20, 3.21], and are listed in Table 3.1.

It has to be pointed out that H_2 and H_2O are not normally intentionally used in high power laser systems, because their effective relaxation to the upper laser level (00^01) in addition to the lowest bending mode (01^10). On the other hand, helium is widely used in CO_2 laser systems. The presence of a large amount of helium in the laser ($\geq$ 10torr) does not affect the upper laser level, because of its high energy level (> 20eV), while deactivating (although less efficient than if H_2 and H_2O are used) of the (01^10) level, resulting in significant reduction of the relaxation time of the 10^00 level [3.35], thereby preventing bottle necking.

Relaxation of 00^01 level

The upper laser level 00^01 is coupled to the lower laser levels by collisions and by stimulated emissions. The processes are described by the following reactions [3.20]:

$$CO_2(00^01) + M \xrightarrow{k_{v_3}} CO_2(n, m^l, 0) + M + E_{trans} \tag{3.11}$$

Mixture	k_{v_2} (Torr^{-1}-sec^{-1})
CO_2	194
$CO_2 - H_2$	6.5×10^4
$CO_2 - He$	3.27×10^3
$CO_2 - H_2O$	4.5×10^5
$CO_2 - CO$	2.5×10^4
$CO_2 - N_2$	6.5×10^2

Table 3.1 Relaxation Rate Constants k_{v_2} for CO_2 in various gas mixtures at $T = 300°K$ (after [3.20])

and

$$CO_2(00^01) \xrightarrow{S_{ul}I_{laser}} CO_2(10^00) \text{ or } CO_2(02^00) + h\nu \qquad (3.12)$$

In fact, there is a third process, i.e. the diffusion process associated with the wall of the gas vessel, which plays a role in the deactivation of the excited CO_2 molecules. However, for P_{CO_2} > 1torr, the diffusion is negligible [3.36].

To measure the relaxation times of the 00^01 CO_2 upper laser level in various gas mixtures commonly used in CO_2 laser systems, two techniques have been introduced. They are the induced fluorescence technique [3.37-3.38] and the afterglow pulse gain technique [3.33, 3.35]. The first approach provides unambiguous measurements of gas composition. The second approach can yield information concerning the relaxation times of both the upper and the lower laser levels simultaneously; such information is considered much more relevant to CO_2 laser performance because of the experimental conditions similar to those for operating CO_2 lasers.

Table 3.2 lists the values of k_{v_3} in variety of gas mixtures measured by Cheo [3.33, 3.35] with the pulse gain method, in direct comparison with those measured by Moore et al [3.37, 3.39] with the fluorescence method. It can be seen that the addition of N_2 and CO increases the upper level lifetime by a factor of two over that for a pure CO_2 discharge, owing to the rapid resonant transfer and the formation of mixed states. While both H_2 and H_2O have drastic effect on the relaxation of the upper laser level, little effect is shown in the presence of helium and xenon.

Relaxation of 10^00 and 02^00

Fermi resonance between the two lower laser levels 10^00 and 02^00 leads to the formation of two mixed states $(10^00, 02^00)'$ and $(10^00, 02^00)''$. Both levels can decay to the 01^10 level through resonant processes such as

$$CO_2(10^00,02^00)' + CO_2(00^00) \xleftrightarrow{k(v_1,2v_2)} 2CO_2(01^10) - 50cm^{-1} \qquad (3.13a)$$

$$CO_2(10^00,02^00)'' + CO_2(00^00) \xleftrightarrow{k(v_1,2v_2)} 2CO_2(01^10) + 52cm^{-1} \qquad (3.13b)$$

Mixture	P_{CO_2} (Torr)	P_X range (Torr)	k_{ν_3} (Torr^{-1}-sec^{-1})	
			Pulse gain	Fluorescence[a]
CO_2	1-8	*b*	385	350
$CO_2 - H_2$	3	0.5-3.0	4.5×10^3	3.8×10^3
$CO_2 - He$	1	1-8	0-50	85
$CO_2 - H_2O$	2	0.05	4.2×10^4	2.4×10^4
$CO_2 - N_2$	1	1-7	115[c]	106
$CO_2 - CO$	2	1-5	193	-
$CO_2 - Xe$	2	0.1-1.0	0-50	30

[a] Date by Moore et al [3.37, 3.39] at much higher gas pressure than pulse gain measurements

[b] Other species such as CO-O_2 are also present owing to dissociation of CO_2.

[c] Obtained for largest P_x values

Table 3.2 Relaxation Rate Constants k_{ν_3} for CO_2 in various gas mixtures X at T = 300°K (after [3.20])

Because of the strong collisional coupling between the lower laser level and the bending mode (01^10), only trapped values of the rate constants $k^{eff}_{(v_1,2v_2)}$ are measured (as listed in Table 3.3) owing to the accumulation of population at the 01^10 level [3.33]. As shown in Table 3.3, these measurements, except for those taken with a pure CO_2 gas in which a considerable amount of CO (> 10%) is present owing to dissociation of CO_2, are reasonably close to the k_{v_2} value. This indicates that the effective relaxation rates of the lower laser levels are essentially limited by that of the 01^10 level.

Rotational relaxation

Compared to vibrational relaxations, the rotational relaxation within a given vibration state is an extremely fast process. Rotational relaxation rate constants of the upper laser level 00^01 corresponding to $J = 19$ for CO_2-CO_2, CO_2-N_2, CO_2-He collisions are given in Table 3.3. The data are from references [3.40] and [3.41] and are obtained by directing a $P(20)$ 10.6μm pulse of 20ns duration into a cw 9.6μm *P(J)* amplifier and measuring the gain recovery time at 9.6μm after the gain is disturbed by the passage of the short laser pulse. Note the rotational upper laser level $J = 19$ is shared by the 10.6μm and the 9.6μm transition.

It is seen that the rotational relaxation rate is very similar for pure CO_2, or mixture of CO_2 with addition of He or N_2, at a order of $1 \times 10^7 Torr^{-1}\text{-}sec^{-1}$. This implies that the thermal equilibrium governed by the Boltzmann distribution can be recovered very quickly after one or more of the rotational levels are disturbed. For a 3/1/1 ($He/CO_2/N_2$) gas mixture at a total pressure of 50-100torr, as typically used in the amplifier system under investigation in this thesis, the relaxation time is in the order of 5-10ns. Thus, for laser pulse amplification with pulse length in the order of micro-seconds, it is reasonable to assume that the rotational levels remain in equilibrium.

3.3 WAVEGUIDE LASER RESONATORS

A basic waveguide laser resonator consists of one waveguide with two external curved mirrors, one at each end. In the absence of the waveguide, the two-mirror structure would form an open

Mixture	P_{CO_2} (Torr)	P_X range (Torr)	$k^{eff}_{(\nu_1,2\nu_2)}$ (Torr^{-1}-sec^{-1}) Pulse gain [3.15]
CO_2	1-8	*a*	2.2×10^3
$CO_2 - H_2$	3	0.5-3.0	3.3×10^4
$CO_2 - He$	1	1-8	4.7×10^3
$CO_2 - H_2O$	2	0.05	1.2×10^6
$CO_2 - N_2$	1	1-7	26
$CO_2 - CO$	2	1-5	4.1×10^3
$CO_2 - Xe$	2	0.1-1.0	5×10^3

[a] Other species such as CO-O_2 are also present owing to dissociation of CO_2

Table 3.3 Effective rate constants $k^{eff}_{(\nu_1,2\nu_2)}$ of CO_2 in various gas mixture X (after [3.20])

X	CO_2	He	N_2
$k^{rot}_{CO_2-X}$ (10^7Torr^{-1}-sec^{-1})	1.1 ± 0.2	0.7 ± 0.1	1.0 ± 0.2

Table 3.4 Rotational relaxation rate constant $k^{rot}_{CO_2-X}$ of CO_2 (00^01, J = 19) for X = CO_2, He and N_2 [3.20, 3.40-3.41]

resonator whose characteristics are governed by Gaussian beam theory [3.42]. When the waveguide is present, the axial and transverse mode structure of the resonator is changed significantly and a new description is required. In general, the function of a waveguide laser resonator is to create certain field distributions (resonator modes) that repeat themselves after one round trip to within an arbitrary multiple of 2π in phase and an arbitrary loss factor in amplitude. An ideal waveguide laser resonator must ensure the lowest loss waveguide mode to be in good approximation to the fundamental free space Gaussian mode TEM_{00}, to provide an output beam containing a transverse mode that is reliably quasi-TEM_{00}. It can be shown that this lowest loss mode EH_{11} provides ~ 98% of power overlap to the TEM_{00} mode for both circular [3.43] and square guides [3.44].

In single-mode coupling theory, by expanding the normalised EH_{11} Bessel function in Laguerre-Gaussians with their waists in the guide aperture plane, calculation of the EH_{11} coupling loss [3.9, 3.43] for circular guides and finite-aperture curved mirrors (for a range of the radii of curvature of the mirror R_M and the distance to the waveguide aperture plane z) revealed three waveguide laser resonator configurations of very low EH_{11} loss, as shown in Fig. 3.7. These low loss cases are special examples of phase-matched mirrors, i.e., mirrors whose surfaces coincide with the phase fronts of the EH_{11} "approximating Gaussian". This classification of resonators can also apply to waveguide lasers with square bore guides.

Case I is the simplest and most compact, corresponding to large-radius-of curvature (in the limit, plane) mirrors placed very near the guide, where all outgoing radiation is re-coupled back to the guide, with little diffraction incurred. In case II, large-radius-of curvature mirrors are placed with their centres of curvature lying approximately at the guide entrance. Because the mirror is in the far-field, the phase fronts of the free space beams propagating between the guide and the mirror are roughly spherical waves that appear to come from a point source near the aperture. Both case I and II offer low coupling loss for all modes and have poor mode discrimination. Case III uses mirrors of moderate curvature placed at a distance $R_M/2$. It combines very low coupling loss with excellent mode discrimination.

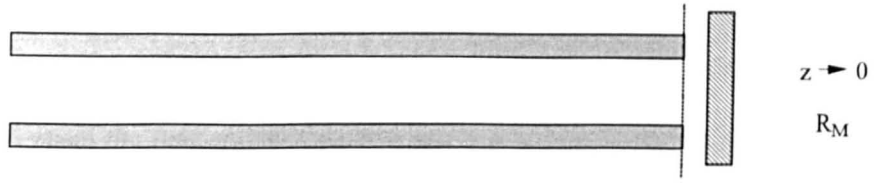

(a) Case I

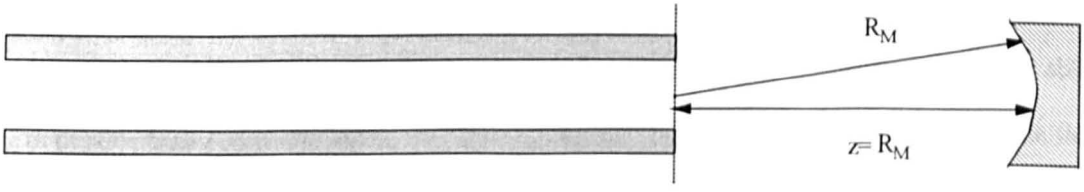

(b) Case II

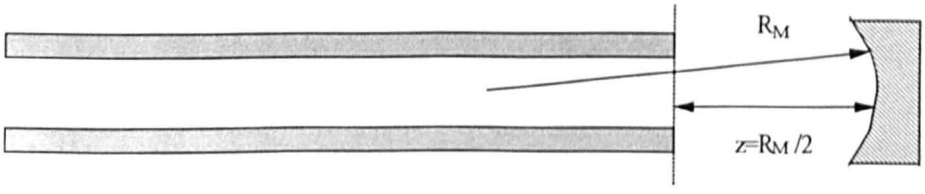

(c) Case III

Figure 3.7 Low coupling loss waveguide laser resonator configurations

For planar waveguide lasers, the slab geometry has a narrow transverse gap no more than a few millimetres and a wide lateral width which may be up to 100-200mm. Thus, a hybrid waveguide laser resonator is required, which combines the waveguide nature in the transverse direction with the free space feature in the lateral direction. In the transverse direction, the beam propagation is governed by the waveguide mode theory, where only the lowest order mode is desired. In the lateral direction, the beam propagation follows the conventional Hermite-Gaussian beam theory, where the fundamental Gaussian mode is preferred. So far, the most popular and successful resonator has been the one which is laterally the *confocal unstable* resonator and transversely the Case I resonator. As schematically shown in Fig. 3.8, this type of resonator is actually classified as the *positive branch unstable laser resonator*, which has a focal point outside the laser cavity, and the *negative branch unstable laser resonator*, which has an intracavity focus, both being able to provide high power extraction. The positive branch unstable resonator is sensitive, while the negative branch unstable resonator is less sensitive, to misalignment.

3.3 RF-DISCHARGE EXCITATION

3.4.1 Advantages of RF-discharge Excitation

In laser engineering, RF-discharges usually refer to high-frequency ac discharges in the frequency range of 1 to 200MHz. The utilisation of the RF-discharges can be traced back to the early experiments of gas laser physics [3.2, 3.18, 3.45]. However, it was not until the early 1980's that the potential of the RF-discharge excitation technology was widely recognised and systematic research activities on the combination of transverse RF-discharges and optical propagation in hollow dielectric waveguide began [3.46-3.47], following the pioneering activities of Laakmann and colleagues at Hughes Aircraft Company in the late 1970's [3.48-3.51] with regard to waveguide CO_2 lasers.

The RF-discharge excitation technique is advantageous in many aspects, particularly over DC-discharge pumping [3.11]. Stable RF-discharges can be operated between large area parallel electrodes with the electric field direction transverse to the optical axis and with voltages of a few hundred volts rms compared to typically 5-15kV of DC-discharge excited waveguide CO_2 lasers.

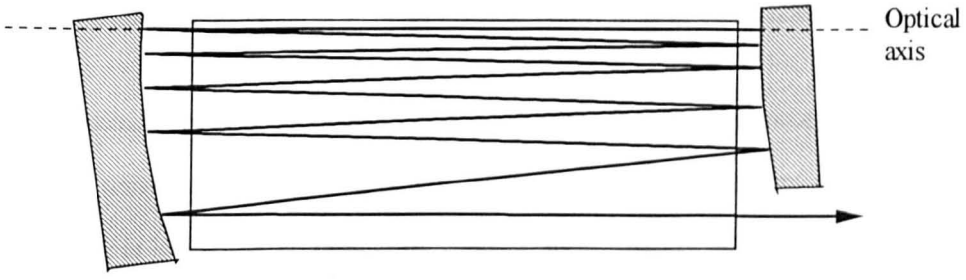

(a) Positive branch, off-axis, confocal, unstable resonator

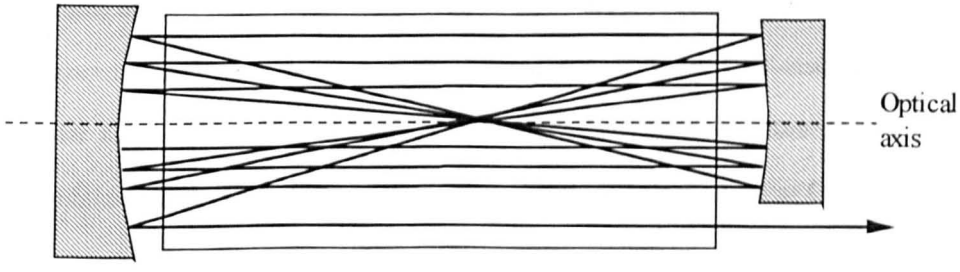

(b) Negative branch, off-axis, confocal, unstable resonator

Figure 3.8 Confocal, off-axis, unstable resonators for planar waveguide lasers

In addition, the length scaling of the RF-discharge is straightforward, owing to the transverse character of the discharges. Because of the absence of high voltages, there is no need for excessive insulation to prevent unwanted breakdown. Moreover, multiple parallel waveguide channels can be excited from a single RF power source. This has allowed recently the construction and operation of a two-dimensional array laser of 64 channels [3.17].

DC discharge excited waveguide lasers are negative-resistance devices and thus require series ohmic resistance as stabilising ballast where a considerable amount of power is consumed, resulting in low power efficiency. By contrast, RF-discharges exhibit a positive slope in the I-V characteristic curve; therefore, no series ohmic resistance is necessary. Besides, it is recognised that RF-discharges are actually "electrodeless" and thus the secondary emission processes at metallic electrodes are not required to maintain the discharge. This leads to the use of ceramic materials such as alumina or beryllia in constructing waveguides. In addition, the increases of lifetime of sealed-off RF-excited waveguide lasers are expected, as the result of decreases of CO_2 dissociation compared to DC discharge excited devices. Finally, RF-discharges are stable over a wider range of operating conditions. This allows increased opportunity for one to select the conditions for the performance optimisation of molecular lasers such as CO_2.

3.4.2 Alpha and Gamma RF-Discharges

Fundamentally, there exist two different forms of stable transverse RF-discharges, i.e., the α discharge and the γ discharge, as firstly recognised by Levitskii [3.52]. The α discharge corresponds to the low-current discharge, where volume ionisation is the dominant electron production mechanism. In the α discharge, which occurs at a relatively low power density level, two distinct regions are observable from its appearance: the central plasma zone which provides the laser excitation, and a pair of bright emission regions adjacent to each electrode, which contain high positive ion concentration and are referred to as "sheath" zones. The γ discharge corresponds to the high-current discharge, where electron generation is confined mainly to the plasma electrode boundary region. The α to γ discharge transition is a sudden process. It happens when the applied RF power is increased to a particular level with the discharge collapsing toward

the centre of the electrodes. This α to γ discharge transition is also accompanied by a large increase in RF current as the result of the considerable reduction of the net plasma impedance.

It has been suggested [3.53, 3.54] that the α to γ discharge transition results from the neutralisation of the α discharge positive ion sheaths by electrons produced by secondary emission processes at the walls which increase with applied RF power. This neutralisation leads to a substantial increase in the conductivity of the sheath and eventually to its breakdown. In the γ discharge, the near-electrode regions are similar to the near-cathode regions (cathode sheath, negative glow and Faraday dark space) of the DC glow discharge [3.53]. In addition, the γ discharge is sustained by wall ionisation processes and has relatively thin electrode boundary sheaths and high values of displacement and conduction current. Although it has a diffusive plasma column which is uniform, the high power dissipation in the near electrode ion sheaths together with the low electron temperatures in the negative glow make the γ discharge useless for molecular laser excitation [3.54].

Thus, for CO_2 waveguide lasers, the γ discharge is considered as an undesirable instability and only the α discharge is suitable. The α discharge, corresponding to relatively low power density, has positively charged sheaths near each electrode boundary and is sustained largely by volume ionisation. This form of RF-discharge is also characterised by a stable and positive impedance characteristic, although the plasma region has a near flat current-voltage curve [3.55], similar to that of the conventional positive column DC discharge. This indicates that this positive voltage-current characteristic is a consequence of the behaviour of the sheath, rather than being due to the properties of the plasma region and thus the capacitative sheaths, which are characteristic of the RF-discharge, perform a crucial role in stabilising the plasma. It is also recognised that the sheath regions do not contribute significantly to the molecular laser excitation processes and thus it is advantageous to operate the discharge under conditions where the sheaths occupy only a relatively small fraction of the total discharge volume.

the centre of the electrodes. This α to γ discharge transition is also accompanied by a large increase in RF current as the result of the considerable reduction of the net plasma impedance.

It has been suggested [3.53, 3.54] that the α to γ discharge transition results from the neutralisation of the α discharge positive ion sheaths by electrons produced by secondary emission processes at the walls which increase with applied RF power. This neutralisation leads to a substantial increase in the conductivity of the sheath and eventually to its breakdown. In the γ discharge, the near-electrode regions are similar to the near-cathode regions (cathode sheath, negative glow and Faraday dark space) of the DC glow discharge [3.53]. In addition, the γ discharge is sustained by wall ionisation processes and has relatively thin electrode boundary sheaths and high values of displacement and conduction current. Although it has a diffusive plasma column which is uniform, the high power dissipation in the near electrode ion sheaths together with the low electron temperatures in the negative glow make the γ discharge useless for molecular laser excitation [3.54].

Thus, for CO_2 waveguide lasers, the γ discharge is considered as an undesirable instability and only the α discharge is suitable. The α discharge, corresponding to relatively low power density, has positively charged sheaths near each electrode boundary and is sustained largely by volume ionisation. This form of RF-discharge is also characterised by a stable and positive impedance characteristic, although the plasma region has a near flat current-voltage curve [3.55], similar to that of the conventional positive column DC discharge. This indicates that this positive voltage-current characteristic is a consequence of the behaviour of the sheath, rather than being due to the properties of the plasma region and thus the capacitative sheaths, which are characteristic of the RF-discharge, perform a crucial role in stabilising the plasma. It is also recognised that the sheath regions do not contribute significantly to the molecular laser excitation processes and thus it is advantageous to operate the discharge under conditions where the sheaths occupy only a relatively small fraction of the total discharge volume.

3.4.3 Longitudinal RF-discharge Uniformity

When an RF field is applied to a waveguide laser, discharge nonuniformity may occur in the longitudinal direction as the result of the significant variation of the transverse RF inter-electrode voltage between the RF power feed point and the end of the waveguide [3.56-3.58], if no appropriate measures are taken. This is accurately predicted by modelling the laser head as a lossy transmission line [3.11]. The longitudinal discharge nonuniformity is not significant for low RF frequencies and/or very short, low capacitance laser structures. However, the longitudinal discharge nonuniformity problem is serious, thus solutions must be found, for most practical laser systems, where high RF frequencies and large scale waveguides are preferred for optimum overall laser performance. The use of multiple RF power feed points may be effective in reducing the longitudinal voltage variation [3.58], but it is not considered as a "good" solution, because of considerable precautions it requires in adjusting the phase of the ac wave input so as to avoid destructive interference effects. Notably in the literature, three methods have been proved to be successful solutions, i.e., Inductive Termination, Multiple-Shunt Inductor Voltage Compensation, and Distributed Parallel Resonance.

Inductive Termination

As a consequence of the longitudinal standing waves in the transverse RF voltage, the longitudinal voltage varies cosinusoidally. If one uses a coil Z_L, which is inductive therefore consumes no power, at the end of the waveguide (where is also the termination of the transmission line), the longitudinal voltage variation will be added with an additional phase part, which is related to the characteristic impedance of the laser structure and the RF frequency. With correct value of Z_L, this added phase shift will flatten the longitudinal voltage variation along the waveguide so that good discharge uniformity can be achieved. If one sets an acceptable limit for the voltage variation, say 5%, then for a waveguide constructed with alumina ceramic side-walls, the maximum waveguide length (in unit of cm) is related to the RF frequency f (in unit of MHz) as [3.58]:

$$x_{max} \leq \frac{1.21 \times 10^3}{f} \tag{3.14}$$

Obviously, this method is only suitable for low RF frequency cases. For cases where high RF frequencies are used, the maximum waveguide length with discharge uniformity within acceptable level is limited.

Multiple-Shunt Inductor Voltage Compensation

As recognised and demonstrated by Griffiths [3.57], this method is very effective for achieving good discharge uniformity and high power efficiency. This method involves the use of multiple-shunt inductors placed in parallel with the laser-discharge resistance at intervals longitudinally along the waveguide. The starting point is to overcome the frequency/waveguide length limitation described by Eq. (3.15). The mechanism is, with periodic placement of shunt induction which exhibits negative admittance, to compensate for the effect of the distributed structure capacitance that rotates the phase angle in the negative direction and hence causes voltage variation.

It must be pointed out, however, that this method, as the same as the inductive termination method, relies on shunt inductance to introduce a phase shift in the basic cosine variation to smooth the voltage variation.

Distributed Parallel Resonance

This method was invented by Chenausky and Newman [3.56, 3.59] and is considered most effective. It depends on establishing conditions of distributed parallel resonance, where both the distributed and parallel resonance features are crucially important. The major advantage is, while acting as a complete solution for the discharge nonuniformity problem, it imposes no strict limitation for RF frequencies and allows the use of high-capacitance laser structures, both being essential for large scale, high power, effective waveguide laser construction.

Fig. 3.9 illustrates the basic idea of distributed parallel resonance, where an elemental inductor l_p shunts each parallel RC stage in the distributed-element transmission line model of the laser structure [3.12]. By distributing a number of parallel inductors l_p along the waveguide to match to some degree the distributed nature of the structure capacitance, the desired situation of voltage

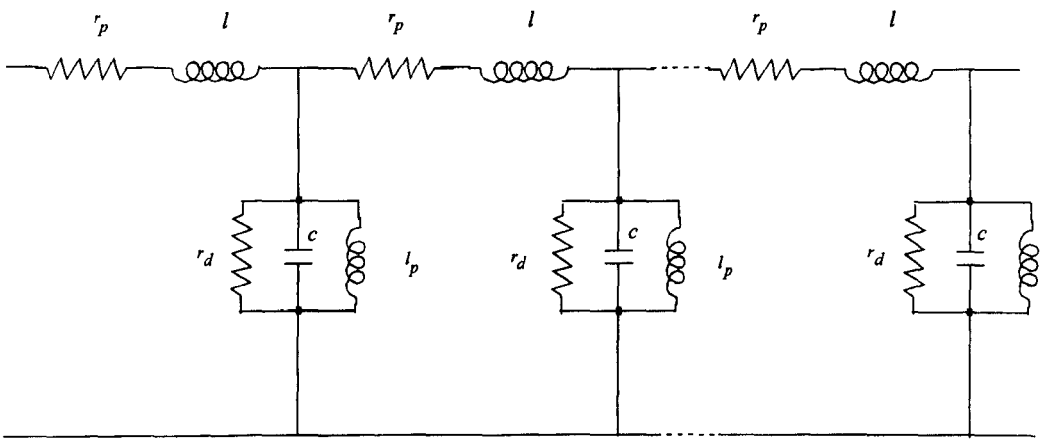

Figure 3.9 Transmission line model of a RF excited waveguide channel, including "distributed" shunt inductance

uniformity is reached when the net capacitance of a "unit cell" of the structure is zero. This requires the careful selection of the l_p value which satisfies the parallel resonance condition:

$$\omega^2 l_p c = 1 \tag{3.15}$$

where ω is the angular RF frequency and c is the distributed capacitance corresponding to each "unit cell". In practice, the number of inductors (coils) required is determined by the acceptable voltage uniformity, and may be restricted by the actual structure of the waveguide laser.

3.5 SUMMARY

This chapter began with a brief review of the waveguide CO_2 lasers, following the steps of the development from early days to the current state of the art. This was followed by a summary of the vibrational and rotational structure of the CO_2 molecules, leading to an introduction to the excitation and de-activation mechanism for CO_2 lasers. Resonance energy transfer from vibrationally excited N_2, also CO, to CO_2 (00^01) and additional vibrational and rotational relaxation processes were seen to provide a basis for understanding the relaxation pumping processes in laser amplification, particularly the pulsed mode as to be studied in Chapter 7. Next, in section 3.3, waveguide laser resonators were introduced, including the two types of most often used unstable resonators in planar CO_2 waveguide lasers. In later chapters, it will be seen that in the MOPA system under investigation, the negative branch unstable resonator is used as the master oscillator, while the positive branch unstable resonator is made use of for the multipass configuration of the amplifier. Finally, the concept of RF-discharge excitation was presented, with emphasis on techniques for achieving longitudinally uniform RF-discharge, which is essential for the performance of both laser oscillators and amplifiers.

REFERENCES

3.1 E. A. J. Marcatili and R. A. Schmeltzer, "*Hollow Metallic and Dieletric Waveguides for Long Distance Optical Transmission and Lasers*," *Bell Syst. Tech. J.*, **43**, 1783(1964)

3.2 P. W. Smith, *Appl. Phys. Rev.*, **136A**, 1187(1964)

3.3 T. J. Bridges, E. G. Burkhardt, and P. W. Smith, "*CO_2 Waveguide lasers*," *Appl. Phys. Lett.*, **20**, pp.403-405(1972)

3.4 E. Snitzer, *J. Opt. Soc. Am.*, **31**, 491(1961)

3.5 K. D. Laakmann and W. H. Steier "*Waveguides: characteristic modes of hollow rectangular dielectric waveguides*" *Appl. Opt.* **15**, 1334-1340 (1976)

3.6 K. D. Laakmann, *Appl., Opt.*, **15**, 2029(1076)

3.7 R. L. Abrams and A. N. Chester, "*Resonator Theory for Hollow Waveguide Lasers*," *Appl. Opt.*, **13**, pp.2117-2125(1974)

3.8 A. N. Chester and R. L. Abrams, *Appl. Phys. Lett.*, **21**, 576(1972)

3.9 J. J. Degnan and D. R. Hall, "*Finite-aperture Waveguide-Laser Resonators*," *IEEE J. Quant. Electron.*, **QE-9**, pp.901-910(1973)

3.10 J. J. Degnan, "*The Waveguide Laser: A Review*," *Appl. Phys. Lett.*, **11**, pp.1-33(1976)

3.11 D. R. Hall and C. A. Hill, "*Radiofrequency-Discharge-Excited CO_2 Lasers*," in Handbook of Molecular Lasers, P.K.Cheo, Ed., New York, Marcel Dekker, 1987

3.12 K. M. Abramski, A. D. Colley, H. J. Baker and D. R. Hall, "*Power scaling of large-area transverse radio frequency discharge CO_2 lasers*," *Appl. Phys. Lett.*, **54**, pp.1833-1835, 1989.

3.13 A. D. Colley, H. J. Baker, and D. R. Hall, "*Planar waveguide, 1kW cw, carbon dioxide laser excited by a single transverse RF-discharge*," *Appl. Phys. Lett.*, **61**(2), pp.136-138, July, 1992

3.14 C. J. Shackleton, K. M. Abramski, H. J. Baker and D. R. Hall, "*Lateral and transverse mode properties of CO_2 slab waveguide lasers*," *Opt. Comm.*, **89**, pp.423-428(1992)

3.15 "*Product Catalogue*," Rofin-Sinar Laser GmbH, 1998

3.16 R. H. Abram, "*High Power Waveguide Array Lasers*," *PhD thesis*, Heriot-Watt University, September 1998

3.17 A. I. Dutov, I. Yu. Evstratov, A. A. Kuleshev, S. A. Motovilov, N. A. Novoselov, V. E. Semenov, P. E. Smirnov, A. A. Sokolov, M. S. Yur'ev, "*Slab waveguide high power pulsed RF-excited CO_2-laser*," *Pro. SPIE*, V3574, 1998, pp.171-178

3.18 C. K. N. Patel, W. L. Faust and R. A. McFarlane, "*Continuous Wave Laser Action on Vibrational Rotational Transitions of CO_2*," *J. Phys. Rev.*, 136A, pp.1187-1193(1964)

3.19 J. B. Howard and E. B. Wilson, Jr., *J. Chem. Phys.*, 2, 620 (1934)

3.20 P. K. Cheo, "*Lasers*," Vol. 3, Chapter 2, (A.K.Levine and A.J.DeMaria eds), Marcel Dekker, New York (1971)

3.21 W. J. Witteman, "*The CO_2 laser,* " Published by Springer-Verlag Berlin Heidelberg 1987

3.22 D. M. Dennison, *Rev. Mod. Phys.* 12, 175 (1940)

3.23 E. Fermi, *Z. Physik*, 71, 250(1931)

3.24 G. Herzberg, "*Infra-red and Raman Spectra*," p.379, Princeton New Jersey

3.25 J. T. Verdeyn, "*Laser Electronics*," Chapter 15, Prentice Hall International Inc., New Jersey, 1995

3.26 A. V. Phelps, *Rev. Mod. Phys.*, 40, 399(1968)

3.27 R. D. Hake, A.Phelps, *Phys. Rev.*, 158(1) 70(1967)

3.28 M. J. W. Boness and G. J. Schulz, *Phys. Rev. Lett.*, 21(15) 1031(1968)

3.29 J. Lowke, A. Phelps and B. Irwin, *J. Appl. Phys.*, 44(10) 4664(1973)

3.30 P. O. Clark and M. R. Smith, *Appl. Phys. Lett.*, 9, 367(1966)

3.31 C. B. Moore, *Fluorescence* (G.G.Guilbault, ed.), Dekker, New York, 1967, chapter 3.

3.32 H. Statz, C. L. Tang, and G. F. Koster, *J. Appl. Phys.*, 37, 4278 (1966)

3.33 P. K. Cheo, *Appl. Phys. Lett.*, 11, 38 (1967); *IEEE J. Quant. Electron.*, 4, 587(1968)

3.34 P. K. Cheo, *J. Quant. Electron.*, 4, 587(1968)

3.35 P. K. Cheo, *J. Appl. Phys.*, 38, 3563(1967)

3.36 M. Kovacs, D. R. Rao, and A. Javan, *J. Chem. Phys.*, 48, 3339(1968)

3.37 C. B. Moore, R. E. Wood, B. Hu, and T. J. Yardley, *J. Chem. Phys.*, 46, 4222(1967)

3.38 L. O. Hocker, M. A. Kovacs, C. K. R. Rhodes, G. W. Flynn, and A. Javan, *Phys. Rev. Lett.*, 17, 233(1966)

3.39 R. D. Sharma and C. A. Brau, *Phys. Rev. Lett.*, 19, 1273(1967)

3.40 R. L. Abrams and P. K. Cheo, *Appl. Phys. Lett.*, **15**, 177(1969)

3.41 P. K. Cheo and R. L. Abrams, *Appl. Phys. Lett.*, **14**, 47(1969)

3.42 H. Kogelnik and T. Li, *Appl. Opt.*, **5**, 1550(1966)

3.43 R. L. Abrams, *J. Quant. Electron.*, **8**, 838(1972)

3.44 D. M. Henderson, Appl. Opt., **15**, 1066(1976)

3.45 A. Javan, W. R. Bennett, Jr., and D. R. Herriott, *Phys. Rev.*, **6**, 106(1961)

3.46 P. P. Chenausky, *paper TUKK4, Conference on Lasers and Electro-optic Systems (CLEOS), San Diego* (1980)

3.47 G. Allcock and D. R. Hall, *Opt. Commun.*, **37**, 49(1981)

3.48 K. D. Laakmann, *Proceedings of lasers'78 Conference, Orlando, Florida*(1978)

3.49 K. D. Laakmann, *Proceedings of lasers'79 Conference, Orlando, Florida*, pp.741-743(1979)

3.50 L. V. Sutter, *Proceedings of SPIE Meeting, Washington, D.C.*, **227**, (1980)

3.51 G. A. Griffiths, *Proceedings of SPIE Meeting, Washington, D.C.*, **227**, pp.6-11(1980)

3.52 S. M. Levitskii, "*An Investigation of the Breakdown Potential of a High-Frequency Plasma in the Frequency and Pressure Transition Regions*," *J. Sov. Phy.-Tech. Phys.*, No **2**, 887(1957)

3.53 N. A. Yatsenko, *Sov. Phys. Tech. Phys.*, **26**, 678(1981)

3.54 P. Vidaud, S. M. A. Durrani, and D. R. Hall, "*Alpha and gamma RF capacitative discharges in N_2 at intermediate pressures*,"*J. Phys. D: Appl. Phys.* **21** pp.57-66(1988)

3.55 P. P. Vitruk, H. J. Baker and D. R. Hall, "*The characteristics and stability of high power transverse radio frequency discharges for waveguide CO_2 slab laser excitation*," *J. Phys. D: Appl. Phys.* **25**, pp.1767-1776(1992)

3.56 P. P. Chenausky, R. A. Hart, L. A. Newman, and N. N. Hoffman, *Paper TLN2, Proceedings of Conference on Lasers and Electrooptics, Technical Digest* (1982)

3.57 G. A. Griffiths, "Improved Discharge Uniformity for Transverse Radio Frequency Waveguide CO_2 lasers," *Proc. SPIE*, **335**, 69(1982)

3.58 D. He and D. R. Hall, *J. Appl. Phys.*, **54**, 4367(1983)

3.59 P. P. Chenausky and L. A. Newman, U.S. Patent 4, 443, 877

CHAPTER FOUR

BEAM CHARACTERISATION AND TRANSFORMATION

4.1 INTRODUCTION

A MOPA system requires effective beam coupling between the master oscillator and the amplifier, in terms of both the power and the mode properties of the beam [4.1]. As will be seen in the next chapter, optimum beam coupling (or mode matching) requires a well-defined input beam. Thus, before considering the design of a MOPA system, it is necessary to indicate how a laser beam is characterised and how it can be transformed as desired.

The theory of laser beams has been well developed over the last forty years or so. Gaussian beam theory derives from basic concept of electromagnetism, and its basic elements were developed in early 1960's [4.2-4.5] to describe the modes in laser resonators [4.6-4.7]. The characteristics of Gaussian beams and their relationship with laser resonators were systematically analysed and summarised in several publications [4.7-4.8], and are reviewed in many textbooks [4.10-4.12]. Kogelnik and Li [4.9] derived equations that govern the propagation of the fundamental Gaussian beam in free space and used them to describe the variation of the beam radius and the wavefront radius of curvature with propagation distance. Higher order modes have a phase front of identical radius of curvature to the fundamental Gaussian mode but their transverse distributions are modified by Hermite-polynomials (for a rectangular co-ordinate system) or Laguerre polynomials (for a cylindrical co-ordinate system). In paraxial systems, where aperture diffraction effects can be neglected, the transformation of Gaussian beams through any optical system can be conveniently designed using the well-known *ABCD* law, by making use of the complex beam parameter, q [4.11].

In the early 1990's, based on a definition of beam width in terms of the second moment, a theory [4.13-4.15] was developed which uses the beam quality factor M^2 to characterise general laser beams, either Gaussian or non-Gaussian, and to quantify their transverse beam quality. This

approach has become widely recognised and was adopted in an ISO standard draft [4.16-4.18] which concerns measurements of laser beam width, divergence and beam propagation factor and so on.

In this chapter, a review will be made of the literature of laser beam characterisation and propagation, leading to discussions of real laser beam transformation through optics, to be used in designing and building the MOPA format amplifier system.

4.2 GAUSSIAN BEAMS

4.2.1 Wave Equation

Gaussian beams are derived as approximate solutions of the Wave Equation under the boundary conditions defined by the open laser resonators [4.9] where large apertures are assumed so that diffraction effects can be neglected. An electromagnetic wave u must satisfy the scalar wave equation:

$$\nabla^2 u + \kappa^2 u = 0 \tag{4.1}$$

where $\kappa = 2\pi/\lambda$ is the propagation constant in the medium. As laser beams are to some extent similar to plane waves, but with non-uniform intensity distributions which are concentrated near the axis of propagation, and are with curved phase fronts, one defines the light travelling in the z direction as:

$$u = \psi(x, y, z)\exp(-j\kappa z) \tag{4.2}$$

Here $\psi(x, y, z)$ is a complex function which is assumed to vary slowly with z thus $\partial^2\psi / \partial^2 z$ can be neglected. Inserting Eq. (4.2) into Eq. (4.1) one obtains:

$$\frac{\partial^2\psi}{\partial x^2} + \frac{\partial^2\psi}{\partial y^2} - 2j\kappa\frac{\partial\psi}{\partial z} = 0 \tag{4.3}$$

This differential equation is known as the paraxial wave equation; it is valid for the description of almost all optical resonators and beam propagation problems, as long as the optical beams are travelling with half cone-angles less than $0.5rad$ (p.630 of [4.19]). Given certain boundary

conditions, solutions are obtained that correspond to Gaussian beams, either lowest order fundamental mode or higher order modes, as summarised in the following sections.

4.2.2 Fundamental Gaussian Beams

For paraxial beams in free space, there are several approaches that can be used to derive the Gaussian-spherical wave solution and its higher order extensions. These include the complex source point derivation, the differential equation approach, direct substitution of the Gaussian-spherical solution into the Huygens-Fresnel integral and the so-called plane wave expansion approach [4.9].

With the differential equation approach [4.9], if one assumes a trial solution for the paraxial wave Eq. (4.3) as:

$$\psi = \exp\left[-j(p + \frac{\kappa}{2q}r^2)\right] \tag{4.4}$$

where $r^2 = x^2+y^2$ and P represents a complex phase shift associated with the propagation of light beam. q is the so-called complex beam parameter, describing the Gaussian variation in transverse beam intensity as well as the curvature of the phase front, which is normally spherical near the axis. Then the solution for the fundamental Gaussian mode can be obtained as:

$$u(r,z) = \frac{w_0}{w(z)}\exp\left[-\frac{r^2}{w^2(z)}\right]\exp\left\{-j\kappa\left[z + \frac{r^2}{2R(z)}\right]\right\}\exp(-\Phi) \tag{4.5}$$

where w_0 is the beam waist, corresponding to the minimum diameter $2w_0$ of the beam in the plane along the z axis where the phase front is plane. Other parameters in this equation will be discussed below.

Eq. (4.5) consists of two parts - the amplitude part and the phase part. The amplitude part shows that the intensity distribution of the fundamental mode is Gaussian in every beam cross section, and that the width of the Gaussian intensity profile changes along the axis. $w(z)$ is a measure of the decrease of the field amplitude with the distance from the axis. It corresponds to the distance

at which the amplitude is $1/e$ times that on the axis and is called the beam radius or spot size. The factor $w_0 / w(z)$ indicates the expected intensity decrease on the axis due to expansion of the beam.

From the amplitude part, the power intensity profile of the fundamental Gaussian beam at z can be obtained as:

$$I(r) = I(0)exp\left[-2\frac{r^2}{w^2(z)}\right] \tag{4.6}$$

By integrating Eq. (4.6) within the radius $w(z)$, one can see that the power enclosed within the beam radius is $1/e^2$ or 86.5% of the total beam power.

From the phase part, one can see that $R(z)$ is the radius of curvature of the wavefront that intersects the axis at z. Φ represents a phase shift difference between the Gaussian beam and an ideal plane wave and is equal to $arctan(\lambda z/\pi w_0^2)$. The radius of curvature of the phase front $R(z)$ and the beam spot size $w(z)$ are related by the complex beam parameter q by the equation:

$$\frac{1}{q(z)} = \frac{1}{R(z)} - j\frac{\lambda}{\pi w^2(z)} \tag{4.7}$$

At the beam waist position where the phase front is plane, the radius of curvature of the phase front is infinite and the complex beam parameter is purely imaginary as follows:

$$q_0 = j\frac{\pi w^2{}_0}{\lambda} \tag{4.8}$$

In addition, there exists a simple relationship for the q parameters at different positions along the z axis. For a given q_1 at z_1, q_2 at the position z_2 with a distance z away from z_1 can be obtained as:

$$q_2 = q_1 + z \tag{4.9}$$

Thus, the beam parameter at a distance z away from the beam waist can be expressed as:

$$q(z) = j\frac{\pi w^2{}_0}{\lambda} + z \tag{4.10}$$

Combining Eqs. (4.7) and (4.10) gives:

$$w^2(z) = w^2{}_0 + (\frac{\lambda}{\pi w_0})^2 z^2 = w^2{}_0 \left[1 + (\frac{z}{z_r})^2 \right] \tag{4.11}$$

and

$$R(z) = z \left[1 + (\frac{z_r}{z})^2 \right] \tag{4.12}$$

here $z_r = \pi w_0^2/\lambda$, and is known as Rayleigh range.

Eq. (4.11) describes the variation of the beam radius along the propagation axis z at both directions. The geometry of a fundamental Gaussian beam is shown in Fig. 4.1. As can be seen, in the region - z_R to + z_R the beam is approximately collimated. The half-cone far field angle of the beam defined at the $1/e^2$ of the intensity can be obtained as:

$$\theta_{far} = \lim_{z \to \infty} \frac{w(z)}{z} = \frac{\lambda}{\pi w_0} \tag{4.13}$$

Eq. (4.12) describes the phase front radius of curvature of the beam. A minimum value of $R(z) = 2z_R$ exists at $z = z_R$. In addition to the plane phase front $R(z) \to \infty$ at $z = 0$, the phase fronts also approach plane wave configuration when $z \to \infty$, and the centre of the curvature is at the beam waist. The regime where $z >> z_R$ corresponds to a spherical wave diverging from a point source at $z = 0$.

4.2.3 Higher Order Gaussian Beams

The fundamental Gaussian mode is not the only solution of the wave equation (4.3). There are also other solutions which have similar properties to that of the fundamental Gaussian mode and form a complete and orthogonal set of functions, i.e., the higher order Gaussian modes. In rectangular (x,y,z) geometry, the Hermite-Gaussian modes take the form of:

$$\psi = g\left[\frac{x}{w(z)}\right] h\left[\frac{y}{w(z)}\right] \exp\left\{ -j\left[p + \frac{\kappa}{2q(z)}(x^2 + y^2) \right] \right\} \tag{4.14}$$

where $g[x/w(z)]$ is a function of x and z, and $h[y/w(z)]$ is a function of y and z. For real $g[x/w(z)]$ and $h[y/w(z)]$ this indicates mode beams with intensity patterns which scale

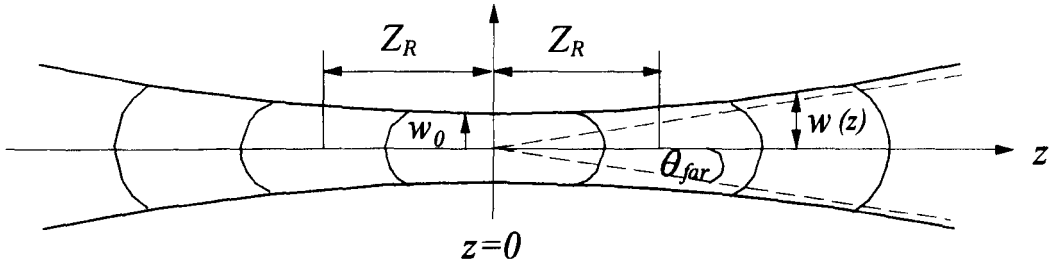

Figure 4.1 The geometry of a fundamental Gaussian beam

according to the width $2w(z)$ of a Gaussian beam. Inserting the trial solution (4.14) into the paraxial wave equation (4.3), one obtains [4.9, 4.19, 4.20]:

$$g\left[\frac{x}{w(z)}\right]h\left[\frac{y}{w(z)}\right] = H_m\left[\sqrt{2}\frac{x}{w(z)}\right]H_n\left[\sqrt{2}\frac{y}{w(z)}\right] \tag{4.15}$$

where m and n are the transverse mode numbers, $H_m(x)$ and $H_n(y)$ are the Hermite polynomials of order m and n. A similar derivation applies to modes in a cylindrical co-ordinate system (r, φ, z), where the Laguerre-Gaussian modes take the form:

$$\psi = g\left[\frac{r}{w(z)}\right]\exp\left\{-j\left[p+\left(\frac{\kappa}{2q(z)}r^2+l\Phi\right)\right]\right\} \tag{4.16}$$

and $g(r/w(z))$ is found to be:

$$g\left[\frac{r}{w(z)}\right] = \left[\frac{2^{1/2}r}{w(z)}\right]L^l{}_p\left[\frac{2r^2}{w^2(z)}\right] \tag{4.17}$$

here Lp^l is a generalised Laguerre polynomial, p and l are the radial and angular mode numbers. Eqs. (4.15) and (4.17) show that the Laguerre intensity pattern of a higher order beam is described by the product of Hermite (in a rectangular co-ordinate system) or Laguerre (in a cylindrical co-ordinate system) and Gaussian functions. In either Hermite-Gaussian modes or Laguerre-Gaussian modes, $w(z)$ is the same for modes of all orders. So is the $R(z)$, indicating that the phase front curvature is the same and changes in the same way for all modes with different order numbers. Thus, Eq. (4.9) for fundamental Gaussian beam also holds for higher order Gaussian beams. However, the phase shift Φ depends on mode numbers and is expressed as:

$$\Phi = (m+n+1)arctan\left(\frac{\lambda z}{\pi w_0{}^2}\right) \tag{4.18}$$

for Hermite-Gaussian modes or

$$\Phi = (2p+l+1)arctan\left(\frac{\lambda z}{\pi w_0{}^2}\right) \tag{4.19}$$

for Laguerre-Gaussian modes.

4.2.4 Gaussian Beam Transformation

The transformation of Gaussian beams through optics has been well-described in the literature. When a laser beam passes through an optical system, its beam parameters *R(z)* and *w(z)* will normally be changed. However, the transverse field distribution will maintain unchanged if the optical system is ideal. As the beam parameters *R(z)* and *w(z)* are the same for modes of all orders, the following discussion based on these two parameters and their function *q(z)* is valid for either fundamental mode or higher order modes.

The transformation of beam passing through an ideal thin lens (or equivalently reflecting from an ideal mirror) is the simplest case. This is illustrated in Fig. 4.2 in which the incoming beam is labelled with subscript 1 and the outgoing beam with subscript 2. Two methods can be used to derive the relationship linking the incoming and outgoing beams, i.e. the geometrical optical approach and the *ABCD* Law using the *q* parameters. Both give the same results, describing the relationships between the incoming and outgoing beams in a straightforward manner as:

$$l_2 = F(1+\frac{F}{R_{F1}}) = F + \frac{(L_1 - F)F^2}{(L_1 - F)^2 + (Z_R)^2} \tag{4.20}$$

and

$$\frac{1}{w_{02}^{\ 2}} = \frac{1}{w_{01}^{\ 2}}(1-\frac{l_1}{F})^2 + \frac{1}{F^2}(\frac{\pi w_{01}}{\lambda})^2 \tag{4.21}$$

plus

$$2w_{F1} = F\theta_2 \tag{4.22a}$$

$$2w_{F2} = F\theta_1 \tag{4.22b}$$

Eq. (4.22b) provides an effective means for measurement of the far-field divergence angle of a Gaussian beam, that is, by launching a Gaussian beam through a single lens or mirror, the far-field divergent angle is determined by the spot size at the focal plane in the image side, divided by the focal length of the lens or mirror.

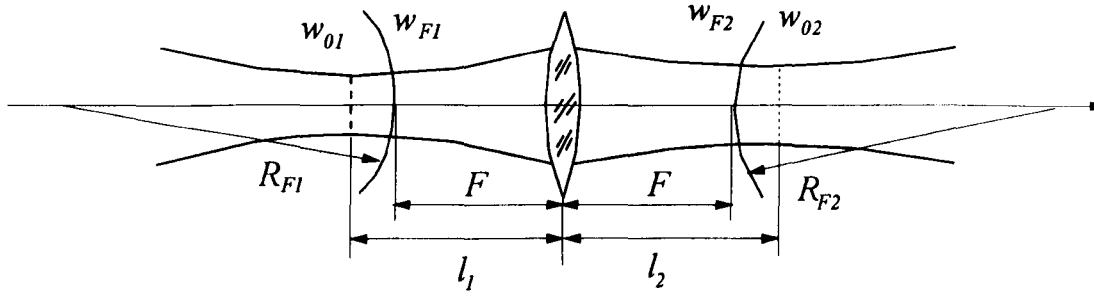

Figure 4.2 Fundamental Gaussian beam transformation through a thin lens (for derivation with geometrical optical approach)

For more complicated optical structures, if only consisting of thin lenses or mirrors, transformation may be made by repeated use of Eqs. (4.20) and (4.21). However, the *ABCD* matrix approach is more general. If the *ABCD* matrix for the transfer of paraxial rays through the optical structure is known, then the complex beam parameter of the outgoing beam q_2 can be calculated according to that of the incoming beam q_1 as [4.8, 4.9, 4.21]:

$$q_2 = \frac{Aq_1 + B}{Cq_1 + D} \tag{4.23}$$

This equation is known as the *ABCD* law. In this manner, the parameters of the outgoing beam, such as the beam waist position and spot size, can be obtained according to Eqs. (4.7) to (4.9).

4.3 ARBITRARY REAL LASER BEAMS

Gaussian beam theory had been well-established by the later 1970's and rather sophisticated in dealing with issues related to Gaussian beams in laser research and engineering. However, Gaussian beam theory was found insufficient in many practical cases where either the laser beams were not pure single Gaussian mode, or their mode components were hardly known. Thus, there arose a need to develop a general approach to the characterisation of the "quality" of the laser beams and their propagation parameters, assuming that there is no prior knowledge of the modes (and their amplitude weighting) which make up the "arbitrary" laser beam. This led to the idea of using a single number to quantify the beam quality [4.21] and eventually to the development of the M^2 theory. Practical laser beams, including multimode or partially incoherent beams, beams with astigmatism or asymmetry, and other real and imperfect laser beams, are referred to by Siegman [4.13] as arbitrary real laser beams.

4.3.1 M^2 - Beam Quality and Propagation Factor

The M^2 concept was introduced during early 1990's [4.13-4.15], which uses a single number M^2 to quantify the transverse beam quality of arbitrary laser beams, and characterises the propagation of general laser beams with a few propagation parameters and a set of relationships similar to

those in Gaussian beam theory. The definition for M^2 and its physical meaning will be given below.

Based on the second-moment definition, for an arbitrary real laser beam, the beam width or spot size $W_x(z)$ in the x direction at any plane along its propagation direction z is twice the value of $\sigma_x(z)$, the standard deviation of the time-averaged beam intensity profile $I(x, y, z)$ at the plane z:

$$W_x(z) = 2\sigma_x(z) \tag{4.24}$$

where

$$\sigma_x(z)^2 = \frac{\iint x^2 I(x,y,z)dxdy}{\iint I(x,y,z)dxdy} \tag{4.25}$$

A similar expression can be written for the beam size in the y direction. This spot size defined based on the value of the second-moment propagates in free space according to the hyperbolic expression [4.13]:

$$W_x(z)^2 = {W_{0x}}^2 + {M_x}^4 (\frac{\lambda}{\pi W_{0x}})^2 z^2 \tag{4.26}$$

which may be re-written as:

$$W_x(z)^2 = {W_{0x}}^2 \left[1 + (\frac{z}{z_{R_X}})^2 \right] \tag{4.27}$$

where

$$z_{R_x} = \frac{\pi {W_{0x}}^2}{\lambda {M_x}^2} \tag{4.28}$$

The relations for $W_y(z)$ are similar to (4.26)-(4.28). Comparing Eqs. (4.11) and (4.26), it is seen that the second-moment-based (and time-averaged) real beam spot sizes $W_x(z)$ and $W_y(z)$ for any real laser beam propagate exactly like the corresponding Gaussian beam spot sizes $w_x(z)$ and $w_y(z)$, except for the inclusion of ${M^2}_x$ and ${M^2}_y$, the so-called beam propagation factors, which are often referred to as the M-squared factors or as the beam quality.

The M^2 factors are defined as the ratio of the *real-beam space-beamwidth product* to the *ideal-Gaussian space-beamwidth product* [4.13], characterising the additional spreading of a real or non-ideal laser beam in the far field, as seen from the product of the waist spot size and the far field spot size. For an ideal Gaussian beam, this product is given from Eq. (4.11) as:

$$w_0\theta_{far} = \frac{\lambda}{\pi} \tag{4.29}$$

where θ_{far} is the far-field beam divergence. For an arbitrary real laser beam the same product is given from Eq. (4.26) as (the subscript x are removed for simplicity):

$$W_0\theta_{far} = M^2\frac{\lambda}{\pi} \tag{4.30}$$

where θ_{far} is now the far-field divergence of the *real laser beam*. Similar discussions can be made in a cylindrical co-ordinate system if one defines radial or cylindrical variances as [4.13]:

$$\sigma^2_r(z) = \sigma^2_x(z) + \sigma^2_y(z) \tag{4.31}$$

and

$$\sigma^2_p = \sigma^2 s_x + \sigma^2 s_y \tag{4.32}$$

thus obtains a cylindrical M^2 factor as:

$$M^2_r = 2\pi\sigma_r\sigma_p \tag{4.33}$$

and a cylindrical spot size as:

$$W_r(z) = 2^{1/2}\sigma_r(z) \tag{4.34}$$

The M^2 factors have the property that is $M^2 \geq 1$, and reduce to $M^2 = 1$ for an ideal, fully coherent fundamental TEM_{00} Gaussian beam. In this sense, the M^2 factors have also been referred to as the beam quality and are widely used to quantify the quality of laser beams.

For laser beams with known mode mixture, the M^2 factor may be obtained by computation based on the second moment definition. The calculated M^2 factors of a few high order Gaussian beams can be found in reference [4.23]. The M^2 factors of beams composed of the lowest and higher order Hermite-Gaussian modes or Lauguerre-Gaussian modes can be expressed in terms of order

number and the relative amplitude of each mode [4.13]. Similar computation process can give the transverse M^2 factors of laser beams from waveguide lasers, made up of either single mode or mixed modes. However, for "real" laser beams of unknown arbitrary mode mixture, the M^2 value must be determined experimentally.

4.3.2. Real Laser Beam Characterisation

Using the M^2 parameter, one is able to characterise the actual propagation characteristics of real laser beams. This leads to the use of the name "beam propagation factor". With the second-moment method of description, using Eq. (4.26) or (4.27), the propagation of any arbitrary real laser beam in free space or in any paraxial or *ABCD* optical system can be fully characterised by six parameters. These are the waist size w_0, waist position z_0 and the beam propagation factor M^2 in each of the two orthogonal transverse directions. Theoretically, the determination of these six parameters for any laser beam can be made according to Eq. (4.26) by measurements of the transverse beam widths at any three positions along the beam. Practically measurements at a large number of points are needed to give accurate results by fitting the large number of data points to the hyperbolic Eq. (4.26). A procedure for the measurements of the beam parameters is proposed in ISO/TC172/SC9 WG1 N38 [4.18] and such measurements can now be carried out using available commercial beam analysers usually incorporating *CCD* camera or beam scanning systems.

It has to be pointed out that although for cw laser beams the process of determining the beam propagation parameters is rather straightforward, for short-pulsed laser beams, the process is more complicated; for example it may be necessary to take account of the nature of the temporal evolution of the beam profile which is likely to give rise to time varying M^2 factors [4.24]. In all cases described in this thesis where M^2 values are quoted, these are the result of multiple beam profile measurements and curve fitting.

Limitation of the M^2 theory

Although the use of the M^2 parameter to characterise arbitrary real laser beams is a rather general and universal approach, its validity does have a limitation. This occurs when the laser beam has an infinitely sharp or discontinuous edge, such as, for example, an ideal single slit or "top hat" beam, where the spatial-frequency variance σ^2_s of such a beam diverges and approaches infinity. Siegman has suggested possible solutions [4.13] to overcome the conceptual difficulty with sharp edged beams such as by rounding off the spatial intensity distribution or truncating the spatial-frequency distribution so as to eliminate large-angle and especially evanescent waves. Nevertheless, to our knowledge, there are no publications on this issue to date.

4.4 BEAM TRANSFORMATION OPTICS

4.4.1 Real Laser Beam Propagation through Optics

The second-moment based M^2 concept provides an approach for beam transformation design and calculations for arbitrary real laser beams. To do so we use the propagation expressions in Eqs. (4.26) to (4.28) assuming that the real laser beam behaves like a Gaussian beam with a Gaussian beam waist size $w_0 = W_{0x}$, but with its wavelength increased to $M^2_x\lambda$. Making this assumption, we can treat the propagation of this real laser beam as though it is a Gaussian beam.

A more useful technique for interpretation is to think of the real laser beam with waist size W_{0x} and $M^2 > 1$ as having contained within it an imaginary or hypothetical "embedded Gaussian beam" (see Fig. 4.3) whose Gaussian spot size $w_x(z)$ is smaller than the real beam width or spot size $W_x(z)$ by just the value of M_x, that is, $W_x(z) = M_x w_x(z)$, at every value of z along the beam including the waist plane z_{0x} where $W_{0x} = M_x w_{0x}$.

This then leads to a straightforward procedure for optical beam transfer design. Given the real beam waist size W_{0x}, waist location z_{0x} and the beam propagation factor M^2_x, one can first analyse and design an optical system suitable for the imaginary embedded Gaussian beam with wavelength λ and Gaussian spot size $w_{0x} = W_{0x}/M_x$ at position z_{0x}, making use of all the usual Gaussian beam and paraxial $ABCD$ matrix techniques that are normally used for ideal Gaussian

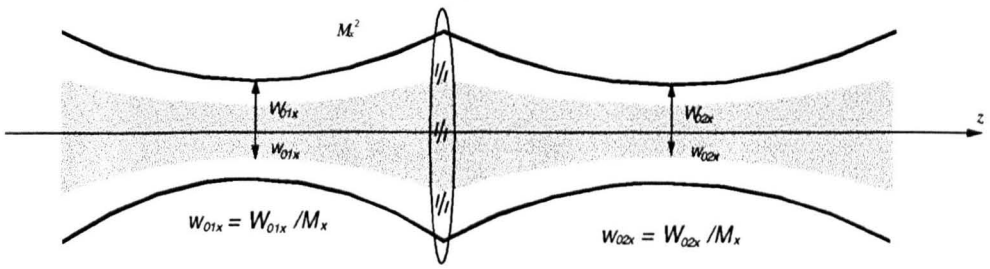

Figure 4.3 Real beam propagation through optical systems (using a lens as an example) with its waist at exactly the same position as an embedded Gaussian beam, but its actual spot size M_x times larger

beams, as discussed in section 4.2.4. The real beam when propagating through this system will then have all its waists at exactly the same positions as the embedded Gaussian beam, but the actual spot size $W_x(z)$ will be exactly M_x times larger than the $w_x(z)$ value of the embedded Gaussian beam at every plane along the optical system.

As illustrated in Fig. 4.4, given a source beam which has a beam propagation factor of M^2 and a beam waist W_{01}, to transform it into one having a beam waist W_{02}, the optical system design must meet the *ABCD* law expressed by Eq. (4.23) with:

$$q_1 = z_{01} + j\frac{\pi}{\lambda}(\frac{W_{01}}{M})^2 \tag{4.35}$$

and

$$q_2 = z_{02} + j\frac{\pi}{\lambda}(\frac{W_{02}}{M})^2 \tag{4.36}$$

Here z_{01} is the distance of the source beam waist from the first optical surface, and z_{02} is the required position of the image beam waist with respect to the last optical surface of the optical system.

One can obtain the expression of the *ABCD* matrix of a particular optical system from its layout, components and positions with respect to the beams by the techniques described [4.8]. Then the parameters, such as focal lengths, incident angles, positions and orientations of the components etc., of the optical system can be determined by combining Eqs. (4.23, 4.35, 4.36). There may be more variables than the number of equations; however, this provides increased flexibility for the design that are very useful in practical cases.

For circular beams, at low power levels, normal lenses may be used. However, if mirrors are to be used, the incident angles should be kept as small as possible for cases where aberration-induced beam distortion must be avoided. For rectangular beams, the beam transformation must be performed in two orthogonal directions independently. This perhaps involves the use of cylindrical components or large incident angles to give different focal lengths, therefore different modifications for the beam in and normal to the plane of the tilt.

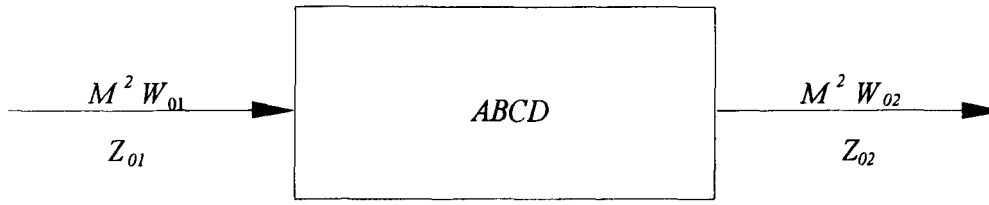

Figure 4.4 Schematic of beam transformation system using ABCD matrix

In all the discussions so far, the beam propagation factor of a beam passing through an optical system has been assumed to be unchanged. As a matter of fact, for a practical optical system, elementary aberrations such as spherical aberration, coma, and astigmatism may exist, due to defects of the optical components and possible thermal effects in the presence of high power beams, leading to beam quality degradations [4.25]. This suggests the necessity of a small amount of modification of the M^2 factor of the image beam in the design procedure, and enough room for final adjustment of the system.

4.4.2 Transformation Optics for Planar Waveguide Amplifiers

Requirements for the transformation optics

The success of the oscillator-amplifier configuration depends critically on the transfer of the beam from the waveguide in the oscillator, through free space optical components to the amplifier waveguide. Since both the beam produced by the oscillator and that required by the amplifier are rectangular, the transformation optical system is required to satisfy the following requirements:

- The transverse beam size from the oscillator is adjustable to match the transverse mode of the amplifier, maximising the excitation of the fundamental waveguide mode.
- The lateral beam size from the oscillator can be adjusted to match the input requirements of the unstable resonator type of multi-pass fold optics.
- The beam waists in both directions are located at the entrance of the amplifier waveguide.
- An opportunity exists for the use of a beam-clean-up aperture, particularly in the lateral direction.
- To be a non-critical arrangement, ideally making use of standard mirror radii, etc.
- To be relatively compact.

Beam parameters measurement of the Master Oscillator

The first step is to measure the parameters of the beam provided by the master oscillator laser. The set-up is illustrated in Fig. 4.5. A beam waist is formed by the 1m concave radius steering

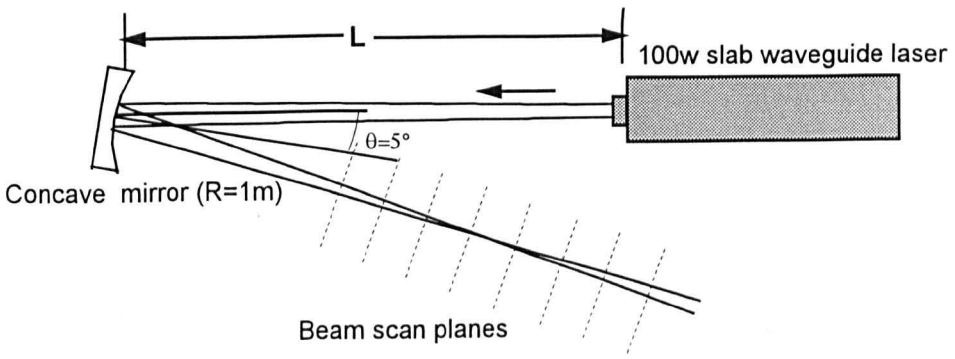

Figure 4.5 Experimental set-up for beam parameters measurement

mirror and passes through a rotating mirror laser beam scanner. The scanner is essentially a one dimensional instrument, which scans a beam over an IR detector with a spatial resolution of ~ 100μm. The scanner module is translated to a series of positions along the beam path through a focal region. The module is also oriented in either the vertical or horizontal plane to measure the lateral and transverse beam profiles at different axial positions. The beam scanner waveforms are recorded by a digital oscilloscope and processed using SigmaPlot software in a PC, to give the second moment values of the beam profiles. With the second moment values obtained for a range of scanning positions through the beam waist region, the waist sizes and locations of the beam in both planes are obtained, along with the corresponding values of M_x^2 and M_y^2 by curve fitting using Eq. (4.26). Finally, the beam parameters are transformed back through the 1m focusing mirror using the *ABCD* law calculation to determine the parameters of the actual beam produced by the laser.

Analysis of the experimental measurements indicated that in the transverse direction (i.e. the waveguide direction), beam parameters were $W_{0y} = 0.65mm$ and $M_y^2 = 1.18 \pm 0.05$ while in the lateral direction, after beam clean-up to remove the side-lobes, we have $W_{ox} = 1.65mm$ with $M_x^2 \cong 1.2$. However, the transverse and lateral beam waists do not occur in the same axial plane.

Transformation optics

A general view of a beam transformation system is shown in Fig. 4.6. The *Z*-fold arrangement uses a pair of concave gold mirrors for beam transformation, providing complete flexibility for adjustment of the axis alignment, beam waist sizes and locations. In addition a lateral aperture can be placed in the far-field plane between the mirrors, to "clean-up" the beam profile of the oscillator, and also eliminate mis-aligned paths for parasitic oscillation between the oscillator from the amplifier. The use of off-axis spherical mirrors allows different focal power in the transverse and lateral directions.

However, the design of such a general system has proved to be complicated by the large number of degrees of freedom available, and therefore two simpler arrangements are considered; they are

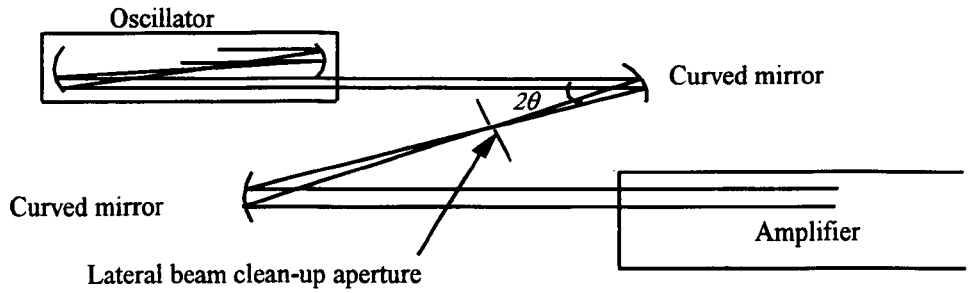

Figure 4.6 General beam transformation system using two off-axis curved mirrors

the one off-axis curved mirror system and the two off-axis curved mirror telecentric system. These systems are investigated to simplify the general transformation method shown in Fig. 4.6 to reduce the complexity of the set-up and the difficulty in the practical implementation.

a) One mirror system

The simplified system in Fig. 4.7 uses the properties of an off-axis curved mirror to provide two focal lengths, allowing mode matching independently in the transverse and lateral directions. The focal lengths of the spherical mirror of radius R in the plane of tilt and normal to the plane of tilt vary with the incident angle θ as described below:

Normal to the plane of tilt $$f_x = \frac{(R/2)}{\cos\theta} \tag{4.37}$$

In the plane of tilt $$f_y = (R/2)\cos\theta \tag{4.38}$$

The transformation of both sets of beam parameters may be controlled with the single off-axis mirror, using the six variable parameters: R, θ, oscillator to mirror distance, d_{1x} (d_{1y}) and amplifier to mirror distance, d_{2x} (d_{2y}). While d_{1x} and d_{1y} may not be equal depending on the beam characteristics of the laser oscillator, d_{2x} and d_{2y} are generally required to be equal, to ensure both the transverse and the lateral waists of the transformed beam can be positioned at the entrance of the waveguide of the amplifier. However, it has the disadvantage that there are no additional degrees of freedom to control the position of an intermediate Fourier plane in the lateral direction for spatial filtering of the oscillator beam, and the only opportunity to accomplish this filtering is at the amplifier input.

The basic equations for this one mirror system can be obtained from Eqs. (4.20) and (4.21) as:

$$W_2 = \frac{W_1}{\sqrt{\left(1-\frac{d_1}{f}\right)^2 + \frac{\pi^2 W_1^4}{M^4 \lambda^2 f}}} \tag{4.43}$$

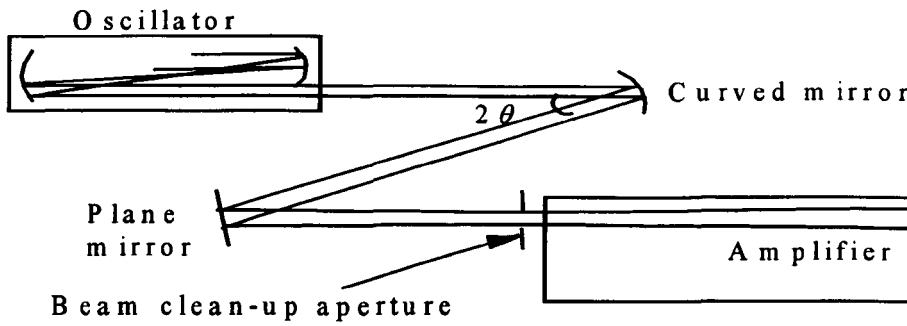

Figure 4.7 Simplified beam transformation system using one off-axis curved mirror

$$d_2 = f + \frac{(d_2 - f)f^2}{(d_1 - f)^2 + \frac{\pi^2 W_1^4}{M^4 \lambda^2}} \tag{4.44}$$

where f is the focal length, W_1 the beam waist of the source, W_2 the transformed beam waist and M^2 the beam propagation factor.

These equations are applied separately to the two orthogonal directions using the appropriate forms for the focal length of the off-axis curved mirror (Eqs. (4.37-4.38)) and the measured source spot sizes, locations and beam quality. Given a trial value of the radius of curvature R, a numerical search is made using Mathcad Plus 5.0 to find the mirror angle θ, d_1 and d_2 which simultaneously produce the desired beam waists at the amplifier input for the two orthogonal directions.

For this one mirror system, it is found that the correct orientation of the fold plane is in the transverse direction for the oscillator.

b) Telecentric system

Interests in the telecentric beam transformation optical system arises from the fact that the oscillator is already characterised in terms of planar waveguide modes and the correct view should be the imaging of these modes on to the entrance plane of the amplifier. A symmetric two mirror telecentric relay system is shown in Fig. 4.8 which maps the oscillator beam at its waveguide exit onto the amplifier input plane, conserving both the spatial size and phase front curvature. This method should be capable of very effective coupling, by avoiding the errors arising from the approximations made in the beam transformation calculations. Also, there is a naturally occurring Fourier plane between the two curved mirrors where beam clean-up is available. For simplicity, small angles of incidence are used at the curved mirrors to avoid significant astigmatism. The mirrors should have appropriate radii of curvature to give just enough room to allow additional plane mirrors to fold the arrangement into the available space. In addition, the transformed transverse beam waist size is controlled by the magnification of the system determined by the ratio of the waveguide height of the amplifier to that of the oscillator.

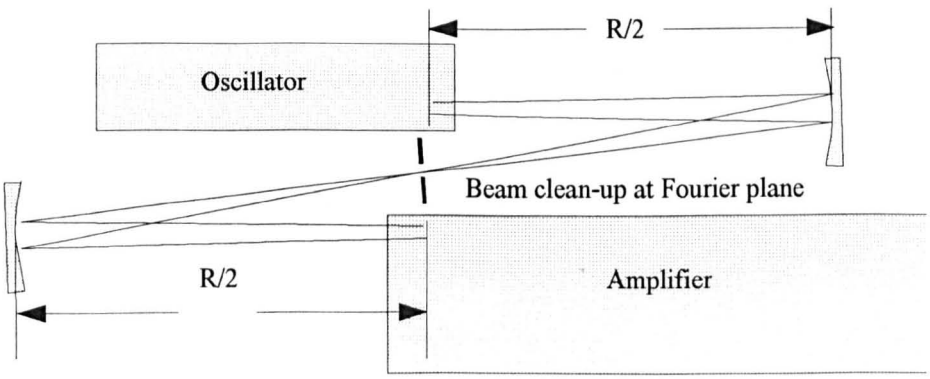

Figure 4.8 Symmetric telecentric relay between oscillator and amplifier

Thus, in the case of different waveguide heights, an asymmetric system is needed. However, in the lateral direction, cylindrical components may be needed to adjust the lateral beam width to some extent as required by the multi-pass folding configuration.

4.5 SUMMARY

In this chapter, Gaussian beam theory, including characterisation, propagation and transformation of the fundamental and higher order Gaussian beam has been summarised. This leads to a brief review of the M^2 theory, which describes the beam quality of any real laser beams using the well known M^2 factor, and in a rather general manner, together with the beam width based on the second moment definition, characterises the propagation of the arbitrary real laser beams through free space and optical systems.

Finally, a discussion of optical systems for real laser beam transformation is presented. One-mirror and two-mirror off-axis transformation optical systems, particularly the telecentric system, are described as examples of beam coupling optics required between the planar waveguide master oscillator and the planar waveguide power amplifier.

REFERENCES

4.1. Q. Cao, H. J. Baker, D. R. Hall, "*Transverse mode propagation and gain coefficients in RF-excited planar waveguide CO_2 laser amplifiers*," to be published

4.2. G. D. Boyd and J. P. Gordon, "*Confocal multimode resonator for millimeter through wavelength masers*," *Bell Sys. Tech. J.*, **40**, pp.489-508, March 1961

4.3. G. D. Boyd and H. Kogelnik, "*Generalised confocal resonator theory*," *Bell Sys. Tech. J.*, **41**, pp.1347-1369, July 1962

4.4. J. R. Pierce, "*Modes in sequences of lenses*," *Proc. Nat'l Acad. Sci.*, **47**, pp.1808-1813, November 1961

4.5. G. Goubau and F. Schwering, "*On the guided propagation of electromagnetic wave beams*," *IRE Tran. on Antennas and Propagation*," **AP-9**, pp. 248-256, May 1961

4.6. A. L. Schawlow and C. H. Townes, "*Infrared and optical masers*," *Phys.Rev.*, **29**, pp.1940-1949, December 1958

4.7. A. G. Fox and T. Li, "*Resonant modes in an optical maser*," *Proc. IRE (correspondence)*, **48**, pp. 1904-1905, November 1960

4.8. H. Kogelnik, "*On the propagation of Gaussian beams of light through lenslike media including those with a loss or gain variation*," *Appl. Opt.*, **4**, pp.1562-1569, December 1965

4.9. H. Kogelnik and T. Li, "*Laser beams and Resonators*," *Appl. Opt.*, **5**, No. 10, pp.1550-1567, October 1966

4.10. "*The Physics and Technology of Laser Resonators*," Edited by D. R. Hall and P. E. Jackson, published by IOP Publishing Ltd, 1989

4.11. A. E. Siegman, "*Lasers*," University Science Books, 20 Edgehill Road, Mill Valley, California 94941, Chapter 20

4.12. J. T. Verdeyen, "*Laser Electronics*," Prentice Hall (Third edition, 1995)

4.13. A. E. Siegman, "*New developments in laser resonators*," *SPIE* **1224** Optical Resonators (1990)

4.14. A. E. Siegman, M. W. Sasnett, and T. F. Johnston, Jr., "*Defining and measuring laser beam quality: the M^2 factor*," *IEEE J. Quantum Electron.*, **27**, April 1991, p1098

4.15. M. W. Sasnett, T. F. Johnston, Jr., "*Beam characterization and measurement of propagation attributes*," *SPIE* **1414** Laser Beam Diagnostics (1991) pp.21-32

4.16. D. Wright, P. Greve, J. Fleischer, L. Austin, "*Laser beam width, divergence and beam propagation factor - an international standardization approach*", *Opt. and Quant. Electronics*, **24** (1992) pp.s993-s1000

4.17. D. Wright, "*Beam width of a diffracted laser using four proposed methods*," *Opt. and Quant. Electronics*, **24** (1992) pp.s1129-s1135

4.18. ISO TC 172 SC 9 WG 1: "*Standard for the Measurement of Beam Width, Beam Divergence, and Beam Propagation Factor*"

4.19. A. E. Siegman, "*Lasers*," University Science Books, 20 Edgehill Road, Mill Valley, California 94941, Chapter 16

4.20. S. Saghafi and C. J. R. Sheppard, "*Near field and far field of elegant Hermite-Gaussian and Laguerre-Gaussian modes*," *Journal of Modern Optics*, 1998, **45**, No. 10, pp.1999-2009

4.21. H. Kogelnik, "*Imaging of optical mode-Resonators with internal lenses*," *Bell Sys. Tech. J.*, **44**, pp.455-494, March 1965

4.22. L. Marshall, *Laser Focus*, pp.26-28, April 1971

4.23. M. W. Sasnett, "*Propagation of Multimode Laser Beams - The M^2 Factor*," *part one of "The Physics and Technology of Laser Resonators,"* Edited by D. R. Hall and P. E. Jackson, published by IOP Publishing Ltd, 1989

4.24. A. Caprara, G. C. Reali, "*Time varying M^2 in Q-switched lasers*," *Opt. and Quant. Electronics*, **24** (1992) pp.s1001-s1009

4.25. A. E. Siegman, "*Analysis of laser beam quality degradation caused by quartic phase aberrations*," *Appl. Optics*, **32**, 20 October 1993, pp.5893-5901

CHAPTER FIVE

TRANSVERSE MODE MATCHING

5.1 INTRODUCTION

Transverse mode matching plays a key role in determining the performance characteristics of a planar waveguide amplifier, including beam quality preservation, power transmission (and loss) as well as the gain and power amplification properties. It concerns the efficient launching of a laser beam from free space into the waveguide of the amplifier. In the ideal case, the input beam should be matched to the required amplitude and phase profile of the fundamental waveguide mode, with minimum angular and beam offset errors so as to minimise the degree of power coupling to other waveguide modes. Then, if the propagation is in an ideal hollow waveguide, which is perfectly homogeneous and perfectly straight, there will be no mode coupling and the exit beam will closely approximate a fundamental waveguide mode. This mode matching concept also applies to any waveguide laser whose cavity includes external sections where re-coupling of the laser beam into the waveguide is required.

It has long been realised that mode excitation in a waveguide by the beam launched into it depends on variety of factors, such as the machining and assembly of the waveguide, the quality of optical components incorporated both inside and outside the waveguide and the most important of all, the properties and launch conditions of the probe beam. In general, multi-mode excitation may be expected unless some particular conditions are satisfied. Since the early 1970's, a number of theoretical and experimental investigations have been reported for a limited case in which the probe beam was assumed to be a perfect fundamental Gaussian beam. It was proposed that, to couple optimally a Gaussian beam into a hollow dielectric waveguide, the beam waist w_0 should be equal to 0.64 of the bore radius for a cylindrical guide [5.1-5.2], or 0.345 [5.3-5.4] of the gap of the square bore for a square guide, with input beam waist located at the waveguide entrances. In both cases, 98% of the incident power is allowed to be coupled into the fundamental mode.

This is a consequence of the near-perfect mapping of the TEM_{00} mode beam and the fundamental EH_{11} waveguide mode.

However, when applying these criteria to cases where the beams to be coupled are not perfectly Gaussian, the previous analysis seems to be incomplete, and to some extent inappropriate. As is well-known (see Chapter 4), an arbitrary real laser beam, if based on second-moment beam width definition, needs three parameters to be fully characterised [5.5]. These are the beam waist w_0, beam waist location z_0 and the propagation factor or beam quality, M^2. In the past, for simplicity it was assumed for most cases that a non-Gaussian beam could be approximated as a Gaussian. This approximation does give reasonably good results [5.6] when the beam quality of the input beam is very good, however, few modally resolved results have been reported.

In addition to searching for the optimum mode matching condition, investigations were also conducted on the behaviour of multimode propagation along hollow waveguides, although to our knowledge not many results have been published. Roullard et al [5.7] suggested that for a hollow circular waveguide, when only the two lowest-order modes EH_{11} and EH_{12} were excited with a TEM_{00} input field, periodic regeneration of the input field should occur along the guide axis where the modes have the same relative phase relationship as at the guide entrance. Jenkins et al [5.8] further revealed a strong periodic component in addition to the anticipated exponential decay of the guide-length-dependent attenuation characteristics through measurements with a 1.0mm-bore hollow silica waveguide.

However, one question that remains unanswered relates to the propagation characteristics of multimode radiation in a hollow waveguide laser amplifier, i.e. a waveguide with gain excited by a gas discharge. For this case, it is relevant to ask what effects would be expected in modifying the transverse modes generated by the input beam, due to discharge associated factors such as spatial variations in refractive index and gain induced mode coupling and modal phase shift.

In this chapter, results for transverse mode matching and mode coupling in planar waveguide amplifiers are presented for both passive and active waveguides. Firstly, a brief review of the

characteristics of planar waveguide modes is given. Following this is a discussion of the waveguide mode diagnostic technique that has been developed in order to quantify the mode coupling effects. This technique uses computer simulation to synthesise the far-field beam profile of a waveguide mode mixture which matches most closely that observed experimentally, with details on relative mode intensity variation, phase shift and individual mode gain characteristics in the active gain medium. Experiments that were undertaken to quantify the transverse mode content of the light launched into the planar waveguide amplifier and to observe the discharge-induced perturbations in the planar waveguide gain medium are then presented.

5.2 REVIEW OF THE TRANSVERSE MODES IN PLANAR WAVEGUIDES

5.2.1 Field Expressions of Planar Waveguide Modes

A waveguide mode is a field distribution that propagates unchanged along the waveguide. Physically it is a solution $E(r, \phi, z)$ or $E(x, y, z)$ of Maxwell's equations, which satisfies the appropriate boundary conditions at the guide walls and has a z (waveguide axis) dependent phase factor $exp(i\kappa z)$, where $\kappa = \beta + i\alpha$ is the mode dependent propagation constant, that has a phase part β and an attenuation part α. A waveguide supports a number of modes, depending on its transverse dimensions with respect to the radiation wavelength. Typically hollow laser waveguides have dimensions larger than 100λ and support a few tens of modes.

Planar waveguides are rectangular guides [5.9-5.10] with one of the transverse dimensions much larger than the other. Their field expressions can be derived from those of the rectangular waveguides. Fig. 5.1(a) shows a typical rectangular waveguide with width $2b$ and height $2a$, which is composed of two dielectric materials with different complex relative dielectric constants:

$$\varepsilon_a = (n_a - i\kappa_a)^2 \qquad \varepsilon_b = (n_b - i\kappa_b)^2$$

where n_a and n_b are the refractive indices, and κ_a and κ_b are the extinction coefficients. They are all positive real numbers. Practically, some waveguides may use only a single material, but many others are hybrid, using one or two metal walls, which may be used as electrodes for transverse

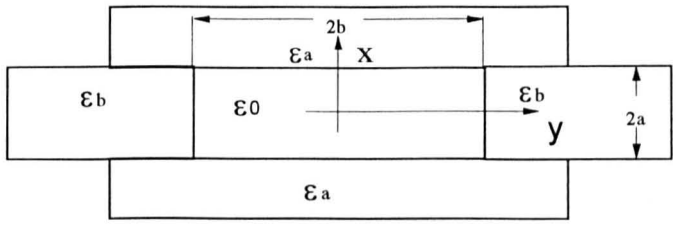

(a) A typical hollow dielectric rectangular waveguide

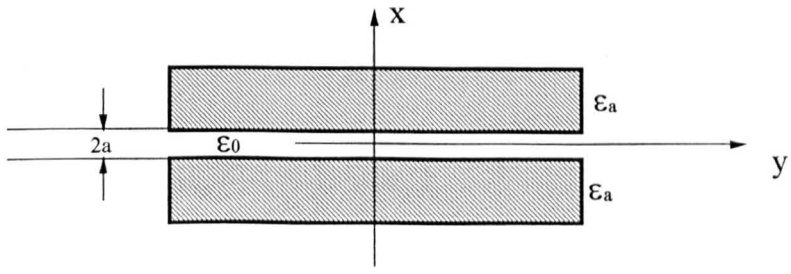

(b) A typical hollow dielectric planar waveguide

Figure 5.1 Geometry of typical hollow dielectric waveguides

RF excitation. The permittivity within the guide is supposed to be ε_0, the free space value. The permeability of all media is assumed to be μ, the same as that of the free space.

Because of the difficulties in matching boundary conditions, it is practically impossible to have an exact analytical solution for the hollow rectangular waveguide. However Laakmann and Steier [5.3] obtained an approximate solution that offers good insight to the modes and gives sufficiently accurate mode parameters. All the modes are hybrid modes, with all three components of the electric and magnetic field present. If we ignore all terms that vary as $(\lambda/a)^{n'}$ *where* $n' > 1$ and λ is the free space wavelength, it is clear that the rectangular hollow dielectric waveguide supports two sets of linearly polarised EH_{mn} hybrid modes, that is, the horizontally polarised EH^y_{mn} modes and vertically polarised EH^x_{mn} modes, where m and n are integers, and all transverse fields approximately vanish at the boundaries. If all terms in the expression for the field components of first order or greater in (λ/a) are ignored, both the external fields and the longitudinal internal fields vanish everywhere, and the internal transverse fields vanish at the boundaries. Now we obtain the simplified transverse field expressions for vertically polarised EH^x_{mn} modes (Eq. (5.1)) and for horizontally polarised EH^y_{mn} modes (Eq. (5.2)):

$$(E_x)^i = \left(\frac{\mu}{\varepsilon_0}\right)^{1/2} \times (H_y)^i \tag{5.1}$$

$$(E_y)^i = \left(\frac{\mu}{\varepsilon_0}\right)^{1/2} \times (H_x)^i \tag{5.2}$$

The simplified forms of the transverse fields for both vertically and horizontally polarised modes EH_{mn}, can be mathematically expressed as:

$$E(x,y) = (\frac{\mu}{\varepsilon_0})^{1/2} \cos(\frac{m\pi x}{2a})\cos(\frac{n\pi y}{2a})e^{i(\kappa_{mn}z-\omega t)} \qquad (m, n \text{ are odd}) \tag{5.3a}$$

$$E(x,y) = (\frac{\mu}{\varepsilon_0})^{1/2} \sin(\frac{m\pi x}{2a})\sin(\frac{n\pi y}{2a})e^{i(\kappa_{mn}z-\omega t)} \qquad (m, n \text{ are even}) \tag{5.3b}$$

Here κ_{mn} are the propagation constants for the modes EH_{mn} and are expressed as:

$$\kappa_{mn} = \beta_{mn} + i\alpha_{mn} \tag{5.4}$$

For x polarised modes,

$$\alpha_{mn} = \frac{1}{a}\left(\frac{m\lambda}{4a}\right)^2 \mathrm{Re}\left[\frac{\varepsilon_a}{\varepsilon_0}\left(\frac{\varepsilon_a}{\varepsilon_0}-1\right)^{-1/2}\right] + \frac{1}{b}\left(\frac{n\lambda}{4b}\right)^2 \mathrm{Re}\left[\left(\frac{\varepsilon_b}{\varepsilon_0}-1\right)^{-1/2}\right] \tag{5.5}$$

$$\beta_{mn} = \frac{2\pi}{\lambda}\left[1 - \frac{1}{2}\left(\frac{m\lambda}{4a}\right)^2 - \frac{1}{2}\left(\frac{n\lambda}{4b}\right)^2\right] \tag{5.6}$$

For y polarised modes,

$$\alpha_{mn} = \frac{1}{a}\left(\frac{m\lambda}{4a}\right)^2 \mathrm{Re}\left[\left(\frac{\varepsilon_a}{\varepsilon_0}-1\right)^{-1/2}\right] + \frac{1}{b}\left(\frac{n\lambda}{4b}\right)^2 \mathrm{Re}\left[\frac{\varepsilon_b}{\varepsilon_0}\left(\frac{\varepsilon_b}{\varepsilon_0}-1\right)^{-1/2}\right] \tag{5.7}$$

$$\beta_{mn} = \frac{2\pi}{\lambda}\left[1 - \frac{1}{2}\left(\frac{m\lambda}{4a}\right)^2 - \frac{1}{2}\left(\frac{n\lambda}{4b}\right)^2\right] \tag{5.8}$$

We now have the field expressions and propagation constants for hybrid modes that exist in rectangular hollow waveguides and this allows us to derive those of the planar waveguides (as in Fig. 5.1(b)). The mathematical process appears to be rather straight forward, that is, to let one of the transverse dimensions approach infinity in Eqs. (5.3-5.8). Let us suppose that b is infinite, and only consider horizontally polarised modes. The reason is as noted previously [5.10] that in ceramic-metal hybrid waveguides, the horizontally polarised modes are usually favoured over the vertically polarised modes, mainly due to the loss factors related to the metal. Eq. (5.3) now evolves to the expression of the transverse electric modes TE_m (m = *1, 2, 3...*) for planar waveguides:

$$E(x)_m = \left(\frac{\mu}{\varepsilon_0}\right)^{1/2} \cos\left(\frac{m\pi x}{2a}\right) e^{i(\kappa_m z - \omega t)} \qquad (m = 1, 3, 5\ldots) \tag{5.9a}$$

$$E(x)_m = \left(\frac{\mu}{\varepsilon_0}\right)^{1/2} \sin\left(\frac{m\pi x}{2a}\right) e^{i(\kappa_m z - \omega t)} \qquad (m = 2, 4, 6\ldots) \tag{5.9b}$$

with the attenuation and phase part of the propagation constants κ_{mn} as:

$$\alpha_m = \frac{1}{a}\left(\frac{m\lambda}{4a}\right)^2 \mathrm{Re}\left[\left(\frac{\varepsilon_a}{\varepsilon_0} - 1\right)^{-1/2}\right] \tag{5.10}$$

$$\beta_m = \frac{2\pi}{\lambda}\left[1 - \frac{1}{2}\left(\frac{m\lambda}{4a}\right)^2\right] \tag{5.11}$$

With Eqs. (5.9-5.11), we are now ready to examine the features of planar waveguide modes. Here we only discuss those that are relevant for the subsequent work.

5.2.2 Mode Dependent Phase Shift and Waveguiding Loss

The mode propagation constants κ_m consist of two parts, the real part or phase constants β_m and the imaginary part or attenuation constants α_m, as expressed respectively by Eqs. (5.10) and (5.11). The phase constants β_m indicate that the waveguide modes travel along within the waveguide with different phase velocities. This mode dependency leads to length-periodic effects which are reportedly observable in passive waveguides, amplifiers and lasers [5.7-5.8, 5.11-5.12]. Also, as we will see later in this chapter, different combinations of mode phase can produce rather different transverse beam profiles for laser beams even with the same mode mixture. The attenuation constants, α_m characterise waveguiding losses which the waveguide modes incur when travelling within the waveguide. Apart from the strong association with the dielectric material that forms the waveguide, the waveguiding losses are mode dependent, and increase with the square of the order number of the mode. This mode dependency of the waveguiding loss provides a useful mechanism for mode discrimination in waveguide lasers, so that in principle it is possible for the single fundamental mode to operate at the lowest loss.

5.2.3 In-waveguide Mode Intensity Distribution

From Eq. (5.9), we can see that any mode when travelling within the waveguide will keep the same transverse field distribution with its phase varying periodically along the longitudinal direction. The transverse intensity patterns of the modes inside the planar waveguide can be plotted with a computer using appropriate software. For reference, the in-waveguide intensity

patterns of the four lowest order modes TE_1, TE_2, TE_3 and TE_4 are illustrated in Fig. 5.2, calculated using Mathcad Plus 5.0, for a planar waveguide with electrode spacing of 1.75mm. We can see that each mode has a number of peaks equal to its mode order, with the fundamental mode having a single peak. It is also noted that higher order modes spread closer to the walls of the waveguide. This may imply that high order modes can develop themselves by using the inverted population located away from the centre of the waveguide, in spite of the prevailing spatial competition from the fundamental mode that dominates the centre of the waveguide.

5.3 WAVEGUIDE MODE DIAGNOSTIC TECHNIQUE

The diffraction of any of the waveguide modes from the exit aperture follows the Kirchhoff-Huygens diffraction integral and Fourier transformation. Thus the transverse amplitude profile of the *m*th mode emitted from a planar waveguide at a distance z' away from the output aperture can be expressed as [5.13]:

$$\psi(x',z')_m = A_m \frac{z'}{\sqrt{z'(x'^2+z'^2)}} \int_{-a}^{a} \psi(x)_m \exp\left[-i\kappa_0\left(\frac{x'^2}{2z'} - \frac{x'x}{z'} + \frac{x^2}{2z'}\right)\right]dx \qquad (5.12)$$

where

$$\kappa_0 = \frac{2\pi}{\lambda} \qquad (5.13)$$

$$\psi(x)_m = \begin{cases} \cos\left(\frac{m\pi x}{2a}\right) & m = 1,3,5... \\ \sin\left(\frac{m\pi x}{2a}\right) & m = 2,4,6... \end{cases} \qquad (5.14)$$

Here the planar waveguide is assumed to have an electrode separation of *2a*. By making use of Eqs. (5.12) and (5.14), the transverse pattern of any mode at any position z', either in the near field or in the far field, can be plotted out. A few examples are shown in Fig. 5.3. It can be seen that the higher the order of the mode, the faster it diverges. In addition, the transverse appearance of the modes gives a good reason for preferring the fundamental mode in laser applications, because it has only one dominant lobe and its spread is far less significant.

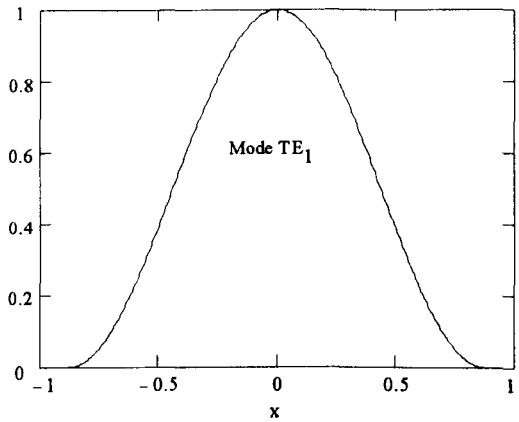

(a) Mode TE_1 (The fundamental mode)

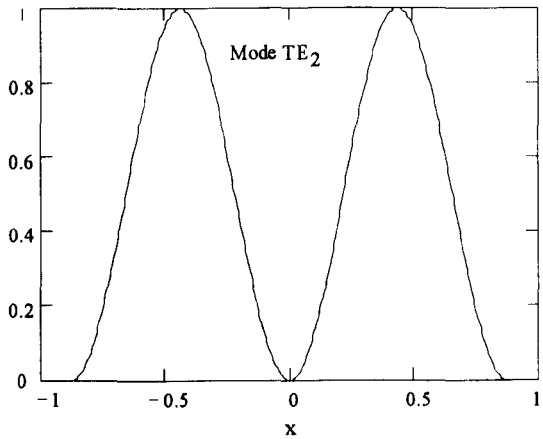

(b) Mode TE_2

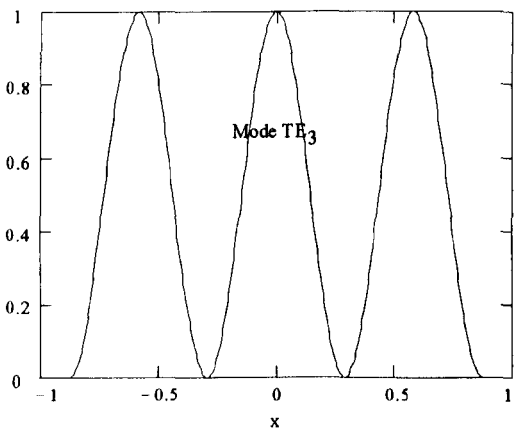

(c) Mode TE_3

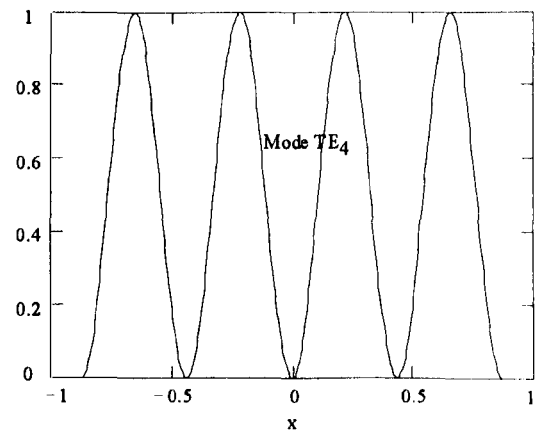

(d) Mode TE_4

Figure 5.2 In-waveguide intensity patterns of the four lowest order planar waveguide modes

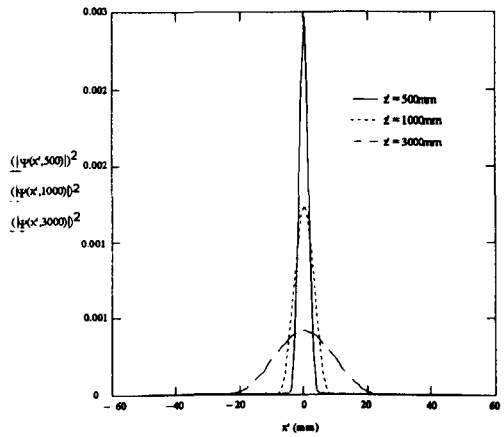

(a) Mode TE_1

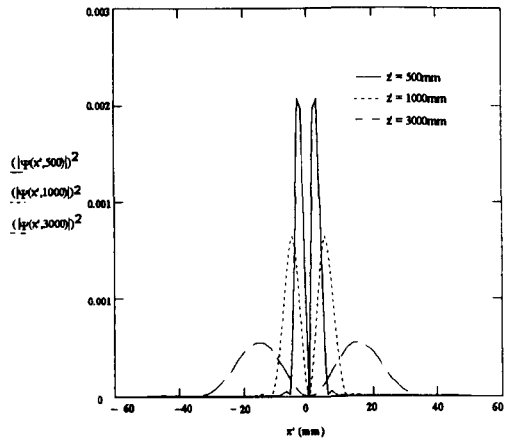

(b) Mode TE_2

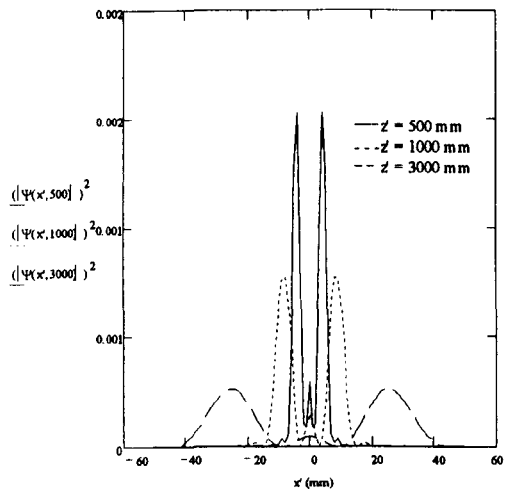

(a) Mode TE_3

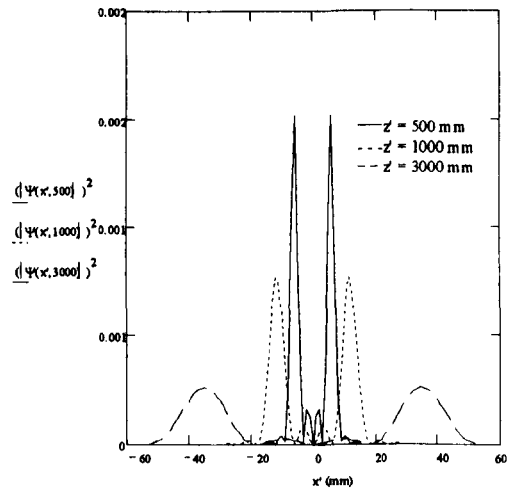

(b) Mode TE_4

Figure 5.3 Field patterns of the four lowest planar waveguide modes at different distance z' from the waveguide for an electrode separation of 1.75mm.

However, in mode analysis, it is convenient to use far field patterns rather than those in the near field, for the absence of the parameter z', the distance from the waveguide output aperture, provides great flexibility in experimental set-up and data processing. If we let z' go to infinity, Eq. (5.12) is simplified to:

$$\psi(\theta)_m = A_m \int_{-a}^{a} \psi(x)_m \exp\left(-i\frac{2\pi}{\lambda}\theta x\right)dx \tag{5.15}$$

where the angular coordinate θ is the far-field divergent angle.

The output beam can be considered as a coherent superposition of a set of excited waveguide modes diffracting from the waveguide aperture, with a differing phase for each mode caused for example by the effect of Eq. (5.11) in a passive waveguide. Then, in the far-field, the beam can be represented in angular co-ordinate θ by its Fourier transform, but with an additional phase factor φ_m for each mode related to the source:

$$A(\theta) = \int_{-a}^{a}\left[\sum_{m=1}^{j} A_m \psi(x)_m \exp(i\phi_m)\right]\exp\left(-i\frac{2\pi\theta}{\lambda}x\right)dx \tag{5.16}$$

The intensity profile of this superposition of far-field mode patterns can be calculated using proper software, here Mathcad Plus 5.0. It is then possible to adjust manually the relative phase ϕ_m and amplitude A_m of modes in a mixture and compare the calculated intensity profile with that measured in the experiment. Practically, this turns out to be easy to do when a limited set of modes is sufficient, say j up to 4, and where the experimental profile has characteristic features such as side lobes, asymmetry, or a shape which appears wider than the expected fundamental mode. The result is an experimental picture of both the relative intensity of multiple waveguide modes and their relative phases.

The measurement of the far-field transverse pattern of the beam emitted from a planar waveguide can be obtained with a set-up as illustrated in Fig. 4.2. According to beam propagation theory (see section 4.2.4), when a Gaussian beam is transformed by a thin lens or a mirror, its beam size at the focal plane in the image side is equal to the far-field divergence of the source beam multiplied by the focal length of the lens or the mirror (see Eq. (4.22b)). It is not difficult to prove that this

also applies to non-Gaussian beams when characterised by the second moment definition. Thus the far-field profile of the source beam, Gaussian or non-Gaussian, expressed in angular co-ordinate θ, can be represented by the profile of the beam at the focal plane in the image side, but with its transverse dimension divided by the focal length. Also if convenient the lens in the set-up can be replaced by a spherical mirror.

This diagnostic technique has been applied to studies of mode mixtures in passive guides and also in active guides with some degree of approximation. One example is shown in Fig. 5.4, where the far-field pattern of the master laser oscillator used in the MOPA system is compared with one simulated by a computer. The beam is found to be well matched by intensity fractions of ~ 98.2% TE_1, ~ 1.8% TE_3 and ~ 0.1% TE_4 modes of the 1.9mm gap waveguide, very consistent with a measured M^2 of 1.18.

5.4 EXPERIMENTAL INVESTIGATION

5.4.1 Experimental Set-up

The experimental set-up is illustrated in Fig. 5.5. It consists of a source laser, a planar waveguide configured as an amplifier and a beam transformation optical system in between. The source laser, to be used as the master oscillator (MO) laser in the power amplification system, was a commercial device and originally designed as the source laser for a high speed matrix marking system. This laser is a RF discharge excited planar waveguide device, with a negative branch confocal unstable resonator, producing a beam with differing parameters (beam size, beam waist and location, divergence, and beam quality M^2) in the lateral and transverse directions. Its transverse beam quality is measured to be 1.18 ± 0.05 and the transverse beam waist is 0.65mm. With optimised clean-up of the lateral side lobes, its lateral beam quality is measured to be 1.2 with a beam waist of 1.65mm. In addition, it operates in a pulsed-discharge mode, with a maximum pulse repetition rate of 10kHz and maximum duty cycle of 50% producing ~ 100 W average output power.

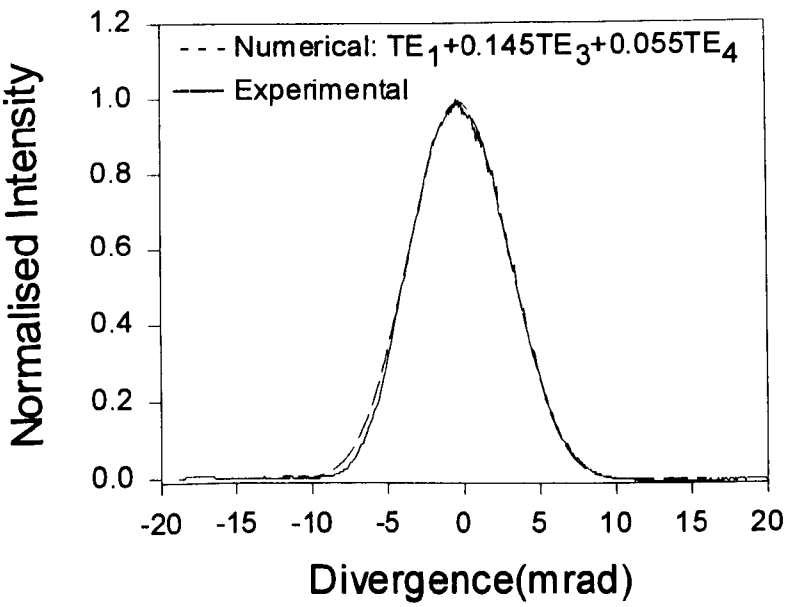

Figure 5.4 Transverse far-field pattern of the source beam produced by the slab waveguide laser oscillator.

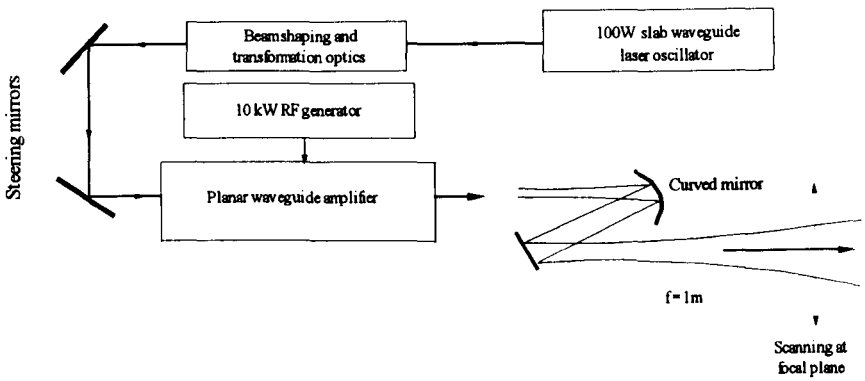

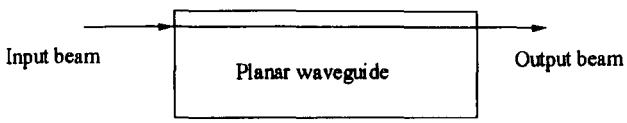

(a) Single pass configuration

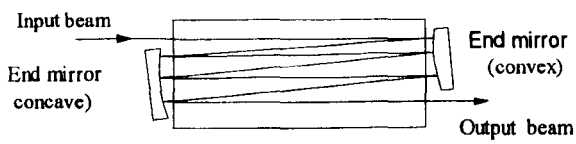

(b) Multipass configuration

Figure 5.5 Experimental set-up for mode matching investigation

The planar waveguide passive/active amplifier module includes two aluminium alloy electrodes, separated by 1.75mm and with drilled internal water cooling channels, giving an active area of $95 \times 770mm^2$. It can be configured as either a single pass or a multi-fold amplifier. In the latter configuration, the folding system is based on a positive branch confocal unstable resonator design with a geometric magnification of 1.34, consisting of two gold coated copper mirrors of radii 6.535m concave and 4.893m convex respectively. The two mirrors are separated by 0.82m, with the output coupling mirror laterally displaced by an amount which depends on the required number of passes, to provide the coupling port. The electrodes are mounted within a rectangular aluminium vacuum vessel that contains a 40mm diameter invar rod, to which the folding mirrors are mounted independently of the main discharge structure. AR coated zinc selenide windows are mounted in flanges at each end of the amplifier, to permit entry of the probe beam and for the exit of the amplified beam.

The whole laser amplifier vessel may be back-filled to the desired gas pressure, with a standard 3:1:1 mixture of helium, nitrogen and CO_2, plus an additional 5% xenon for the data presented in this chapter. This planar waveguide is driven by a RF generator which is connected to the laser head by a single 50ohm coaxial cable, via a reactive impedance matching network at the centre of the electrodes. The beam transformation optics can be either a single spherical mirror system or one with two spherical mirrors, as discussed in Chapter 4, to provide both vertical and lateral modification of the source beam to satisfy the requirements for both transverse mode matching and lateral beam folding. A beam splitter can be inserted into the beam path to reduce the laser power to be coupled into the waveguide amplifier for operations at low power levels.

An arrangement based on the principle described in sections 4.2.4 and 5.3 (also see Fig. 4.2) is included in the set-up to facilitate the measurement of the far-field profile of the exit beam of the amplifier, which may be expressed in angular co-ordinate θ. In the arrangement, a 2m radius spherical mirror, placed 1 ~ 1.5m in front of the exit, is used instead of a lens, and the measurement is assisted with a rotating mirror scanner as mentioned in Chapter 4. The measured beam profiles are monitored and recorded by a digital oscilloscope which can then transfer the

data to a computer via a computer network. In addition, two flat steering mirrors are placed after the transformation optics to facilitate the launching of the beam into the waveguide. These serve the twin purposes of providing vertical and horizontal adjustment, and also to allow one to vary the beam waist location with respect to the entrance of the waveguide.

5.4.2 Multimode Excitation and Propagation in Planar Waveguide Amplifiers

At the output of an amplifier, the beam characteristics are determined by two factors: which modes are excited at the input and how these modes are affected by their propagation within the 'active' waveguide. In this section, multimode excitation conditions are deliberately created by launching an undersized beam into the planar waveguide; significant discharge effects are observed as the multimode beam propagates through the amplifier.

a) Beam launching into waveguides

It is obvious that, for a perfect waveguide, the mode excitation depends on the properties of the input beam and its alignment to the waveguide axis. The output beam is very sensitive to tilt and displacement, leading to high order modes being generated. This is confirmed by computer simulation. Assuming a Gaussian beam input and using Mathcad, one can include one or more of the following: the curvature of wavefront, angular tilt and decentering, then the amplitude ratio of any high order mode to the fundamental mode can be calculated for a given beam size. The calculation shows that the high order mode excitation induced by the tilt and decentering is significant compared with that produced by the curvature of wavefront which is negligible within $\pm$ 2 dioptres.

In the first experiment the amplifier is configured to have a single pass with no involvement of the folding mirrors. The beam from the source laser is transformed by a single curved mirror transformation system, producing a transverse waist of 0.49mm which is positioned close to the entrance of the waveguide. The corresponding beam quality M^2, however, is degraded to be 1.36, due to aberrations resulted from the large incident angle of the beam to the transformation optics. Its transverse far-field pattern is illustrated in Fig. 5.6, which is well matched by a mixture of

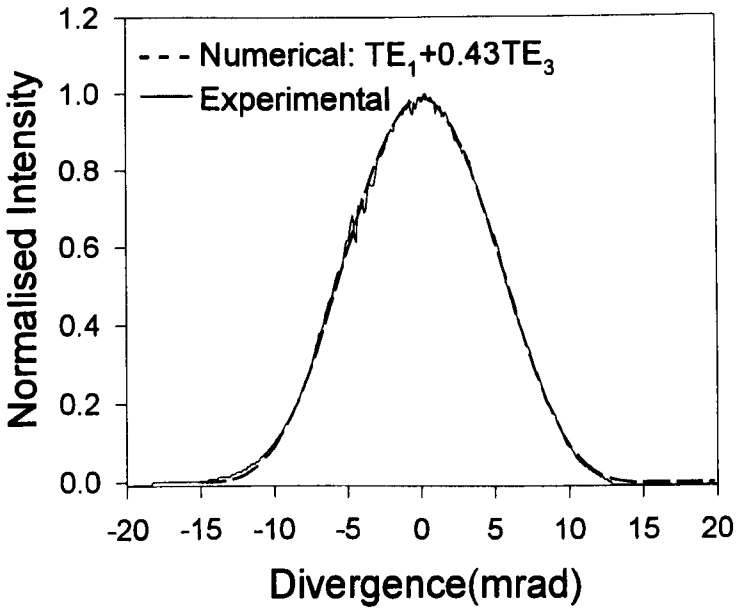

Figure 5.6 The far-field pattern of the probe beam after transformation (ready for launching into the waveguide of the amplifier).

~ 88% TE_1 and ~ 12% TE_3 modes of the 1.75mm gap amplifier waveguide. The laser power carried by the beam is 20 watts or so. This beam is obviously undersized for the 1.75mm waveguide. Thus significant high order mode excitation may be expected.

Although in practice the alignment adjustment at the input is very difficult to achieve, the optimum alignment can be found by observing the far-field nature of the output beam after a single pass through the amplifier. In Fig. 5.7(a) and (b), two examples of the output for a mis-aligned input beam are compared with the well-aligned case (*c*), all in cases with and without the RF discharge. In addition to clear evidence of amplification, this sequence shows some interesting effects in which the relative phase of modes are affected by the presence of the discharge. In Fig. 5.7(*a*), the beam is mis-aligned with an angle of about 1.1mrad in the transverse plane, which creates a single peaked and nearly symmetric far-field profile. In addition to its "good" appearance, it corresponds to the maximum power transmission, probably due to the presence of a significant fraction of the TE_2 mode (~ 2%) which has an attenuation constant much smaller than that of the mode TE_3, thus it may easily be mistaken as being well aligned. However, when the amplifier is turned on, the profile is distorted and a clear interference fringe moves into the beam due to additional phase shifts between modes induced by the discharge. The opposite effects can be observed as in Fig. 5.7(b), where a different input alignment produces a symmetric, well-shaped profile when the discharge is on but a rather different one when the discharge is turned off.

A well aligned input produces an almost symmetric pattern as in Fig. 5.7(c) with highest amplitude and smallest beam width using the second moment definition, consisting of a mixture of TE_1 and TE_3 modes, predominantly determined by the input mode content as in Fig. 5.6. The pattern is transformed to one with side lobes by the differential phase shift introduced by the mode dependent phase delays given by Eq. (5.11). A small fraction of the mode TE_2 (~ 0.8%) results in more or less asymmetry of the profile. In this case analysis shows that small changes in both relative phase and relative mode amplitude are produced by the presence of the discharge. Overall, the shape of the far-field profile does not change significantly. In other words, when the beam is well aligned to the waveguide axis, the profile of the output beam is almost unchanged before and after the discharge is turned on.

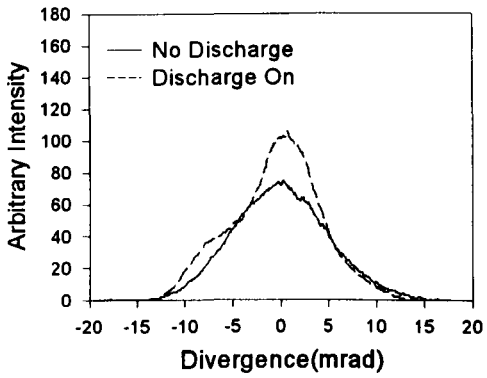

(a) Misaligned but having a profile with a single peak in the far-field when discharge off. The profile changes when the discharge is turned on

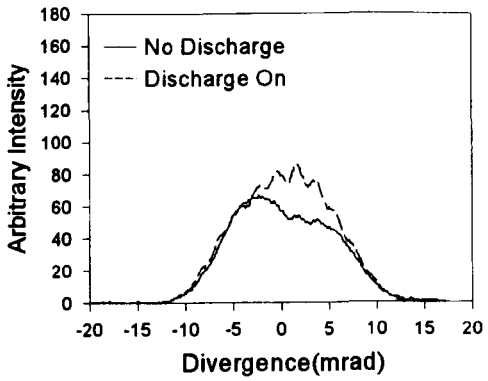

(b) Mis-aligned but having a profile with a single peak in the far-field when the discharge is turned on.

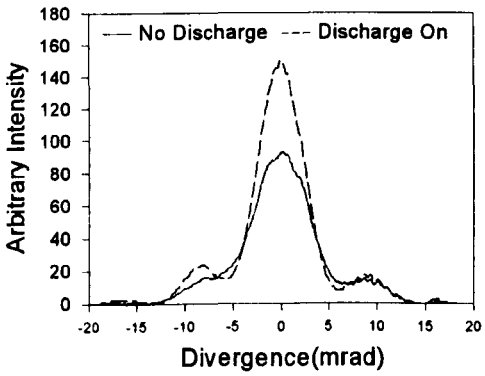

(c) Well-aligned with a nearly symmetric far-field profile. The change of the profile is not significant when the discharge is turned on.

Figure 5.7 Alignment effects in beam launching on exit beam profiles observed in the far-field with discharge on and off.

Variation of the far-field beam profiles at the output are observed when moving the input beam a few centimetres towards or away from the waveguide. Analysing the experimental data using the mode diagnostic technique shows that, at best alignments, while the beam profiles are varying, the mode mixture stays almost the same and such variation is caused by the relative phase shift among modes. This occurs because, in the under-filled waveguide, the beam hits different positions of the waveguide wall and thus travels different distances through the waveguide when its beam waist moves with respect to the waveguide. This also indicates that in the under-filled case, the effect of the curvature of the wavefront is negligible. However, this effect may be significant for large beam waist size. Therefore, it is preferred for the beam waist to be positioned at the entrance of the waveguide.

b) RF discharge effects on multimode propagation in the amplifier

The data presented above show that the active medium significantly modifies the propagation of higher order transverse modes relative to the fundamental, under conditions of small signal, single-pass amplification. If multiple modes are present in the amplifier, this will result in exit beam quality variation with amplifier conditions. Consequently, a more detailed study has been undertaken under varying conditions of RF power input and fill pressure. Fig. 5.8 shows four examples from the sequence of exit far-field profiles for near-optimum input alignment and operation between 30 and 85torr. A clear progression of changes in both relative phase and amplified mode ratio is seen by analysis of these profiles.

Very little previous work has been reported on waveguide mode behaviour when the waveguide amplifier volume is active. However, a qualitative interpretation of the effects can be based on two known properties of the active waveguide. The first relates to the approximately parabolic gas refractive index caused by discharge heating in the diffusion-cooled laser. This adds a negative lens to the waveguide that modifies the modal propagation constants given in Eq. (5.11):

$$\beta_m = \frac{2\pi}{\lambda}\left(1 - \frac{m^2\lambda^2}{32a^2}\right) + \Delta\beta_m(p,W) \tag{5.17}$$

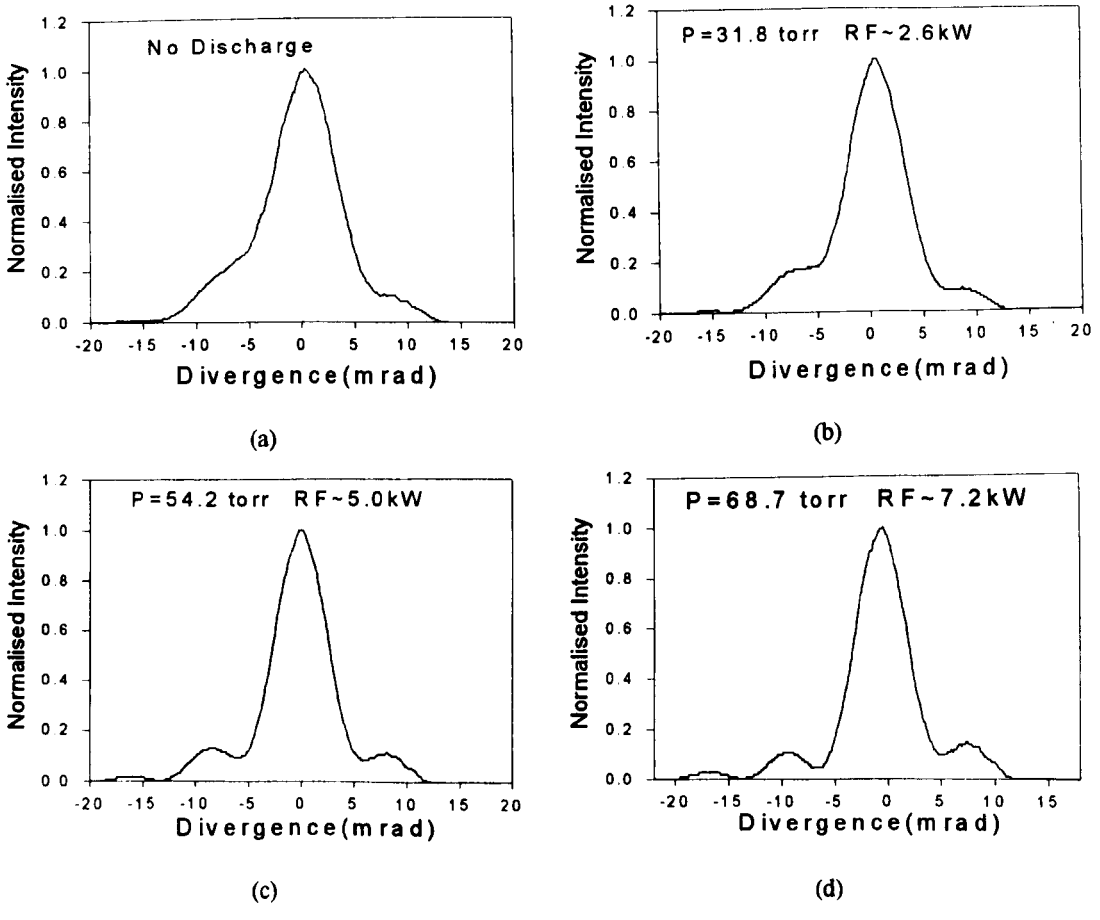

Figure 5.8 Variation of exit beam profiles caused by discharge-induced effects with varying gas pressure and input RF power, observed in the far-field in the single pass configuration. The input beam is slightly mis-aligned and the waist size is ~ 0.49mm.

where $\Delta\beta_m$ is a function of fill pressure p through the gas refractive index, and of the discharge power density W through the change in gas density produced by discharge heating. Using the waveguide mode diagnostic technique described in section 4.3, the phase shift $\Delta\beta_m L$ of the mode TE_2 and TE_3 relative to the fundamental mode TE_1 are obtained as shown in Fig. 5.9 as a function of gas pressure, by analysing a sequence of the far-field profiles of the exit beam (four examples are shown in Fig. 5.8) from the single pass amplification, where the amplified output power is 27-44 watts. It is seen that the refractive index effect is stronger at higher RF power and pressure, in agreement with explanation in terms of the gas thermal lens. Also the refractive index effect has more influence to the lower order mode.

In addition to the phase shift, an analysis of the sequence of the far-field profiles also yields information on the amplitude variation of the individual mode for different operational conditions. This suggests the mode dependence of the gain, which may be expected to vary in detail with RF power, and also pressure and excitation frequency. In theory, by working out the power fraction of each mode before and after the discharge is turned on, it is possible to calculate the relative gain coefficient for each individual mode in any particular case at small signal level as:

$$\gamma_m = \gamma_0 + \frac{1}{L}\ln\left(\frac{Y_m}{y_m}\right) \tag{5.18}$$

where γ_m is the relative small signal gain coefficient of mode TE_m, γ_0 the total small signal gain coefficient and L, the gain length. y_m and Y_m are the power fraction of the mode TE_m before and after discharge on, respectively. However, quantitative conclusions for the individual mode gain coefficient are not available since precise calculations require substantial amount of reliable data. Nevertheless, several qualitative points have been made from the calculation as now described. The initial mode ratios of the beam at the output is $1(TE_1):0.13(TE_2):0.48(TE_3)$. Their in-cavity intensity patterns are shown in Fig. 5.10. When the RF discharge is turned on, this ratio varies progressively with increased pressure and, accordingly, increased RF power deposited in the discharge, indicating different gain characteristics for individual modes at this small signal level. The fundamental mode TE_1 has the highest gain coefficient, even larger than that of the total gain coefficient. This is understandable, for the total gain coefficient is an overall effect concerning all

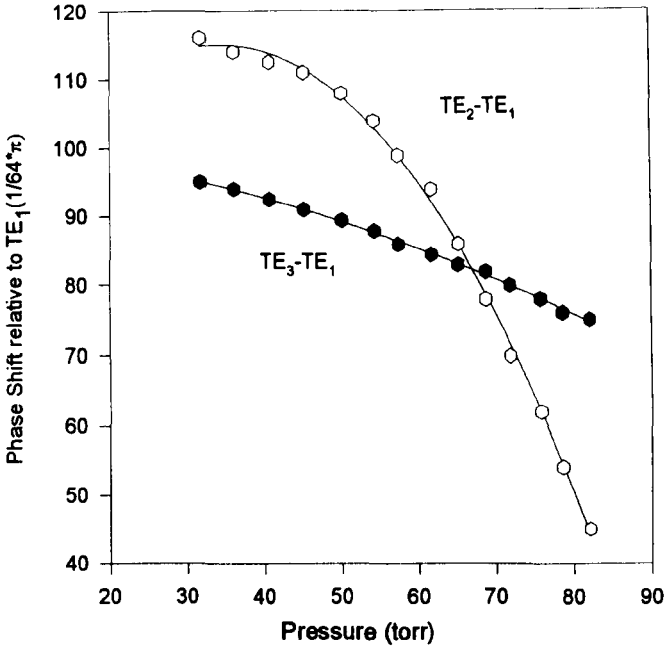

Figure 5.9 Phase shifts of mode TE_2 and TE_3 relative to TE_1 versus gas pressure in an active gain medium. The amplified power output is 25-44 watts.

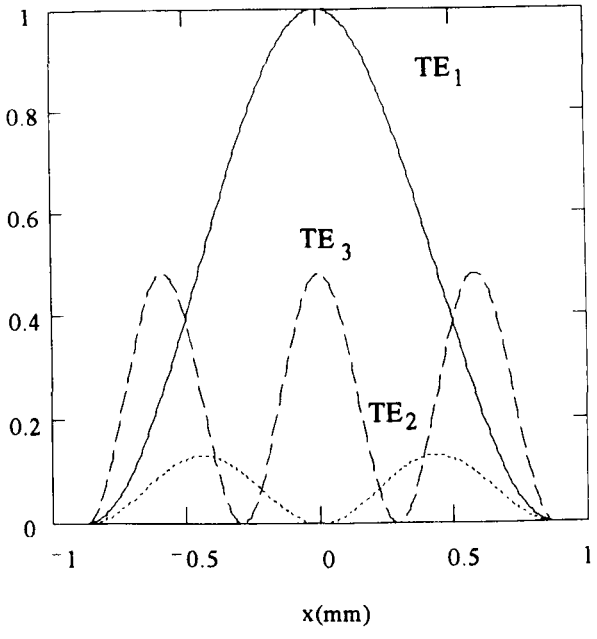

Figure 5.10 In-cavity mode intensity patterns before the discharge is turned on for the beam used for the discharge-induced effects investigation. The mode ratio is $TE_1:TE_2:TE_3 = 1:0.13:0.48$)

modes. In addition, the fundamental mode dominates the laser beam, therefore it prevails over other modes in spatial competition to build up its power. The gain coefficient of the mode TE_3 is significant and larger than that of mode TE_2. Because mode TE_3 has two wings spreading out of the dominant TE_1, it is possible for it to build up power by using the inversion population located away from the centre where the fundamental mode TE_1 dominates. The power of the mode TE_2 hardly grows, since it is so weak and so close to the centre as to be entirely overlapped by the fundamental mode; therefore in some cases its gain coefficient appears to be negative. It is also found that the optimum operational pressure differs from mode to mode, with the peak of the relative gain coefficient of individual mode tending to move towards higher pressure with increased mode order.

The above discussion of modal gain variations applies to small signal gain, where the effect is caused by the small signal gain profile. Much stronger effects on mode ratios are expected when saturation of the gain is achieved, and this will require further work to quantify. This discharge effect in multimode propagation has negative consequences for the performance of the amplifier, such as degradation and variation of the transverse beam quality, uncertainty of the gain characteristics and so on. Thus, multimode operation of the amplifier should be avoided.

5.4.3 Single Mode Excitation and Propagation in Planar Waveguide Amplifiers

a) Optimum mode matching

We have seen the role that the alignment (or beam launching) plays in mode excitation, and we have also seen how to find the optimum alignment. The remaining key question is how the input beam can be mode-matched to the fundamental mode of the waveguide.

It has been noted that for perfect alignment, the output beam has a mode mixture determined predominantly by the input mode content. This suggests that if the input has only one mode component, i.e. the fundamental mode, it would match that of the waveguide. To prove this, the same beam (W_0 = 0.49mm, M^2 = 1.36), as used in beam launching experiments, was re-launched into a spare waveguide with an electrode separation of 1.0mm. This was chosen because its

fundamental mode has a theoretical far-field profile nearly identical to that of the input beam. As seen in Fig. 5.11, the far-field transverse profiles of the output beam, the input beam and the theoretical TE_1 mode are nearly identical. The M^2 of the output beam is measured to be ~ 1.14, which, considering that the calculated M^2 of the theoretical TE_1 mode is 1.13, indicates that the input beam is well matched to the fundamental mode, with no obvious signs of higher order modes produced. However, for comparison, if this beam was approximated as Gaussian, it would be well matched to a waveguide with a gap of 1.4mm. This has been experimentally proven to be not true; with the gap of the spare waveguide increased to 1.4mm, a far-field profile with significant shoulder-like side lobes is produced, far different from that of the fundamental mode.

This mode matching experiment is repeated by launching a beam of parameters W_0 = 0.65mm, M^2 ~ 1.1 into waveguides with different electrode separations. As shown in Fig. 5.12, when the beam is launched into a 1.75mm waveguide, an exit beam is produced with a far-field profile very similar to that of the fundamental mode, and the two small ripples on both sides were visible. The corresponding power loss is less than 2%, a combination of the truncation loss at the input and the waveguiding loss when propagating within the waveguide. When the electrode separation of the waveguide is increased to 1.90mm, slight but noticeable changes occur in the profile of the output beam, and the power loss reduces to ~ 1.7%, probably due to lower truncation loss.

It is now evident that good mode matching can be achieved as long as the symmetric, undistorted and bell shaped beam has a far-field profile the same as that of the fundamental mode of the waveguide into which the beam is to be launched. This beam does not necessarily have to be Gaussian and there is no obvious limitation on the beam quality. However, for a certain far-field divergence, a higher M^2 value means larger beam waist size ($\theta_{far} = M^2\lambda/\pi W_0$) which, in turn, implies increased truncation loss occurring at the waveguide entrance. In this sense, therefore, high quality probe beams are to be preferred.

Since the optimum mode matching condition [5.3-5.4] to a rectangular waveguide with a Gaussian beam input can be expressed as $W_0 = 0.69a$, where a is the half electrode separation of the waveguide, the corresponding condition for an arbitrary input beam may be expressed as:

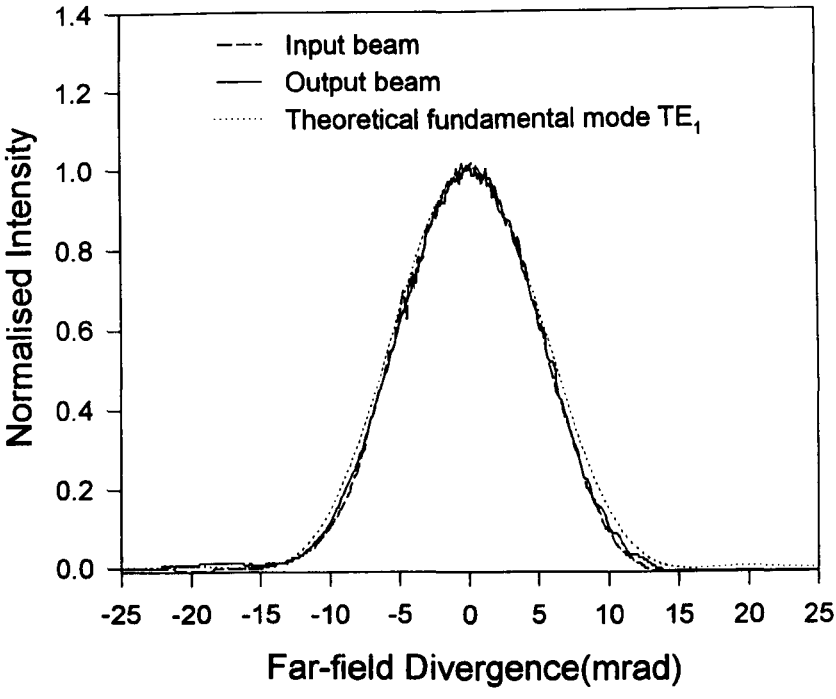

Figure 5.11 Far-field patterns of the input beam, the output beam and the theoretical fundamental mode TE_1, where the beam is ideally matched to the fundamental mode of the waveguide ($2a$ = 1.0mm). Input beam parameters: W_0 = 0.49mm, M^2 = 1.36.

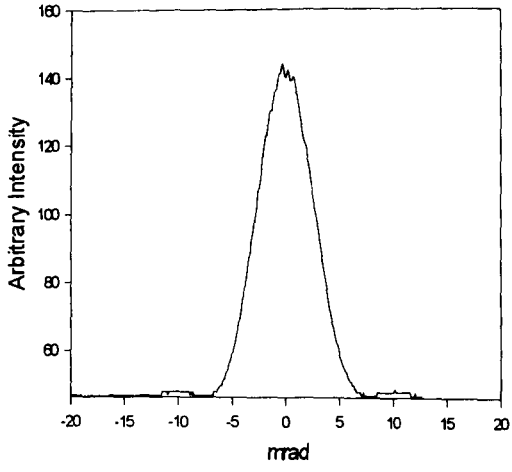

(a) Measured far-field beam profile for the 1.75mm waveguide

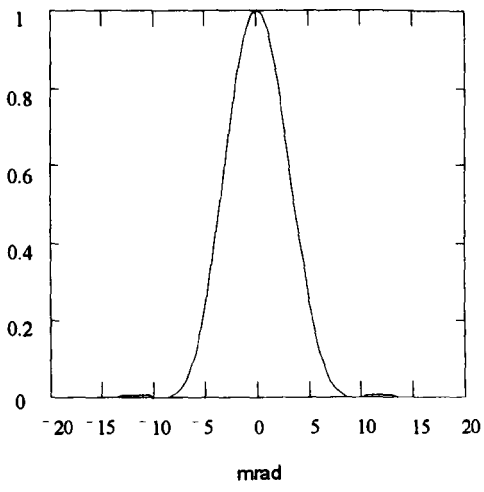

(b) Theoretical far-field beam profile of the fundamental mode for the 1.75mm waveguide

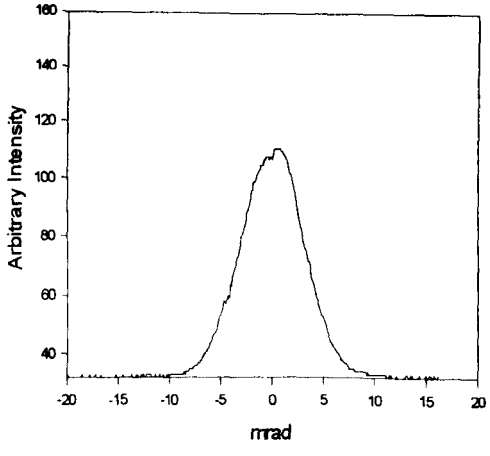

(c) Measured far-field beam profile for the 1.90mm waveguide

Figure 5.12 Far-field transverse beam profile at optimum mode matching (*a*), compared with that of the theoretical fundamental mode (*b*) and that of the near optimum mode matching (*c*). The input beam parameters are: W_0 = 0.65mm, M^2 ~1.1, with the beam waist located at the waveguide entrance.

$$W_0 = 0.69af(M^2) \quad (5.19)$$

where $f(M^2)$ *is a function of the beam quality* M^2. The case where $f(M^2) = 1$ for $M^2 = 1$ corresponds to a fundamental Gaussian beam input. However, the derivation of $f(M^2)$ theoretically requires a precise mathematical expression that universally characterises arbitrary real laser beams.

b) Single mode propagation in planar waveguide amplifier

It has been illustrated that multimode propagation in an active gain medium suffers significant discharge effects. This section presents an investigation of single mode propagation in both one pass and multipass active medium (amplifier) configurations.

A suitable high quality beam may be launched into the waveguide with very efficient coupling to the fundamental TE_1 mode. Fig. 5.13 shows the passive and active far-field beam profiles for this set-up after a single pass. The exit profile had slightly enlarged wings relative to the ideal TE_1, consistent with the presence of only a few percent TE_3. Since the input power is now concentrated in TE_1 there is little effect from the presence of the discharge on the exit beam quality in a single pass. The amplifier optical system is then modified to extend the investigation of transverse mode purity to multipass configurations. Because the mirrors are set up to be off-axis, in the 5-pass configuration, the required mirror tilt varies the non-guided spacing between mirror and guide end between ~ 3 and ~ 10mm across the width of the device. These gaps, combined with the non-optimum mirror curvatures, tend to create significant mode dependent coupling loss at each mirror. Both the accumulative mirror coupling loss and the waveguide loss act to remove the TE_3 component in the beam and the measured far-field profile corresponds very closely to the ideal TE_1 mode. Little effect is produced by the RF discharge, as shown in Fig. 5.14(a) and (b). Moreover, it is evident that the gain is higher under good mode matching conditions.

5.5 SUMMARY AND CONCLUSION

In this Chapter, mode matching for beam coupling between the master oscillator and the amplifier in a MOPA planar waveguide laser amplification system is studied, together with investigations

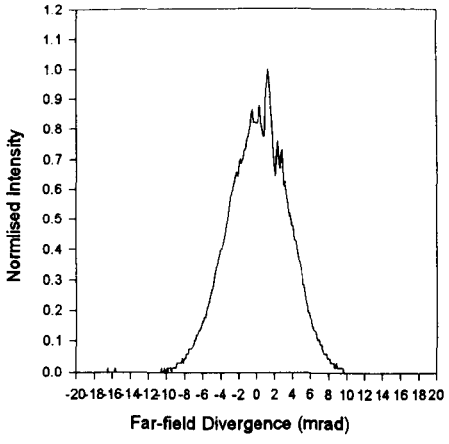

(a) No RF discharge, $\theta = 6.0$mrad

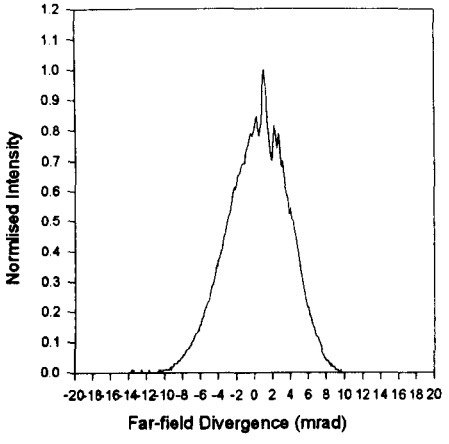

(b) Discharge on, $P = 60$torr, $\theta = 6.1$mrad

Figure 5.13 Transverse beam profiles of the exit beam observed in the far-field with RF on/off for good mode matching after the first pass.

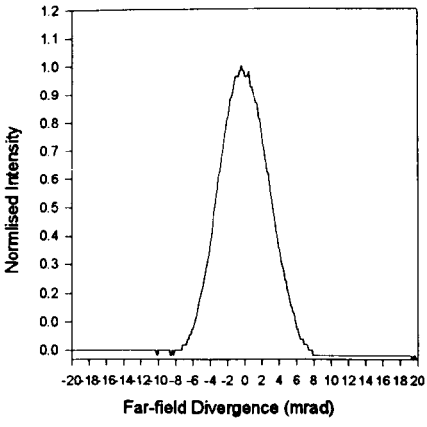

(a) No discharge

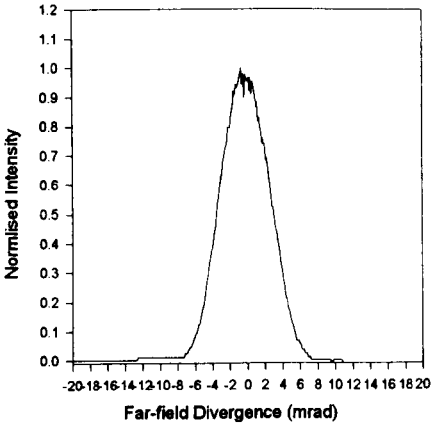

(b) RF discharge is on, $P = 53.1$torr

Figure 5.14 Transverse profiles of the exit beam observed in the far-field in the 5-pass configuration in the case of good mode-matching with RF off/on

on multimode and single mode propagation characteristics in both passive and active planar waveguides.

Compared to a fundamental Gaussian beam input, for an arbitrary real laser beam, it has been shown that the beam waist size $W_0 = 0.69a$ at the waveguide entrance for optimum mode matching has to be modified by a factor $f(M^2) \geq 1$ which is related to the propagation parameter (or beam quality) of the input beam. This indicates increased beam waist size and subsequently higher truncation loss. Optimum mode matching has been achieved with the far-field profile of the input beam being the same as that of the theoretical fundamental mode of the waveguide. Over 97% of the power was coupled into the fundamental mode.

It was found that the power transmitted through the waveguide had an upper limit, in this experiment, of slightly higher than 98%, regardless of the modes excited by the input beam. This is because of a combined effect of the waveguiding loss and the truncation loss. While the truncation loss is low for a small sized input beam, the waveguiding loss is high due to the excitation of high order modes. In contrast, in the case of good mode matching where the power coupled into the fundamental mode is high, implying low waveguiding loss, the truncation is higher due to increased beam size as required by the optimum mode matching condition.

With an undersized beam input, multiple modes were excited in the waveguide. When the waveguide is turned on, significant discharge effects were observed, which caused continuous variation of beam profiles due to mode phase shift and amplitude fluctuation. However, for good mode matching conditions, the discharge effects were negligible.

In conclusion, optimum mode matching between planar waveguides and therefore single fundamental mode operation can be achieved, in spite of the discharge effects observed in multimode propagation. This ensures that under suitable conditions good beam quality may be achieved from planar waveguide amplifiers. Further more, this suggests the preference and possibility of the use of large gap planar waveguides for power amplification at high levels, where

potentially more power may be obtained due to large volume of active gain medium, assuming the same gain saturation level.

REFERENCES

5.1 R. L. Abrams, "*Coupling losses in hollow waveguide laser resonators*," *IEEE J. Quantum Electron.*, **QE-8**, 838(1972)

5.2 D. R. Hall, E. K. Gorton, and R. M. Jenkins, "*10-μm propagation losses in hollow dielectric waveguides*," *Appl. Phy.*, **48**, No. 3, March 1977

5.3 K. D. Laakmann and W. H. Steier, "*Waveguides: characteristic modes of hollow rectangular dielectric waveguides*," *Appl. Opt.* **15**, pp.1334-1340 (1976)

5.4 D. M. Henderson, "*Waveguide lasers with intracavity electrooptic modulators: misalignment loss*," *Appl. Opt.*, **15**, pp.1066-1070(1976)

5.5 A. E. Siegman, "*New developments in laser resonators*," *SPIE* **1224** Optical Resonators (1990)

5.6 S. Somkuarnpanit, D. Su, J. D. C. Jones, H. J. Baker, D. R. Hall, "*Beam launch misalignment effects in hollow infrared waveguides*," to be published

5.7 F. P. Roullard III and M. Bass, "*Transverse mode control in high gain, millimeter bore, waveguide lasers*," *IEEE J. Quantum. Electron.*, **QE-13**, pp.813-818 (1977)

5.8 R. M. Jenkins and R. W. J. Devereux, "*Effect of field regeneration on the TEM_{00} transmission characteristics of a circular-section waveguide*," *Appl. Phys.*, **31**, pp.5086-5091, No. 24, 20 August 1992

5.9 E. A. J. Marcatili, *Bell Syst. Tech. J.*, **48**: 2071(1969)

5.10 C. A. Hill, "*Theory of Waveguide Laser Resonators*", Chapter 3 of "*The physics and technology of laser resonators*," Edited by D.R.Hall and P.E.Jackson, IOP Publishing LTD 1989

5.11 K. D. Laakmann, PhD dissertation, University of Southern California, Oct. 1975.

5.12 R. Gerlach, D. Wei, N. M. Amer, *IEEE J Quantum Electron.*, **QE-20**: 948(1984)

5.13 D. Marcuse, "*Light Transmission Optics*," p.42, Second Edition, Van Nostrand Reinhold Company, 1982

CHAPTER SIX

GAIN CHARACTERISTICS AND POWER AMPLIFICATION WITH CW RF-DISCHARGE

6.1 INTRODUCTION

In the last ten years or so, diffusion-cooled, RF-discharge excited, CO_2 planar waveguide lasers have been well developed and widely used in material processing and related industrial applications, because of their good beam quality, high power extraction and compact, simple structures [6.1-6.3]. Recent interest has been directed towards extending the planar waveguide laser concept further to produce power levels beyond 5kW in both cw and pulsing regime. The basic consideration is, making use of the area scaling nature [6.4], to increase the overall area of the slab-like gain medium, by producing a corresponding increase in the overall electrode area. There are however serious mechanical and electrical difficulties associated with handling very large area planar electrodes which limit power scaling to very high power levels.

There are several approaches other than using one single slab that may be considered to configure laser systems for high power operation with planar waveguide structures. One option can be the use of multiple pairs of parallel electrodes configured in a single plane, thus reducing both the size of the individual electrodes and the RF power distribution problem. This configuration involves intracavity coupling between the series waveguides. However, the whole system is still very large. An alternative can be a combination of multiple slab waveguides in stacked format, in which optically the waveguides can be in series with assistance of coupling optics, or in parallel to form a slab array linked with appropriate phase-locking mechanism. This concept remains unproven.

The Master Oscillator and Power Amplification (MOPA) configuration is a very attractive approach for laser power enhancement, in which, a master oscillator is used, and the power is magnified after one or more stages of power amplification, with the well controlled high beam quality preserved at much higher power levels. With the planar waveguide structure, the sizes of

the electrodes of the amplifier at each stage can be chosen properly so that potential mechanical and RF power distribution difficulties can be handled, and the overall size of the system can be controlled at an appropriate scale. Due to the slab nature of the electrodes, the waveguides at amplification stage can be configured to incorporate multi-folded beam paths, to achieve high filling factors. However, applicable data (e.g. small gain coefficient, saturation intensity etc.) for the design of such a system are not yet available.

In the literature, the gain characteristics of the CO_2 gas medium have been extensively studied analytically and experimentally as a function of gas mixture and pressure in association with the geometry (e.g. bore size) and discharge stability or uniformity (for example, references [6.5-6.8]). For CO_2 lasers/amplifiers with waveguide structures, the gain characteristics have been further found to depend on the transverse modes [6.9] and the transverse position within the waveguide [6.10-6.11]. Generally, the small signal gain in waveguide geometry tends to increase with reduced internal diameter (for circular guides) [6.12] or bore width (rectangular guides) [6.10], due to improved cooling efficiency. Also in association with the cooling efficiency, the gain coefficient in flowing systems is higher than that in sealed-off systems [6.7, 6.13]. However, for the RF-excited slab waveguide lasers, only one published paper [6.14] has been noted which reported an unsaturated gain coefficient of 0.5-0.7%cm^{-1} for cw RF-discharge with a gas mixture of $He:CO_2:N_2:Xe = 6:1:1:0.4$. In parallel to the investigations on the gain characteristics of the CO_2 medium, a number of CO_2 laser oscillator-amplifiers have also been developed [6.10, 6.13, 6.15-6.17] and studied. Most of them were devices with circular cross sections, and utilised multipass configurations to take the advantage of length reduction and improvement of power extraction efficiency.

In this chapter, an investigation is presented of the gain characteristics and power amplification of a *multipass, planar waveguide CO_2 oscillator-amplifier system* in the MOPA format. The laser oscillator incorporated in this system is operated at high pulse repetition rate, producing quasi-cw laser output while the amplifier is driven by cw RF-discharge. This system has been designed and constructed after the investigation on real beam characterisation and transformation described in Chapter 4; and after the understanding of the transverse waveguide mode matching and related

effects on the gain characteristics and power amplification described in Chapter 5, and of the parasitic oscillation to be described in Chapter 8. All data presented in this chapter were obtained by using a gas mixture of 57% He, 19% CO_2, 19% N_2 and 5% Xe.

6.2 OPTIONS OF BEAM FOLDING CONFIGURATIONS

Amplifiers with planar waveguide structures require a folded beam path within the waveguide to give high filling factors and thus high power extraction. There are several approaches for beam folding configuration, each having advantages and disadvantages. Three options are shown in Fig. 6.1 and are described below.

a) Amplifier using zigzag mirrors

Fig. 6.1(a) shows a configuration in which zigzag mirrors are used to fold the beam as parallel passes. This arrangement allows very high fill factor with no beam overlap, and creates no unwanted closed paths, which may support parasitic oscillation. Triangular sections of waveguide may be added to the ends of the discharge electrodes to reduce coupling loss between the waveguide and mirrors. However, this arrangement requires very good match of the beam (beam size and divergence) to the structure of the zigzag mirrors, and the alignment must be very stable.

b) Folding of a diverging beam using wedged plane mirrors

Alternatively, a beam may be folded through a planar waveguide using simple plane mirrors. The folding mirrors must not be in parallel to avoid the occurring of strong parasitic oscillation. Fig. 6.1(b) shows such a configuration where a diverging beam is folded with a pair of plane mirrors with a wedged angle. With this arrangement, an overlapping folded beam path is created with a high fill factor. It is anticipated that amplification in the double passed regions will be saturated more strongly than in the single passed regions. Due to interference of neighbouring beams travelling at opposite direction at an angle, the double pass regions may have lateral fringe structures, and details of spatial hole burning may have to be included in any models of saturation of the amplifier. One disadvantage is that, as the beam of the last pass is not parallel to the input

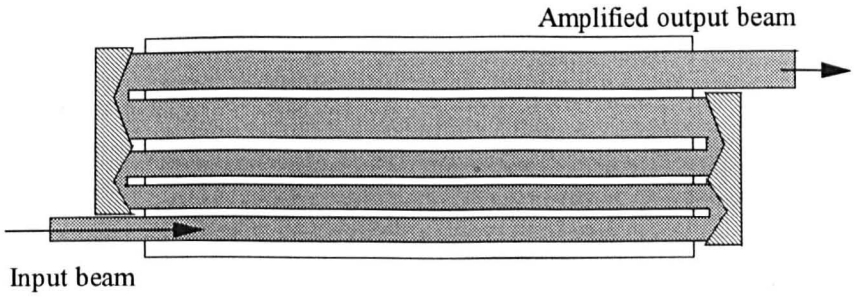

(a) Non-overlapping fold, using zigzag mirrors

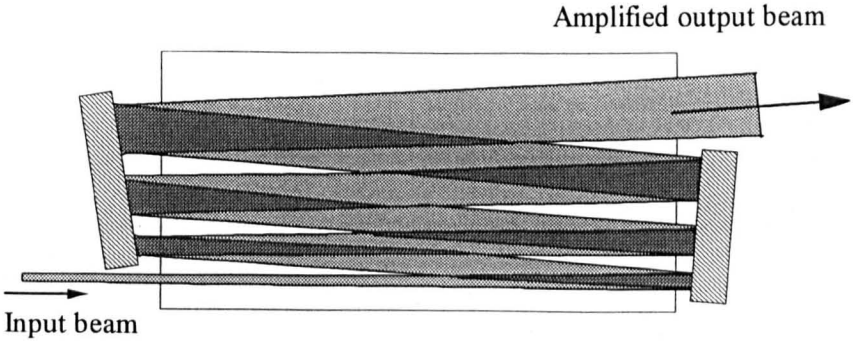

(b) Overlapped fold with a diverging beam using wedged plane mirrors

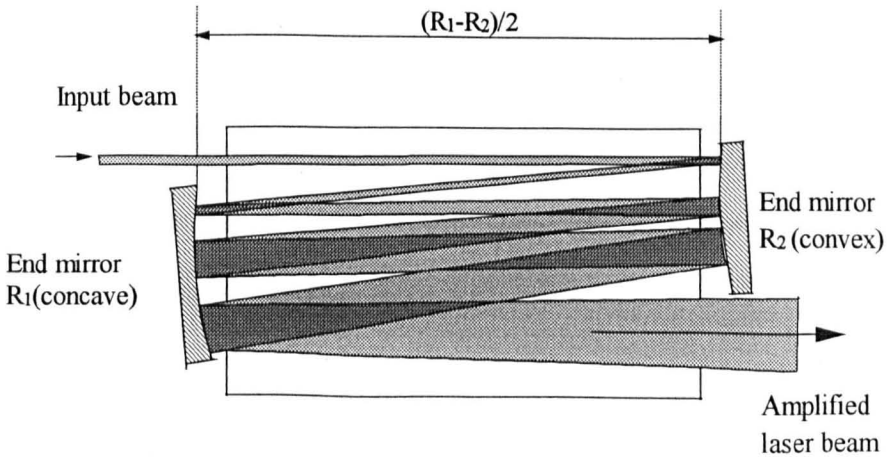

(c) Overlapped fold with an expanding beam using off-axis unstable resonators

Figure 6.1 Options of beam folding configurations for planar waveguide

beam, which propagates along the longitudinal direction of the waveguide, thus requiring additional optical components for the collimation of the output beam.

c) Beam folding using off-axis unstable resonators

In the third option as shown in Fig. 6.1(c) the beam is folded by using a pair of off-axis positioned, positive branch confocal resonator mirrors. Similar to the case used in laser resonators, in this configuration, the separation of the end mirrors should be equal to $(R1\text{-}R2)/2$ to meet the confocal condition, and each round trip gives a fixed beam magnification. This configuration provides the advantage of collimated input and output beams. This approach produces overlap of the folded beams for most of the passes, giving a high fill factor. It also creates an expanding beam to compensate for the growth of the beam intensity, and is thus consistent with the objective of controlling the gain saturation throughout the amplifier. This configuration is incorporated in the amplifier system and will be discussed further in later sections.

6.3 SYSTEM DESIGN AND CONSTRUCTION

Compared to previous work on MOPA systems, the additional feature involved here is the requirement to accommodate the *optical waveguide* nature of the particular power amplifier under investigation, which implies both the need for efficient coupling from free space into the waveguide, and additionally, the avoidance of significant mode coupling, the effect of which would be to compromise the quality of the beam at the output of the power amplifier. This has been discussed in Chapter 5.

Basically, there are three components in this type of system, i.e., the master laser oscillator, the planar waveguide power amplifier and an optical system to transform the probe beam properties to match optimally to the planar waveguide amplifier.

6.3.1 The Master Oscillator

The master oscillator (MO) laser used in the experiments has already been described in Chapter 5. In fact, two such (notionally identical) lasers have been used at different times during the project, due to a failure in the original laser tube. In practice, although there were slight differences in the beam characteristics between the original and the replacement tubes, the net effect is not significant. In the transverse direction, the beam waist is $W_y = \sim 0.65$mm, located near the exit of the waveguide and the beam quality M_y^2 is 1.18 ± 0.05 (the first laser tube) or 1.10 ± 0.02 (the second laser tube). In the lateral direction, side lobes are observed and the beam quality M_x^2 is 3.8 with a beam waist of $W_x = \sim 2$mm located ~ 94mm from outside of the waveguide exit. However, with use of a clean-up aperture at the near field, where diffraction effects may be induced, the beam quality M_x^2 is improved to be ~ 2.5 and the beam waist is equivalent to ~ 2.1mm. With the use of a telecentric optical system and with the beam cleaned-up at the naturally formed Fourier plane between the two curved mirrors, the beam quality M_x^2 is then measured to be ~ 1.2 with the lateral beam waist being equivalent to $W_x = \sim 1.65$mm.

In addition, the oscillator laser has been observed to produce different spectral lines in the $10P16$ to $10P30$ range as the cavity length changes during warm up; such line switching produces a cyclical power variation of ± 10%. Multi-line operation must correspond to operation on different lateral modes of the unstable resonator, and this may be in part responsible for the variations of lateral beam quality.

6.3.2 The Waveguide Amplifier

The planar waveguide amplifier hardware employed in the MOPA system is converted from a previous 1kW laser oscillator device [6.1], and has also been described in Chapter 5. The configuration illustrated in Fig. 6.1(c) is adopted to form a multiple folded beam path within the amplifier waveguide. Two versions (designated A and B) of the planar waveguide power amplifier have been investigated during the course of the project.

Amplifier Configuration A

The general layout of the laser system in configuration A is shown in Fig. 6.2. In this configuration, the electrodes are separated by 1.75mm thick alumina ceramic side walls, which precisely define the waveguide gap, and provide a degree of waveguiding which may affect the characteristics of the unstable resonator optical folding system in the lateral direction. The amplifier is driven by an RF generator, which is capable of a maximum cw power of 10kW at a frequency of 125MHz.

In the earlier work with the amplifier, multiple holes were drilled in the surface of the lower electrode to house fibre optic probes, which were used to monitor the spatial variation of the discharge visible emission. This was used as a sensitive measure of the spatial uniformity of the discharge, and was used to set up the RF power distribution network. Previous use of the fibre optic diagnostic system had shown that uniformly lit RF discharges could be obtained under all required conditions of input power level and gas pressure. In subsequent experiments, a simpler and more easily implemented technique was employed to monitor the longitudinal distribution of the inter-electrode voltage. This involved the use of three voltage probes (Rhode and Schwartz Model URV5-27) positioned near each end and in the centre of the electrode system, and connected to a suitable millivolt-meter.

Amplifier Configuration B

During the course of the experimental programme, it became necessary to investigate the influence of the discharge side walls on the optical propagation characteristics of the beam inside the amplifier, and in particular, the role of the side walls in contributing to the onset of parasitic oscillations. Thus, a new design for electrode mounting was implemented in which the alumina spacers were removed, to produce an arrangement with no side walls. In addition, to meet the requirements from the industrial collaborators, the RF generator frequency is changed from 125MHz to 81MHz. The new configuration permitted either pulsed or cw operation of the amplifier. A schematic diagram of the power amplifier in configuration B, with no ceramic side walls is shown in Fig. 6.3.

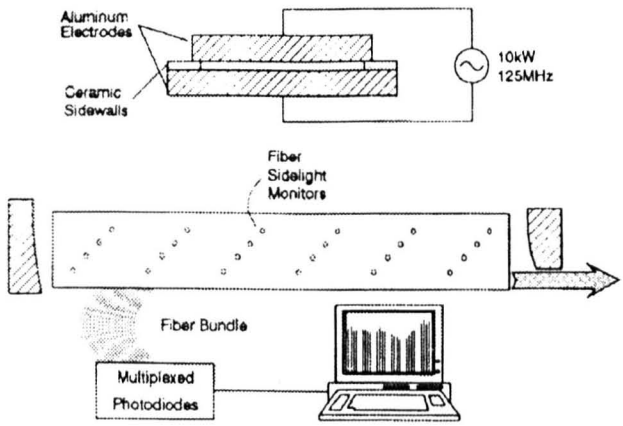

Figure 6.2 Schematic structure of planar waveguide laser amplifier with ceramic side walls (configuration A)

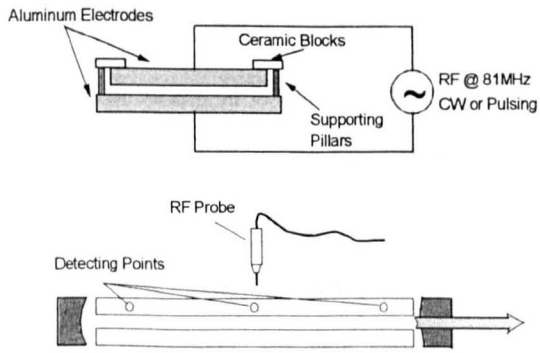

Figure 6.3 Schematic structure of planar waveguide laser amplifier with no ceramic side walls (configuration B)

6.3.3 Beam Transformation and Coupling Optics

The design of the beam transformation optics making use of the second moment-based M^2 concept is made following the general procedure described in Chapter 4. As a matter of fact, during the experimental programme, two different optical arrangements have been used to implement the beam transformation required between the laser oscillator and the waveguide amplifier.

The first arrangement is the so-called one mirror system, which involves the use of a single spherical mirror, as illustrated in Fig. 4.7. The design procedure has been discussed in Chapter 4 and the correct orientation of the fold plane was found to be in the transverse direction for the oscillator as shown later. This system was used in the experiments in combination with the amplifier *configuration A* and this combination will be referred to as ***condition (a)*** in this thesis.

The choice of mirror radius of curvature R has to be aimed at obtaining a system which will fit on a single optical table whilst allowing space for beam diagnostic devices to be used between the oscillator and amplifier. A radius of 1.5m was found to be suitable. Table 6.1 shows part of a listing of results produced by numerically scanning through values of d_1 (oscillator waveguide exit to mirror distance) and searching for a consistent set of mirror angle θ, and mirror to amplifier distances d_2, using the measured beam parameters of $W_x = \sim 2.1$mm, $M_x^2 = 2.5$ as an input. The line in italic-bold was used for as the basis of the practical design. The transverse beam waist of 0.53mm was smaller than $\sim 0.345a = 0.6$mm (a is the waveguide gap), the beam waist of the fundamental transverse waveguide mode [6.18]. This allowed low truncation loss at the entrance of the amplifier waveguide, but with significant multi-mode excitation in the amplifier. However, this facilitated the investigation on multimode effects in active waveguides (see Chapter 5). The beam waist size in the lateral direction was chosen according to calculations of the spot size and beam paths in the confocal unstable amplifier (see section 6.4), which indicated that for $M_x^2 \sim 2.5$ the real beam input spot size must be in the range of 3 to 5mm to obtain the largest number of folds without serious beam overlapping on the mirrors.

d1	*θ*	*W2 (y)*	*W2 (x)*	*d2*
1175.4 mm	48.44°	0.55 mm	4.66 mm	872.8 mm
1183.8 mm	***49.18°***	***0.53 mm***	***4.72 mm***	***847.2 mm***
1193.2 mm	49.91°	0.51 mm	4.78 mm	821.9 mm

Table 6.1 Example of listing from parameter search for a practical coupling set-up using one off-axis curved mirror.

The second arrangement, a symmetric telecentric optical system shown in Fig. 4.8, was introduced into the experiments aimed to improve the transverse mode matching and thus to allow the investigation on single mode propagation and on the beam quality preservation in the amplifier. This system was used in the experiments together with the amplifier *configuration B* and this combination is referred to as ***condition (b)*** in this thesis. Considering that the oscillator is already characterised as regards planar waveguide modes, the correct view should be the imaging of these modes on to the entrance plane of the amplifier. The two-mirror telecentric relay system maps the oscillator beam at its waveguide exit onto the amplifier input plane, conserving both the spatial size and phase front curvature. In addition, there is a naturally occurring Fourier plane between the two curved mirrors where beam clean-up is available with an aperture. The simplicity and the predictability of its behaviour is a great attraction. In practice, small angles of incidence should be used at the curved mirrors to avoid significant astigmatism and additional plane mirrors are required to fold the arrangement into the available table space.

6.3.4 Implementation of the Optical Design in the Amplifier System

The planar waveguide power amplification system was firstly set-up with the one mirror beam transformation optics and with the amplifier configuration A, as illustrated in Fig. 6.4. The laser oscillator was positioned at a higher level than the amplifier, and both devices had their waveguides horizontal. The spherical concave mirror was mounted on a vertical section of breadboard, positioned 1184mm from the exit of the oscillator waveguide, and deflected the beam downward to the level of the amplifier waveguide with an angle of incidence of ~ 49°. The transformed beam was led into the waveguide of the amplifier by three flat mirrors, which were arranged to ensure the beam after flat mirror 1 was horizontally folded, so that no beam rotation would occur. Optical alignment was realised by adjusting flat mirrors 2 and 3 without disturbing the pre-set angle of the transforming mirror. A metal plate was placed near the entrance of the amplifier waveguide to clean the lateral beam profile and to protect the ceramic side wall of the waveguide from being burned by the input laser beam. With the actual radius of curvature of the spherical concave mirror, the beam waists were both found to be smaller ($W_2(y)$ = 0.42mm, $W_2(x)$ = 3.39mm) than the calculated values, and positioned at a nearer point (818mm) to the

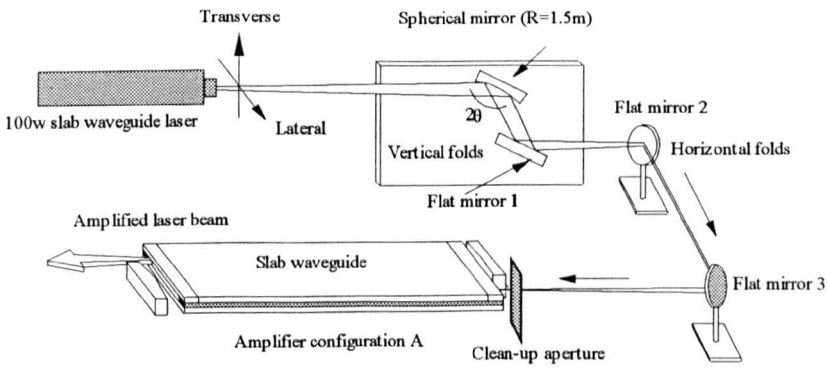

Figure 6.4 System set-up using one mirror beam transformation optics

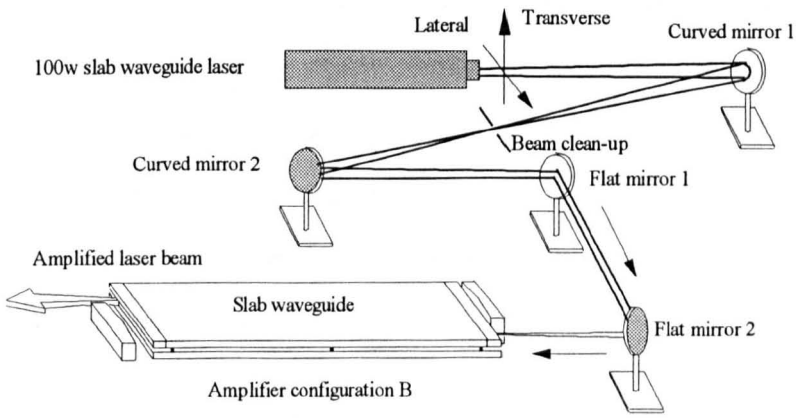

Figure 6.5 System set-up using telecentric beam transformation optics

mirror. This disagreement may result from errors in the measurement of the oscillator beam properties or in the angular positioning of the spherical mirror.

Fig. 6.5 shows schematically the system set-up using a two-mirror symmetric telecentric beam coupling optics. The laser oscillator was now positioned at the same height as the amplifier. The incident angles to the two spherical mirrors were small (< 5°) to avoid significant astigmatism. With both mirrors having same radius of $R = 1.5$m, a 1:1 imaging was given in both beam directions. In practice, the source oscillator had a guide height $a = 1.9$mm, whilst the amplifier gap was 1.75mm, thus the 1:1 imaging slightly overfilled the amplifier waveguide. Nevertheless, this set-up has given very good mode matching at the transverse direction (see Chapter 5). In the lateral direction, the natural beam width after clean-up was ~ 1.65mm. This with 1:1 imaging gave a lateral beam waist of ~ 1.65mm for the amplifier which was later found to be smaller than required by the 7-pass folding system.

6.4 LATERAL BEAM CHARACTERISTICS IN THE AMPLIFIER

6.4.1 Multipass Propagation in Passive Planar Waveguides

The folded beam paths and the beam spot sizes on the resonator mirrors can be obtained by ABCD matrix calculations using appropriate dimensional off-sets of the mirrors, where the beam is characterised by the parameters defined in terms of the second moment to include the effects of the actual (measured) M_x^2 values of the real beam. In the unstable resonator folding system, the mirror radii correspond to a geometrical magnification of 1.3. The calculations suggest that the beam waist should be located near the entrance to the planar waveguide, although there is a tolerance of a few centimetres, giving a degree of flexibility in the system set-up. The input beam is assumed in the lateral direction to have an M_x^2 value of 2.5 and an input spot size of $W = 3.39$mm, as obtained by using a single spherical beam transformation mirror, as shown in Fig. 6.4. In practice, it is comparatively easy to produce a 5-pass fold through the amplifier as shown in Fig. 6.6. However when the folding mirrors are adjusted to create 7 passes within the 95mm width of the amplifier (between side walls in Configuration A), the output beam passes close to the edge of the convex folding mirror, as shown in Fig. 6.7. For this reason, a 9-pass

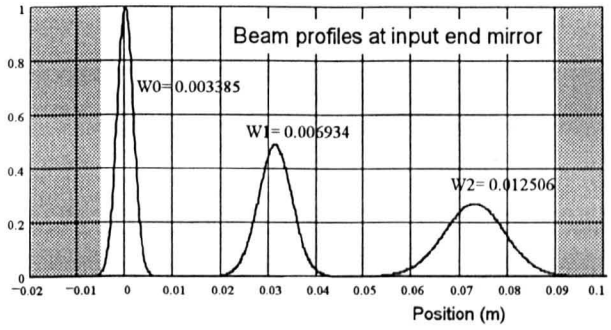

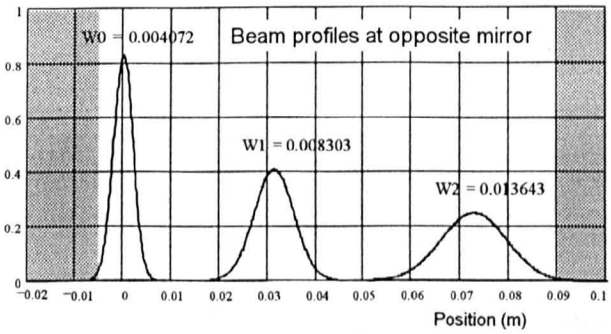

Figure 6.6 Calculated real beam spot sizes on end mirrors in 5 pass confocal unstable amplifier configuration (geometrical magnification of the resonator ~ 1.3, input beam waist W_o ~ 3.39mm, M^2 ~ 2.5, waveguide dimensions ~ 770mm x 95mm x 1.75mm)

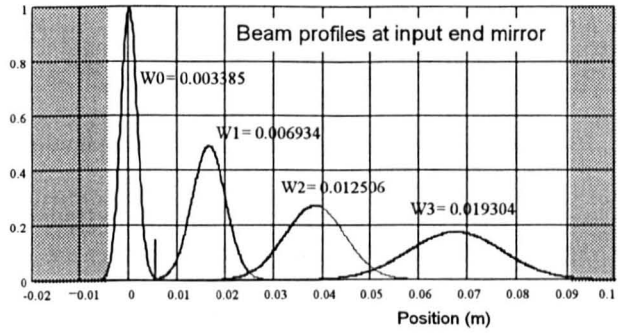

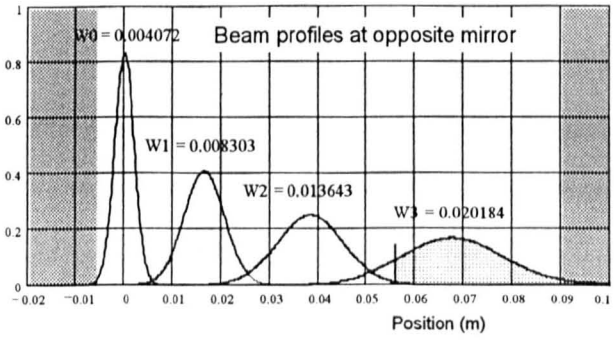

Figure 6.7 Calculated real beam spot sizes on end mirrors in 7 pass confocal unstable amplifier configuration (geometrical magnification of the resonator ~ 1.3, input beam waist W_0 ~ 3.39mm, M^2 ~ 2.5, waveguide dimensions ~ 770mm × 95mm × 1.75mm)

system is not possible, resulting from the magnification factor of $M \sim 1.3$ producing a larger spot size throughout the folded path. However, if the beam quality of the probe beam is enhanced such that M_x^2 falls to a value of 1.2, (as produced by the telecentric transformation optics with optimised beam clean-up), and if, in addition, one sets the lateral input beam spot size to a value of $W \sim 3.0$mm, then further calculations show that for this tighter beam a 7-pass optical folding system is easy to produce without beam overlap, while a 9-pass configuration is possible with a minimal of obscuration by the edge of the folding mirror at the output end.

To aid the preliminary set-up and testing of the folded amplifier, a spare set of electrodes was used as a passive planar waveguide, positioned outside the laser envelope for ease of access and adjustment. In this configuration, the growth in the size of the beam as a function of pass number can be monitored more easily by lateral movement of the mirror at the output end of the amplifier. The passive waveguide was also movable along the direction of the input beam so as to facilitate some variation in the launch condition for the transverse beam.

Fig. 6.8 shows a series of measured beam scans taken at a distance of 450mm beyond the output end of the amplifier, for the cases of 1, 5 and 7 passes through the waveguide. The noise which is evident in these scans is a result of incomplete averaging of the 50% duty pulsing of the oscillator. The beam at the output has a significantly smaller spot size than expected from the above calculations which assumed a value of M_x^2 of 2.5 and $W_x = 3.39$mm as the parameters of the probe beam. It was observed that 7 passes can be obtained without hitting the edge of the mirror with the output beam, but that 9 passes was not possible. This improvement over the calculated values probably reflects an additional positive beam clean-up effect in the lateral direction caused by the aperture at the waveguide entrance. This suggestion is supported by the measured beam sizes, which are consistent with a lateral beam quality of $M_x^2 \sim 1.6$ for the beam propagating within the waveguide.

Power transmission measurements were also made for beams traversing the passive planar waveguide with the specified folding mirrors. For an input power of 22 watts, the transmission

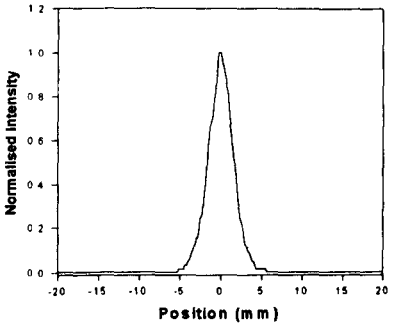

(a) 1 pass (spot size W = 3.61 mm)

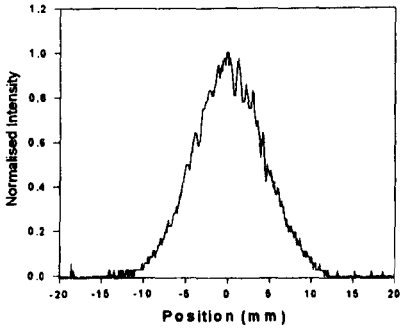

(b) 5 passes (spot size W = 8.21 mm)

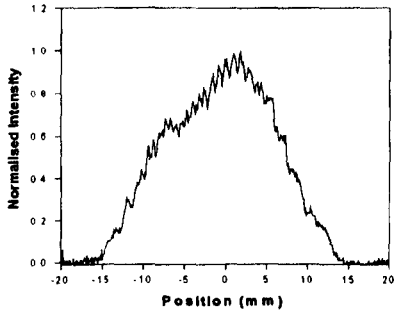

(c) 7 passes (spot size W = 12.3 mm)

Figure 6.8 Beam profiles measured at a distance 450mm from the output aperture of the amplifier (discharge off) using 1, 5 and 7 passes

was measured to be 97.7% for one pass, 77% for 5 passes and 72% for 7 passes. These losses may be understood through a combination of the following effects:

a) Launching loss for the first pass (this is probably low because the input transverse beam size is smaller than that for optimum coupling to the fundamental mode).

b) Waveguiding loss in 0.77m long sections of the waveguide, which depends on the wall material (in this case aluminium alloy) and the quality of the surface finish.

c) Reflection losses of $\geq 1\%$ per bounce from the gold-coated folding mirrors.

d) Repeated coupling losses occurring twice per round trip between the waveguide and the free space sections. These are estimated to be ~ 2% per pass in the present set-up.

Using the present mirrors and a 1.75mm electrode gap, the equivalent distributed loss factor combining waveguide, coupling and reflection loss is of the order of $\sim 0.07 m^{-1}$ from the above data, while the distributed loss factor for the single pass is of the order of $\sim 0.03 m^{-1}$ which combines only the truncation loss at the waveguide entrance and the waveguiding loss along the 0.77m path.

6.4.2 Lateral Beam Characteristics in an Active Waveguide (*Condition a*)

Based on the preliminary trials with a passive waveguide, the folding mirrors were re-installed in the active amplifier casing and positioned with the correct dimensional off-sets. The amplifier has an active length of 0.77m and a fold mirror spacing of 0.82m. Short sections of passive waveguide, constructed from insulating alumina ceramic, were used at each end to allow the mirrors to be placed close to the waveguide ends, thereby reducing coupling losses in the positive branch mirror configuration. With the full power from the master oscillator, the side lobes in the lateral direction may be sufficient to heat and damage the end faces of the ceramic side walls. To prevent this occurring, an additional degree of lateral beam clean-up was introduced near the entrance of the waveguide, where the side lobes were well-separated from the main lobe of the beam. The power output of the source laser was slightly above 100W after the beam transformation and was further reduced by a few percent after this additional clean-up. With the

full oscillator power input, the power transmission through the amplifier, and corresponding beam profiles were similar to those obtained earlier for the passive waveguide, with typical transmitted power levels of 97W for the 1 pass, 79W for 5 passes and 65W for 7 passes.

Examples of lateral beam profiles with amplification are illustrated in Fig. 6.9. Measurements were made both before and after the turn-on of the amplifier discharge. Each set of scans required the movement of the output mirror laterally and the re-alignment of both folding mirrors, so the exact conditions vary for each of the examples. In the 1-pass configuration, the incomplete removal of the side lobes on the MO beam showed up as wings on the otherwise Gaussian shaped beam as in Fig. 6.9(a). In the 5-pass configuration, as shown in Fig. 6.9(b), the shape of the exit beam was found to be very similar, irrespective of whether the discharge was on or off, indicating that the discharge effects on the lateral beam characteristics were not significant, aside from gain saturation effects. It should be noted that lateral misalignment of the folding mirrors might produce imperfect exit beams, and the overlapping of the folded beam may cause interference fringes. In addition, the lateral beam characteristics are associated with the parasitic oscillation, which will be discussed in detail later in Chapter 8.

In the case of deep gain saturation, significant effects may be expected in the amplified profiles, particularly a flattening of the top of the profile, since the centre of the beam will saturate the gain more strongly than the edges due to its higher intensity (see also section 2.2.1). No such saturation effects have been observed, probably because the gain was not saturated enough at currently-available MO power levels. Ideally, further measurements should be carried out with a higher power oscillator laser - probably in the region of 300W average power for this amplifier.

6.5 GAIN MEASUREMENT

6.5.1 Small Signal Gain Coefficient

The small signal gain coefficient is a key parameter in the context of subsequent work on gain saturation, power amplification, scalability and for actual amplifier system design. Experimentally, the small signal gain coefficient may be determined according to Eq. (2.8) from

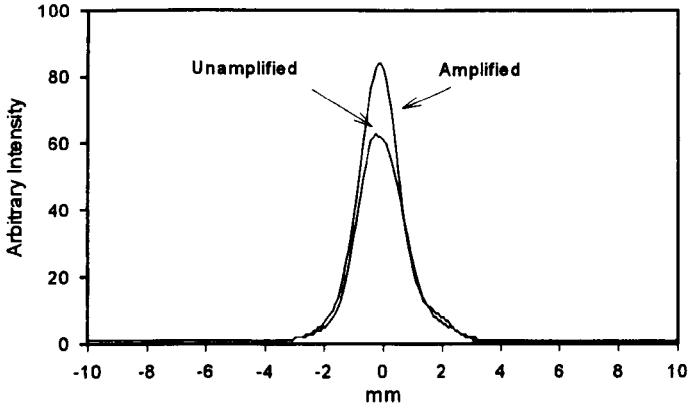

(a) 1 Pass

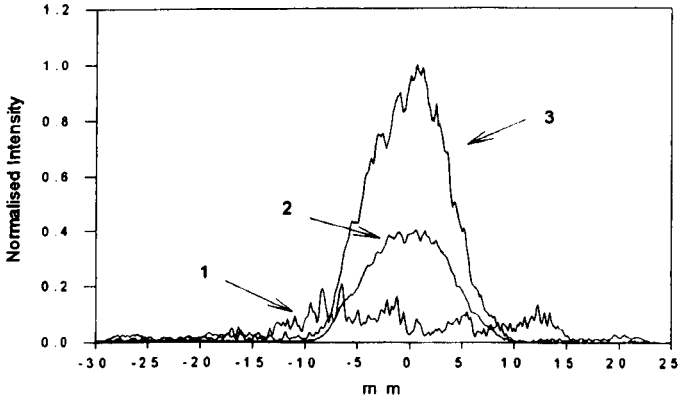

(b) 5Pass: (1) Pure parasitic oscillation: the amplifier is on; the source laser is off

(2) The source laser is on; the amplifier is off

(3) Both the amplifier and the source laser are on

Figure 6.9 Lateral beam profiles measured near the output aperture of the amplifier using 1 and 5 passes with discharge on or off.

measurements of the net gain with a weak optical signal passing through an amplifier where gain saturation is insignificant. However, for a waveguide amplifier, due to existence of losses, such as optical losses occurring at the input and output windows, truncation losses at the entrance of the waveguide etc., accurate measurements of the input and output power, and therefore the loss coefficient α, are difficult. Nevertheless, the small signal gain coefficient can be alternatively determined with the output power at the amplifier on (P_{on}) and off (P_{off}), and is given by

$$\gamma_0 = \frac{1}{L}\ln(\frac{P_{on}}{P_{off}}) \tag{6.1}$$

where L is the active length of the amplifier. This treatment provides an advantage that no exact information on the losses is required. However, low losses are preferred, for high losses may cause inaccuracy due to effects associated with the signal-to-noise ratios in some cases. In the experiments, the small signal gain coefficient was measured in the single pass configuration using much reduced input power to avoid significant gain saturation. The set-up is illustrated in Fig. 6.10. The source laser beam was divided into two beams by placing a plano/plano beam splitter between the source laser and the beam transformation optics. The incident angle to the beam splitter was kept as small as possible so as to minimise the impact on beam alignment and the input beam. The reflected beam was directed to a power meter (PM_1) which was used to monitor the power of the MO source laser. The transmitted beam was then reduced to a low level and acted as the input for the amplifier. The power of the exit beam was measured by the second power meter (PM_2).

If one assumes P_1 as the power measured at PM_1, P_{off} and P_{on} as the power measured at PM_2 when the discharge is off / on, then the small signal gain coefficient is given by Eq. (6.1). The value of P_1 -P_{off} was measured and pre-recorded, as a convenient means of generating a calibration to permit the reading out of P_{off} (by monitoring P_1) when discharge is on, and to avoid the need for repeatedly switching off the discharge. This method permits the determination of the gain coefficient without any need for knowledge of the waveguiding loss, power fluctuation or spectral drift of the source laser. It also avoids the problems associated with frequent switching of the RF discharge on and off.

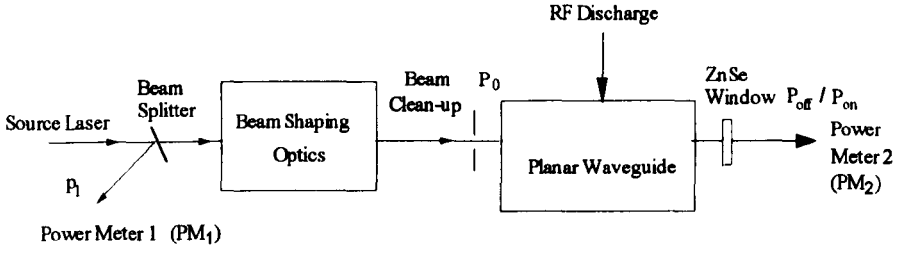

Figure 6.10 Experimental set-up for gain coefficient measurement

In the course of these experiments, it was noticed that the gain coefficient varied with the magnitude of the input laser power, which was observed to be subject to fluctuations of about ± 10% around the average value, a result which was probably caused by line hopping in the source laser. Gain measurement experiments were conducted with input power levels to the amplifier of ~ 10W and ~ 20W respectively, producing very similar values for the gain coefficient in each case, indicating this power range was in the small signal gain regime. Typical results of the experiments are shown in Fig. 6.11, where curve (a) represents the small signal gain coefficient measured under condition (a). It was observed that the highest values appeared in the pressure range of 45-55torr with a maximum value of 0.5%cm^{-1}. This value decreased with increased gas pressure to a value of 0.27% cm^{-1} at 80torr.

However, under condition (b), the small signal gain coefficient, represented by the curve (b) in Fig. 6.11, significantly increased, with maximum observed value of 0.65%cm^{-1}. The enhancement of the small signal gain may be explained mainly as a result of the change of the RF frequency from 125MHz to 81MHz, and partially as the result of the improved transverse mode matching. This former conclusion is derived from the recognition that at 81MHz, operation of the discharge at low RF power levels is possible without causing spatial (area) shrinkage of the discharge. However, at similar values of the RF input power, the small signal gain was similar in each case, with a slight increase for the 81MHz value. The overall variation of the gain coefficient with gas pressure appeared very similar for both frequencies, with the optimum pressure being observed to be within the range 45-55torr.

Further experiments were carried out to investigate the dependency of the gain on other operational conditions. Fig. 6.12 shows the small signal gain coefficient (averaged against the power fluctuation due to the line hopping of the master oscillator) measured under condition (a) as a function of gas pressure and RF power deposition. The dependency on the operational conditions turned to be rather strong, so that for a particular pressure, the input RF power has to be maintained stable in order to avoid significant drop of the gain.

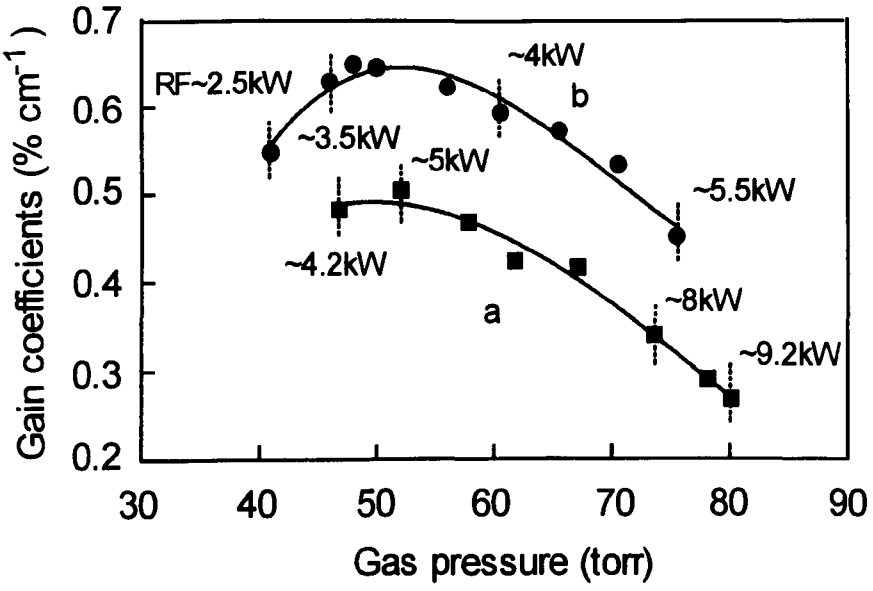

Figure 6.11 Small signal gain coefficient as a function of gas pressure at RF frequency of 125MHz (curve a, input power ~ 20W) and 81MHz (curve b, input power 16 ~ 19W).

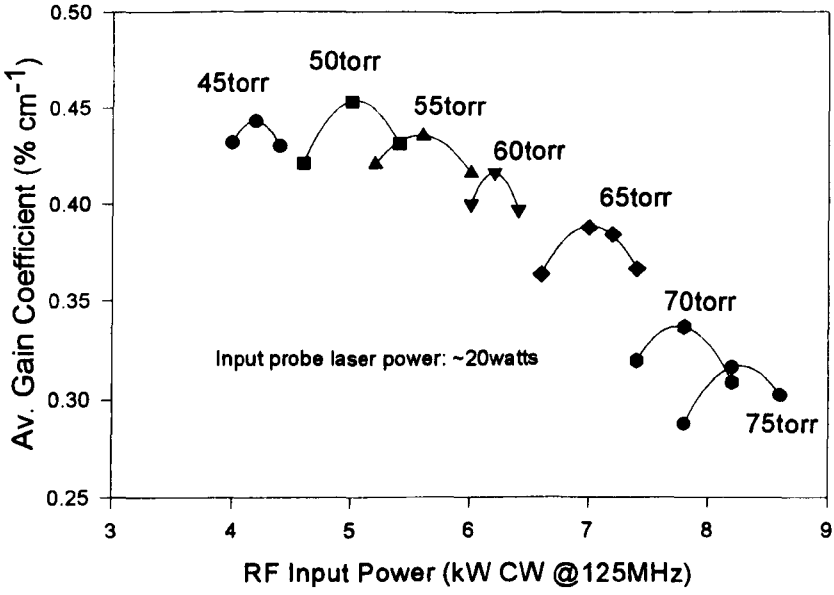

Figure 6.12 Average small signal gain coefficient as a function of RF power deposition for different gas pressures.

6.5.2 Gain Saturation

Gain saturation results from significant reduction of the population inversion between the upper and lower laser levels, due to presence of a strong signal travelling in the gain medium, and is associated with the gain broadening mechanism. It is appropriate to treat the gain saturation characteristics of the CO_2 medium in the waveguide amplifier under investigation as homogeneous, for at pressure of 10torr or above CO_2 medium is dominated by collisional broadening [6.19]. For conditions when the discharge was run between 45-70torr with RF input power varying in the range of 4.5-7.5kW, the power gain was observed to have fallen compared to the low probe power input conditions. In the presence of gain saturation, the gain coefficient was observed to decrease significantly with increased input power in the low pressure region, but only slightly at higher pressures. This is in qualitative agreement with CO_2 laser theory which indicates that the saturation intensity is proportional to the square of gas pressure (see also section 2.2.1).

The saturation intensity (power) may be obtained according to Eqs. (2.20) and (2.21), by making a series of measurements of the output power for a range of input power and plotting P_{out}-P_{in} as a function of $ln(P_{out}/P_{in})$. In the experiments, output power was obtained in the single pass configuration with input power of ~ 20W, ~ 80W and ~ 100W under condition (a). Testing for more input power points was not made due to lack of suitable beam splitters to give continued adjustment for the input power. This hampered the attempt for accurate determination of the P_s (I_s) as a function of gas pressure. However, treatment using the available data has given the order of the saturation power as 165-200W (saturation intensity as 2.5-3.0kW·cm^{-2}) for pressure from 45torr to 55torr, and 230-265W (3.5-4.0kW·cm^{-2}) for pressure from 65torr to 75torr. The average beam size within the waveguide was assumed to be ~ 7.0mm in the lateral direction and 0.6mm in the transverse direction. It has to be pointed out that the distributed loss of ~ 0.03%cm^{-1} has been ignored in the treatment, which is one order smaller than the small signal gain coefficient.

6.6 MULTIPASS POWER AMPLIFICATION

The amplifier has been operated with several different optical folding configurations with different number of folding passes. In the single pass configuration, no fold mirrors were installed inside the amplifier, therefore the laser beam directly exited from the output end through a ZnSe window. Multipass configurations were achieved by adjusting the horizontal tilt of the fold mirrors, with the assistance of a reference He-Ne laser beam, producing multipass paths inside the waveguide with the input-beam and output-beam parallel to each other. The laser beam intensity profile was monitored using a beam scanner, which can be oriented in either a vertical or horizontal plane to measure both the transverse and the lateral beam profile to assure the best possible mode matching, in addition to seeking maximum power transmission.

Amplifier under condition (a)

The power amplification was firstly investigated under condition (a). In the single pass configuration, with an input power of approximately 100W, the maximum amplified output power achieved was 130.9W. This was equivalent to extracting about 30W from an area of ~ 5.4×10^{-3} m^2 or a mean power extraction of ~ $5.5 kW \cdot m^{-2}$, as the lateral beam width was ~ 7mm and the length of the waveguide was 770mm. It was also noted that the performance of the amplification varied slightly for different amplifier resonant frequency conditions. This can be explained in terms of the impact that the resonant frequency has on the RF input power distribution along the waveguide.

The amplified laser output power as a function of the operational pressure in the 5 and 7 pass configuration is shown in Fig. 6.13. The maximum output power obtained was 312W for the 5 pass and 410W for the 7 pass configuration. This is equivalent to a power gain of > 3 for the 5-pass and > 4 for the 7-pass arrangement. It should be noted that the maximum output occurred within the pressure range of 45-60torr, where the potential for serious parasitic oscillation existed, which casts some doubt on the amplifier output power measurements since there may be some contribution from the parasitic oscillations.

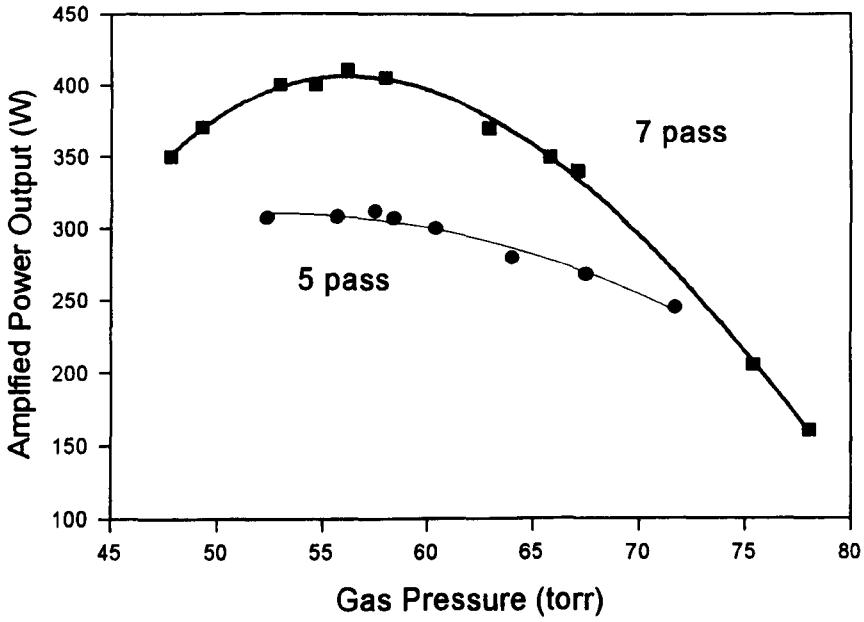

Figure 6.13 5 and 7-pass power amplification under condition (a) with an input power level of ~ 100W

Considering the lateral beam size, It was obvious that the power intensity of the beam remained relatively constant and thus the gain coefficient was similar for either single pass or multipass operation. This confirmed the benefits of the idea of using the laterally-expanding beam to cope with gain saturation effects for power amplification with a long gain path. This also meant that, for fixed input power, further increase in the amplified power gain requires either an improvement of the gain coefficient or an increase of the lateral beam size. The latter, however, is limited by the physical dimension of the waveguide and could reduce the number of folding passes.

Amplifier under condition (b)

Under condition (b), with the ceramic side walls of the waveguide amplifier removed, no evidence of the occurrence of parasitic oscillations was observed (to be discussed in detail in Chapter 8) in the 5-pass amplification. Thus, experimental measurements could now be conducted on the "pure" power amplification characteristics. In the absence of parasitic oscillations, a power magnification factor of 3.3 was achieved in the experiments with the 5-pass configuration. The power amplification as a function of the operational conditions with an input of ~ 80 watts is shown in Fig. 6.14. It is seen that the amplified power output increased rapidly until 70torr and then slowly with the pressure without turning over. The measurement stopped at 85torr. By comparing the power gain with the amplification in the single pass amplification at small signal level, it is evident that although gain saturation in the low pressure region was quite severe, as anticipated, the observed saturation in the high pressure region was relatively insignificant, implying the possibility of operating the amplifier at much higher input power levels with reasonable power gain. However, the 7-pass configuration of the amplifier has not been practical. Due to the small lateral beam size (~ 1.65mm) of the input, the beam expands so much that the structure of the amplifier was not able to provide a port wide enough to allow the exit of the output beam corresponding to the 7th pass, which has a calculated lateral beam size of ~ 17mm.

6.7 SUMMARY AND CONCLUSION

This chapter has investigated the gain characteristics and power amplification of a MOPA format, planar waveguide CO_2 laser amplifier driven by cw RF discharge. Experiments were carried out

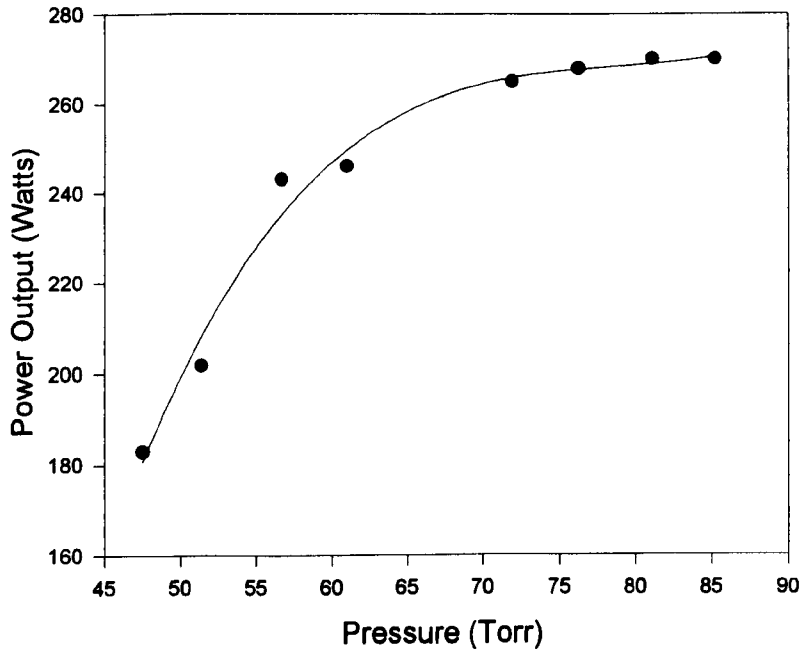

Figure 6.14 5-pass power amplification under condition (b) with an input power level of ~ 80W

under two conditions. Condition (a) corresponded to the use of a *one mirror beam transformation optical system* and the *amplifier configuration A*, in which the waveguide had ceramic side walls and was driven by RF discharge at 125MHz. With a smaller than ideal transverse input beam size, multimode was excited within the amplifier. Condition (b) corresponded to *the amplifier configuration B*, in which the waveguide had no ceramic side walls and was driven by RF discharge at 81MHz. With a two-mirror telecentric beam transformation optical system and a correct transverse input beam size, single mode excitation was achieved. Furthermore, with *the amplifier configuration B*, the parasitic oscillation, an inherent problem in high gain amplifiers, has been completely eliminated in the case of cw RF discharge, and therefore "pure" power amplification in multipass configurations could be conducted with the absence of parasitic oscillations.

The small signal gain coefficient was determined as a function of operational conditions (pressure and RF power deposition). A maximum value of $0.65\%cm^{-1}$ at 48torr was obtained under condition (b). The order of the saturation intensity was also obtained and presented by measurement of the output power at different input power levels. This has been $2.5\text{-}3.0kW\cdot cm^{-2}$ for pressure from 45 to 55torr, and $3.5\text{-}4.0kW\cdot cm^{-2}$ for pressure from 65 to 75torr. In addition, the amplified power output in multipass configuration was presented as a function of operational gas pressure. With a master laser oscillator at power level of 100 watts, power gain of > 3 for the 5-pass, and > 4 for the 7-pass amplification have been achieved.

In addition, as expected, the idea of using a laterally-expanding beam within the amplifier has proved to be satisfying in reducing the spatial dependence of saturation effects while producing a high filling factor. The gain saturation characteristics observed from the experiments indicate that the amplifier has to be operated in the high pressure region to benefit from high saturation intensity, when the traversing power level is much increased and hence the laser beam is deeply saturated. However, due to lack of data for the case of deep saturation, information to permit power amplification scaling to the kilowatt level is not yet available. This requires a higher power level laser oscillator for further experimental investigations.

In conclusion, power amplification with a planar waveguide structure has been demonstrated in a multipass, MOPA format under cw RF discharge. The experimentally determined gain characteristics, together with the complete solutions for the inherent parasitic oscillation problem (see also chapter 8), and knowledge of the mechanism for beam quality preservation (see also chapter 5), provides useful guidelines for future design of practical high power, planar waveguide laser amplifiers.

REFERENCE

6.1 A. D. Colley, H. J. Baker and D. R. Hall, "*Planar Waveguide 1kW CW CO_2 Laser Excited by a Single Transverse RF Discharge,* " *Appl.Phys.Lett.*, **61**, 136(1992)

6.2 A. A. Cameron, "*High pressure slab waveguide CO_2 lasers,* " PhD Thesis, Heriot-Watt University, Edinburgh (1997)

6.3 F. Villarrel, P. R. Murray, Q. Cao, G. A. Markillie, H. J. Baker, D. R. Hall, "*Enhancement of the micromachining capabilities of CO_2 slab waveguide lasers,* " *ICALEO®1999*, November 1999, San Diego, California, USA

6.4 K. M. Abramski, A. D. Colley, H. J. Baker and D. R. Hall "*Power scaling of large-area transverse radio frequency discharge CO_2 lasers,* " *Appl. Phys. Lett.*, **54**, pp.1833-1835(1989)

6.5 P. K. Cheo and H. G. Cooper, "*Gain Characteristics of CO_2 Laser Amplifier at 10.6 Microns,* " *J. Quant. Electron.*, **QE-3**, No. 2, February 1967, pp.79-84

6.6 E. T. Antropov, I. A. Silin-Berkchurin, N. N. Sobolev, and V. V. Sokovikov, "*G-14—Gain Measurement in the CO_2 Laser Discharge,*" *J. Quant. Electron.*, **QE-4**, No. 11, November 1968, pp.790-795

6.7 R. L. Abrams and W. B. Bridges, "*Characteristics of sealed-off Waveguide CO_2 Lasers,*" *J. Quant. Electron.*, **QE-9**, No. 9, September 1973, pp.940-946

6.8 S. A. Trushin and V. V. Churakov, "*Theory of high power CO_2 molecular amplifiers,*" *Sov. J. Quant. Electron.*, 7, No. 2, February 1977, pp.212-216

6.9 K. Janulewicz and P. Szczepanski, *"Approximate analytical method of gain saturation analysis of hollow waveguide lasers,"* *Appl. Optics*, **30**, No. 27, September 1991, pp.3818-3820

6.10 R. J. Morley, *"RF Excited CO_2 Amplifiers for Lidar,"* PhD thesis, Heriot-Watt University, June 1992

6.11 R. C. Sharp, *"Measurement of transverse-gain profiles in rf- and de-excited CO_2 cavities,"* *J. Appl. Phys.*, **61**, June 1987, pp. 5184-5186

6.12 V. V. Grigor'yants, B. A. Kuzyakov, and A. M. Sinitsyn, *"Gain of a CO_2 waveguide laser,"* *Sov. J. Quant. Electron.*, **7**, No. 7, July 1977, pp.836-840

6.13 M. B. Klein and R. L. Abrams, *"10.6-μm Waveguide Laser Power Amplifier,"* *J. Quant. Electron.*, **QE-11**, No. 8, August 1975, pp.609-615

6.14 A. I. Dutov, I. Y. Evstratov, V. N. Ivanova, A. A. Kuleshov, S. A. Motovilov, N. A. Novoselov, V. E. Semelov, V. N. Sokolov, M. S. Yur'ev, *"Experimental investigation and numerical simulation of a slab waveguide CO_2 laser with rf pumping,"* *J. Quant. Electron.*, **QE-26**, No. 6, August 1996, pp.484-488

6.15 H. Kogelnik, T. J. Bridges, *"A Nonresonant Multipass CO_2-Laser Amplifier,"* *J. Quant. Electron.*, **QE-3**, No. 2, Februry 1967, pp.95-96

6.16 G. J. Dezenberg, E. L. Roy, and J. A. Merritt, *"Properties of a 15-cm i.d. Multipass CO_2 Laser Amplifier and Oscillator,"* *Appl. Optics*, **9**, No. 2, Februry 1970, pp.516-517

6.17 D. Wheatley, *"A High Power, High Modulation Bandwidth CO_2 Laser,"* *SPIE Procee.*, **3092**, pp.109-113, GCL'96 Edinburgh

6.18 K. D. Laakmann and W. H. Steier, *"Waveguides: characteristic modes of hollow rectangular dielectric waveguides,"* *Appl. Opt.*, **15**, pp.1334-1340 (1976)

6.19 P. K. Cheo, *"Lasers,"* Volume **3**, Chapter 2, (A. K. Levine and A. J. DeMaria eds), Marcel Dekker, New York (1971)

CHAPTER SEVEN

PULSED LASER AMPLIFICATION

7.1 INTRODUCTION

Short duration laser pulses have recognised advantages in material processing and related applications due to low heat-effected zone effects [7.1-7.2]. Modern planar waveguide CO_2 lasers are capable of producing pulses as short as 50 μs at high average power at 1 to 2 kHz pulse rates, from sealed-off devices without gas flow. The much older TEA CO_2 lasers readily produce sub-microsecond pulses but are only available with low pulse repetition rates (typically under 100Hz) and usually require a complex gas flow system to achieve high average power. However, many material processing tasks such as surface treatment and micro-machining benefit from laser pulse properties intermediate between these two technologies. Using pulse widths between 1 and 20μs for processing of dielectric materials which are strongly absorbing at the 10.6μm wavelength, the penetration depth of heating can be minimised whilst avoiding the severe plasma screening effects associated with sub-microsecond irradiation.

In the literature, only one commercial laser system [7.3] is relevant to this intermediate processing window. It uses an oscillator-acousto-optic-modulator-amplifier configuration to produce high power, high modulation rate CO_2 laser pulses for engraving of flexographic printing plates. However, as it involves gas flow and dc-discharge excitation, the whole system is not mechanically compact or cost-effective. To produce sealed-off, compact, good beam quality, high intensity laser pulses for the 1 to 20μs pulse width processing window, we have converted the RF-excited planar waveguide MOPA system described in the previous chapter to pulsed mode operation. In this system, a long pulse laser master oscillator coupled with an AO modulator is used to provide short pulses at the input to the planar waveguide amplifier, allowing laser pulse amplification over a wide range of pulse width ($\tau_p \geq 1\mu s$). With pulse-shape manipulation capability, the conventional *high spike-low plateau-long tail* image of the laser pulses may be replaced by more desirable shapes, such as bell-shaped or square pulses. In addition, the amplifier

may be extended to provide laser pulse amplification in the 100s of nanosecond regime, such as for power enhancement of Q-switched lasers.

In principle, CO_2 laser pulse amplification may be understood in terms of an optical pulse propagating through a homogeneously broadened gain medium. Such an optical pulse will undergo changes to its shape as a result of radiative and molecular relaxation processes [7.13-7.17], as described in Chapter 2. For pulse amplification in the μs regime, as investigated here, there must be molecular relaxation processes involved, including rotational and vibrational relaxation and resonance energy transfer effects.

This chapter first considers the procedure for using an acousto-optic modulator to obtain short laser pulses, including a review of relevant acousto-optics and an investigation of pulsed characteristics of the slab waveguide master laser oscillator. Then, following a brief introduction to the arrangement of the pulsed MOPA system, experimental results are presented of the pulse shape distortion/manipulation, time-varying gain/pulse energy gain, pulse energy/peak power amplification and the spatial beam profile measurements. This leads to a discussion in which modelling of the pulse amplification is carried out using experimental data as the input. All the experimental results presented in this chapter were obtained in the absence of parasitic oscillations. This issue will be discussed in detail in Chapter 8.

7.2 PULSE SLICING USING ACOUSTO-OPTICAL MODULATOR

7.2.1 Background of Acousto-optics

Acousto-optic effect

Acousto-optical modulators are based on the interaction between light and sound, which occurs in any optical medium in which an acoustic wave and a laser beam overlap; such interactions may be considered as collisions of photons and phonons [7.4]. When an acoustic wave, which is converted from a radio-frequency signal by a piezoelectric transducer incorporated in the AO modulator, is launched into the optical medium, a perturbation in the refractive index is generated

and thus this optical medium behaves like a sinusoidal grating. Then, an incident laser beam will diffract after passing through this grating.

When a plane acoustic wave with an angular frequency Ω is launched into an acousto-optic modulator, for a light of an angular frequency ω_0 with a particular incident angle ϕ_B, there will be two beams, the zero order and first order beam, emerging after transit through the modulator. The zero order beam propagates at the same direction as the incident light, while the first order beam is diffracted at an angle of $\theta = 2\phi_B$ with respect to the zero order beam, and having its angular frequency ω_1 up-shifted or down-shifted by Ω depending on the incident angle with respect to the acoustic wave [7.5]. The angle ϕ_B is referred to as Bragg angle, given by:

$$\sin(\phi_B) = \frac{\lambda \nu}{2V_a} \tag{7.1}$$

where λ is the wavelength of the light, ν, the frequency of the acoustic wave and V_a, the acoustic velocity.

Diffraction efficiency

Diffraction efficiency is a measure of the useful optical throughput of a device and is defined as the percentage of the input light power that is diffracted into the desired beam at a specified RF power used to drive this device. In the Bragg regime, only the first order diffracted light is significant, and its diffraction efficiency is a function of the acoustic frequency and power, material figure of merit, geometric factors and the light wavelength [7.6-7.7].

Risetime

The pulse risetime is a measure of how quickly the diffracted light can be turned on and off and is usually defined as the time it takes for the intensity of the diffracted beam to go from 10% to 90% upon application of a driving RF pulse. The risetime of an AO modulator depends primarily on the transit time τ of the acoustic wave across the laser spot, which can be estimated as $\tau = D/(1.5V_a)$ [7.8], where D is the diameter of the optical beam inside the modulator. The smaller

the spot size, the faster the risetime. However, problems such as degradation in diffraction efficiency and beam distortion may result from too small a spot. Therefore in practice, the risetime of any AO modulator is limited to allow maximum diffraction efficiency and minimum beam distortion.

7.2.2 Characteristics of Conventional Pulsed Slab Waveguide Lasers

In the previous chapters, the slab waveguide laser used as the oscillator in the MOPA system has been well described, with operation in the pulsed mode at a high pulse rate and high duty cycle, producing overlapped laser pulses behaving as a pseudo cw source with a periodical time-varying envelope. A further investigation of the oscillator in pulsed mode has been carried out to gain knowledge of the slab waveguide laser in terms of *peak* power characteristics.

Fig. 7.1 illustrates a set-up which was used for the measurement of laser pulse characteristics. The laser oscillator was driven by a pulsed RF discharge of peak power 2.2kW and frequency 81MHz, equivalent to a power density of ~ 80W/cm^3 for the 40 x 365 x 1.9mm^3 slab waveguide. Most of the laser power was directed by a beam splitter with a reflectivity of 92% onto a power meter where the power output of the laser oscillator was monitored. The beam was further reduced by the second beam splitter and was then incident onto a fast thermopile having a rise time < 1μs at an allowed power level of ≤ 2W (average) or ≤ 20kW/cm^2 (peak). The temporal laser pulse profiles were measured with this thermopile and displayed on a digital oscilloscope (Tektronix Model 2440), then saved via a computer network to which the digital oscilloscope was connected.

The shape and amplitude of the pulse profiles of the laser oscillator exhibited strong dependence on the pulse repetition rate and pulse duration of the RF discharge. Typical results are shown in Fig. 7.2. An optimal duty cycle in terms of maximum peak power output was observed for each pulse repetition rate, which was ~ 20% for 2 to 8kHz, and ~ 10% for higher or lower pulse repetition rates of 8-10kHz or 0.5-1kHz. Further investigations showed that the peak output power was in general inversely proportional to the pulse repetition rate. However, a turn-over in

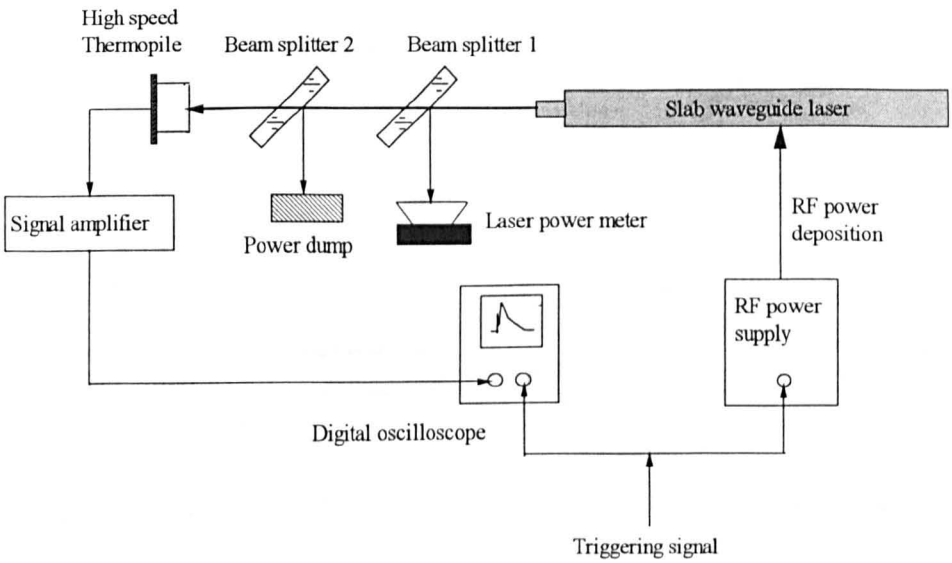

Figure 7.1 Schematic diagram for laser pulse measurement

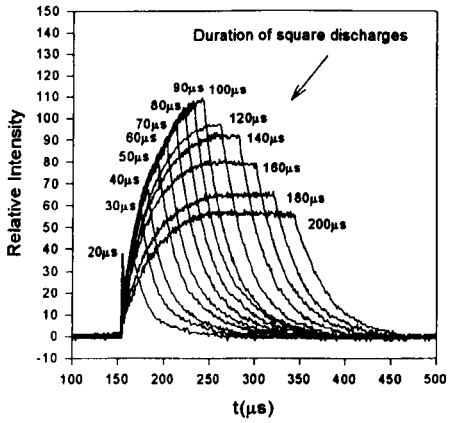

(a) Repetition rate: 2kHz

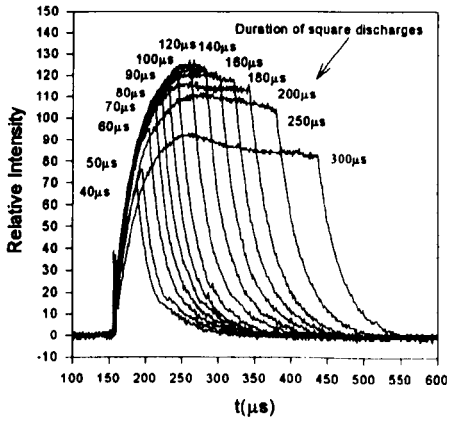

(b) Repetition rate: 1kHz

Figure 7.2 Temporal profiles of laser pulses at fixed repetition rates for varying pulse durations.

maximum peak power was observed at ~ 1kHz, with the peak power value being ~ 320W at a duty cycle of 10-14%.

7.2.3 Pulse Slicing via Acousto-Optic Modulation

Experimental set-up

The experimental arrangement for pulse slicing is shown in Fig. 7.3. The water-cooled AO modulator was made from a single crystal of germanium and had a Bragg angle of 1.49° requiring a linearly and horizontally polarised incident beam. The upper limit for the incident power was 5W/mm^2, or 100W with a beam diameter of 5mm limited by the optical aperture. The insertion loss was less than 15% and the diffraction efficiency was typically 75% with full drive RF power of ~ 30W. The AO modulator was located at a distance ~ 350mm from the output aperture of the laser oscillator, where the rectangular laser beam was expanded to have a maximum beam diameter of 4-5mm, giving a transit time of $\tau = 0.5\text{-}0.6\mu s$ for the acoustic velocity of $V_a = 5.5\text{mm}/\mu s$.

The AO modulator was driven by a 27MHz RF driver which was controlled with a pulsed signal synchronised to the RF power supply driving the laser oscillator. The amplitude of the signal was adjustable; therefore the drive power to the AO modulator and thus the intensity of the diffracted beam could be varied. While the zero order beam which was of no use in the experiment was blocked by a power dump, the first order diffracted beam was used for pulse slicing. With time-delay and pulse width adjustment, the laser "slices" could be selected with different widths and made to originate from anywhere within the long pulse produced by the laser oscillator.

Short laser pulses obtained through slicing

With this experimental arrangement, short laser pulses were readily achievable. The pulse shapes obtained vary with the timing of the modulator relative to the onset of the laser pulse. They can be "sloping roof-top" pulses, as shown in Fig. 7.4(a) where the peaks of the master oscillator (MO) pulses were selected, or nearly square pulses with "flat-tops" as shown in Fig. 7.4(b). Generally, the duration of a pulse selected with this method has no upper limitation. However, there existed a

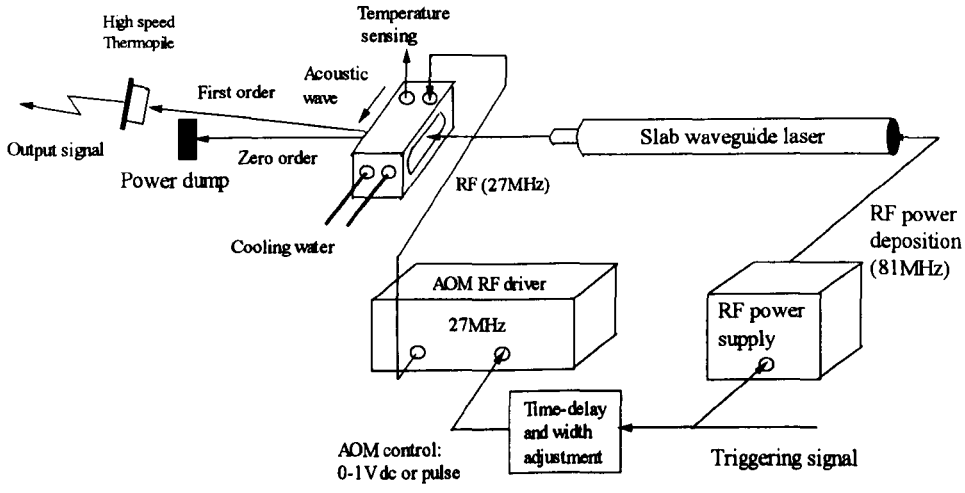

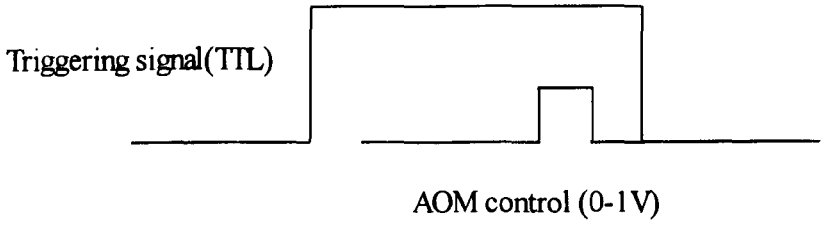

Figure 7.3 Experimental arrangement for pulse slicing using an AO modulator

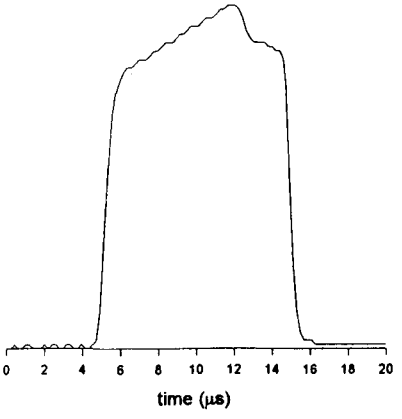

(a) Central peak of the original pulse is selected

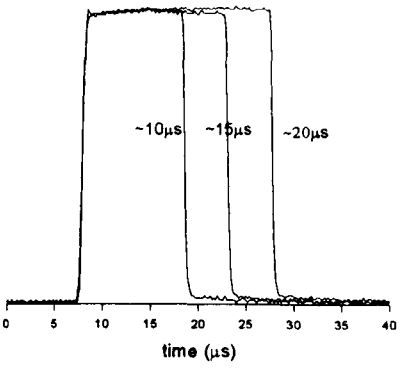

(b) Flat-top (near-square) pulses

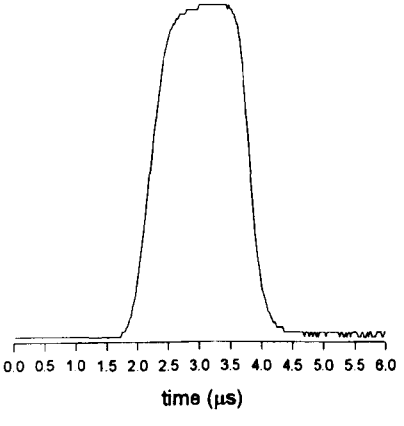

(c) Shortest available square-shaped pulse (~2μs)

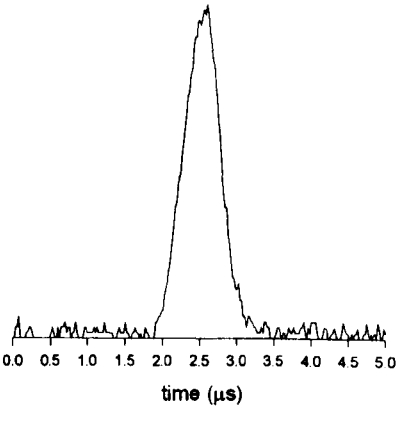

(d) Bell-shaped pulse (~1μs)

Figure 7.4 Examples of laser pulses obtained by slicing through AO modulation

lower limitation resulting from the limited rise-time of the AO modulator, which was ~ 2μs for nearly square pulses or ~ 1μs where the pulses evolved to have bell-shapes. These are shown in Fig. 7.4(c) and (d) respectively.

Distortion of the diffracted beam

Beam distortion of the diffracted light from an acousto-optic modulator is a recognised problem [7.9-7.11]. One of the causes is believed to be the wave-front aberration introduced in the diffracted light by the non-uniform refractive-index distribution induced thermally inside the AOM when the RF power is applied. In the case of low level incident laser power (< 1W), laser induced thermal effects produce little distortion. In addition, the quality of the crystal is found to make little contribution to the degree of aberration [7.10].

In the experiments described here beam distortion was observed when a laser power of 10-50 watts was incident to the AO modulator. The spatial profile of the first order diffracted beam became asymmetric compared to the originally symmetric profile when observed at far-field. This might be explained in terms of the wave-front aberration mentioned above. However, the laser induced thermal effects were believed to be mainly responsible, which were observed in both the transverse and lateral direction and were associated with the laser power loss inside the germanium crystal. In the lateral direction, different effects on either side of the first order diffracted beam were observed in terms of the side lobes. This was perhaps evidence of the temperature gradient in the lateral direction, because the germanium crystal had a rather large lateral dimension but only one of the sides was directly water- cooled.

As a consequence of the beam distortion, some degree of beam quality degradation was observed. Measurements of the first order diffracted beam showed about 10% degradation in the beam quality, causing the M^2 value measured in the transverse direction to increase from ~ 1.15 to ~ 1.30.

Potential effects of frequency shift of the probe laser to amplification

The incident beam had an angle of $90^{\circ}-\phi_B$ to the propagation of the acoustic wave, thus the first order laser beam had a frequency down-shift of 27MHz. However, this amount of frequency shift is insignificant compared to the line width of the amplifier operated at high pressure. For instance, as a result of collision broadening, the bandwidth of the amplifier is about 400-500MHz for a typical operating pressure in the range of 80-100torr [7.12-7.13]. Thus, potential effects of this frequency down-shift upon gain characteristics during amplification are expected to be negligible. However, this was not experimentally investigated in the work presented in this chapter.

7.3 CONSTRUCTION OF THE LASER PULSE AMPLIFICATION SYSTEM

The experimental arrangement for laser pulse amplification incorporating an AO modulator is illustrated in Fig. 7.5. The configuration of the multipass amplifier was similar with that used in the set-up described in the previous chapter, except for the inclusion of two internal masks for elimination of potential parasitic oscillations (see Chapter 8). The amplifier vessel was back-filled to vary the pressure of the gas, which was a 3:1:1 mixture of He, CO_2, N_2, plus 5% of Xe for all the experimental data presented in this chapter unless stated otherwise.

The positioning of the AO modulator with respect to the laser oscillator was the same as in Fig. 7.3 as outlined in section 7.2. The zero order diffracted beam was directed to a power dump (not shown in Fig. 7.5) whilst the first order diffracted beam was designated as the probe beam for amplification. A laterally telecentric beam transformation optical system was incorporated to provide transverse waveguide mode matching while facilitating the lateral beam folding and compensating the beam distortion mentioned above. It consisted of two off-axis spherical mirrors with a radius of curvature of 1.20m for CM1 and 0.71m for CM2. The incident angle was 41.5° for both mirrors. Flat mirrors FM1-FM4 folded the beam over a standard laboratory bench and assisted the beam alignment to the amplifier. A clean-up aperture positioned near the focal plane between the two curved mirrors removed the side-lobes of the beam in the lateral direction.

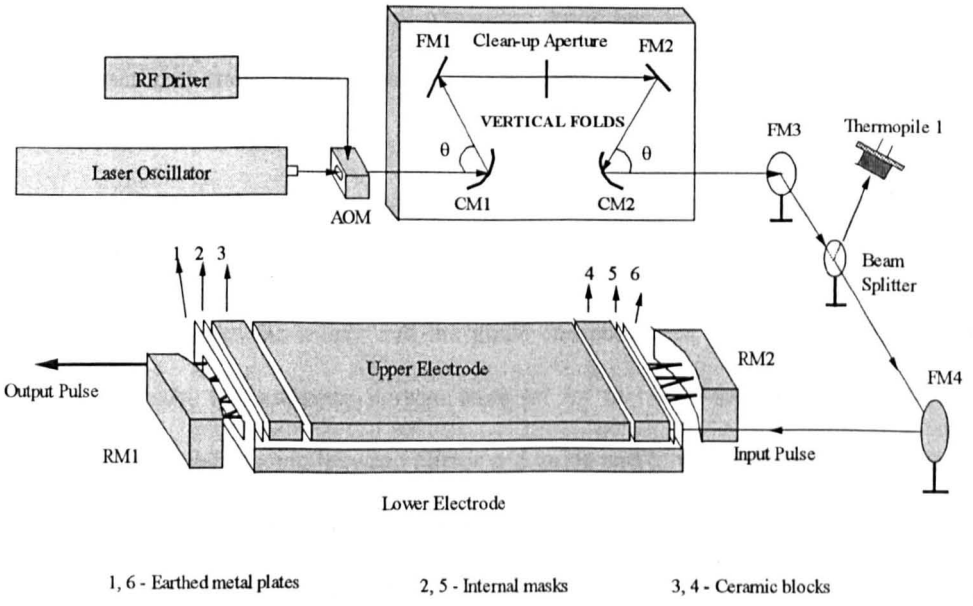

Figure 7.5 System set-up for pulsed laser power amplification (power dump for the zero order diffracted beam not shown)

The coupling optics were designed to have a magnification of 1.7 in the lateral direction, giving an actual lateral beam size of ~ 3.4mm. In the single pass configuration, the power transmission through the amplifier waveguide was ~ 98%. Using the mode diagnostic technique described in Chapter 5, the transmitted beam was found to have over 95% of the incident power included in the fundamental mode, indicating good transverse mode matching. In the 7-pass configuration, the total fractional transmission was 60 ~ 65%, indicating an equivalent loss coefficient of $0.09 \pm 0.01\%cm^{-1}$. The total power loss was mainly a combination of waveguiding loss, losses on the resonator mirrors and the coupling losses occurred as the beam exited and entered the waveguide as many as 14 times. The coupling loss was significant as anticipated, due to the non-guided spacing between the mirror and the guide end combined with the non-optimum mirror curvatures. Because the resonator mirrors were set up to be off-axis, the required mirror tilt caused the non-guided spacing between mirror and guide end to vary from ~ 1mm to over 10mm. The inclusion of the two internal masks added an extra loss, which reduced the passive power transmission in the 7-pass configuration to ~ 55%, equivalent to an average total loss coefficient of $\sim 0.11\%cm^{-1}$. The folded beam was expanding along the beam path and the lateral beam size at the output was calculated to be ~ 11.2mm. Due to the closely folded nature of the beam path, the adjacent beams in the 7-pass configurations were overlapped. The total overlap area was ~ 26% in terms of the whole beam area, or ~ 21% in terms of the electrode area. Overall, this 7-pass configuration gave a fill factor of ~ 81%.

A beam splitter with a reflectivity of 17% was inserted in the beam path between flat mirrors FM3 and FM4, which were placed before the input aperture of the amplifier. The reflected power was directed on to a thermopile, allowing the temporal profiles of the input pulses to be monitored. The inclusion of this beam splitter reduced the peak laser power at the input to the amplifier to ~ 50% of the original value produced by the master oscillator when the AO modulator was driven with full RF power. The output beam of the amplifier was directed to either a power meter, a beam scanner or a detector, allowing the amplified power, and the spatial and temporal beam profiles to be measured. In addition, a synchronisation chain was established as shown in Fig. 7.6 to co-ordinate the four related triggering signals involved in the whole system.

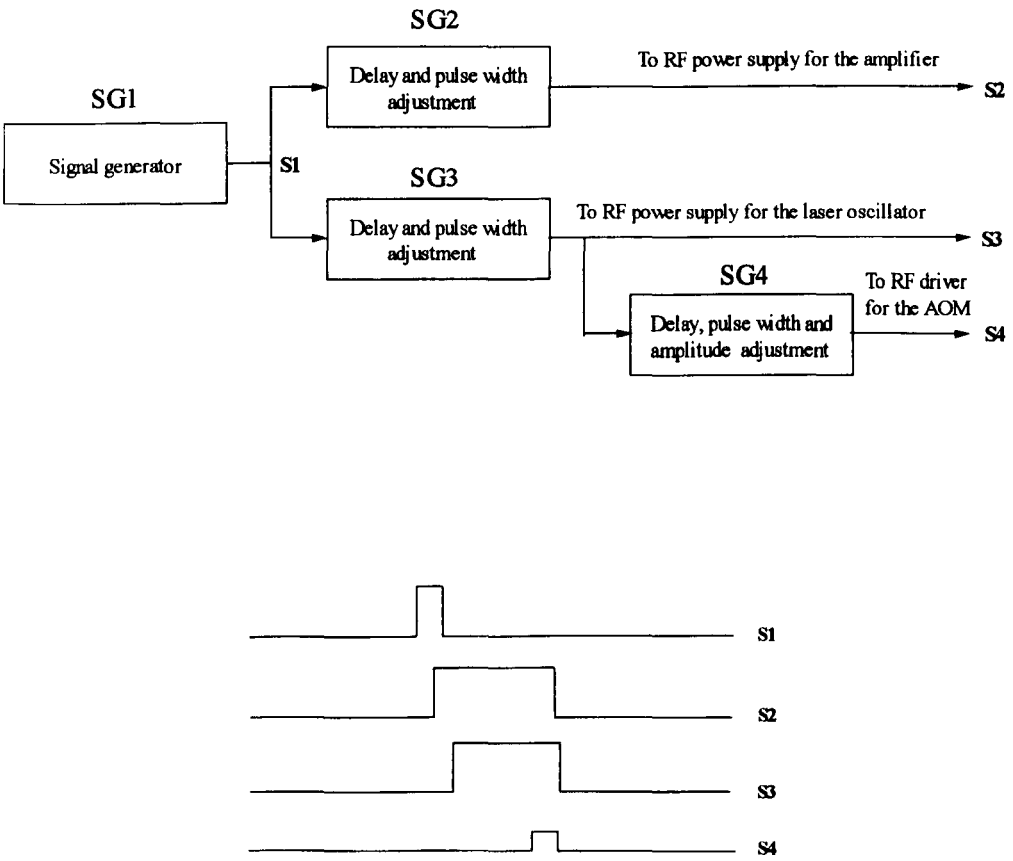

Figure 7.6 Synchronisation chain for the MOPA system

The amplifier was firstly operated in the single pass configuration, where the gain path was 770mm. With no resonator mirrors fitted, some basic parameters of the amplifier were measured. Then, by incorporating the positive branch, unstable resonator mirrors with appropriate adjustment, the amplifier was configured to have a 7-folded beam path with a gain length of 5.39m.

7.4 PULSED GAIN CHARACTERISTICS

7.4.1 Timing of the Input Pulse and Optimum RF-discharge Duration

Before extensive experimental investigations were carried out, a series of time-resolved pulse energy gain measurements were taken to determine the timing of the short input pulse relative to the discharge in terms of maximum pulse energy amplification. The pulse energy gain was found always starting from zero at the beginning of the discharge, and increasing as the pulse moved into the envelope of the discharge. For a short duration discharge, the gain reached a maximum at the termination of the discharge. For sufficiently long discharge pulses, the gain was observed to reach a maximum at a certain point and then start to decrease gradually. In addition, this maximum value was found to decrease with continuing increases in the discharge duration. This indicates the existence of an optimum discharge duration for maximum amplification, which is related to thermal effects introduced by RF power deposition.

The optimum discharge duration was further found to decrease with increased pulse repetition rate in a manner to maintain constant average RF power deposition, giving an optimum duty cycle of ~ 30% for 2-10kHz. However, for lower pulse repetition rates, the optimum discharge duration was found to correspond to smaller duty cycle (~ 18% for 1kHz) due to thermal effects associated with very long discharge pulses.

It is thus clear that the timing of the input pulse in terms of maximum amplification should be at the termination of the discharge if its duration is not longer than the optimum value, or at the position in the time axis corresponding to the optimum discharge duration for long duration discharges. In the remaining part of this chapter, unless otherwise indicated, all experimental data

presented were obtained at optimum discharge duration and best timing of the input pulse relative to the discharge.

7.4.2 Pulse-shape Distortion

This section investigates experimentally the aspects of pulse-shape distortion for CO_2 laser pulse amplification in the μs regime. Examples demonstrating pulse-shape distortion with a square input pulse are shown in Fig. 7.7(a). The pulse came on with a gradually declining top after the single pass amplification and was further distorted with a very sharp spike at the leading edge after the 7-pass amplification. The pulse-shape distortion was found to be less serious when the laser pulse was moved forward or backward far away in the time axis from the termination of the RF discharge pulse, because of decreased gain.

The slope of the output pulse became greater with increased intensity of the input pulse. With weak input pulses, the pulse shape distortion in single pass amplification was insignificant. In contrast, upon 7-pass amplification the pulse shape distortion was always significant, even with weak input signals. This is because with a long gain path, the signal intensity will sooner or later reach such a level that it is strong enough to induce significant gain saturation. It was noted that the dependence of pulse shape distortion on the gas pressure was insignificant for typical pressures of 80-100torr, while the RF discharge was maintained uniform.

Evidence of *probe laser-induced lasing* in the amplifier was observed, due to optical feedback caused by reflection or scattering from mechanical or optical surfaces, which caused the output pulse to have more than one peak in the leading part as shown in Fig. 7.7(b). With the amplifier turned on, similar phenomenon was also observed in the input pulse profiles, measured at positions *before* the amplifier. Due to a lack of an optical isolator between the laser oscillator and the amplifier, the *probe laser-induced lasing* in the amplifier produced optical feedback through the input window, interfering with the input pulses. Consequently, the affected input pulses produced further effects on the output pulses. This process may be associated with the very high initial unsaturated gain, for it terminated after a $1 \sim 2\mu s$ transient period as the gain decreased

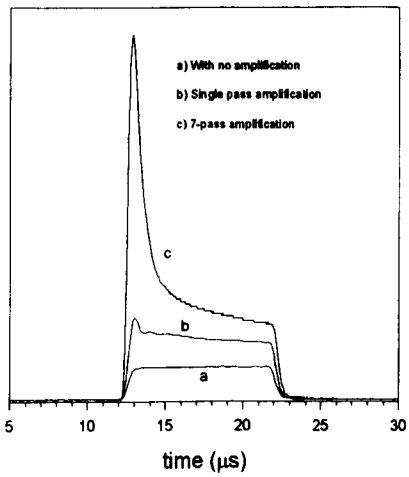

(a) With square input pulses at both single-pass and seven-pass amplification.

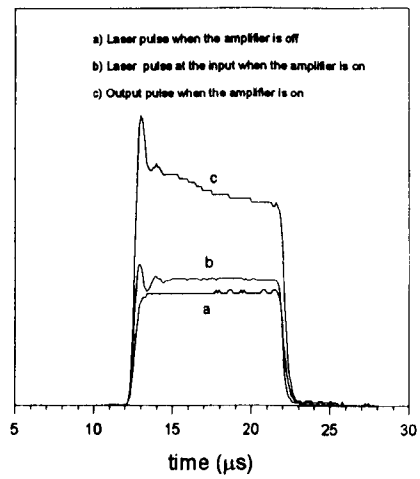

(b) Output and input pulses showing transient effects in the leading parts for single pass amplification with the amplifier turned on.

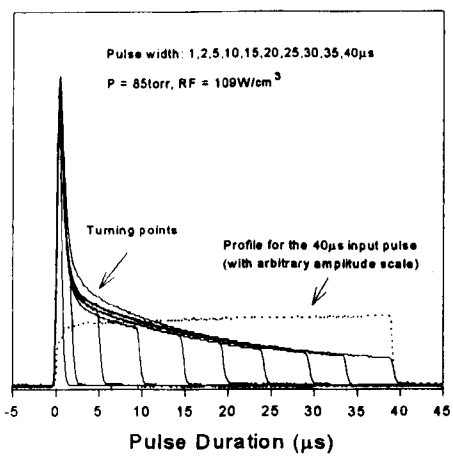

(c) Output pulse profiles with varying pulse duration at 7-pass amplification.

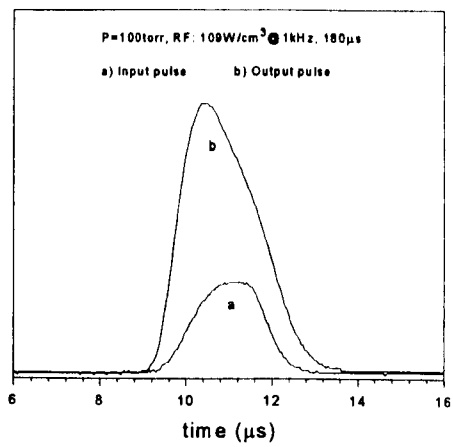

(d) For bell-shaped input pulse, the output pulse appears to move forward in time.

Figure 7.7 Pulse profiles showing pulse shape distortion after amplification (PRF = 1kHz)

considerably. Reducing the intensity of the input pulse, such effects to both the input and output pulse profiles were observed to decrease. However, the detailed mechanism for the occurrence of this phenomenon requires further investigations to specify.

The output pulse profiles were also investigated with different input pulse durations as shown in Fig. 7.7(c) for near-square shaped input pulses. The evolution of the output pulse profiles indicates continuing gain saturation along the pulses. A turning point was observed for each long pulse at ~ 3μs from the leading edge. This reflects the effects of the resonance energy transfer from excited N_2 to CO_2 (00^01), which has a time constant of $\kappa_e = 1.9 \times 10^4$ $Torr^{-1}$-sec^{-1} [7.12] giving a relaxation time of ~ 3μs for typical operating pressures of 80-100torr.

It has been noted from the literature that the leading edge spikes may give rise to negative effects in material processing associated with plasma formation and unwanted laser beam penetration. Thus, it is necessary to have the option to remove the spike from the laser pulse. The solution is to modify the input pulse to have a slow-rising leading edge. This has been achieved by gating the RF drive power to the AO modulator with a triangular wave, giving a flat-top or near-square output pulse as shown in Fig. 7.8.

For a bell-shaped input pulses, the output pulse was observed to be still bell-shaped, but appeared to have moved forward in time compared with the input pulse and to possess a sharper rising edge, as seen in Fig. 7.7(d). This is referred to as the *risetime shortening effect* [7.15]. This effect occurs in amplification with input pulses having rounded leading and trailing edges, because the rising edge receives full amplification, whereas the gain is substantially reduced during the peak and falling edge of the pulse.

7.4.3 Time-varying Gain

Measurement

The *time-varying gain G(t)* as the ratio of peak power intensity of the output pulse over that of the input pulse (see also Eq.(2.31)) characterises the saturation induced gain variation through the

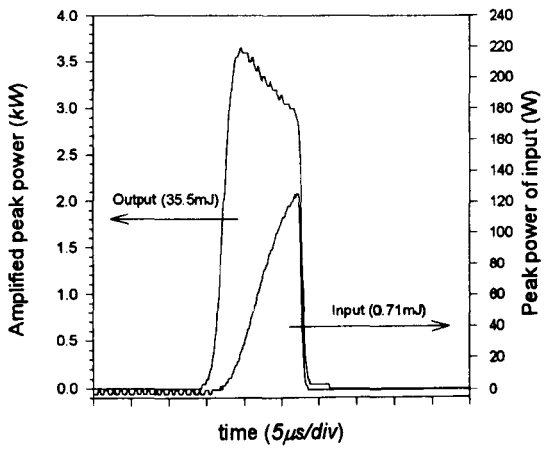

(a)

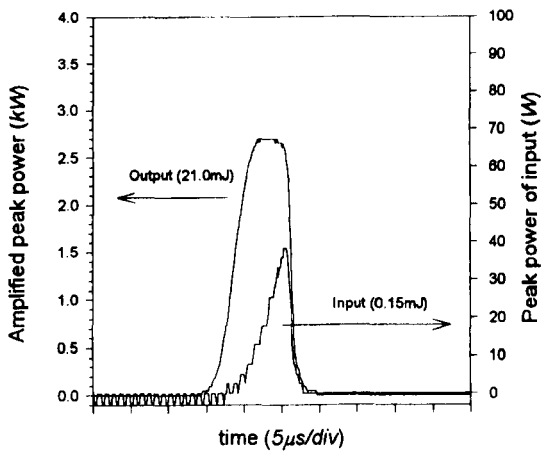

(b)

Figure 7.8 Peak power of the amplified pulses with the leading spikes removed using modified input pulses in the 7-pass configuration (pulse repetition rate 1kHz; RF power deposition 109W/cm^3 @ 180μs duration; gas pressure 100torr; folded gain path 539cm)

pulse. Experimentally it may be obtained knowing the pulse energy and the temporal and spatial profiles. The peak power intensity of a rectangular and symmetric beam at the beam centre is the same as if the total power P were uniformly distributed over an equivalent area of:

$$A = \frac{\pi W_x W_y}{2} \tag{7.2}$$

where W_x and W_y are the lateral and transverse beam sizes respectively. Thus, the peak power intensity distribution in the beam centre may be written as:

$$I(t) = \frac{2P(t)}{\pi W_x W_y} \tag{7.3}$$

where $P(t)$ is the peak power distribution and was obtained in the experiments by evenly distributing the pulse energy over the area defined by the corresponding temporal profile. Then the *time-varying gain* is readily obtained as:

$$G(t) = \frac{P_{out}(t)}{P_{in}(t)} \frac{W_{xin}}{W_{xout}} \tag{7.4}$$

where $P_{out}(t)$ ($P_{in}(t)$) and W_{xout} (W_{xin}) are the peak power distribution and the lateral beam spot size of the output (input) pulse respectively, assuming a constant transverse beam size.

It is anticipated that with a square input pulse, the time-varying gain would always start with a maximum at the leading edge, followed by a decline along the pulse. Furthermore, for square input pulses with the same power intensity but varying pulse duration, the final gain G_f corresponding to the falling edge of the pulses would decrease with increased pulse duration, due to the continuing gain saturation along the pulse. Fig. 7.9 is a collection of plots of typical time-varying gain showing dependence upon gas pressure, RF deposition and intensity of input pulses. In general, the dependence of the overall time-varying gain behaviour on RF power deposition and gas pressure was found to be insignificant under typical operational conditions, although the amplitude might be different. These are shown in Fig. 7.9(a) and (b), which were measured under single pass conditions. In contrast, under the same conditions, the dependence of the time-varying gain on the intensity of the input pulse was significant, as shown in Fig. 7.9(c). In addition, as seen in Fig. 7.9(a) and (d), a rising tail may be observed on each time-varying gain plot. This is

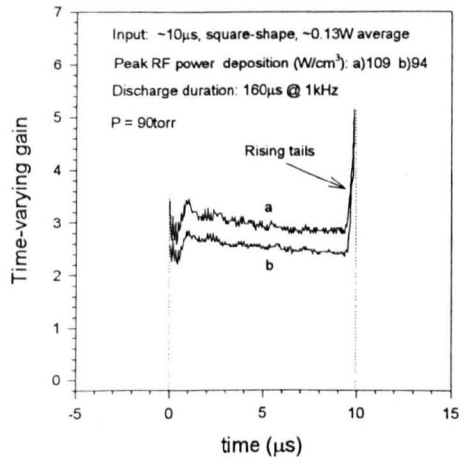

(a) With varying RF deposition at fixed gas pressure and pulse input.

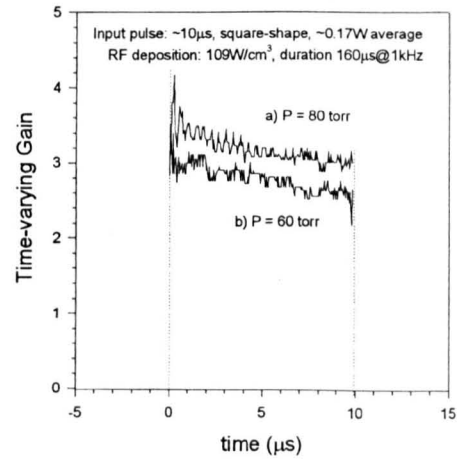

(b) With varying gas pressure at fixed pulse input and RF deposition.

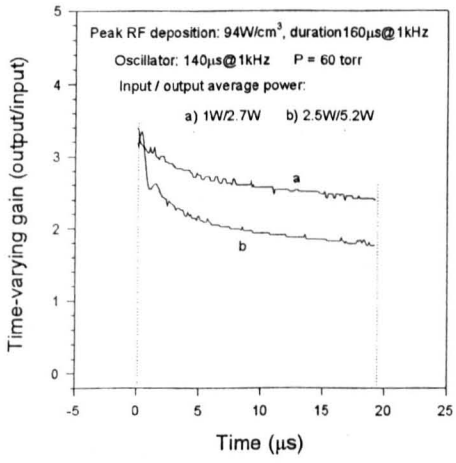

(c) With varying input pulse intensity at fixed gas pressure and RF deposition

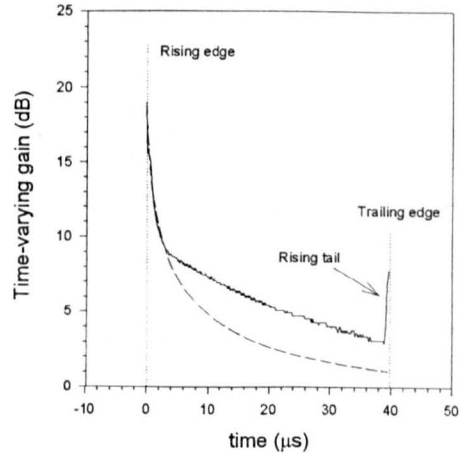

(d) With long pulses in the 7-pass operation

Figure 7.9 Time-varying gain for different conditions

perhaps because the falling edge of the input pulse was not perfectly sharp. When the power intensity of the input pulse corresponding to the falling edge dropped gradually from the peak value to zero, the degree of gain saturation was reduced accordingly, leading to a gain recovery.

The fact that the time-varying gain always starts with an unsaturated or small signal value at the leading edge, regardless of the intensity of the input pulse, provides in principle a method for measuring the unsaturated or small signal gain. With this method, the unsaturated gain coefficient was found to be 1.5-1.9% cm^{-1} for a gas pressure of 80-100torr and a peak RF power deposition of 94-109W·cm^{-3}, measured using single pass amplification. The measurement was taken with a greatly reduced input signal level so that laser beam fluctuations, which affect the measurement accuracy, caused by the *probe laser induced lasing* (see section 7.4.2) became insignificant. The unsaturated gain coefficient was similar to that recorded at a pulse repetition rate of 0.5kHz but higher than that at 1kHz for a gas mixture of $He:CO_2:N_2:Xe = 6:1:1:0.4$ measured by Dutov et al [7.1].

The time-varying gain measured using 7-pass amplification, showed more serious gain saturation effects as a direct result of the long gain path. The gain at the leading edge was found to be rather variable. The typical value was between 60 to 90 at a gas pressure of 80-100torr and peak RF power deposition of 109W·cm^{-3}, the maximum the RF power supply could provide. This was equivalent to a small gain coefficient of $\gamma_0 = 0.90 \pm 0.05\%$ cm^{-1}, taking into account the passive power transmission of 55%. This gain coefficient was smaller than the typical value of 1.5-1.9% cm^{-1} measured in the single pass operation. This may be related to the overlapping nature of the folded beam path — the gain medium that the leading edge of the pulse entered was probably already disturbed by the previous pass. In this sense, the gain at the leading edge of the pulse did not represent the unsaturated gain but a partially saturated one.

Fig. 7.9(d) shows a typical time-varying gain (the solid line) from the 7-pass amplification for an input pulse with a duration of ~ 40μs and a pulse energy of ~ 6mJ. The amplifier was operated with a peak RF deposition of 109W·cm^{-3} for a discharge duration of 180μs at a gas pressure of

100torr. The large difference between the gain at the leading edge and that at the trailing edge indicates the occurrence of significant time-varying gain saturation. The dashed line is a numerical result. Comparison of these two results will be discussed in section 7.7.

7.4.4 Pulse Energy Gain

The *pulse energy gain* is an overall or averaged effect in laser pulse amplification, defined in Eq. (2.35) as the ratio of the *unit area* output energy to the *unit area* input energy. The ratio of the total pulse energy of the output and input pulses is referred to as the *total pulse energy gain* in this thesis.

Small signal pulse energy gain

The pulse energy gain decreases with increased average power because of the gain saturation effect through the pulse. The investigation commenced with measurements using a small signal level, observing the dependence of pulse energy gain on operating conditions. Fig. 7.10(a) demonstrates the dependence of pulse energy gain on the peak input RF power deposition for the single pass configuration at an input signal level of 0.03mJ for a pulse duration of 2μs. The maximum value appeared at a peak RF power deposition in the range of 95-105W/cm^3 at a pressure of 60torr, and tended to occur at higher values of peak RF power deposition for higher pressures. For pressures over 80torr, a rollover was not reached in the experiments, as the output capability of the RF power supply was limited to a maximum of ~ 14kW, equivalent to a peak power deposition density of 109W/cm^3.

The dependence of the pulse energy gain on gas pressure is shown in Fig. 7.10(b), where the RF power supply was operated at its power output limit mentioned above. Curve *a* and *b* represent small signal pulse energy gain, corresponding to input pulses of 2μs and 5μs duration respectively. For the 2μs pulse, the maximum value occurred at around 80torr, with a typical value of 5.0 ~ 5.5dB between 70 to 90torr, equivalent to a gain coefficient of 1.50-1.62%/cm. This value is slightly smaller than the unsaturated or small signal gain obtained from the time-varying gain measurements, because of the presence of gain saturation. Compared to the small

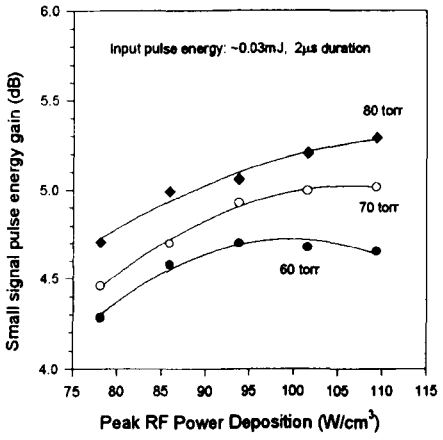

(a) Small signal pulse energy gain against operational conditions at 2μs pulse amplification

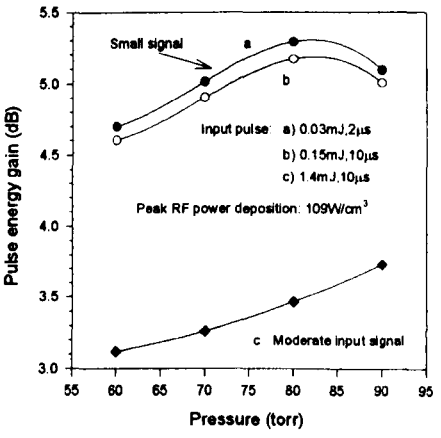

(b) Small signal pulse energy gain, compared with that at moderate pulse input as a function of gas pressure

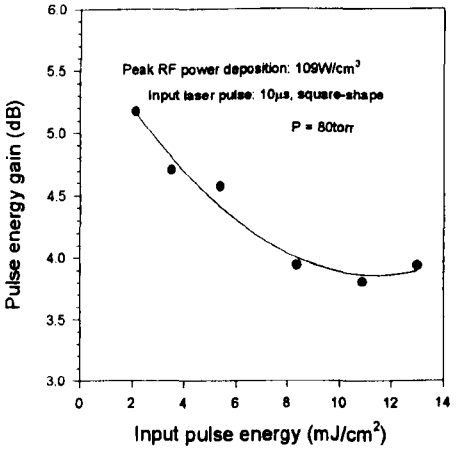

(c) Pulse energy gain as a function of input energy

Figure 7.10 Pulse energy gain at single pass operation (gain length 77cm, pulse repetition rate 1kHz and discharge duration 160μs)

signal gain coefficient of 0.65%/cm in cw amplification as investigated in the previous chapter, the small signal gain coefficient was nearly twice as large, owing to the improved cooling efficiency with a pulsed RF discharge. In addition, due to the increased gain saturation along the pulse, the small signal pulse energy gain decreases with increased pulse width. This is evident through comparison of the small signal pulse energy gain at a pulse width of 2 and 10μs, as shown in Fig. 7.10(b).

Saturation of pulse energy gain

It is anticipated that the pulse energy gain varies with the input pulse energy as a result of the gain saturation. As shown in Fig. 7.10(b), the pulse energy gain for an input pulse energy of 1.4mJ, represented by curve *c*, was observed to be much smaller compared to the small signal value (curve *b*) for the same pulse duration (10μs). In addition, the position of the maximum pulse energy gain had apparently shifted to a higher pressure region. This suggests a higher saturation energy for higher pressures.

Seeking to obtain further insight into the effect of gain saturation on the pulse energy gain, a series of measurements was made with a fixed pulse duration of 10μs but at different input pulse energies. Typical results are shown in Fig. 7.10(c) for the amplifier operating at a pressure of 80torr with peak RF power deposition of 109W/cm^3. With an input energy of about 2mJ/cm^2, a pulse energy gain of over 5dB was achieved for a gain length of 77cm. As the input energy was increased, the pulse energy gain decreased. The value dropped by 1dB when the input energy was increased to 10mJ/cm^2. Experiments at very high input pulse energy were not available due to the limited power capability of the master oscillator.

Pulse energy gain with a folded, long gain path

In pulse amplifiers with long gain paths, serious gain saturation takes place as the pulse energy grows substantially along the gain path, irrespective of the signal level of the input pulse. Here, we will see the behaviour of the pulse energy gain in the 7-pass amplifier. The investigation was carried out with the peak power of the input pulse maintained at 140-160W while the total input

pulse energy varied according to the pulse width. The amplifier was operated at a pressure of 80-100torr with a peak RF deposition density of 100 ± 10W/cm^3.

Fig. 7.11(a) shows the results of the pulse energy gain of the 1μs and 10μs pulses as a function of RF power deposition density at a pulse repetition rate of 1kHz for typical pressures. The pulse energy gain appeared to increase with RF power deposition, and no rollover was observed as the power supply reached its output limit. The desired peak pulse energy gain was estimated to occur at a pressure above 100torr where higher peak power deposition is required to maintain a uniform discharge. Nevertheless, maximum pulse energy gains of 9.5dB and 19.4dB, equivalent to pulse energy gain per unit length of 0.018dB/cm and 0.036dB/cm, were respectively achieved for amplification of 10μs and 1μs pulses. However, these values actually represent a decrease when compared with the values of 0.05dB/cm for the 10μs pulse in the single pass amplification. This is a result of the increasing gain saturation with growing optical pulse energy in the 7-pass amplification. Fig. 7.11(a) also demonstrates the difference of the pulse energy gain for pulses of different widths. This pulse-width dependence was further investigated with measurements for varying pulse width in a wider range. Typical results are shown in Fig. 7.11(b), where the pulse energy gain appears to be rather substantial for short pulses of a few micro-seconds, and decreases considerably for longer pulse durations due to gain saturation through the pulse.

7.5 PULSE ENERGY / PEAK POWER AMPLIFICATION

Having presented the gain characteristics of the laser pulse amplification, it is straightforward to present the achievements of amplified pulse energy and peak power. Unless otherwise indicated, all experimental data presented in this section were obtained using 7-pass amplification at a pulse repetition rate of 1kHz and a peak RF power deposition of 109W/cm^3 for an optimum discharge duration.

7.5.1 Amplified Pulse Energy

The amplified pulse energy is pulse width dependent and has been measured as a function of the operating conditions. Dependence of the pulse energy on the gas pressure and RF power

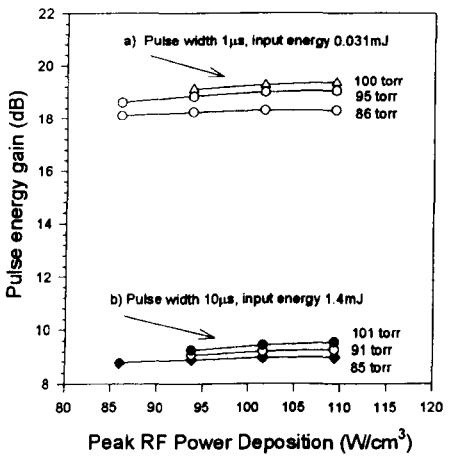

(a) Dependence of pulse energy gain on gas pressure and RF power deposition

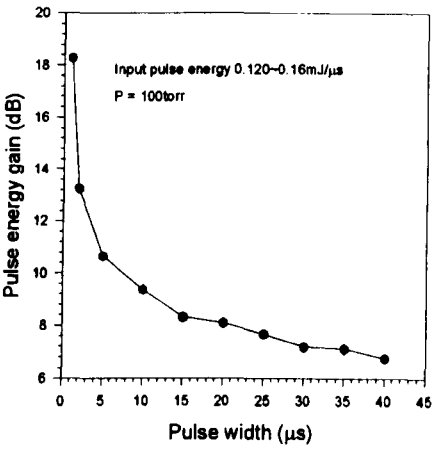

(b) Dependence of pulse energy gain on pulse width (with peak RF power deposition 109W/cm^3)

Figure 7.11 Pulse energy gain in 7-pass amplification (pulse repetition rate 1kHz; folded gain path 539cm; input pulse: square-shape (≥ 2μs), bell-shape (< 2μs); RF discharge duration 180μs)

deposition is similar to that of the pulse energy gain as already investigated, and is as shown in Fig. 7.12. The limited capability of the power supply for operation over 100torr in terms of discharge uniformity prevented the build-up of a complete picture of the pulse energy amplification as a function of operating conditions. The best results were obtained as 9.0 ± 0.5mJ for the 1μs amplification and 40 ~ 43mJ for 10μs amplification at a gas pressure of 100torr.

Under the same conditions measurements were made over a pulse duration range of 0.5-80μs, using near-square input pulses with pulse energies of 0.12-0.16mJ per μs. Results are shown in Fig. 7.13(a) as the solid line, while the dashed line was numerically obtained and will be discussed in section 7.7. It can be seen that the pulse energy rises with increasing pulse duration in a non-linear manner, approaching an upper limit. This appears to be consistent with pulse amplification theory which dictates that more energy can be extracted with longer pulses, while reaching a maximum energy extraction [7.12, 7.14]. It is anticipated that to achieve the maximum energy extraction, a very long input pulse must be used. Fig. 7.13(b) shows the total pulse energy gain/average power gain as a function of the pulse duration. It was ~ 210 for 1μs, and reduced to ~ 27 for 10μs and ~ 11 for 80μs.

Fig. 7.13(b) also shows the unit area pulse energy extraction where the total beam area was taken as 81% of the discharge area as calculated with the geometric method for the 7-pass configuration. Typically, the unit area pulse energy extraction was 1.87J/m^2 for a pulse duration of 80μs, 1.51J/m^2 for 40μs, 660mJ/m^2 for 10μs, and 160mJ/m^2 for 1μs.

The amplifier system has been operated at different pulse repetition rates to investigate further the laser pulse amplification characteristics. It was found that in terms of the pulse energy amplification, the optimum gas pressure increases with reduced pulse repetition rate requiring higher RF power deposition to maintain a uniform discharge. For example, the optimum operational gas pressure shifts from ~ 80torr to ~ 100torr when the pulse repetition rate varies from 10kHz down to 1kHz. The pulse energy amplification was also found to depend strongly on pulse repetition rates. In experiments with a constant input pulse energy of 0.45mJ and a fixed

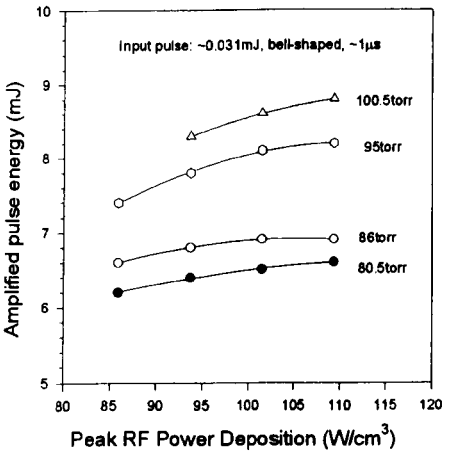

(a) 1μs pulse amplification

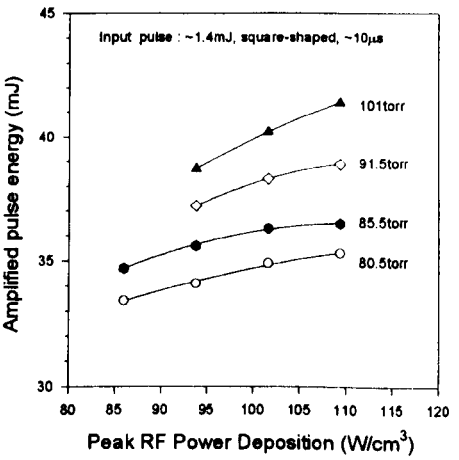

(b) 10μs pulse amplification

Figure 7.12 Amplified pulse energy output from 7-pass operation as a function of peak RF power deposition at different gas pressure (pulse repetition rate 1kHz; RF discharge duration 180μs)

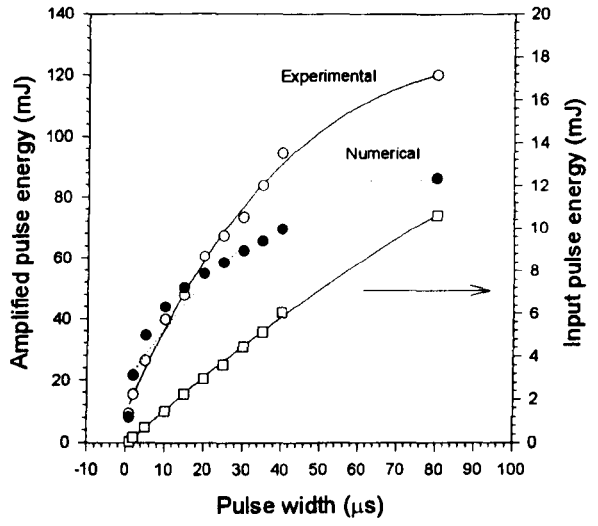

(a) Experimental (the solid line) and numerical (the dashed line) amplified pulse energy versus pulse width.

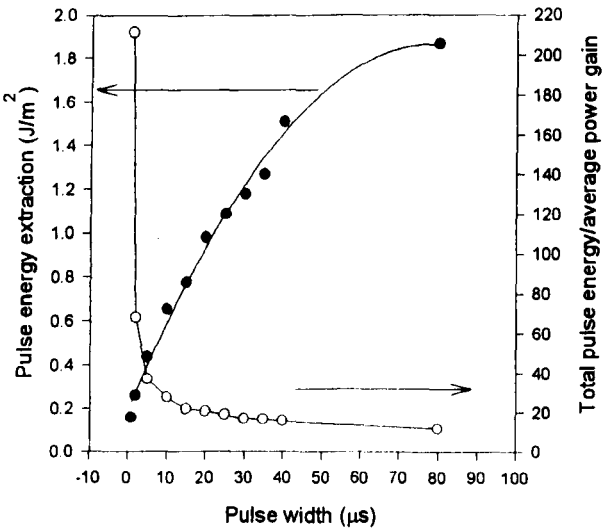

(b) Total pulse energy extraction and total pulse energy/average power gain

Figure 7.13 Pulse energy amplification with varying pulse width in the 7-pass configuration (pulse repetition rate 1kHz; gas pressure 100torr; peak RF power deposition 109W/cm^3 at a discharge duration of 180μs)

pulse duration of 10μs, the optimised amplified average power was observed to be a constant 32-35 watts for varying pulse repetition rates from 1 to 10kHz. The results are shown in Fig. 7.14. This indicates a significant drop in pulse energy with increased pulse repetition rate and is associated with discharge induced thermal effects.

7.5.2 Peak Power Output

The peak power of the amplified laser pulse can now be readily obtained by distributing the pulse energy evenly over the area defined by the corresponding temporal pulse profile. Three typical examples are included in Fig. 7.15 with both the input and output pulse shown in peak power format. It is seen that with a bell-shaped input pulse at a peak power < 100W at ~ 1μs duration (FWHM), a similar bell-shaped output pulse is achieved with the peak power reaching ~ 14kW. For square shaped input pulses of slightly higher intensity, the output pulses have a peak power of a few kW for the slope plateau, and around 12-14kW for the leading spike. The peak power at the trailing edge depended on the pulse width and was related to the gain saturation through the pulse. To smooth out the intense leading spike, triangular pulses instead of square pulses were used for the input. A peak power > 2.7kW was achieved for near-square output pulses, or > 3.5kW if the pulse profile was not required to be absolutely square. These are shown in Fig. 7.8, where the pulse duration was ~ 5-15μs.

7.6 BEAM QUALITY ASSESSMENT — SPATIAL BEAM PROFILES

Here the term beam quality is used to describe the spatial characteristics of the laser beam; it has been widely used for assessing the propagation and focusing performance of lasers. As previously stated in Chapter 5 and 6, for a planar waveguide amplifier, the beam quality in the transverse direction is determined by mode matching of the probe beam to the waveguide, plus discharge-induced effects upon the travelling beam. In the lateral direction, it is mainly determined by the nature of the probe beam and may be complicated by the effects of gain saturation especially in the presence of deep gain saturation.

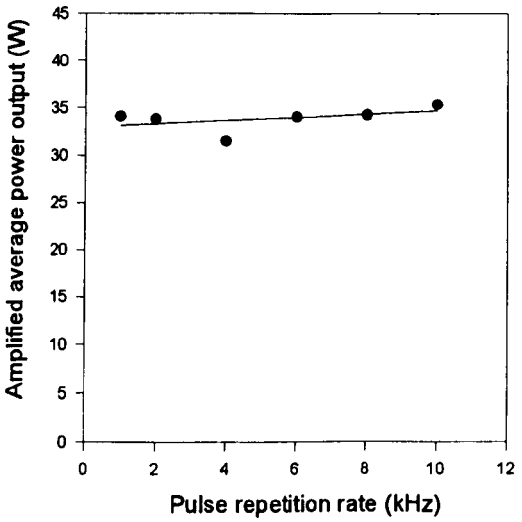

Figure 7.14 Amplified average power output as a function of pulse repetition rate with constant input pulse energy of 0.45mJ at pulse duration of 10μs under optimised gas pressure and RF power deposition.

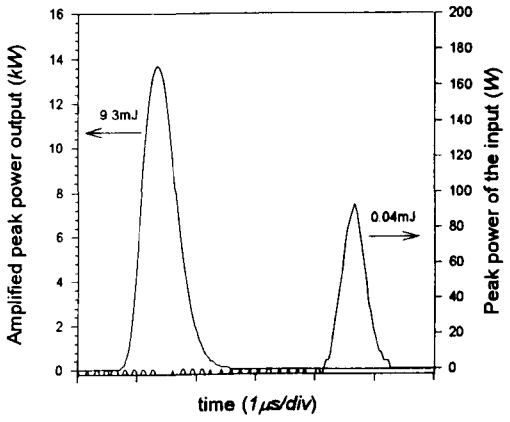

(a) Pulse width ~ 1μs

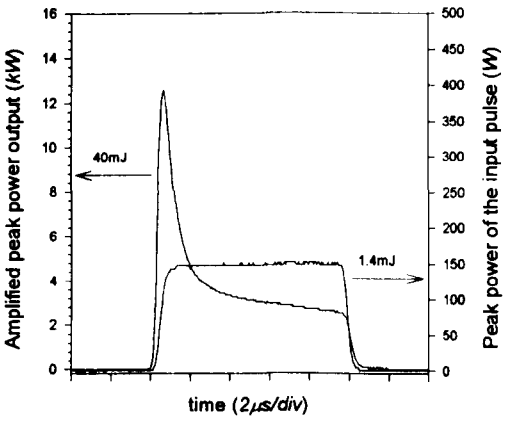

(b) Pulse width ~ 10μs

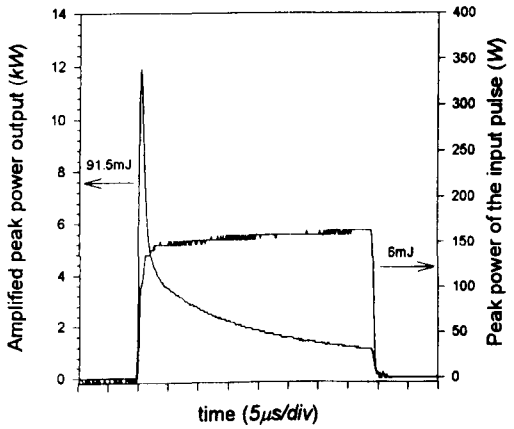

(c) Pulse width ~ 40μs

Figure 7.15 Peak output power of the amplifier in the 7-pass configuration with bell-shape and square-shape input pulses (operating conditions are the same as in Fig. 7.8)

As indicated in Chapter 4, the general procedure for the measurement of beam quality involves making a large number of spatial beam profile measurements along the beam path through a focal plane. When the measurement concerns short laser pulses, the process is not as straightforward as for a cw or long pulsed laser beam. The spatial patterns may be measured with a camera system that is synchronised with the short laser pulses. However, in our experiments, a rotating beam scanning system was used, as has been described in previous chapters. Because the duration of the laser pulses was of the order of μs, the probability is very small for the laser beam to be intercepted by the scanning mirror rotating at a frequency of 10Hz when not synchronised with the laser pulses. Thus, a very large number of scans were required to obtain a complete beam profile. The signal provided by the scanner was collected by a computer which used the software package Labview to sample the signal at a time interval equivalent to a spatial resolution of 0.2mm. For each point, the maximum was picked up as the final value of this point from a large number of scans. With this method, consistent beam profiles have been obtained with the number of scans being several thousands.

In the transverse direction the beam profile appeared to be single lobed, symmetric and very similar in the far-field to the numerically generated one of the fundamental mode of the planar waveguide. In the lateral direction, the beam profile was rather similar to that of the filtered input beam. It contained no side lobes as a conventional slab waveguide laser oscillator usually does, because there is no edge effect in an amplifier when the beam passes through the output aperture. The far-field profiles of the output beam in both the transverse and lateral direction are shown in Fig. 7.16.

7.7 MODELLING OF THE PULSE AMPLIFICATION PROCESS

In the experimental investigation presented above, the pulses have been in the μs regime and therefore there are molecular relaxation effects involved in the amplification process. In this section, a numerical analysis of the pulse amplification process will be given by extending the model developed by Schappert [7.18] to include rotational and vibrational relaxation effects. The

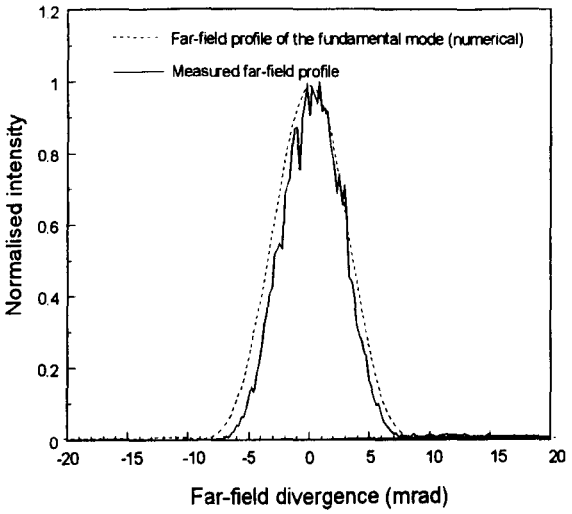

(a) In the transverse direction

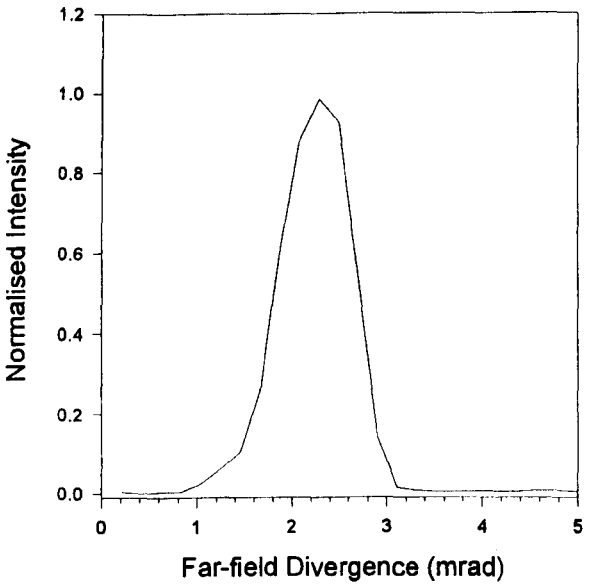

(b) In the lateral direction

Figure 7.16 Far-field beam profiles of the amplified laser pulse (pulse duration 10μs; pulse repetition rate 1kHz; output pulse energy ~ 40mJ)

effect of resonance energy transfer from N_2 (υ = 1-4) to CO_2 ($00^0 1$) will be considered separately in a qualitative manner to simplify the mathematical process.

Schappert's model considers plane-wave pulse amplification in a uniform CO_2 medium of length L travelling along the z axis. In this model, for P branch transitions, with j and $j+1$ corresponding to the upper and lower rotational levels respectively, it is assumed that $P(j) \cong P(j+1)$ in thermal equilibrium, where $P(j)$ defines the number of molecules distributed in the rotational level j in a vibrational state [7.16]. Here we further assume υ_1 and υ_2 as the lower and upper vibrational laser levels, $P(\upsilon)$ defining the number of molecules distributed in the vibrational level υ in thermal equilibrium. The following equations describe the situation:

$$\frac{\partial I(z,t)}{\partial t} + c\frac{\partial I(z,t)}{\partial z} = c\sigma I(z,t)\delta_j(z,t) \tag{7.5a}$$

$$\frac{\partial \delta_j(z,t)}{\partial t} = -\frac{2\sigma}{h\nu} I(z,t)\delta_j(z,t) - \frac{\delta_j(z,t) - P(j)\Delta(z,t)}{\tau_R} \tag{7.5b}$$

$$\frac{\partial \Delta(z,t)}{\partial t} = -\frac{2\sigma}{h\nu} I(z,t)\delta_j(z,t) - \frac{\Delta(z,t) - N(z,t)[P(\upsilon_2) - P(\upsilon_1)]}{\tau_\upsilon} \tag{7.5c}$$

$$\frac{\partial N(z,t)}{\partial t} = -\frac{\sigma}{h\nu} I(z,t)\delta_j(z,t) \tag{7.5d}$$

where $I(z,t)$ is the intensity of the radiation field, $\delta_j(z,t)$, the population inversion density between the two rotational laser levels, $\Delta(z,t)$, the population inversion density between the upper and lower vibrational levels and $N(z,t)$, the total number of excited molecules. In addition, c is the speed of light; h is Planck's constant; ν is the frequency of the incident optical signal and σ is the cross section for the stimulated emission between the upper and lower rotational laser levels. τ_R and τ_υ are the rotational and vibrational relaxation time constants respectively. Both constants are of the order of 10^6-10^7 S^{-1}-$Torr^{-1}$ [7.19, 7.20]. Eq. (7.5d) is based on the assumption that any CO_2 molecule arriving at the lower vibrational laser level from the upper vibrational laser level via stimulated transition will immediately return to the ground state, thus the production of *one* photon will result in the loss of *one* excited CO_2 molecule.

We assume that the rotational and vibrational levels are initially in thermal equilibrium. However, the presence of the stimulated emission induced by the input laser pulse will disturb the equilibrium situation. Consequently, the depletion of the population inversion between the upper and lower laser levels will give rise to energy exchange among all the rotational levels, and subsequently among all the vibrational levels, tending to restore the equilibrium condition. In the case of long laser pulse amplification in the μs regime, both the rotational and the vibrational relaxation processes [7.20] are "instantaneous" and cannot be resolved on the time scale of μs. Thus, it may be adequate to assume that the equilibrium of the rotational and vibrational levels are immediately restored after being disturbed. With this assumption, we have $\Delta(z,t) \approx N(z,t)[P(\upsilon_2) - P(\upsilon_1)]$ and $\delta_j(z,t) \approx P(j)[P(\upsilon_2) - P(\upsilon_1)]N(z,t)$. Therefore, Eqs. (7.5a) and (7.5d) can be re-written as

$$\frac{\partial I(z,t)}{\partial t} + c\frac{\partial I(z,t)}{\partial z} = c\sigma P(j) I(z,t)[P(\upsilon_2) - P(\upsilon_1)]N(z,t) \tag{7.6a}$$

$$\frac{\partial N(z,t)}{\partial t} = -\frac{\sigma P(j)}{h\upsilon} I(z,t)[P(\upsilon_2) - P(\upsilon_1)]N(z,t) \tag{7.6b}$$

Note that these two equations have the same forms as those in the two level model [7.14]. Thus, $I(z,t)$ and $N(z,t)$ as solutions of Eqs. (7.6a) and (7.6b), and other relevant parameters, will take the same forms as they are in the two-level model (see Chapter 2), with appropriate definitions as $G_0 = exp(\sigma P(j)[P(\upsilon_2)\text{-}P(\upsilon_1)]N_0 L)$ for the initial gain corresponding to the rising edge of the pulse, and $E_s = h\nu/\sigma P(j)[P(\upsilon_2)\text{-}P(\upsilon_1)]$ for the saturation energy, where N_0 denotes the initial number of all the excited CO_2 molecules. However, both G_0 and E_s now correspond to all the rotational and vibrational levels rather than only the upper and lower rotational laser levels.

Making use of Eq. (2.31), the experimental results of the time varying gain for short pulses and the input energy from the 7-pass amplification, the saturation energy E_s was calculated as 26-30mJ/cm^2 for pressures in the range of 80-100torr, where G_0 is assumed to be 80. With these two known parameters, the time varying gain may be calculated using Eq. (2.31). One example is shown in Fig. 7.8(d) (the dashed line). The two curves are only consistent in the first 3-4μs. This

is evidence of the effect of the resonance energy transfer from N_2 (υ= 1-4) to CO_2 (00^01) [7.12], because this effect is not included in the above modelling process. In addition, this time scale (3-4μs) is consistent with the time constant of $\kappa_e = 1.9 \times 10^4$ $Torr^{-1}$-sec^{-1} [7.12] for typical pressures used in the amplifier under investigation. This effect can also explain the occurrence of a turning in the output pulse profile at 3-4μs from the leading edge of the pulse (see Fig. 7.7).

A numerical analysis using the above model has been applied to the 7-pass amplifier. The amplified pulse energy as a function of pulse width has been calculated using the actual data in the experiments for the input, for parameters $G_0 \sim 80$, $E_s \sim 28 mJ/cm^2$ and $\alpha \sim 0.11\% cm^{-1}$, assuming a pulse repetition rate of 1kHz. The results are shown in Fig. 7.12 (the dashed line) for comparison with the experimental results (the solid line). It can be seen that the two sets of data are very close for pulse durations of $\tau_p < 20\mu s$, while the difference increases with pulse durations of $\tau_p > 20\mu s$. This is anticipated as the numerical model does not consider the effect associated with the N_2 energy reservoir, which is considerable for long pulses. Thus, for pulses of duration $\tau_p \sim$ 1-20μs, where the effect associated with the N_2 energy reservoir appears to be insignificant, the above numerical model is adequate in providing guidelines for the description of the amplification process and design of practical CO_2 laser amplifiers. With this numerical analysis, a broad view of the pulse amplification is given for the amplifier under investigation for varying input pulse energy at different pulse durations (1, 5, 10, 20μs). The numerical results of the output pulse energy and pulse energy extraction efficiency (see Eq. (2.36)) are shown in Fig. 7.17 for typical parameters, assuming square input pulses and a pulse repetition rate of 1kHz. Fig. 7.17(a) shows that the output pulse energy at fixed pulse duration increases monotonically with the input energy, but tends to approach a limit as a direct result of increased gain saturation with increasing input signal. Fig. 7.17(b) indicates that the pulse energy extraction efficiency may be improved by either increasing the pulse energy level or using longer pulses. To extract ~ 80% of the maximum energy available associated with the rotational and vibrational levels of the CO_2 molecules, an input energy of only ~ 2mJ (equivalent to a peak power of ~ 100W) is required if the pulse duration is 20μs. However, to achieve the same energy extraction efficiency, the peak power of the input pulse must be at least double if the pulse duration reduces to 10μs.

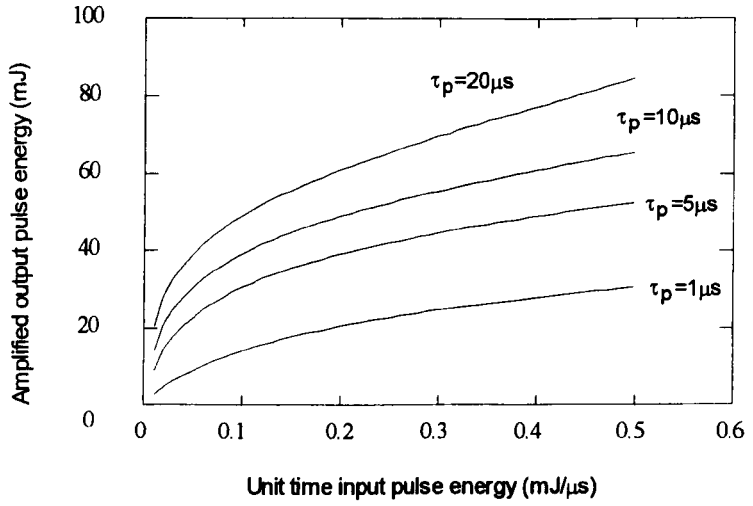

(a) Output pulse energy

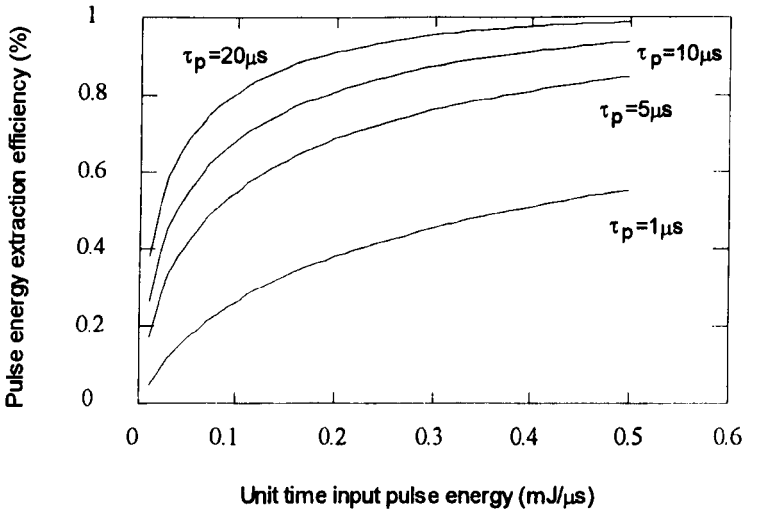

(b) Pulse energy extraction efficiency

Figure 7.17 Numerical results for the amplifier under investigation as a function of input pulse energy at different pulse durations (τ_p ~ 1-20μs), assuming square input pulses, excluding the effect associated with the N_2 energy reservoir. (Waveguide dimensions of the amplifier 770mm × 95mm × 1.75mm; 7-pass configuration with lateral beam spot sizes of 3.4mm (input) and 11.2mm (output) ; initial gain coefficient γ_0 ~ 0.92%cm^{-1}, loss coefficient α ~ 0.11%cm^{-1}; gain path L ~ 539cm; saturation energy E_s ~ 28mJ·cm^{-2}; PRF = 1kHz)

Nevertheless, for pulse amplification at 1μs, pulse energy extraction of > 60% is very difficult to achieve.

The above numerical process has also been applied to a planar waveguide amplifier of similar structure but a larger electrode area of 1.25m × 0.2m, using the same amplification parameters determined from the experiments, to scale up the pulse energy (peak power), as shown in Fig. 7.18. This larger waveguide may be configured to incorporate a folded beam of 11 passes, with slight overlapping of the adjacent beams on the resonator mirrors. The beam spot size at the output aperture is calculated to be 27.8mm, where the input beam is considered as the same as that used in the experiments described in this chapter.

As seen in Fig. 7.18, considerable increases in pulse energy have been produced with a 3.4 times increase in area. It is noted that the pulse energy increases are inversely proportional to pulse duration. This reflects the occurrence of very strong gain saturation through the pulse, where a significant part of the pulse near its end experiences little amplification and the increase of the pulse duration has little effect on the overall pulse energy amplification. Moreover, the pulse energy output is only found to be dependent strongly on the input pulse energy when the input signal level is low (< 0.1mJ/μs). This is again related to gain saturation effects. Because of the long gain path, irrespective of the input signal level, very strong gain saturation will occur. Therefore, with a moderate input signal, the characteristics in the output end will not be sensitive to the signal variation at the input. This may suggest the possibility of using a not-so-powerful laser oscillator, allowing flexibility for the system build-up and reducing the thermal effects induced by high laser power associated with AO modulation.

It is not too difficult to obtain a pulse energy output of 200mJ for pulse durations of 1μs, equivalent to a peak power level of over 200kW, with a peak input signal level of ~ 40W. In addition, a pulse energy of ~ 400mJ may be achieved with an input signal of ~ 8mJ at a pulse duration of 20μs. The pulse energy extraction efficiency has also been significantly increased. At an input peak power level of ~ 150W as used in the experiments, pulse energy extraction efficiency can be ~ 70% for pulses of 1μs duration, or over 90% for pulses of 20μs duration. The

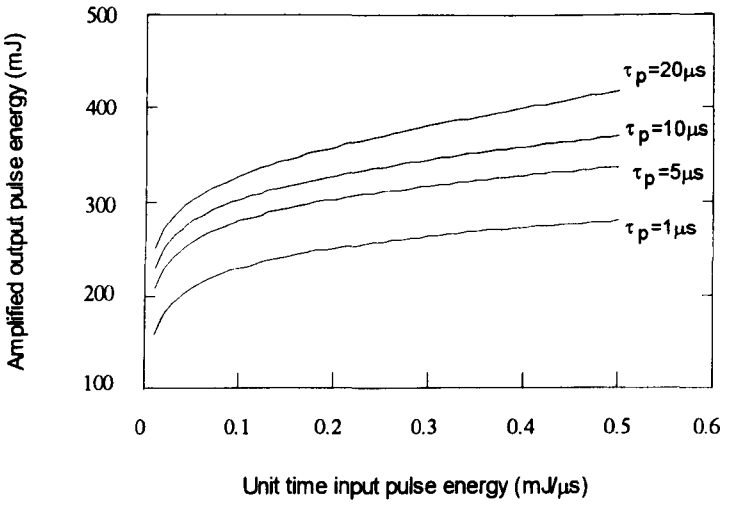

(a) Output pulse energy

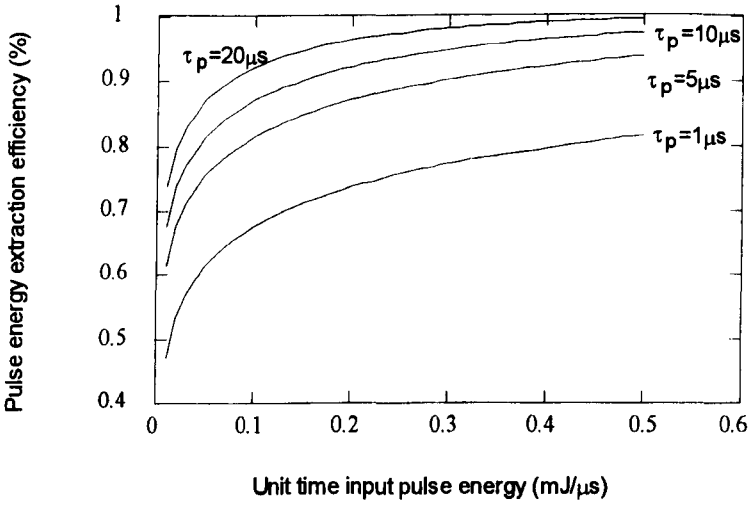

(b) Pulse energy extraction efficiency

Figure 7.18 Numerical results of the performance of an area-increased amplifier for varying input pulse energy and pulse durations (τ_p ~ 1-20μs), supposing square input pulse, excluding the effect associated with the N_2 energy reservoir. (Conditions: waveguide dimensions of the amplifier 1.25mm × 200mm × 1.75mm; 11-pass configuration with lateral beam spot sizes of 3.4mm for the input and 27.8mm for the output; initial gain coefficient $\gamma_0 \sim 0.92\%cm^{-1}$; loss coefficient $\alpha \sim 0.11\%cm^{-1}$; gain path L = 13.75m; saturation energy $E_s \sim 28$ mJ·cm^{-2}; PRF = 1kHz)

value of the pulse energy extraction efficiency indicates the degree that the final gain G_f approaches unity. Thus, high pulse energy extraction efficiency implies deep gain saturation occurring along the pulse. This, in turn, suggests strong pulse narrowing effects. In this sense, laser pulse amplification is an effective approach for power enhancement of short laser pulses.

7.8 SUMMARY AND CONCLUSION

In this chapter, CO_2 laser pulse amplification with a planar waveguide structure in the MOPA format has been studied, particularly for the pulse duration in the range of 1-20μs. Experimental investigations have been carried out on the gain characteristics (time varying gain and pulse energy gain), pulse shape distortion and manipulation, pulse energy and peak power amplification. With both the time-varying gain and pulse energy gain approach, the small signal gain coefficient (unsaturated gain coefficient) has been experimentally determined as $1.7 \pm 0.2\%cm^{-1}$, with the amplifier operated at a pulse repetition rate of 1kHz and a gas pressure of 80-90torr in the single pass configuration. A total pulse energy gain of ~ 210 has been achieved for pulses of $\tau_p \sim 1\mu s$, and ~ 27 for pulses of $\tau_p \sim 10\mu s$.

An acousto-optic modulator has been used as a pulse slicer to generate short laser pulses at the input to the amplifier. With near-square input pulses, the amplifier produces tail-free output laser pulses, but normally with leading edge spikes as a result of non-linear gain saturation effects. However, these leading spikes can be smoothed out by modifying the input pulse profiles. With the 7-pass amplifier operated at a pulse repetition rate of 1kHz, peak powers of ~ 14kW have been achieved at a pulse duration of 1μs with a bell-shaped temporal profile. In addition, near-square laser pulses have also been achieved at the output, with typical peak powers of 3-4kW for a pulse duration of ~ 5-15μs.

By extending the model developed by Schappert [7.18] to include both the rotational and vibrational relaxation effects, a numerical analysis has been made, which is reasonably consistent with the experimental results for pulse duration in the range of 1-20μs, thus giving useful guidelines for a description of micro-second pulse amplification and design of practical pulsed

CO_2 laser amplifiers. Saturation energy has been determined as 26-30mJ/cm^2 for a pulse repetition rate of 1kHz, including all vibrational and rotational levels, but excluding the effects of the resonance energy transfer between excited N_2 and CO_2 (00^01). In addition, a numerical analysis has been applied for an increased waveguide area.

In conclusion, the MOPA approach has been successfully applied in a planar waveguide structure for the power enhancement of short CO_2 laser pulses. Peak power output of 3-14kW has been achieved with good spatial beam characteristics for pulse durations in the range of 1-20μs. The temporal pulse profiles can be manipulated to suit a wide variety of applications. The availability of very high peak power pulsed laser systems will clearly enhance the capability of CO_2 lasers in material processing and related applications.

REFERENCES

7.1 A. I. Dutov, A. A. Kuleshev, N. A. Novoselov, V. N. Sokolov, "*Slab waveguide RF-excited CO_2 laser for material processing*," *Proc. SPIE*, **2713**, pp.51-57, 1995

7.2 I. A. Watson, C. R. Chatwin, D. Mcdonald, B. F. Scott, H. A. Abdullah, "*Enhanced Aluminium Processing with a High Frequency, Pulsed CO_2 Laser*," *ICALEO (1995)*, pp.294-301

7.3 D. Wheatley, "*A High Power, High Modulation Bandwidth CO_2 Laser*," *SPIE Procee.*, Vol. **3092**, pp.109-113, GCL'96 Edinburgh

7.4 R. Adler, "*Interaction between light and sound*," *IEEE Spectrum*, **4**(5), pp.42-54 (1967)

7.5 T. C. Poon, M. D. McNeill, D. J. Moore, "*Modern optical signal processing experiments demonstrating intensity and pulse width modulation using an acousto-optic modulator*," *Am. J. Phys.* **65**(9), September 1997

7.6 W. R. Klein, B. D. Cook, "*Unified approaches to ultrasonic diffraction*," *IEEE Trans. Sonics Ultrason.* **SU-14**, 123 (1967)

7.7 M. A. Dugan, J. X. Tull and W. S. Warren, "*High-resolution acousto-optic shaping of unamplified and amplified femtosecond laser pulses*," *J. Opt. Soc. Am. B*, **14**, No.9, pp.2348-2358, September 1997

7.8 "*Acousto-Optic Products Catalog*," Neos Technologies, Inc., USA, 1999

7.9 L. W. Casperson, L. M. Davis, and J. Harvey, "*Thermal hystersis in acoustic resonators*," *J. Acoust. Soc. Am.* **71**(6), pp.1412-1416, June 1982

7.10 T. Honda, H. Matsumoto, "*Aberration correction of acousto-optically modulated laser beams by phase conjugation*," *Opt. Letters*, **15**, No. 6, pp308-309, March 15, 1990

7.11 D. Pantzer, J. Politch, L. Ek, "*Technical note*," *Optics and Laser Technology*, pp.102-103, April 1985

7.12 P. K. Cheo, "*CO_2 Lasers*," *Chapter 2, Lasers*, edited by Levine and Demaria, 1971, Marcel Dekker, Inc., New York

7.13 T. J. Bridges, H. A. Haus, and P. W. Hoff, *IEEE J. Quant. Electron.*, **4**, 777(1968)

7.14 L. M. Frantz, J. S. Nodvik, "*Theory of pulse propagation in a laser amplifier*," *J. Appl. Phys.*, **34**, pp.2346-2349, 1963

7.15 A. Siegman, "*Lasers*," Chapter 9 and 10. University science books, California, 1986

7.16 W. J. Witteman, "*The CO_2 Laser*, " Springer-Verlag, New York, 1987

7.17 F. A. Hopf, C. K. Rhodes, "*Influence of Vibrational, Rotational, and Reorientational Relaxation on Pulse Amplification in Molecular Amplifiers*," *Phys. Rev.* **A8**, pp.912-929, August 1973

7.18 G. T. Schappert, "*Rotational relaxation effects in short-pulse CO_2 amplifiers*," *Appl. Phys. Lett.*, **23**, No.6, 15 September 1973, pp.319-321

7.19 R. R. Jacobs, K. J. Pettipiece, and S. J. Thomas, "*Rotational relaxation rate constants for CO_2*," *Appl. Phys. Lett.*, **24**, No.8, 15 April 1974, pp.375-377

7.20 I. Burak, Y. Noter, and A. Szoke, "*Vibration-Vibration Energy Transfer in the v_3 Mode of CO_2*," *J. Quant. Electronics*, **QE-9**, No.5, May 1973, pp.541-544

CHAPTER EIGHT

PARASITIC OSCILLATION

8.1 INTRODUCTION

As mentioned in earlier chapters, parasitic oscillations (spontaneous laser oscillation, or spontaneous self-oscillation or parasitic self-lasing) were observed during the multipass operations of the amplifier. However, this is not an unexpected occurrence for high net gain amplifiers, where parasitic oscillation has long been realised [8.1-8.2] to be an inherent and potentially serious problem. Parasitic oscillation may be induced by light reflection or scattering of the main signal from surfaces of optical components or other elements, however, in most cases it results from so-called amplified spontaneous emission (ASE), which can build-up power considerably in the presence of high net gain even in the absence of an incident signal to the amplifier.

ASE is a process that produces a broadband spectrum which matches the gain profile of the amplifier. It extracts energy from the active gain medium, producing undesired optical power, which is superimposed incoherently on the amplified signal. Although the existence of ASE enables us in some cases to generate intense radiation without an optical cavity [8.3], the effects of ASE are usually negative: it is the source of the noise that is added to the signal propagating through the amplifier, causing degradation of SNR (the signal to noise ratio), intensity fluctuation of the amplifier output, nonlinearity of the gain saturation and so on [8.4-8.5]. In cases where very serious parasitic oscillations are present, significant power output may be produced, ruining the whole performance of the amplifier.

Over the past forty years, theoretical and extensive experimental studies have been carried out on the nature of the ASE-induced noise added to the signal [8.6-8.8]. Particular attention has been paid to the spectral density and profile of the noise in laser amplifiers in telecommunication systems and laser radar for homodyne, heterodyne and direct detection [8.9-8.12], aimed at

improving the signal-to-noise ratio. To cope with ASE induced noise and parasitic oscillation, a number of potential solutions have been investigated in the literature. Dezenberg et al [8.2] used a mask placed in front of the segmented mirrors to prevent self-oscillation in a multipass amplifier. Schawlow and Townes [8.13], Geusic and Scovil [8.14] suggested the use of aperture stops to eliminate excess noise. Shepherd and Vaughan [8.15] introduced the so-called noise cancellation technique, which had been well-established in acoustic [8.16] and electronic signal processing [8.17], into the optical amplifier area. In their experiments, the noise that originated from beating between the lasing mode and the light emitted into the two adjacent sub-threshold modes [8.18], one on each side, was significantly reduced, when one of the sidebands was eliminated by optical filtering, demonstrating cancellation of strongly anticorrelated noise sidebands.

However, for power amplifiers designated for use in the material processing arena, apart from the power and the spectral features of the parasitic oscillation, what is equally important is how it will affect the beam quality, the near-field and far-field feature of the amplifier output beam. There appear to be few theoretical or experimental investigations on this subject that are reported in the literature. One issue has to be addressed here is the optical feedback to the master laser oscillator, which may be rather strong when parasitic oscillations are present and which may cause instabilities to the output of the master oscillator. In turn, these instabilities may result in fluctuation of the output of the amplifier. A typical approach to the circumvention of this problem is the insertion of one or more optical isolators [8.19] between the master oscillator and the amplifier. The most common techniques for optical isolation either make use of the polarisation features of the laser beams [8.20] or depend on the Faraday effect [8.21]. However, isolations have not been investigated in the work presented here.

In this chapter an investigation of the nature of the parasitic oscillation induced by ASE in multifold planar waveguide amplifiers is described. The main emphasis is on the dependence of the parasitic power output on the operational conditions (pressure and RF power deposition) and the interaction between the parasitic oscillation and the main signal travelling in (and exiting

from) the amplifier. It is aimed at seeking possible solutions to reduce or eliminate the parasitic oscillation, which represents a problem commonly encountered in high gain amplifiers.

8.2 BACKGROUND THEORY

In this section, a theory that addresses the characteristics of the noise induced by ASE in a laser amplifier is reviewed, along with factors that may affect the magnitude of the noise, and the power produced by parasitic oscillation.

8.2.1 Calculation of Noise Power Induced by ASE

Kogelnik and Yariv [8.6] used a simple amplifier model to derive the magnitude of the noise power induced by spontaneous emission. As shown in Fig. 8.1, the amplifier has a length of L, with the active gain medium with an inversion density (n_2-n_1) uniformly distributed between the planes $z = 0$ and $z = L$. An absorbing screen is placed at the output plane with an aperture in the centre to provide a passage for the signal. The aperture is assumed to be circular in cross section for convenience in mathematical derivation, although this is not physically necessary. The gain of the light at frequency ν passing through the gain medium at an angle θ with respect to the optic axis z can be expressed as:

$$G(\theta, z) = e^{\gamma_0(\nu) z / \cos(\theta)} \tag{8.1}$$

where $\gamma_0(\nu)$ is the small signal gain coefficient and has been described in Chapter 2 by Eq. (2.6), in which we may replace A_{21} with $1/t_{spont}$, where A_{21} is the spontaneous emission Einstein coefficient and t_{spont} is the spontaneous emission lifetime for transition from level 2 to level 1.

Considering a volume element dV of a medium with a density n_2 of excited states, and assuming that the propagation of noise can be described in terms of geometrical optics, then the amount of noise power at frequencies between ν and $\nu + d\nu$ radiated into a solid angle $d\Omega$ can be obtained as:

$$dN(\nu) = h\nu \frac{n_2 g(\nu)}{t_{spont}} \frac{d\Omega}{4\pi} d\nu dV \tag{8.2}$$

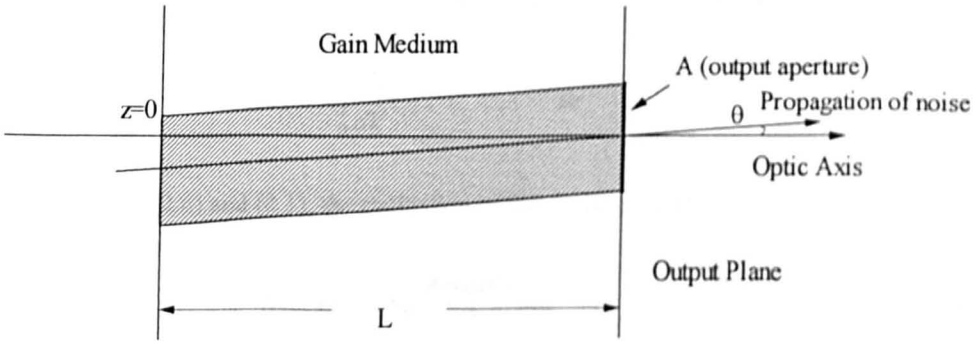

Figure 8.1 Amplifier model for ASE induced noise radiation characterisation

where h is Plank's constant. Noise emitted at z and propagating at an angle θ with respect to the z axis is amplified by a factor $exp[\gamma_0(\nu)(L-z)/cos(\theta)]$ (supposing that the noise is not intense enough to induce significant gain saturation) until it reaches the output aperture or is intercepted by the screen. For a given θ and a polar angle φ, only noise originated from within the shaded cylinder shown in Fig. 8.1 can escape through the output aperture into the differential element $d\Omega$ of solid angle. Thus, the noise power $N(\theta)$ contributed by all volume elements within the cylinder and radiated through the output aperture A at an angle θ into $d\Omega$ can be obtained as:

$$N(\theta,\nu) = A\int_0^L \frac{dN}{dV} e^{\gamma_0(\nu)(L-z)/\cos(\theta)} dz \tag{8.3}$$

Making use of Eqs. (2.6) and (8.1), the evaluation of this integral yields:

$$N(\theta,\nu) = 2N_0 \frac{A\cos(\theta)}{\lambda^2} d\Omega \tag{8.4}$$

here λ is the wavelength and N_0 is defined as

$$N_0 = h\nu d\nu \frac{n_2}{n_2 - n_1(g_2/g_1)}[G(\theta) - 1] \tag{8.5}$$

which is usually called the amount of "noise per mode" representing the amount of noise radiated into a solid angle that can be associated with a single black-body mode. Integrating over all solid angles, the total amount of noise escaping through the output aperture is obtained as:

$$N_{tot} = 2N_0 \frac{\pi A}{\lambda^2} \tag{8.6}$$

8.2.2 Noise Power Including Optical Losses

It is obvious that optical losses associated with the transmission of a signal through an amplifier will also affect the magnitude of the noise as it propagates along the amplifier. Thus, optical losses have to be taken account of to provide a realistic description of the noise or parasitic oscillation in actual amplifiers. Let us assume that the attenuation caused by optical losses is evenly and continuously distributed along the path of the noise and define α as the attenuation

coefficient, $\alpha_t = exp(-\alpha L)$ as the net transmission. Then, if only the case of $\theta \quad 0$ is considered, combining Eq. (8.2) with Eq. (8.3) gives the noise radiated through the output aperture of area A into the solid angle $d\Omega$ as:

$$N(\nu) = 2\frac{\gamma_0(\nu)}{\gamma_0(\nu) - \alpha}[\alpha_t G(\nu) - 1]\frac{A}{\lambda^2} P d\Omega \tag{8.7}$$

here P is the so-called *population inversion quality parameter* (sometimes known as the *excess noise parameter*) and is defined as:

$$P = \frac{n_2}{n_2 - n_1(g_2 / g_1)} \tag{8.8}$$

Eq. (8.7) relates the amount of the noise or ASE with the optical loss (or transmission), the gain of the medium and the population inversion (represented by P). This relationship indicates that the amount of the noise or ASE (and the parasitic oscillation that may be induced) depends on the optical and mechanical structure of the amplifier and operating conditions. One critical point to be drawn from Eq. (8.7) is that the amplification of spontaneous emission (ASE) may occur only when $\alpha_t G(\nu) \geq 1$, confining the expected result that ASE occurs when the net gain reaches 1. This condition also applies to parasitic oscillation induced by ASE.

Generally, the noise and the signal travel together so they suffer similar losses. If this is not the case, e.g. the noise or ASE propagates independently of the main beam, it is possible to increase the loss just for the travelling noise or ASE without affecting the transmission of the main signal, thereby reducing considerably the noise level and possibly preventing ASE induced parasitic oscillation from occurring at all. This has in practice been very important and served as a starting point for our investigations of solutions to parasitic oscillation problems.

8.3 EXPERIMENTAL INVESTIGATION

8.3.1 Parasitic Oscillation Measurements

The parasitic oscillation measurements were made in two stages. The first stage investigated the characteristics of the parasitic oscillation with no incident optical signal to the amplifier. The

second stage was carried out when the whole system was in full operation, to see the interaction between the main signal and the parasitic oscillation induced optical power.

The experimental set-up was the same as that for the single or multipass amplification, as described in Chapter 6 and 7. No optical isolators were inserted between the master oscillator and the power amplifier. Two AR/AR coated ZnSe windows were used for the input and output apertures, and both were initially mounted vertically and therefore perpendicular to the planar waveguide. The amplifier was initially operated in cw mode at an RF generator frequency of 125MHz with ceramic side walls to define the 1.75mm waveguide gap. Subsequently it was modified to operate at 81MHz either in cw or pulsed mode, with the ceramic side walls removed All data presented here were obtained by using a gas mixture of 57% He, 19% CO_2, 19% N_2 plus 5% Xe.

8.3.2 Parasitic Oscillation in the Waveguide Amplifier with Ceramic Side Walls

With no input signal to the amplifier and with the amplifier having ceramic side walls in place, significant parasitic oscillations were observed in the multipass configurations, though no power output was observed in the single pass configuration. The output power produced by the parasitic oscillation process was found to increase as the fold mirrors were adjusted to provide larger number of folding passes, as the direct result of increased net gain. The output power measured at the exit end of the amplifier as a function of the gas pressure is shown in Fig. 8.2, where the amplifier was operated with the RF discharge in cw mode.

The maximum observed parasitic oscillation power reached 95W in the 5-pass configuration, and 150W in the 7-pass configuration. The parasitic power was found to decrease dramatically as the pressure increasing towards ~ 55torr for the 5-pass case, (and ~ 66torr for the 7-pass case) and eventually quenched at higher pressures. This can be explained as the consequence of the drop in amplifier gain associated with operation of the amplifier at increased pressures. This is clear evidence for the inescapable fact that there is a tendency to produce spontaneous parasitic oscillation as a consequence of the existence of high net gain in the amplifier.

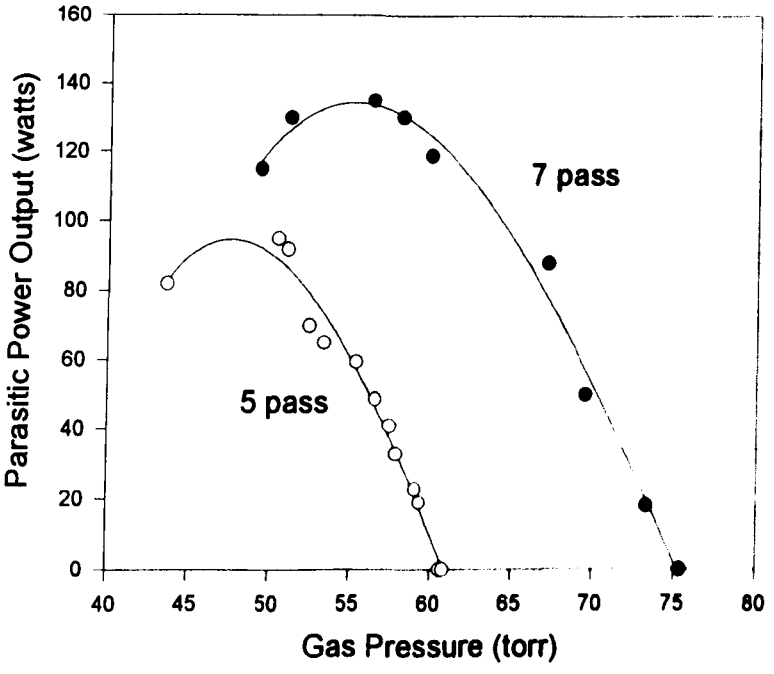

Figure 8.2 Output power in the form of parasitic oscillation with parallel input and output windows in a multipass amplifier using a 1.75mm waveguide with ceramic side walls (cw RF discharge @ 125MHz).

Further investigations revealed that parasitic oscillation gave rise to power output from both ends of the amplifier simultaneously (see Fig. 8.3). The power measured in the input end was smaller than that in the output end, which was probably mostly due to the use of a smaller aperture. At the intended output end, the beam was observed to travel with an angle of ~ 9mrad with respect to the main beam axis, and was found to be convergent in association with the concave resonator mirror in the input end. At the input end, the out-bound beam was found to travel with an angle of ~ 33mrad relative to the input main beam axis, and appeared to be divergent in association with the convex resonator mirror in the output end. If one traces along the beam produced by parasitic oscillation back into the amplifier, one can easily see clear evidence that the path for parasitic oscillation involves reflections from both the ceramic side walls and the folding mirrors. In addition, the two input and output ZnSe windows might also be partially responsible for the optical feedback due to more or less reflections from their inner surfaces. As they were both perpendicular to the propagation direction, the reflected power could be easily coupled back into the waveguide amplifier.

The spatial intensity profiles of the beams which comprised the parasitic oscillation radiation emissions were also investigated. The beam in the transverse direction was found to show clear evidence of waveguiding. This might be anticipated since in the transverse direction, when well-aligned, the amplifier is very similar to a laser oscillator, therefore the (parasitic) oscillation is contained in lowest order waveguide modes. In addition, in the multipass configuration, the folding mirrors were tilted horizontally thus they were somewhat further away from the waveguide ends compared to in an oscillator, increasing coupling loss to the waveguide for higher order modes. In the lateral direction, the beam profile was more arbitrary. As can be seen from Fig. 6.9(b), when the source laser was off and the amplifier was on, the parasitic oscillation gave rise to output power which exited from the entire aperture at the output with a multi-peaked profile.

The experiments then proceeded to the second stage, i.e. the study on the interaction between the main beam and the parasitic oscillation. The measurements were made with both the source laser and the amplifier turned on. In the transverse direction, little impact on the distribution of the

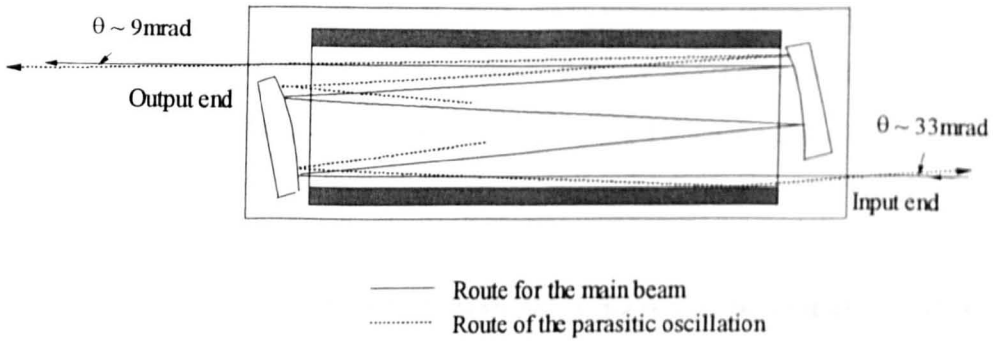

Figure 8.3 Experimentally observed directionality of the parasitic oscillation-induced optical beams

main beam was observed due to the facts discussed in the previous paragraph. However, from the standpoint of the lateral beam, the near-arbitrary shaped parasitic oscillation profile did not produce severe impacts on the main laser beam, as shown in Fig. 6.9(b). Once the source laser was on, the quite significant parasitic oscillation was largely, though not entirely, suppressed, leaving only superimposed noise on the contour of the main beam. This may be explained as the direct consequence of the considerably stronger stimulated emission induced by the probe laser beam, when compared to the spontaneous emission which induces the parasitic oscillation. The fact that the parasitic oscillation is not entirely extinguished may be associated with the existence of some areas that are not part of the passage for the main laser beam but are part of the path for the parasitic oscillation.

8.4 APPROACHES TOWARDS SOLUTIONS FOR PARASITIC OSCILLATION

8.4.1 Basic Consideration

In this work, two approaches have been considered to find solutions for ASE induced parasitic oscillations. The first aims to create extra loss and therefore to reduce the optical feedback for the parasitic oscillation without affecting the main MOPA beam. This is possible, since the optical signal resulting from parasitic oscillation propagates along a different path from the main beam as investigated in the last section. The second approach is to reduce the amplifier gain just sufficiently for the parasitic oscillation to be significantly reduced or eliminated while the extent of the reduction of the amplification of the main signal is at an acceptable level. The main emphasis was on the first approach, because clearly the latter approach works at the expense of the desired amplified laser power, and thus is not preferred.

The principal losses relevant to parasitic oscillation mainly include the following:

a) The waveguiding loss, assuming a loss coefficient α_l. This loss should be similar for the main beam and the beam induced by parasitic oscillation, if they have a similar waveguide mode mixture.

b) The truncation or coupling loss for the parasitic beam entering the waveguide from its two ends. This loss should be higher than that for the main beam which is carefully designed to match the waveguide. We define a parameter T_{trun} to describe this loss as $1-T_{trun}$ for each time the parasitic beam enters the waveguide.

c) The loss on the two resonator mirror surfaces which should be the similar to that for the main beam for each bounce. Here we assume R as the reflectivity for both mirrors.

d) The loss due to reflection on the ceramic side walls. We assume R_{cer} as the reflectivity for the ceramic surfaces.

e) The loss due to reflection at the internal surface of the amplifier aluminium outer-envelope. Similarly, we assume R_{alu} as the reflectivity of the aluminium surfaces.

We further assume m as the times that the parasitic beam enters the waveguide, n as the number of times that the parasitic beam bounces from the resonator mirrors, and j_{cer} and j_{alu} as the number of times that the parasitic beam hits the ceramic side walls and the internal aluminium surface of the amplifier outer-envelope respectively. Then the one trip net gain (corresponding to $\alpha_t G(\nu)$ in Eq. (8.7)) that the parasitic beam experiences can be expressed in terms of all major relevant factors as:

$$G_{ps,net} = \left[\exp(\gamma_0 Z)\times\exp(-\alpha_1 Z)\right]\times(T_{trun})^m \times R^n \times (R_{cer})^{j_{cer}} \times (R_{alu})^{j_{alu}} \qquad (8.9)$$

where γ_0 is the small signal gain coefficient and Z is the total length of the parasitic beam passing through (not necessarily following the main signal) the gain medium. The dependence of the reflectivity on the incident angle to any of the surfaces mentioned above is ignored for simplicity. Each term in Eq. (8.9) may direct to a potential approach for suppressing or eliminating parasitic oscillations, by either reducing the gain $\exp(\gamma_0 Z)$ or increasing any of the losses. However, in most practical cases it is not preferred to reduce the gain at the expense of the amplification efficiency of the main signal. Several approaches were considered and experimentally implemented in the research, as described below.

8.4.2 Experimental Implementation

a) Operating the amplifier at high pressure

It has been observed that the parasitic oscillation quenches above a certain pressure, due to the decrease of the gain in high pressure region. This indicates a solution by simply operating the amplifier at high pressures. However, this is only practical at high power operation, where the gain coefficient at low pressures decreases significantly due to gain saturation, while it is less affected in the high pressure region because of the higher saturation intensity. In contrast, operations in the relatively lower pressure region are preferred for low power level amplification, to make use of higher gain (see Chapter 6).

b) Using vertically tilted input and output windows

It is evident that the occurrence of parasitic oscillations involves optical feedback created by reflections from surfaces of optical or mechanical components. As mentioned above (see section 8.3.2), there exist several possible mechanisms whereby optical feedback may be produced. One such route to providing unwanted feedback is the possibility of reflections from the two nominally-parallel ZnSe windows. They were vertically mounted and were in close proximity and nominally perpendicular to the planar waveguide, so that any reflection could easily re-enter the waveguide. Tilting the windows would increase the truncation loss for any reflected parasitic beams when entering the waveguide. However, it was observed that when the two windows were tilted from the notional vertical plane by 5 degrees the output power due to parasitic oscillation at output end was reduced only by ~ 20%.

c) Removing the ceramic side walls

With the presence of the ceramic side walls the parasitic beam is hardly able to escape from either side of the waveguide. Thus, the loss part $(R_{alu})^{j_{alu}}$ in Eq. (8.9) corresponding to reflection from the aluminium surfaces is negligible, and the reflection $(R_{cer})^{j_{cer}}$ from the ceramic side walls is the main contribution to the optical feedback for the parasitic oscillation. To reduce optical reflection from the ceramic side walls, two possible approaches were considered. The first was to

roughen the inner ceramic surfaces so as to reduce the reflectivity. The second approach was to remove the ceramic side walls from the waveguide. However, since the first approach was only a partial solution, it was decided to proceed with the complete solution, by modifying the electrode mounting system to permit complete removal of the ceramic side walls.

Now without ceramic side walls, the parasitic optical light will exit from the edges of the waveguide into free space where they expand rapidly in the vertical direction. Upon reaching the internal walls of the aluminium outer envelope that contains the amplifier, such beams may be reflected, however, back to the waveguide, with some loss at the non-optical finished surface. Before re-entering the waveguide, these beams will suffer considerable coupling loss at the waveguide entrance, due to vertical expansion, resulting in significantly increased truncation loss for the parasitic oscillation. It is important to note that the loss for the main beam remains unaffected. In Eq. (8.9) the term $(R_{cer})^{jcer}$ should now be cancelled, and replaced by another term $(T'_{trun})^{m'}$, which represents the truncation or coupling loss for the parasitic beam entering the waveguide from either of its two sides. Due to the expansion of the parasitic beam, the value of T'_{trun} will be much smaller than that of T_{trun}. Besides, the loss part $(R_{alu})^{jalu}$ in Eq. (8.9) corresponding to reflection from the aluminium surfaces is no longer negligible. Note that $j_{alu} \approx j_{cer}$, and R_{alu} is in the same order as R_{cer}, thus removing the ceramic side walls introduces an additional loss term $(T'_{trun})^{m'}$. This loss factor has significant impacts on the potential parasitic oscillation. For example, assuming $T'_{trun} \approx 60\%$, after the parasitic beam leaves and re-enters the waveguide through either of the edges for 10 times, the net gain for the parasitic beam $G_{ps,net}$ will be two orders smaller than that with ceramic side walls present.

The modified structure is shown in Fig. 6.3. It had a new mechanism to support the upper electrode and to provide the correct electrode separation so as to obtain the right waveguide gap. The frequency of the RF power generator was changed to 81MHz to meet the requirements of collaborators. With the modified amplifier and with a cw discharge, no evidence of parasitic oscillation was observed in the 5-pass configuration after extensive experimental investigation

over a range of operational conditions. These conditions cover the parasitic oscillation quench point and the pressure range where parasitic oscillation was found to be most serious in previous work with the amplifier having ceramic side walls.

Further experiments were conducted in the set-up for pulsed discharge laser amplification (see Chapter 7) with no ceramic side walls and for a 7-pass configuration. While there was no evidence of parasitic oscillation at high pulse repetition rate, it was observed at low pulse repetition rate operation and exhibited strong dependence on the operating pressure and the pulse repetition rate. The parasitic oscillation started from a discharge interval of ~ 180μs for 72torr, ~ 200μs for 80torr and ~ 280μs for 92torr. At 1kHz, the parasitic oscillation did not quench even at a pressure up to 100torr. No dependence on the duty cycle was observed. Thus, the removal of the ceramic side walls is only a partial solution.

Now the parasitic beam was found propagating with a small angle with respect to the main beam path axis, indicating no involvement of the optical reflection from the internal aluminium walls of the outer envelope. Thus, the parasitic beam was believed to travel via bounces between the two resonator mirrors. In this case, Eq. (8.9) can be simplified as

$$G_{ps,net} = \left[\exp(\gamma_0 Z) \times \exp(-\alpha_1 Z)\right] \times (T_{trun})^m \times R^n \qquad (8.10)$$

where we may have $m = n$. Note that the loss terms in Eq. (8.10) are independent of the operational conditions of the amplifier. Thus the dependence of the parasitic oscillation on the operational conditions reflects the variation of the gain under different operational conditions. Furthermore, as the average gain increases with decreased pulse repetition rate, the fact that the power produced by parasitic oscillation decreases with increased pulse repetition rate and finally quenches indicates the existence of a threshold for the parasitic oscillation.

We have seen in section 8.3.2 that with power amplification in cw mode, parasitic oscillation may be suppressed to some extent by the main beam. However, this is not the case in short pulse amplification, where parasitic oscillation was observed to be hardly affected in the same way, due to the very narrow laser pulse width compared to the discharge duration. The relatively large

average power produced by the parasitic oscillation, compared to the relatively low average power of the main signal, makes the parasitic oscillation extremely damaging.

d) Defining the beam path in the amplifier with masks

This is a familiar method owing to the work reported by Dezenberg et al [8.2]. In an amplifier with a multipass configuration, the main beam bounces back and forth from the resonator mirrors for a limited number of bounces determined by the configuration, leaving more or less space unused between passes on the mirrors. On the contrary, the parasitic oscillation may make use of the whole of the surfaces of the mirrors with probably a far larger number of bounces before exiting the amplifier. The idea of using masks is to block the "blank" spaces unused by the main beam, therefore creating significant loss to the parasitic oscillation with little negative effects on the main beam. This can also be explained according to Eq. (8.10). With the use of masks, the original number of bounces n of the parasitic beam on the resonator mirrors when no masks are used may be divided into two parts, that is, the number of bounces n' on the mirrors and the number of bounces $n-n'$ on the masks. Now Eq. (8.10) can be rewritten as

$$G_{ps,net} = \left[\exp(\gamma_0 Z) \times \exp(-\alpha_1 Z)\right] \times (T_{trun})^m \times R^{n'} \times R_{mask}^{n-n'} \tag{8.11}$$

where the reflectivity of the surfaces of the masks is assumed as R_{mask}, which is normally considerably smaller than R, the reflectivity of the mirrors. By selecting small value of R_{mask} therefore introducing a high loss factor, the net gain $G_{ps,net}$ for the parasitic oscillation may be sufficiently reduced so as to prevent the parasitic oscillation from occurring. This can also be considered as to increase the threshold for parasitic oscillation.

As shown in Fig. 8.4, in the limited spaces between the folding mirrors and the ends of the waveguide, two copper sheet masks, whose surfaces were roughened using sand papers to reduce their reflectivity, were sandwiched, one on each end, between the ceramic blocks and the earthed end metal plates. The masks had 'teeth' preventing any light travelling at an angle to the main beam from reaching the resonator mirrors whilst allowing the main beam to get through. In addition, the teeth were tilted slightly backwards, creating an angle to the waveguide for any

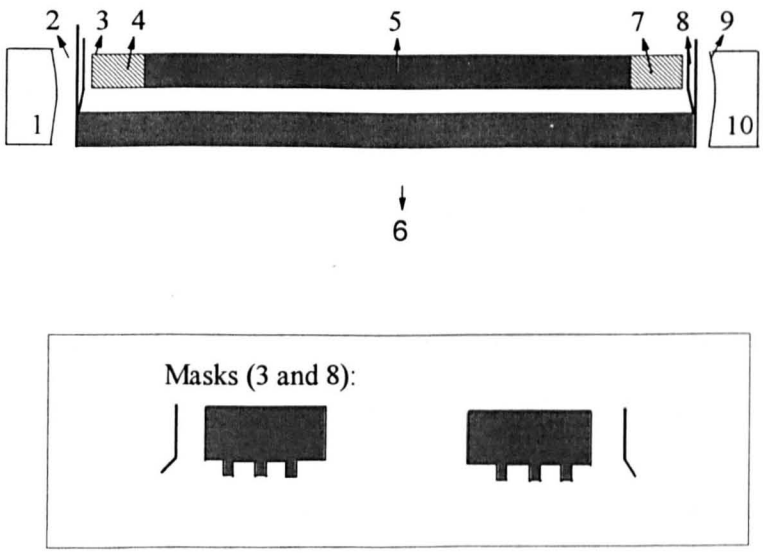

1, 10 - Resonator mirrors 2, 9 - Earthed end plates 3, 8 - Masks

4, 7 - Ceramic blocks 5 - Upper electrode 6 - Lower electrode

Figure 8.4 7-pass amplifier system with internal masks for the elimination of potential parasitic oscillations

reflected light originally from inside the waveguide. The masks had varying distances from a few millimetres to over 10 millimetres to the resonator mirrors which were horizontally tilted. A He-Ne beam originally for assisting the alignment of the multipass configuration was made use of to define the sizes and positions of the main beam on the folding mirrors, and to help locate the 'teeth' of the masks. Due to the partially overlapping nature of the beam path, in the 7-pass configuration, about 10% power loss was resulted from the use of the masks. This loss may be reduced by using masks with narrower teeth with risk of weak parasitic oscillation taking place. However, no obvious impact was observed on the beam profile of the main beam at the exit. It may be anticipated that power loss due to the use of masks is associated with the number of passes of the multipass configuration. More power loss is expected in configurations with larger number of folding passes because of increased overlapping of adjacent beams.

With the inclusion of the masks in front of the resonator mirrors, no parasitic oscillation was observed when the 7-pass system was operated at low repetition rates with pressure from 70torr to over 100torr. This enabled the successful operation of the multipass laser pulse amplification. Nevertheless, weak parasitic oscillation was still observed when the amplifier was operated at a pulse repetition rate of 0.5kHz or lower, indicating continuing increase of gain with decreased pulse repetition rate. However, the parasitic oscillation decreased with increased pressure, and quenched at 95torr. Because the optimum operational pressure is above 95torr for amplification operations at a pulse repetition rate of $\leq$ 0.5kHz, the existence of the parasitic oscillation is *no longer a problem for the amplifier system* under investigation.

8.5 SUMMARY AND CONCLUSION

In this chapter, some theoretical and experimental aspects of the ASE induced noise and parasitic oscillation have been described. Based on the amplifier model used by Kogelnik and Yariv [8.6], an expression for the amount of noise power radiated through an output aperture into a solid angle was derived, giving an insight about how the ASE induced noise (and parasitic oscillation) is linked to the gain, the loss and the population inversion. Both theoretical and experimental investigations indicate the existence of a threshold for the occurrence of the parasitic oscillation.

Thus, the solution for preventing the parasitic oscillation from occurring can be either to reduce the gain to below the threshold or to create extra loss to increase the threshold for parasitic oscillation whilst maintaining the main signal unaffected. As the former method also limits the gain for the main signal thus it is by no means satisfactory, it is the latter approach that makes the basic principle for suppressing or eliminating parasitic oscillations.

With the waveguide amplifier having ceramic side walls, measurements were made in the 1, 5 and 7 pass configurations with cw RF discharge. No parasitic oscillation was observed with the single pass configuration, while considerable parasitic oscillation was observed in the multipass configurations. The power produced by parasitic oscillation was found to be dependent on the operational conditions (the gas pressure and the RF power required to maintain uniform discharge) and increasing with folding passes due to increased net gain. In addition, optical beams produced by parasitic oscillations were observed to exit the amplifier from both the input and output aperture, and to be travelling at an angle with respect to the main beam axis, indicating the involvement of the ceramic side walls in providing sufficient optical feedback for parasitic oscillation.

Several possible solutions for dealing (at least in part) with parasitic oscillation have been discussed. While the optical power induced by parasitic oscillation was reduced by ~ 20% through the use of vertically tilted input and output windows, parasitic oscillations were observed to be completely absent when the ceramic side walls were removed from the amplifier waveguide in the 5-pass and 7-pass configurations with RF discharge in cw mode or pulsed mode at repetition rates higher than 6kHz. However, parasitic oscillations still exist even with the ceramic side walls removed when the system was operating in pulsed mode at low repetition rates due to increased gain level. This parasitic oscillation problem was finally solved by incorporating masks in front of the resonator mirrors to define the main beam and to block potential parasitic oscillations.

Overall, parasitic oscillations in high gain laser amplifiers can be much reduced or even fully eliminated by measures which effectively reduce the optical feedback for potential ASE induced

parasitic oscillations without affecting the main signal. In short, the issue of parasitic oscillation for the multipass planar waveguide CO_2 laser amplification system has been successfully solved.

REFERENCES

8.1 H. Kogelnik and T. J. Bridges, "*A nonresonant multipass CO_2 laser amplifier*," *IEEE J. Quantum Electron.* **QE-3**, pp.95-96 (1967)

8.2 G. J. Dezenberg, E. L. Roy and J. A. Meritt, "*Properties of a 15 cm i.d. multipass CO_2 laser amplifier and oscillator*," *Appl. Opt.*, **9**, pp.516-517 (1970)

8.3 J. T. Verdeyen, "*Laser Electronics*," *Third edition*, Prentice Hall, Englewood Cliffs, New Jersy 07632

8.4 K. R. Manes, D. L. Smith, R. A. Haas, and S. S. Glaros, *IEEE J. Quantum Electron.* **QE-11**, 635(1975)

8.5 J. B. Moreno, G. A. Fisk, and J. M. Hoffman, "*Amplified spontaneous emission and gain-saturation nonlinearity in high-gain optical amplifiers: The biased amplifier*," *J. of Appl. Phys.*, **48**, No.1, January 1977, pp.238-242

8.6 H. Kogelnik, A. Yariv, "*Consideration of noise and scheme for its reduction in laser amplifiers*," *Proc. IEEE*, **52** 165 (1964)

8.7 M. Harris, R. Loudon, "*Optical amplification and spontaneous emission in an Ar+ discharge*," *J. of Mod. Optics*, 1992, **39**, No. 6, pp.1195-1203

8.8 J. W. Hahn and Y. S. Yoo, "*Suppression of amplified spontaneous emission from a four-pass dye laser amplifier*," *Appl. Optics*, 20 July 1998, **37**, No. 21, pp.4867-4870

8.9 G. R. Walker, R. C. Steele and N. G. Walker, *IEEE J. Lightwave Tech.*, **8(9)** 1409 (1990)

8.10 J. A. Arnaud, *IEEE J. Quant. Electron.*, **4(11)** 893 (1968)

8.11 N.A.Olsson, *IEEE J. Quant. Electron.*, **22(5)** 671 (1986)

8.12 R. J. Morley, H. J. Baker, D. R. Hall, M. Harris and J. M. Vaughan, "*Enhancement of coherent laser radar performance by predetection amplification*," *Appl. Optics*, **33**, No. 18, pp.3951-3963, 20 June 1994

8.13 A. L. Schawlow and C. H. Townes, "*Infrared and optical masers*," *Phys. Rev.*, **112**, pp.1940-1949, December 1958

8.14 J. E. Geusic and H. E. D. Scovil, "*A unidirectional travelling wave optical maser*," *Bell Syst. Tech. J.*, **41**, pp.1371-1397, July 1962

8.15 T. J. Shepherd and J. M. Vaughan, "*Noise cancellation in laser emission*," *Phys. Rev. Lett.*, **69**, No. 16, pp.2360-2363, October 1992

8.16 G. E. Warnaka, Noise Control Engineering, pp.100-110 (May-June 1982)

8.17 S. Haykin, "*Adaptive Filter Theory*," Prentice Hall, Eaglewood Cliffs, NJ, 1991, second edition

8.18 M. Harris, R. Loudon, "*Noise and gain in sub-threshold laser modes*," *Opt. Comm.*, 91 (1992), pp.383-389

8.19 K. Tsushima, "*Overview of magneto-optic isolator materials and devices*," *J. Appl. Physics*, **63**, No.8, p.3118, 1988

8.20 D. J. Biswas and R. G. Harrison, "*Optical isolator for single mode TEA CO_2 laser*," *J. Phys. E: Sci. Instrum.*, **18**, pp.256-257, 1985

8.21 K. Shiraishi, F. Tajima, S. Kawakami, "*Compact Faraday rotator for an optical isolator using magnets arranged with alternating polarities*," *Opt. Lett.*, **11**, No.2, pp.82-84, 1986

CHAPTER NINE

CONCLUSIONS AND PROPOSALS FOR FUTURE WORK

This thesis has presented an investigation of the gain and power amplification characteristics of RF-discharge excited planar waveguide amplifiers. This project was initiated from the fact that scaling of diffusion-cooled planar waveguide carbon dioxide laser oscillators to very high average power levels (> 5 kilowatts) is limited by mechanical constraints. The principal objective was to develop a concept for power enhancement based on the master oscillator power amplifier (MOPA) concept, with the planar waveguide gain medium structures. Experimental data are reported over a range of operating parameters (gas pressure, RF power density, input beam intensity etc.) for both pulsed and cw input beams and also for single and multiple (folded) passes of the planar waveguide amplifier, which was filled with a gas mixture of $He(3):N_2(1):CO_2(1)+Xe(5\%)$.

Short pulses at the input to the amplifier ($\tau_p \geq 1\mu sec$) were generated using a long pulse oscillator and an acousto-optic modulator as a pulse slicer. Beam transformation optics were designed and utilised to ensure the excitation of the fundamental waveguide mode with minimal mode coupling, enhanced by modelling and experimental studies of discharge-induced mode matching effects (phase shifts, amplitude variations). In addition, techniques for the elimination of parasitic oscillation were also developed. This MOPA format power amplification technology utilising the planar waveguide structures provides useful outlines for future high power laser applications.

9.1 MAIN CONCLUSIONS

The main conclusions arising from this research can be summarised as follows:

a) The well-known M^2 theory, which is based on the beam width defined in terms of the second moment value, has been used to characterise the laser beam produced by the slab waveguide master oscillator, and to perform the beam transformation through free space and optical systems. Several beam transfer optical systems, including the one-mirror system and the

telecentric system, were investigated to provide optimal mode matching to the planar amplifier in the transverse direction, and to facilitate the beam fold configurations of the amplifier in the lateral direction.

b) A waveguide mode diagnostic technique was developed to analyse the mode mixture evident in the beams produced by planar (slab) waveguide lasers. This technique uses computer simulation to synthesise the far-field beam profile of a waveguide mode mixture which matches most closely that observed experimentally, with details on relative mode intensity variations, phase shifts and so on.

c) Mode matching between the planar waveguides of the master oscillator and the amplifier has been studied. For an arbitrary real laser beam, to obtain optimum mode matching to a planar waveguide, it has been found that the matching condition $w_0 = 0.69a$ for a fundamental Gaussian input beam must be modified with a factor $f(M^2) \geq 1$ which is related to the propagation parameter (or beam quality) of the input beam. Optimum mode matching has been achieved experimentally, with over 97-98% of the power coupled into the fundamental mode, and with the loss being a combination of the waveguiding loss and the truncation loss.

d) Multiple modes and single mode propagation characteristics in both passive and active planar waveguides have been investigated. The active gain medium has been found to modify significantly the modes propagating through the waveguide. If multiple modes are present in the amplifier, these discharge-induced effects will cause continuous variation of beam profiles with varying operating conditions, and thus a variability of exit beam quality due to phase shifts and mode amplitude fluctuations. However, under optimum mode matching conditions, where a "pure" fundamental mode is excited, the discharge-induced effects are negligible. This also indicates that under suitable conditions good beam quality can be achieved from planar waveguide amplifiers.

e) The nature of the parasitic oscillation has been investigated for the planar waveguide amplifiers, operated in both cw and pulsed modes in the multiple beam-folding

configurations. The principle for solving the parasitic oscillation problem is to create extra loss and therefore to reduce the optical feedback just for the parasitic oscillation without affecting the main signal. In this project, the elimination of parasitic oscillation was realised by removing the ceramic side-walls defining the gap of the planar waveguide, combined with the use of masks on the resonator mirrors.

f) Lateral beam characteristics in an active waveguide have been investigated. The discharge effects on the lateral beam characteristics were found to be not significant, apart from the transversely varying saturation effects, which, however, were not obvious at the input power level of ~ 100W, probably because the gain was not saturated enough.

g) With a cw input beam and a cw mode RF discharge, the small signal gain coefficient has been measured for a wide range of operating conditions (gas pressure and RF power deposition) at two RF frequencies (125MHz and 81MHz). A maximum value of 0.65%cm^{-1} at ~ 48torr was obtained for the RF frequency of 81MHz. The order of the saturation intensity was also obtained, which was 2.5-3.0kW/cm^2 for pressures from 45torr to 55torr, and 3.5-4.0kW/cm^2 for pressures from 65torr to 75torr. With an input power level of ~ 100 watts, power gain of > 3 for the 5-pass, and > 4 for the 7-pass amplification have been achieved.

h) Pulsed laser amplification has been conducted for a range of gas pressures and discharge conditions, with an acousto-optic modulator as a pulse slicer to provide short input pulses ($\tau_p \geq 1\mu$sec) for the planar waveguide amplifier. Experimental investigations were carried out on the gain characteristics (time varying gain and pulse energy gain), pulse shape distortion/manipulation, pulse energy/peak power amplification and so on. The unsaturated gain coefficient (small signal gain coefficient) has been determined using single pass amplification as 1.7 ± 0.2%cm^{-1} for a pulse repetition rate of 1kHz and typical gas pressures in the range of 80-90torr. In the 7-pass configuration, at the same pulse repetition rate, saturation energy has been determined to be 26-30mJ/cm^2, which excluds effects of resonance energy transfer from excited N_2 and CO to CO_2 ($00^0 1$). Peak output power of ~ 14kW has been achieved for bell-shaped pulses of $\tau_p \sim 1\mu$s. Near square pulses have also been obtained

at the output, with peak powers of 3-4kW at $\tau_p \sim$ 5-15μs. Higher peak power may be expected by increases of the waveguide area.

9.2 PROPOSALS FOR FUTURE WORK

Investigations presented in this thesis indicate that the MOPA format planar waveguide amplifiers provide a promising technology to produce high average or high peak power laser sources for material processing in industrial applications. A large number of key problems have been addressed and largely resolved, particularly the issues of efficient MO beam coupling, and the avoidance/minimisation of mode-coupling and thereby the preservation of good beam quality in the passage of the beam through the waveguide amplifier. This power enhancement concept may be extended to provide laser beams of special characteristics. Besides, further investigations may be required for the scaling of the planar waveguide laser oscillator/amplifier to average power of 5-10kW, or peak power over 100kW for short pulses.

The following proposals are outlined for future work:

a) To investigate the amplifier performance under fully saturated conditions with a higher input power level. This requires a master oscillator with output power in the range of 700-1000W to ensure full gain saturation, and may be extended to operations of the input power at 2-3kW with increased electrode area.

b) To use a tuneable laser as the master oscillator to provide single (selected) transition line in the range of 9-11μm, to produce amplified, wavelength selectable laser beams as required by a number of wavelength-specific applications.

c) Operating both the master oscillator and the amplifier at cw or quasi-cw mode, with an acousto-optic modulator chopping the MO beam, to produce high modulation rate (up to 100-200kHz) short laser pulses (1-20μs).

d) Development of a versatile MOPA system using planar waveguide structures, with capability of providing laser output at either cw or pulsed mode, or laser beams of special characteristics (such as what mentioned above in b and c). This system requires a *compact* telecentric beam

transformation optical system to map the oscillator beam at its waveguide exit onto the amplifier input plane, and thus to provide naturally optimum beam coupling. In addition, an acousto-optic modulator is needed to control the pulse characteristics (pulse width, shapes and duty cycle). The shift from one function to another will be realised *electronically*, with no or minimum optical adjustment.

e) To extend the MOPA format laser oscillator/amplifier structure to the *stacked format* combining multiple planar waveguides driven by a single power generator. Optically the waveguides can be in series by using coupling optics, or in parallel to form a slab array linked with a certain phaselocking mechanism.

f) Investigations of other potential power enhancement structures. One of the options is the *combination of multiple pairs of slab electrodes configured in a single plane in series*. This approach can reduce both the sizes of the individual electrodes and the RF power distribution problems, although the system may be very large.